Search for radiative B decays to orbitally excited mesons at LHCb

Boris Quintana

▶ To cite this version:

HAL Id: tel-02476983
https://theses.hal.science/tel-02476983

Submitted on 13 Feb 2020

UNIVERSITÉ CLERMONT AUVERGNE
ÉCOLE DOCTORALE DES SCIENCES FONDAMENTALES

THÈSE

présentée pour obtenir le grade de

Docteur d'Université

Spécialité : CONSTITUANTS ÉLÉMENTAIRES

par

QUINTANA Boris

Search for radiative B decays to orbitally excited mesons at LHCb

Thèse soutenue publiquement le 25 Novembre 2019 devant la commission d'examen :

Examinateurs :	Miriam CALVO GOMEZ	Rapporteur
	Isabelle RIPP-BAUDOT	Rapporteur
	Arantza DE OYANGUREN CAMPOS	
	Sébastien DESCOTES-GENON	
	Frédéric BLANC	
Directeurs de thèse :	Vincent TISSERAND	
	Olivier DESCHAMPS	

Remerciements

La thèse est une aventure des plus marquantes. D'abord, elle nous tente par ambition. Elle encourage notre motivation, et empreint d'enthousiasme notre travail. Je me suis vite destiné à vivre ça. . . mais sans connaitre le revers de la médaille. Tout ce que j'ai accompli pendant cette thèse, c'est avant tout grâce à l'aide que j'ai reçue. En tout premier lieu, et comme il est de bon ton, je remercie les membres du jury de thèse, ainsi que l'Université Clermont Auvergne, et puis le labo de physique de Clermont.

Ma profonde gratitude va, avant tout, vers mon directeur de thèse Olivier Deschamps, car c'est tout d'abord grâce à son soutien sans faille, et aussi à sa patience à toute épreuve, que j'ai finalement décroché la timbale. Comme aurait pu le dire un empereur romain : il est comme ces chefs exceptionnels qui, car ils ont tous en commun ce pouvoir secret, ne se battent que pour la dignité des faibles. J'adresserai de même ma reconnaissance, car ils l'auront tout de même bien mérité, à mes mentors et collègues d'LHCb : Eric, Giampi, Régis, Ziad, et Vincent, qui me prêta son nom sans hésitations. Et aussi Stéphane et ses cours –presque- parfaits, qui m'a toujours –apparemment- laissé gagner, que ce soit au billard ou au tennis de table. A mes "jeunes" amis doctorants à présent : Guillaume, pour cet amour sans failles, merci. Yannick merci pour les conseils en escalade, et la liste sans fin de groupes de métal. Merci à Florian pour sa philosophie, les nombreux projets voués à la réussite, et pour la métrique constante de ces lignes. Elle a un rire à faire pâlir les sorcières, un esprit dérangé, a son propre langage, mais Manon a toujours été de bon conseil. Bon courage à vous tous pour finir votre thèse ! Cédric merci pour les vacances au chalet, et aussi les repas à rallonge au Saxo.

Et que ne feindrait-il pas d'être indifférent, si par négligence j'osais l'oublier, lui. Ce rital sans manières, vulgaire au possible. Du tout début de ma thèse jusqu'à la fin, il m'aura aidé beaucoup plus qu'il ne le pense. Je t'attends pour une frame, Giulio. Je pense maintenant aux amis Poitevins, qu'il me tardait de revoir pendant les vacances: Maud, Marie, Julien, Thibaut et Dimitri. Mine de rien on a tous atteint notre but !

Il y a quelqu'un que je ne peux oublier, quelqu'un qui m'a soutenu plus que tous les autres, qui m'a motivé plus longtemps que tout le reste. Pour tout ce que tu as pu m'apporter, merci. Et puis finalement il y a ma famille. Merci à ma mère, à mon père, à Florian. Sans eux tout ça n'aurait pas eu beaucoup de sens.

C'est grâce à vous tous, et ce sans exception, que j'ai finalement réalisé ce rêve.

The Road goes ever on and on
Down from the door where it began.
Now far ahead the Road has gone,
And I must follow, if I can,
Pursuing it with eager feet,
Until it joins some larger way,
Where many paths and errands meet.
And whither then? I cannot say.

– John Ronald Reuel Tolkien, *The Lord of the Rings*

Abstract

This document presents studies of radiative decays of B^0 and B_s mesons to orbitally excited states, produced in proton collisions at the Large Hadron Collider (LHC) of CERN (European Council for Nuclear Research). It takes place in the context of the search for new physics processes beyond the standard model of particle physics. The work is based on the data collected at the LHCb experiment during the Run 1(2011-2012) and the Run 2 (2015-2018) of the LHC, which corresponds to an integrated luminosity of about 8.7 fb^{-1}. First, an optimised selection of the final states comprising of two charged tracks and a high energy photon is put in place, regrouping a large samples of B hadron radiative decays. Then, a mass model is fit to the data distribution, allowing to statistically subtract the background contributions in the data set.

A first amplitude analysis is then developed to study the hadronic structure in the $B_s \to K^+ K^- \gamma$ decay mode. Resulting from this analysis is the first observation of the $B_s \to f_2'(1525)\gamma$ mode together with a relative branching ratio measurement:

$$\frac{\mathcal{B}(B_s \to f_2'\gamma)}{\mathcal{B}(B_s \to \phi\gamma)} = (24.1 \pm 0.9 \text{ (stat)} \ {}^{+1.6}_{-0.8} \text{ (syst)} \ \pm 0.6 \text{ (BR)}) \times 10^{-2}$$

It is the second radiative decay mode observed for the B_s meson. A similar analysis is performed on the $B^0 \to K^\pm \pi^\mp \gamma$ mode, allowing a preliminary measurement of the relative branching ratio of $B^0 \to K_2^*(1430)\gamma$:

$$\frac{\mathcal{B}(B^0 \to K_2^{*0}(1430)\gamma)}{\mathcal{B}(B^0 \to K^{*0}(892)\gamma)} = (36.4 \pm 0.4 \text{ (stat)} \ \pm 1.3\text{(BR)})\%$$

However, a detailed systematics study is needed to assess its competitivity with previous measurements of this decay mode. Making use of a similar selection strategy, a preliminary study of $B \to K_S^0 hh\gamma$ modes is also set up during the thesis to estimate the available statistics for these modes at LHCb, which are particularly interesting to measure the photon polarisation in the $b \to s\gamma$ transition. This work will be the starting point of an analysis comprising the future data that will be collected during the Run 3 of the LHC.

Keywords:

Résumé

Cette thèse présente une étude des désintégrations radiatives des mésons B^0 et B_s, produits lors des collisions de protons du Grand Collisionneur de Hadrons (LHC), au Laboratoire Européen de Physique des Particules (CERN), vers des états orbitallement excités. Elle s'inscrit dans le contexte de recherche indirecte de physique au-delà du Modèle Standard de la Physique des Particules. Les données récoltées par le détecteur LHCb pendant le Run 1(2011-2012) et le Run 2 (2015-2018) du LHC, correspondant à une luminosité intégrée de 8.7 fb^{-1}, sont utilisées pour l'analyse. Une sélection optimisée des états finals comprenant deux traces chargées et un photon est mise en place, permettant de regrouper un très grand échantillon de désintégrations radiatives de hadrons beaux. Un modèle est ajusté à la masse invariante du système, permettant de soustraire statistiquement les différentes contributions de bruit de fond polluant les données.

Une première analyse en amplitude est ensuite mise enplace pour une étude détaillée de la structure hadronique dans le mode $B_s \to K^+ K^- \gamma$. Elle permet la première observation du mode $B_s \to f_2'(1525)\gamma$ avec une mesure de rapport d'embranchement normalisé à celui du mode dominant $B_s \to \phi\gamma$:

$$\frac{\mathcal{B}(B_s \to f_2'\gamma)}{\mathcal{B}(B_s \to \phi\gamma)} = (24.1 \pm 0.9 \text{ (stat)} \ ^{+1.6}_{-0.8} \text{ (syst)} \ \pm 0.6 \text{ (BR))} \times 10^{-2}$$

C'est également le second mode de désintégration radiative du méson B_s jamais observé. Une analyse similaire est faite pour le mode $B^0 \to K^{\pm}\pi^{\mp}\gamma$, et permet une mesure préliminaire du rapport d'embranchement du mode $B^0 \to K_2^*(1430)\gamma$, normalisé à celui du mode dominant $B^0 \to K^{*0}\gamma$:

$$\frac{\mathcal{B}(B^0 \to K_2^{*0}(1430)\gamma)}{\mathcal{B}(B^0 \to K^{*0}(892)\gamma)} = (36.4 \pm 0.4 \text{ (stat)} \ \pm 1.3\text{(BR))}\%$$

Une étude détaillée des erreurs systématiques affectant la mesure reste néanmoins nécessaire pour connaitre sa compétitivité vis-à-vis des mesures actuelles. Utilisant une stratégie similaire, une sélection préliminaire des modes $B \to K_S^0 hh\gamma$ est aussi mise en place pour estimer la statistique disponible à LHCb pour ces modes qui permettraient de mesurer la polarisation du photon dans la transition $b \to s\gamma$. Ce travail sera à la base d'une analyse portée sur les données du Run 3 du LHC.

Mots Clés:

Expérience LHCb - Modèle Standard - Physique des Saveurs - Courants Neutres Changeant la Saveur (FCNC) - Désintégrations radiatives des mésons beaux - $B_s \to \phi\gamma$ - $B^0 \to K^{*0}\gamma$.

Contents

Introduction

The Standard Model (SM) of Particle Physics has been very successful in describing the fundamental interactions and elementary constituents of matter. As incomplete as it is, since it does not include a description of gravity nor an explanation for the colossal matter-antimatter asymmetry in the universe, this theory has proved in many ways over the last decades its capacity of prediction with an unprecedented accuracy. In particular, one of the last and most outstanding achievement was the confirmation of the existence of the Brout-Englert-Higgs boson, the 4th of July 2012, at the LHC. However, the few deficiencies it suffers from has led to the general agreement in the particle physics community that the SM might be the effective version of an underlying broader theory. Tensions between the Standard Model and experimental results have to be investigated in order to find any indication of New Physics (NP), or physics Beyond the Standard Model (BSM). The approach of experimental flavor physics is to determine with the highest precision possible physical observables related to the parameters of the SM in order to constrain the new theories. The studies conducted during this thesis are directed towards this goal of finding deviations in the behaviour of nature with respect to the predictions of the SM. More precisely, this work is focused on the study of radiative decays of B hadrons, as they are rare decays occuring through a $b \to s(d)\gamma$ quark transition and therefore can be a great probe for the search of New Physics. One of the most interesting observables to measure in these decays is the polarization of the photon : as it has predominantly a left-handed helicity in the SM, any sizeable amount of right-handed photon would be a clear sign of New Physics. The LHCb collaboration has observed the polarized nature of the photon in $B^+ \to K^+\pi^+\pi^-\gamma$ decays [1] and has performed various studies of $B^0 \to K^{*0}\gamma$ and $B_s \to \phi\gamma$ decays. This document presents a study of the hadronic structure in $B^0 \to K^{\pm}\pi^{\mp}\gamma$ and $B_s \to K^+K^-\gamma$ decays that aims at an observation of radiative B decays to orbitally excited (L$\neq$0) mesons. A secondary work has also been conducted on the study of $B \to K_s^0 h^+ h^-\gamma$ decays.

While Chapter 1 gives an introduction to the Standard Model and its phenomenology, with an emphasis on the description of $b \to s\gamma$ decays, Chapter 2 focuses on describing the experimental framework at LHCb and in particular the specificities of the work with neutral objects. Chapter 3 is dedicated to the multichannel selection of $h^+h^-\gamma$ final states that has been set up to prepare samples of good purity and high statistics of B^0, B_s and Λ_b radiative decays. The amplitude analyses making use of this selection are then developed in Chapter 4 and 5. Finally, the preliminary work towards the study of $B \to K_s^0 h^+ h^-\gamma$ decays is presented in Appendix.

Chapter 1

Theoretical framework

1.1 The Standard Model

The current best theory to describe the fundamental constituents of matter and their interactions is the Standard Model (SM) of particle physics. Established within the Quantum Field Theory (QFT) formalism, it allows to describe in a unified way the strong, weak and electromagnetic interactions, and separates the elementary particles between fermions of half-integer spins (matter particles) and bosons of integer spins, that mediate the interactions. In QFT, particles correspond to excitations of the fundamental underlying quantum fields, while the fundamental forces comes from interaction terms between the fields. Furthermore, the SM is a local gauge theory described by the product of symmetry groups [2] :

$$SU(3)_C \times [SU(2)_L \times U(1)_Y] \,, \tag{1.1}$$

The $SU(3)_C$ group describes the strong interaction, mediated by 8 massless gluons carrying color charge (C). The group $SU(2)_L \times U(1)_Y$ describes the electroweak interaction associated to the three massive gauge bosons $W^{\pm}$, Z and the photon γ. Y is the weak hypercharge and is defined by the Gell-Mann-Nishijima relation $Q = I_3 + Y/2$, where Q is the electric charge and I_3 the third component of the weak isospin.

In the SM there are three generations of fermions divided into quarks, that carry color charge, and leptons. Each generation consists of five representations of the group $SU(3)_C \times [SU(2)_L \times U(1)_Y]$:

$$Q_{Li}^I(3,2)_{+1/6}, \quad u_{Ri}^I(3,1)_{+2/3}, \quad d_{Ri}^I(3,1)_{-1/3}, \quad L_{Li}^I(1,2)_{-1/2}, \quad l_{Ri}^I(1,1)_{-1} \tag{1.2}$$

and a single scalar representation composed by two complex scalar fields

$$\phi(1,2)_{+1/2} = \begin{pmatrix} \phi^+ \\ \phi^0 \end{pmatrix} \,. \tag{1.3}$$

This means for instance that left-handed quarks $Q_L^I = (u_L^I, d_L^I)^T$ (where T stands for transposed) are triplets of $SU(3)_C$, doublets of $SU(2)_L$ and carry hypercharge $Y = +1/6$.

The upper-index I denotes interaction eigenstates. The lower-index $i = 1, 2, 3$ is the generation index. The u_R^I and d_R^I singlets are generic right-handed up-type and down-type quarks, $L_L^I = (\nu_L^I, e_L^I)^T$ are three $SU(2)_L$ leptonic doublets and l_R^I are three right-handed charged leptonic singlets. The summary table of the fundamental particles of the SM is shown in Fig. 1.1. As can be noticed, the table also shows the Higgs boson that was

Figure 1.1: *Standard Model fundamental fermions and bosons and their properties.*

observed for the first time in 2012 at the LHC by ATLAS [3] and CMS [4] experiments. ATLAS [5] and CMS [6] confirmed the scalar nature of the new particle. The current world average measurement of the Higgs boson mass reported on the Particle Data Group (PDG) is $m_H = 125.09 \pm 0.24$ GeV [7].

The most general renormalizable lagrangian that describes the SM interactions can be divided into four different parts:

$$\mathcal{L}_{SM} = \mathcal{L}_{Gauge} + \mathcal{L}_{Kinetic} + \mathcal{L}_{Higgs} + \mathcal{L}_{Yukawa} . \tag{1.4}$$

The first term is related to the propagation of the gauge fields and is given by

$$\mathcal{L}_{Gauge} = -\frac{1}{4} G_{\mu\nu}^a (G^a)^{\mu\nu} - \frac{1}{4} W_{\mu\nu}^d (W^d)^{\mu\nu} - \frac{1}{4} B_{\mu\nu} B^{\mu\nu}, \tag{1.5}$$

with

$$G^a_{\mu\nu} = \partial_\mu G^a_\nu - \partial_\nu G^a_\mu + g_s f_{abc} G^b_\mu G^c_\nu ~, \tag{1.6}$$

$$W^d_{\mu\nu} = \partial_\mu W^d_\nu - \partial_\nu W^d_\mu + g\epsilon_{def} W^e_\mu W^f_\nu ~, \tag{1.7}$$

$$B_{\mu\nu} = \partial_\mu B_\nu - \partial_\nu B_\mu ~, \tag{1.8}$$

where:

- $G^a_{\mu\nu}$ is the Yang-Mills tensor which involves eight ($a = 1, 2, \ldots, 8$) gluon fields G^a_μ, the strong coupling constant g_s and the $SU(3)_C$ structure constants f_{abc}.

- $W^d_{\mu\nu}$ is the weak field tensor which involves three ($d = 1, 2, 3$) gauge fields W^d_μ, the weak coupling constant g and the $SU(2)_L$ structure constants ϵ_{def}.

- $B_{\mu\nu}$ is the electromagnetic tensor which involves the $U(1)_Y$ gauge field B_μ.

Permutation terms $f_{abc} G^b_\mu G^c_\nu$ and $\epsilon_{def} W^e_\mu W^f_\nu$ in $G^a_{\mu\nu}$ and $W^d_{\mu\nu}$ reflect a crucial property of strong and weak interactions, namely they are non-abelian theories in which gauge fields can directly couple and self-interact. This is not true for the electromagnetic interaction which is an abelian theory and forbids the photon self-interaction.

The second term of $\mathcal{L}_{SM}$ describes the kinetic energy of fermions and their interaction with the gauge fields. It is given by

$$\mathcal{L}_{Kinetic} = \overline{\psi}\gamma^\mu i D_\mu \psi ~, \tag{1.9}$$

where γ^μ are the Dirac matrices, $\overline{\psi} = \psi^\dagger \gamma^0$ and the spinor fields ψ are the three fermion generations of Eq. 1.2. D_μ is the total covariant derivative defined as

$$D_\mu = \underbrace{\partial_\mu + \frac{ig}{2} W^d_\mu \sigma_d + \frac{ig'}{2} B_\mu Y}_{\nabla_\mu} + \frac{ig_s}{2} G^a_\mu \lambda_a ~. \tag{1.10}$$

where σ_d, Y and λ_a are respectively the generators of $SU(2)_L$, $U(1)_Y$ and $SU(3)_C$ symmetry groups, g' is the hypercharge coupling constant and ∇_μ stands for the covariant derivative only in the electroweak sector. σ_d are the 2×2 Pauli matrices and λ_a are the 3×3 Gell-Mann matrices.

The third part of Eq. 1.4, the Higgs lagrangian, describes the mechanism of spontaneous electroweak symmetry breaking (EWSB) through which the gauge boson mediators of the weak interaction acquire masses. This lagrangian is written as

$$\mathcal{L}_{Higgs} = (\nabla_\mu \phi)^\dagger (\nabla^\mu \phi) + \underbrace{\mu^2 \phi^\dagger \phi + \lambda(\phi^\dagger \phi)^2}_{V(\phi^\dagger \phi)} ~, \tag{1.11}$$

where the first term expresses the kinetic energy of the Higgs field and its gauge interactions. The two other terms, the mass term and the self-interaction term, represent the Higgs

potential $V(\phi^\dagger\phi)$: μ and λ are free parameters named respectively "mass" and "quartic coupling". The essential aspect of the Higgs mechanism is the introduction of the complex scalar doublet ϕ of Eq. 1.3, which modifies the vacuum state making it not symmetrical. This field is present everywhere in the space-time and weakly self-interacting. By means of this field the masses of all particles are dynamically generated through their interaction with ϕ. The Higgs boson is nothing but the excitation of this field. For $\mu^2 < 0$ and $\lambda > 0$ the potential $V(\phi^\dagger\phi)$ has the shape of a "mexican hat" (see Fig. 1.2) and the vacuum state $\phi = 0$ becomes a local maximum which disturbs the symmetry of the system, making the configuration unstable. This way, by setting $\phi^+ = 0$, $\phi^0 = v$ and $Y = 1$, the Higgs field acquires a non-trivial vacuum expectation value $\langle\phi\rangle_0$ given by

$$\langle\phi\rangle_0 = \frac{1}{\sqrt{2}}\begin{pmatrix} 0 \\ v \end{pmatrix} \qquad \text{with} \qquad v = \sqrt{\frac{-\mu^2}{\lambda}} \simeq 246 \text{ GeV} , \qquad (1.12)$$

that causes the EWSB and the SM gauge symmetry breaking $G_{SM} \longrightarrow SU(3)_C \times U(1)_{EM}$.
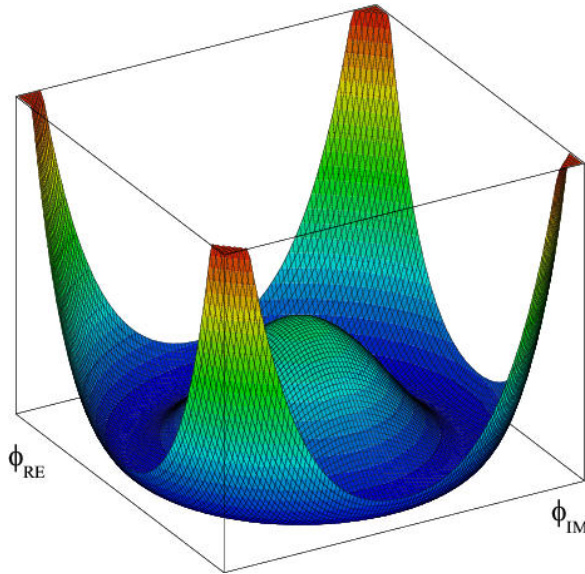
Figure 1.2: *Shape of the Higgs potential for $\mu^2 < 0$ and $\lambda > 0$ as a function of $\phi_{RE} = \mathfrak{Re}\,(\phi)$ and $\phi_{IM} = \mathfrak{Im}\,(\phi)$.*

By means of this dynamics the $W^\pm$ and Z bosons acquire mass together with the Higgs boson H, that has mass $m_H = \sqrt{-2\mu^2} = \sqrt{2\lambda}v$. Table 1.1 shows the masses and mass-eigenstates of the weak bosons together with the ones of the photon ($A = \gamma$).

The last term of $\mathcal{L}_{SM}$ is the Yukawa lagrangian which describes the interactions between fermions and the Higgs field. It is given by

$$\mathcal{L}_{Yukawa} = -Y_{ij}^d\overline{Q_{Li}^I}\phi d_{Rj}^I - Y_{ij}^u\overline{Q_{Li}^I}\tilde{\phi}u_{Rj}^I - Y_{ij}^l\overline{L_{Li}^I}\phi l_{Rj}^I + h.c. , \qquad (1.13)$$

where $\tilde{\phi} = i\sigma_2\phi^\dagger$, $Y^{u,d,l}$ are 3×3 complex matrices and i, j are generation labels. Neglecting leptons, when EWSB occurs the lagrangian of Eq. 1.13 yields mass terms for quarks. The

16

Boson	Mass-eigenstate	Mass
$W_\mu^\pm$	$\dfrac{1}{\sqrt{2}}(W_\mu^1 \mp iW_\mu^2)$	$m_W = \dfrac{gv}{2}$
Z_μ	$\cos\theta_w W_\mu^3 - \sin\theta_w B_\mu$	$m_Z = \dfrac{m_W}{\cos\theta_w}$
A_μ	$\sin\theta_w W_\mu^3 + \cos\theta_w B_\mu$	$m_A = 0$

Table 1.1: *Mass-eigenstates and masses of the fundamental vector bosons; θ_w is the Weinberg mixing angle.*

physical states can be obtained diagonalizing the Y^f matrix using four unitary matrices $V_{L,R}^f$ such that

$$M_{diag}^f = \frac{v}{\sqrt{2}}V_L^f Y^f V_R^{f\dagger} \ , \tag{1.14}$$

where $f = u, d$ and $v/\sqrt{2} = \langle\phi\rangle_0$. As a consequence of this diagonalization, the charged current interactions are then given by

$$\mathcal{L}_{W^\pm} = -\frac{g}{\sqrt{2}}\overline{u}_{Li}\gamma^\mu \left(V_L^u V_L^{d\dagger}\right)_{ij} d_{Lj}W_\mu^+ + h.c. \ , \tag{1.15}$$

and weak-eigenstates and mass-eigenstates of quarks become mixed. The product $\left(V_L^u V_L^{d\dagger}\right) = V_{CKM}$, that contains the couplings of an up-type antiquark and a down-type quark to the charged W bosons, is called Cabibbo-Kobayashi-Maskawa (CKM) matrix [8], [9] and allows to write the interaction-eigenstates as

$$\begin{pmatrix} d^I \\ s^I \\ b^I \end{pmatrix} = V_{CKM}\begin{pmatrix} d \\ s \\ b \end{pmatrix} = \begin{pmatrix} V_{ud} & V_{us} & V_{ub} \\ V_{cd} & V_{cs} & V_{cb} \\ V_{td} & V_{ts} & V_{tb} \end{pmatrix}\begin{pmatrix} d \\ s \\ b \end{pmatrix}. \tag{1.16}$$

By convention, the interaction-eigenstates and the mass-eigenstates are chosen to be equal for the up-type quarks, whereas the down-type quarks are chosen to be rotated. This important matrix will be extensively discussed in the following.

1.2 The $\mathcal{C}, \mathcal{P}$ and $\mathcal{T}$ symmetries

Symmetries are a very important topic in quantum field theory since they help restricting classes of models, providing stability and simplifying calculations as well as results. Symmetries, which are broadly divided into spacetime and internal ones, are some transformations of fields and coordinates that map solutions of the equations of motion to other, allowing to generate a whole class of solutions from a single one.

A spacetime symmetry is a transformation that acts directly on spacetime coordinates, like a Poincaré translation

$$x'^\mu = \Lambda^\mu_{\ \nu}(x^\nu + a^\nu),$$

where a^ν is an arbitrary constant four vector and $\Lambda^\mu_{\ \nu}$ is the Lorentz matrix. An example of internal symmetry is a global phase transformation which maps a field into another without making reference to its spacetime dependence:

$$\psi'(x) = e^{iq\alpha}\psi(x), \qquad \overline{\psi'}(x) = \overline{\psi}(x)e^{-iq\alpha}, \qquad 0 \le \alpha < 2\pi,$$

where q is the particle electrical charge. Unlike spacetime symmetries, internal symmetry transformations involve peculiar field degrees of freedom such as the electric charge, the weak charge and the colour charge. From the Noether's theorem, if these transformations of coordinates and fields make null the variation of the action $S = \int \mathcal{L} \, \mathrm{d}^4x$, they are called *continuous symmetries* and correspond to definite constants of motion like energy or electrical charge.

In addition to these symmetries, there is another relevant class of transformations that belongs to the category of internal ones, the *discrete symmetries* such as $\mathcal{C}$, $\mathcal{P}$ and $\mathcal{T}$ transformations. These operations are named charge conjugation, parity transformation and time reversal: their transformation rules will be shown only for the spinor field, neglecting bilinears like mass terms $\overline{\psi}(x)\psi(x)$ and current terms $\overline{\psi}(x)\gamma^\mu\psi(x)$.

The charge conjugation $\mathcal{C}$ is the operation under which a particle is transformed into its antiparticle of equal mass, momentum and spin, but opposite quantum numbers like electric charge. Its action is given by $\psi^\mathcal{C}(x) = \mathcal{C}\psi(x)\mathcal{C}^\dagger$ with $\mathcal{C} = \mathcal{C}^\dagger = \mathcal{C}^{-1}$ and $\mathcal{C}^2 = \mathbb{I}$ and the transformation rules for the fields are :

$$\psi^\mathcal{C}(x) = \mathcal{C}\psi(x)\mathcal{C} = \gamma^2\left(\psi^\dagger(x)\right)^T = \left(\psi^\dagger(x)\gamma^2\right)^T = \left(\overline{\psi}(x)\gamma^0\gamma^2\right)^T, \qquad (1.17)$$

$$\overline{\psi^\mathcal{C}}(x) = \mathcal{C}\overline{\psi}(x)\mathcal{C} = \psi^{\mathcal{C}\dagger}(x)\gamma^0 = \left(-\gamma^2\psi(x)\right)^T\gamma^0 = \left(-\gamma^0\gamma^2\psi(x)\right)^T.$$

The parity transformation $\mathcal{P}$ or spatial inversion is the operation that reflects the space coordinates $\mathbf{x}$ into $-\mathbf{x}$ and is equivalent to a mirror reflection followed by a rotation. Its action is given by $\psi^\mathcal{P}(x) = \mathcal{P}\psi(t,\mathbf{x})\mathcal{P}^\dagger$ with $\mathcal{P} = \mathcal{P}^\dagger = \mathcal{P}^{-1}$ and $\mathcal{P}^2 = \mathbb{I}$ and the transformation rules are

$$\psi^\mathcal{P}(x) = \mathcal{P}\psi(t,\mathbf{x})\mathcal{P} = \gamma^0\psi(t,-\mathbf{x}) , \qquad (1.18)$$

$$\overline{\psi^\mathcal{P}}(x) = \mathcal{P}\overline{\psi}(t,\mathbf{x})\mathcal{P} = \overline{\psi}(t,-\mathbf{x})\gamma^0 .$$

Since the spin direction is left unaltered a very important consequence of this operation is that the helicity of the particle, or the projection of the spin onto the direction of momentum, is reversed: this means that under the parity transformation a left-handed particle becomes right-handed.

Finally, we have the time reversal transformation $\mathcal{T}$ that reflects the time coordinate t into $-t$ leaving $\mathbf{x}$ unchanged: this means that while spatial relations must be the same, all momenta and angular momenta must be reversed. For this reason the $\mathcal{T}$ operation represents the reversal of motion. Its action is given by $\psi^\mathcal{T}(x) = \mathcal{T}\psi(t,\mathbf{x})\mathcal{T}^\dagger$ and defining the matrix Θ

$$\Theta = -\gamma^1\gamma^3 = -i\begin{pmatrix} \sigma_2 & 0 \\ 0 & \sigma_2 \end{pmatrix}, \qquad (1.19)$$

that fulfills the relations $\Theta\Theta^* = -\mathbb{I}$ and $\Theta\Theta^\dagger = \mathbb{I}$, we find the transformation rules for the fields

$$\psi^{\mathcal{T}}(x) = \mathcal{T}\psi(t, \mathbf{x})\mathcal{T}^\dagger = \Theta\psi(-t, \mathbf{x}), \tag{1.20}$$
$$\overline{\psi^{\mathcal{T}}}(x) = \mathcal{T}\overline{\psi}(t, \mathbf{x})\mathcal{T}^\dagger = \overline{\psi}(-t, \mathbf{x})\Theta^\dagger \quad .$$

The experimental evidence actually shows that the electromagnetic and strong interactions as well as classical gravity respect $\mathcal{C}$ and $\mathcal{P}$ symmetries and, therefore, their combination $\mathcal{CP}$. On the other hand weak interactions violate both $\mathcal{C}$ and $\mathcal{P}$ in the strongest possible way. For example the $W^\pm$ bosons couple only to left-handed particles and right-handed antiparticles, but neither to right-handed particles nor to left-handed antiparticles. Parity violation, that was prompted first by C. N. Yang and T. D. Lee in 1956 [10], was confirmed the next year in both nuclear [11] and pion beta decay [12], [13]. After this discovery, the combined $\mathcal{CP}$ symmetry was proposed as a symmetry of Nature.

This aspect is crucial because if $\mathcal{CP}$ was an exact symmetry, the laws of Nature would be the same for matter and antimatter. However, $\mathcal{CP}$ is violated in certain rare processes and thus only the combined discrete $\mathcal{CPT}$ symmetry transformation is an exact symmetry of Nature.

1.3 The CKM matrix

In the SM, the $\mathcal{CP}$ symmetry is broken by the quarks' Yukawa couplings with the Higgs field which are described by the lagrangian of Eq. 1.13 limited to the quark sector. After the EWSB and the mass diagonalization of Eq. 1.14, the weak-eigenstates and mass-eigenstates of quarks become mixed and the charged current interactions are given by

$$\mathcal{L}_{W^\pm} = -\frac{g}{\sqrt{2}}\overline{u}_{Li}\gamma^\mu \left(V_{CKM}\right)_{ij} d_{Lj}W_\mu^+ + h.c.,$$

where V_{CKM} is the Cabibbo-Kobayashi-Maskawa matrix, previously defined in Eq. 1.16. The fundamental property of the CKM matrix is its unitarity: $V_{CKM}^\dagger V_{CKM} = V_{CKM}V_{CKM}^\dagger = \mathbb{I}$. This condition determines the number of free parameters of the matrix. A generic $N \times N$ unitary matrix contains N^2 independent parameters, $2N - 1$ of which can be eliminated redefining the phase of the N up-type and N down-type quarks as

$$u_{Li} \rightarrow e^{i\varphi_i^u}u_{Li} , \qquad d_{Lj} \rightarrow e^{i\varphi_j^d}d_{Lj} , \tag{1.21}$$

in such a way to reduce free parameters to $(N - 1)^2$. The remaining parameters can be further splitted into mixing angles and complex phases as follows

$$\underbrace{\frac{1}{2}N(N - 1)}_{\text{mixing angles}} + \underbrace{\frac{1}{2}(N - 1)(N - 2)}_{\text{complex phases}} = (N - 1)^2 . \tag{1.22}$$

As can be noticed, the case $N = 2$ leads to only one free parameter that is the Cabibbo mixing angle θ_C contained in the Cabibbo matrix [8]

$$V_C = \begin{pmatrix} \cos\theta_C & \sin\theta_C \\ -\sin\theta_C & \cos\theta_C \end{pmatrix} .$$ (1.23)

The $N = 3$ case leads to the generalization of the V_C matrix, the V_{CKM} matrix, which contains four physical parameters, namely three mixing angles and one complex phase. This phase causes the $\mathcal{CP}$ violation in the SM.

Between the many possible conventions, a standard choice to parametrize V_{CKM} is [7]

$$V_{CKM} = \begin{pmatrix} c_{12}c_{13} & s_{12}c_{13} & s_{13}e^{-i\delta} \\ -s_{12}c_{23} - c_{12}s_{23}s_{13}e^{i\delta} & c_{12}c_{23} - s_{12}s_{23}s_{13}e^{i\delta} & s_{23}c_{13} \\ s_{12}s_{23} - c_{12}c_{23}s_{13}e^{i\delta} & -c_{12}s_{23} - s_{12}c_{23}s_{13}e^{i\delta} & c_{23}c_{13} \end{pmatrix}$$ (1.24)

where $s_{ij} = \sin\theta_{ij}$, $c_{ij} = \cos\theta_{ij}$ and δ is the $\mathcal{CP}$ violating phase. All the angles θ_{ij} can be chosen to lie in the first quadrant, so that $s_{ij} \geq 0$ and $c_{ij} \geq 0$. They must vanish if there is no mixing between two quark generations i, j: in particular, in the limit $\theta_{13} = \theta_{23} = 0$ the CKM matrix would reduce to V_C. The presence of a complex phase in the mixing matrix is a necessary but not sufficient condition for having $\mathcal{CP}$ violation. As pointed out in [14], another key condition is

$$(m_t^2 - m_c^2)(m_t^2 - m_u^2)(m_c^2 - m_u^2)(m_b^2 - m_s^2)(m_b^2 - m_d^2)(m_s^2 - m_d^2) \times J_{CP} \neq 0 \quad , \quad$$ (1.25)

where

$$J_{CP} = |\mathfrak{Im}(V_{ij}V_{kl}V_{il}^*V_{kj}^*)| \qquad (i \neq k, j \neq l)$$ (1.26)

is the Jarlskog invariant. The mass terms in Eq. 1.25 reflect the fact that the CKM phase could be eliminated through a transformation of the quark fields like Eq. 1.21 if any two up-type or down-type quarks were degenerate in mass. Consequently, the origin of $\mathcal{CP}$ violation is deeply connected to other important questions of particle physics like the "flavour problem", the hierarchy of quark masses, and the number of fermion generations. The Jarlskog invariant J_{CP} is a phase-convention-independent measurement of the size of $\mathcal{CP}$ violation, that according to the standard parametrization of Eq. 1.24 can be written as

$$J_{CP} = s_{12}s_{13}s_{23}c_{12}c_{23}c_{13}^2 \sin\delta .$$ (1.27)

According to the tiny $\mathcal{CP}$ violation effects observed within the SM, it corresponds to the very small value [15]

$$J_{CP} = (3.099^{+0.052}_{-0.063}) \times 10^{-5} .$$ (1.28)

1.3.1 Magnitude of the matrix elements

Now we give an overview of the main measurements leading to the experimental values of the CKM matrix elements. The size of following $|V_{ij}|$ elements can be directly determined from the following tree-level processes [7]:

$|V_{ud}|$: Nuclear β decays or neutron decay $n \to pe^-\overline{\nu}_e$;

$|V_{us}|$: Semileptonic kaon decays $K \to \pi l \nu_l$ and hadronic tau decays $\tau^- \to K^- \nu_\tau$. It is also accessible through $|V_{us}/V_{ud}|$ measuring the ratios $K^+ \to \mu^+ \nu_\mu(\gamma)/\pi^+ \to \mu^+ \nu_\mu(\gamma)$ (where (γ) indicates that radiative decays are included) and $\tau^- \to K^- \nu_\tau/\tau^- \to \pi^- \nu_\tau$;

$|V_{cd}|$: Semileptonic D meson decays $D \to \pi l \nu_l$ and leptonic decay $D^+ \to \mu^+ \nu_\mu$. It can also be accessed through measurement of charm-production fractions in neutrino interactions;

$|V_{cs}|$: Semileptonic D decays and semileptonic D_s decays;

$|V_{cb}|$: Exclusive and inclusive semileptonic decays of B mesons to charm;

$|V_{ub}|$: Semileptonic $B \to X_u l \nu$ decays;

$|V_{tb}|$: Branching fractions $\mathcal{B}(t \to Wb)/\mathcal{B}(t \to Wq)$ with $q = b, s, d$ from top decays and single top-quark-production cross section.

The $|V_{td}|$ and $|V_{ts}|$ elements cannot be measured using tree-level processes and need to be determined from the measurement of the oscillation frequencies of the $B^0 - \overline{B}^0$ and $B_s^0 - \overline{B}_s^0$ systems. They can also be accessed through $|V_{td}/V_{ts}|$ as extracted from decays occurring via $b \to q\gamma$ radiative transitions, where $q = s, d$. In Fig. 1.3 are shown the Feynman diagrams for some important processes that allow to extract the experimental values of the first five CKM matrix elements of the list above.

CKM matrix element	Fitted value
$|V_{ud}|$	$0.974334^{+0.000064}_{-0.000068}$
$|V_{us}|$	$0.22508^{+0.00030}_{-0.00028}$
$|V_{cd}|$	$0.22494^{+0.00029}_{-0.00028}$
$|V_{cs}|$	$0.973471^{+0.000067}_{-0.000067}$
$|V_{cb}|$	$0.04181^{+0.00028}_{-0.00060}$
$|V_{ub}|$	$0.003715^{+0.000060}_{-0.000060}$
$|V_{td}|$	$0.008575^{+0.000076}_{-0.000098}$
$|V_{ts}|$	$0.04108^{+0.00030}_{-0.00057}$
$|V_{tb}|$	$0.999119^{+0.000024}_{-0.000012}$

Table 1.2: *Magnitudes of the CKM matrix elements [15].*

Since the probability of a particular quark transition is proportional to the square modulus $|V_{ij}|^2$ of the relative matrix element, the knowledge of these elements is very important to determine the amplitudes of weak decays. The CKM matrix elements can be
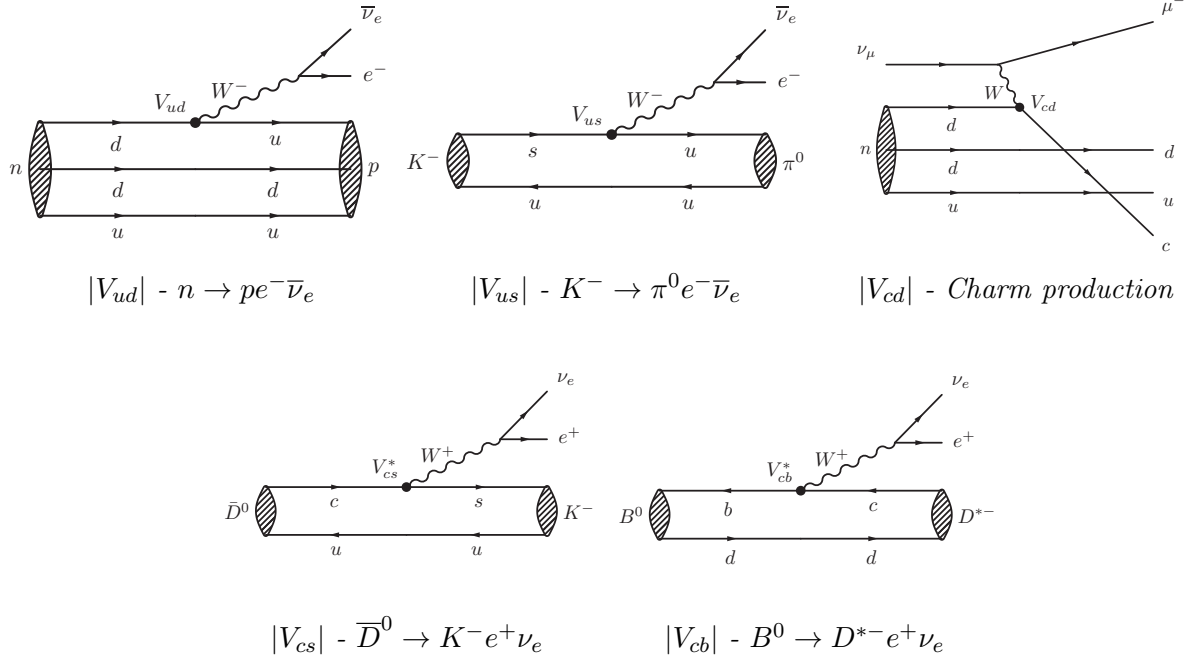
Figure 1.3: *Feynman diagrams of some specific processes important for determining five of the $|V_{ij}|$ matrix elements.*

most precisely determined by a global fit that combines all the available measurements and imposes the SM constraints. Tab. 1.2 summarizes the current knowledge of the magnitudes of the CKM matrix elements using the latest CKMfitter results [15]. The uncertainties reported in this table correspond to a 68% confidence level (CL). Transitions within the same quark generation, corresponding to the diagonal elements of the CKM matrix, are strongly favoured while transitions between different generations, corresponding to the off-diagonal elements, are disfavoured (see Fig. 1.4). Transitions between the first and second generations are suppressed by a factor $\mathcal{O}(10^{-1})$, those between the second and third generations are suppressed by a factor $\mathcal{O}(10^{-2})$ and those between the first and third generations are strongly suppressed by a factor $\mathcal{O}(10^{-3})$.
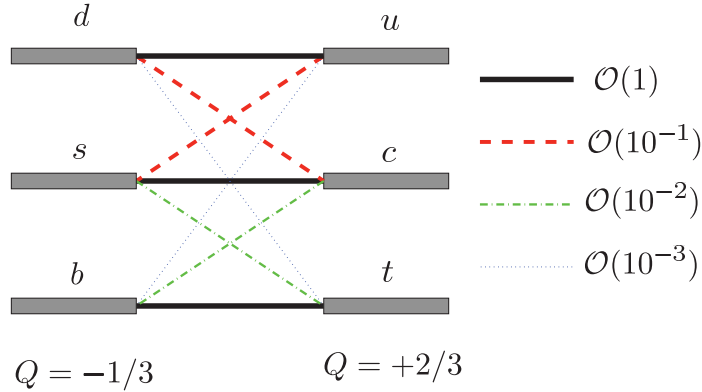
Figure 1.4: *Graphical representation of the transition hierarchy between the different quark generations.*

1.3.2 Wolfenstein parametrization and unitarity triangles

Given the experimental knowledge of the $|V_{ij}|$ matrix elements it can be stated that exists a clear hierarchy in the mixing of quarks, namely

$$1 \gg s_{12} \gg s_{23} \gg s_{13} \ . \tag{1.29}$$

From this evidence, by introducing the following identities known as "Wolfenstein parametrization" [16],

$$s_{12} = \lambda = \frac{|V_{us}|}{\sqrt{|V_{ud}|^2 + |V_{us}|^2}} \ , \tag{1.30}$$

$$s_{23} = A\lambda^2 = \lambda \left| \frac{V_{cb}}{V_{us}} \right| \ , \tag{1.31}$$

$$s_{13}e^{i\delta} = V_{ub} = A\lambda^3(\rho - i\eta) \ , \tag{1.32}$$

we can rewrite the CKM matrix of Eq. 1.24 in power series of the parameter λ obtaining a different parametrization of V_{CKM}. This way, expanding up to the fifth order, we have [17]

$$V_{CKM} =$$
$$\begin{pmatrix} 1 - \frac{1}{2}\lambda^2 - \frac{1}{8}\lambda^4 & \lambda & A\lambda^3(\rho - i\eta) \\ -\lambda + \frac{1}{2}A^2\lambda^5[1 - 2(\rho + i\eta)] & 1 - \frac{1}{2}\lambda^2 - \frac{1}{8}\lambda^4(1 + 4A^2) & A\lambda^2 \\ A\lambda^3[1 - (1 - \frac{1}{2}\lambda^2)(\rho + i\eta)] & -A\lambda^2 + \frac{1}{2}A\lambda^4[1 - 2(\rho + i\eta)] & 1 - \frac{1}{2}A^2\lambda^4 \end{pmatrix} + \mathcal{O}(\lambda^6).$$
$$\tag{1.33}$$

In this parametrization the Jarlskog invariant defined in Eq. 1.27 becomes

$$J_{CP} = \lambda^6 A^2 \eta, \tag{1.34}$$

where η is the $\mathcal{CP}$ violating parameter.

A very important aspect of the CKM matrix is that the unitarity property, $(V_{CKM}^\dagger V_{CKM})_{ij} = (V_{CKM} V_{CKM}^\dagger)_{ij} = \delta_{ij}$, corresponds to a set of nine complex equations that connects the V_{ij} elements: three of these involve the diagonal terms and are equal to 1, while the other six equations, those ones involving the off-diagonal terms, vanish. The equations for the off-diagonal elements $(i \neq j)$ can be represented as triangles of area $J_{CP}/2$ and are respectively:

$$\underbrace{V_{ud}V_{us}^*}_{\mathcal{O}(\lambda)} + \underbrace{V_{cd}V_{cs}^*}_{\mathcal{O}(\lambda)} + \underbrace{V_{td}V_{ts}^*}_{\mathcal{O}(\lambda^5)} = 0, \tag{1.35}$$

$$\underbrace{V_{us}V_{ub}^*}_{\mathcal{O}(\lambda^4)} + \underbrace{V_{cs}V_{cb}^*}_{\mathcal{O}(\lambda^2)} + \underbrace{V_{ts}V_{tb}^*}_{\mathcal{O}(\lambda^2)} = 0, \tag{1.36}$$

$$\underbrace{V_{ud}V_{ub}^*}_{\mathcal{O}(\lambda^3)} + \underbrace{V_{cd}V_{cb}^*}_{\mathcal{O}(\lambda^3)} + \underbrace{V_{td}V_{tb}^*}_{\mathcal{O}(\lambda^3)} = 0, \tag{1.37}$$

$$\underbrace{V_{ud}^*V_{cd}}_{\mathcal{O}(\lambda)} + \underbrace{V_{us}^*V_{cs}}_{\mathcal{O}(\lambda)} + \underbrace{V_{ub}^*V_{cb}}_{\mathcal{O}(\lambda^5)} = 0, \tag{1.38}$$

$$\underbrace{V_{cd}^*V_{td}}_{\mathcal{O}(\lambda^4)} + \underbrace{V_{cs}^*V_{ts}}_{\mathcal{O}(\lambda^2)} + \underbrace{V_{cb}^*V_{tb}}_{\mathcal{O}(\lambda^2)} = 0, \tag{1.39}$$

$$\underbrace{V_{ud}^*V_{td}}_{\mathcal{O}(\lambda^3)} + \underbrace{V_{us}^*V_{ts}}_{\mathcal{O}(\lambda^3)} + \underbrace{V_{ub}^*V_{tb}}_{\mathcal{O}(\lambda^3)} = 0, \tag{1.40}$$

where each product $|V_{ij}V_{kl}^*|$ represents the lenght of the corresponding triangle side. These triangles are the so-called "unitarity triangles". Two triangles, namely those of Eq. 1.37 and 1.40, have all their sides length of the order of $\mathcal{O}(\lambda^3)$. The other four equations contain terms with different powers of λ and hence give rise to "squashed" triangles.

The triangle of Eq. 1.37 is of particular importance and is commonly known as the Unitarity Triangle (UT). It can be represented in the complex plane $(\overline{\rho}, \overline{\eta})$, where the $\overline{\rho}$ and $\overline{\eta}$ parameters are defined as

$$\overline{\rho} = \rho \left(1 - \frac{\lambda^2}{2}\right) \quad \overline{\eta} = \eta \left(1 - \frac{\lambda^2}{2}\right). \tag{1.41}$$

The UT angles are given by

$$\alpha \equiv \phi_2 = \arg\left(-\frac{V_{td}V_{tb}^*}{V_{ud}V_{ub}^*}\right), \quad \beta \equiv \phi_1 = \arg\left(-\frac{V_{cd}V_{cb}^*}{V_{td}V_{tb}^*}\right), \quad \gamma \equiv \phi_3 = \arg\left(-\frac{V_{ud}V_{ub}^*}{V_{cd}V_{cb}^*}\right), \tag{1.42}$$

where two conventions exist in the literature, and their sides are defined as

$$R_u = \left|\frac{V_{ud}V_{ub}^*}{V_{cd}V_{cb}^*}\right| = \sqrt{\overline{\rho}^2 + \overline{\eta}^2}, \quad R_t = \left|\frac{V_{td}V_{tb}^*}{V_{cd}V_{cb}^*}\right| = \sqrt{(1-\overline{\rho})^2 + \overline{\eta}^2}. \tag{1.43}$$

The apex of the triangle is then given by

$$\overline{\rho} + i\overline{\eta} \equiv -\frac{V_{ud}V_{ub}^*}{V_{cd}V_{cb}^*} \equiv 1 + \frac{V_{td}V_{tb}^*}{V_{cd}V_{cb}^*} = \frac{\sqrt{1-\lambda^2}(\rho + i\eta)}{\sqrt{1-A^2\lambda^4} + \sqrt{1-\lambda^2}A^2\lambda^4(\rho + i\eta)} \quad . \tag{1.44}$$

The graphical representation of the unitarity triangle is shown in Fig. 1.5. In Table1.3 are summarized the values of the A, λ, $\overline{\rho}$ and $\overline{\eta}$ parameters, where the uncertainties correspond to a 68% CL. In Fig. 1.6 are superimposed all the latest CKM constraints determined under the SM hypothesis in the $(\overline{\rho}, \overline{\eta})$ plane.
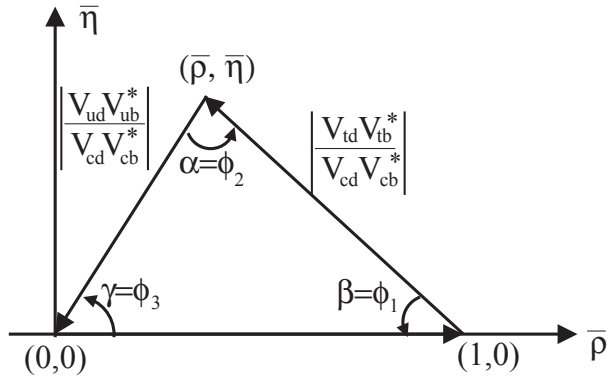
Figure 1.5: *Graphical representation in the complex plane $(\overline{\rho}, \overline{\eta})$ of the unitarty triangle of Eq. 1.37 as normalized to $V_{cd}V_{cb}^*$: $1 + V_{ud}V_{ub}^*/V_{cd}V_{cb}^* + V_{td}V_{tb}^*/V_{cd}V_{cb}^* = 0$.*

As a last remark, let us notice that the two matrix elements $|V_{ts}|$ and $|V_{cb}|$ have the same order of magnitude. Looking at Tab. 1.2 we can see that their values are indeed extremely close. As a consequence, the R_t side of Eq. 1.43 can be rewritten as

$$R_t \approx \left| \frac{V_{td}V_{tb}^*}{V_{cd}V_{ts}^*} \right| \quad . \tag{1.45}$$

This means that, by measuring the ratio $|V_{td}/V_{ts}|$, we can constrain the right side of the unitarity triangle.

1.4 The GIM mechanism

While the CKM matrix describes flavour-changing transitions mediated by the $W^\pm$ boson, the SM provides also neutral weak currents mediated by the neutral boson Z^0 , which should in principle be responsible for flavour-changing interactions aswell. However, experimental measurements show that the rate of flavour-changing neutral current (FCNC) decays is strongly suppressed :

Parameter	Fitted value
A	$0.8250^{+0.0071}_{-0.0111}$
λ	$0.22509^{+0.00029}_{-0.00028}$
$\overline{\rho}$	$0.1598^{+0.0076}_{-0.0072}$
$\overline{\eta}$	$0.3499^{+0.0063}_{-0.0061}$

Table 1.3: *Current values of the Wolfenstein parameters [18].*
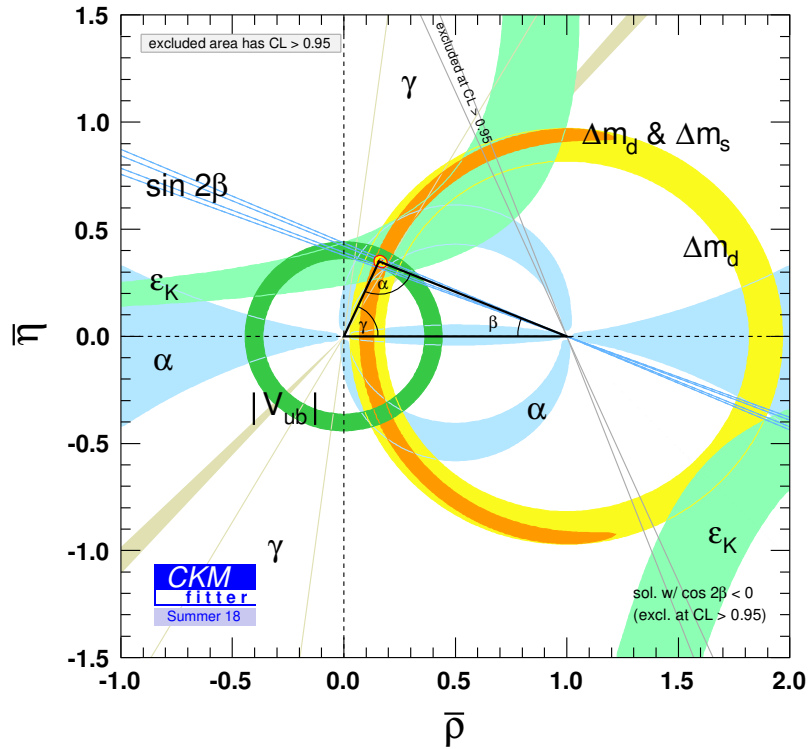
Figure 1.6: *Constraints on the unitarity triangle at a 95% confidence level [15].*

$$\Gamma\left(s \rightarrow dZ^0\right) \ll \Gamma\left(s \rightarrow uW^-\right) \tag{1.46}$$

To try to describe this effect, Glashow, Iliopoulos and Maiani introduced for the first time the charm quark and showed a possible cancellation mechanism for the neutral current terms in the weak lagrangian. This GIM mechanism [19] explains that, at the Z^0 tree-level vertex, only the $\overline{q}_i q_i$ flavour conserving contributions would survive (e.g. $\overline{u}u$), while the flavour-changing contributions from the first quark generation would be cancelled by the ones from the second generation due to the unitarity of the CKM matrix. As a result,

FCNC are not allowed in the SM only at tree level, but is possible through loop diagrams.

1.5   Neutral B meson oscillations

The neutral B^0 (B_s) meson is a pseudoscalar particle with bottomness $B = +1$ composed by the $\bar{b}d$ ($\bar{b}s$) quark-antiquark pair, that can oscillate into its antiparticle $\overline{B}^0$ ($\overline{B}_s^0$) composed by the $b\bar{d}$ ($b\bar{s}$) pair and with $B = -1$. These $B^0 \longleftrightarrow \overline{B}^0$ ($B_s \longleftrightarrow \overline{B}_s^0$) oscillations, also referred to as mixing, are due to second order virtual transitions $\Delta B = 2$ associated to the box diagrams shown in Fig. 1.7. In this section we discuss only the mixing of the B^0 and B_s mesons, but a similar formalism can be applied to K^0 and D^0 mesons.

Because of the oscillations, at any time t the B_q^0 generic meson (where $q = d, s$ and $B_d^0 = B^0$) can be seen as a superposition of states described by the following wave function

$$|B_q^0(t)\rangle = a(t)|B_q^0\rangle + b(t)|\overline{B}_q^0\rangle + \sum_f c_f(t)|f\rangle \ , \tag{1.47}$$

where $|B_q^0\rangle$ and $|\overline{B}_q^0\rangle$ represent the particle and antiparticle states of the B_q^0 meson, $|f\rangle$ are the possible finale states in which the meson is allowed to decay and $c_f(t)$ are the coefficients of each final state. In the case of a time range much larger than the typical
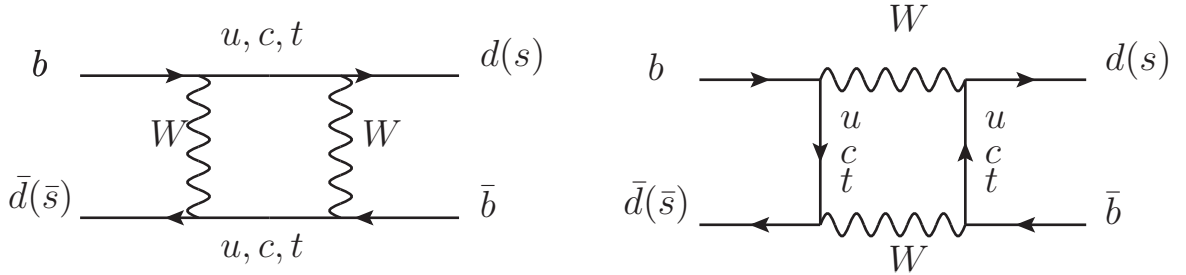
Figure 1.7: *Box diagrams describing the $B^0 - \overline{B}^0$ and $B_s^0 - \overline{B}_s^0$ mixing.*

strong interaction scale, we can exploit the so called Weisskopf-Wigner approximation that allows to use the simplified formalism [20], [21]

$$|B^0(t)\rangle = a(t)|B^0\rangle + b(t)|\overline{B}^0\rangle \ , \tag{1.48}$$

with $|a(t)|^2 + |b(t)|^2 = 1$. The subscript q is here suppressed to simplify the discussion. This wave function obeys the Schrödinger equation $i(\partial/\partial t)|B^0(t)\rangle = \mathcal{H}_{eff}|B^0(t)\rangle$ where the effective Hamiltonian is given by

$$\mathcal{H}_{eff} = \mathbf{M} - \frac{i}{2}\mathbf{\Gamma} = \begin{pmatrix} M & M_{12} \\ M_{12}^* & M \end{pmatrix} - \frac{i}{2} \begin{pmatrix} \Gamma & \Gamma_{12} \\ \Gamma_{12}^* & \Gamma \end{pmatrix}. \tag{1.49}$$

The diagonal elements of $\mathcal{H}_{eff}$ are associated to flavour-conserving transitions $B^0 \to B^0$ and $\overline{B}^0 \to \overline{B}^0$, while the off-diagonal ones are associated to flavour-changing transitions $B^0 \longleftrightarrow \overline{B}^0$. The diagonal elements of $\mathcal{H}_{eff}$ are equal because of the assumption of $\mathcal{CPT}$ invariance [22]. This Hamiltonian is not Hermitian otherwise mesons would not oscillate and not decay, but the $\mathbf{M}$ and $\mathbf{\Gamma}$ matrices are. The $\mathbf{M}$ matrix represents transitions via dispersive intermediate state ("off-shell" or short-range transitions), and $\mathbf{\Gamma}$ represents transitions via absorptive intermediate states ("on-shell" transition). The solution of the eigenvalue equation for $\mathcal{H}_{eff}$ gives two eigenstates

$$|B_H^0\rangle = p|B^0\rangle - q|\overline{B}^0\rangle, \qquad |B_L^0\rangle = p|B^0\rangle + q|\overline{B}^0\rangle, \tag{1.50}$$

which corresponds to the eigenvalues

$$\lambda_H = M - \frac{i}{2}\Gamma + \frac{q}{p}\left(M_{12} - \frac{i}{2}\Gamma_{12}\right) = M_H - \frac{i}{2}\Gamma_H,$$

$$\lambda_L = M - \frac{i}{2}\Gamma - \frac{q}{p}\left(M_{12} - \frac{i}{2}\Gamma_{12}\right) = M_L - \frac{i}{2}\Gamma_L, \tag{1.51}$$

where p and q are complex coefficients satisfying $|p|^2 + |q|^2 = 1$ and whose ratio is given by

$$\frac{q}{p} = \sqrt{\frac{M_{12}^* - (i/2)\Gamma_{12}^*}{M_{12} - (i/2)\Gamma_{12}}} \ . \tag{1.52}$$

The real parts of the eigenvalues $\lambda_{H,L}$ represent the masses, $M_{H,L}$, and their imaginary parts represent the widths, $\Gamma_{H,L}$, of the two eigenstates $|B_{H,L}^0\rangle$: by convention the subscripts H and L label respectively the heavy and the light eigentstates. The mass and width differences between the two eigenstates are

$$\Delta m = M_H - M_L, \qquad \Delta\Gamma = \Gamma_L - \Gamma_H, \tag{1.53}$$

where Δm is positive by definition and the sign of $\Delta\Gamma$, which is unknown a priori, has to be experimentally determined and is expected to be positive within the Standard Model. Now, defining the functions

$$g_+(t) = \left(\frac{e^{-i\lambda_H t} + e^{-i\lambda_L t}}{2}\right), \qquad g_-(t) = \left(\frac{e^{-i\lambda_H t} - e^{-i\lambda_L t}}{2}\right), \tag{1.54}$$

and inserting Eq. 1.50 we can write the expressions for the time evolution of pure B^0 and $\overline{B}^0$ particle states as follows

$$|B^0(t)\rangle = g_+(t)|B^0\rangle + \frac{q}{p}g_-(t)|\overline{B}^0\rangle, \qquad |\overline{B}^0(t)\rangle = g_+(t)|\overline{B}^0\rangle + \frac{p}{q}g_-(t)|B^0\rangle, \tag{1.55}$$

with the square modulus of the $g_\pm(t)$ functions given by

$$|g_\pm(t)|^2 = \frac{1}{4}\left(e^{-\Gamma_H t} + e^{-\Gamma_L t} \pm 2e^{-\Gamma t}\cos\Delta m t\right) \tag{1.56}$$

$$= \frac{e^{-\Gamma t}}{2}\left(\cosh\frac{\Delta\Gamma t}{2} \pm \cos\Delta m t\right) \ .$$

This quantity represents the time-dependent probability to conserve the initial flavour $(+)$ or oscillate into the opposite one $(-)$. We now recall the subscript q and write the Γ, $\Delta\Gamma$ and Δm expression for the generic B_q^0 meson

$$\Gamma_q = \frac{\Gamma_{qH} + \Gamma_{qL}}{2}, \qquad \Delta\Gamma_q = \frac{\Gamma_{qL} - \Gamma_{qH}}{2}, \qquad \Delta m_q = M_{qH} - M_{qL} , \qquad (1.57)$$

where Γ_q fulfills the natural role of decay constant, $\Gamma_q = 1/\tau_q$.

The $B^0 - \overline{B}^0$ and $B_s - \overline{B}_s^0$ systems have very different oscillation frequencies and these are determined by the Δm_q terms, which contain the short-distance contributions associated to the Feynman diagrams of Fig. 1.7. The main contribution to the box is that one coming from the top quark. The SM transition amplitude for the B_q^0 mixing is given by [23]

$$\langle B_q^0 | \mathcal{H}_{eff}^{\Delta B=2} | \overline{B}_q^0 \rangle = \langle B_q^0 | \frac{G_F^2 M_W^2}{16\pi^2} (\mathcal{F}_d^0 \mathcal{Q}_1^d + \mathcal{F}_s^0 \mathcal{Q}_1^s) + h.c. \, | \overline{B}_q^0 \rangle, \qquad (1.58)$$

where $\mathcal{H}_{eff}^{\Delta B=2}$ is the simplest effective Hamiltonian and the four-fermion operators $\mathcal{Q}_1^q$ are defined as

$$\mathcal{Q}_1^q = [\bar{b}\gamma_\mu(1 - \gamma_5)q][\bar{b}\gamma^\mu(1 - \gamma_5)q]. \qquad (1.59)$$

G_F is the Fermi coupling constant, M_W is the mass of the $W^\pm$ boson and $\gamma_5 = i\gamma^0\gamma^1\gamma^2\gamma^3$. The short distance function $\mathcal{F}_q^0$ in Eq. 1.58 is

$$\mathcal{F}_q^0 = \lambda_{tq}^2 S_0(x_t) \qquad (1.60)$$

with

$$\lambda_{tq} = V_{tq}^* V_{tb} \qquad (1.61)$$

and where $S_0(x_t)$ is an Inami-Lim function with $x_t = m_t^2/M_W^2$. It describes the basic electroweak box contributions without QCD. This leads to the SM prediction of the Δm_q mass difference

$$\Delta m_q = \frac{G_F^2 M_W^2}{6\pi^2} m_{B_q} \eta_{2B} S_0(x_t) f_{B_q}^2 \hat{B}_{B_q} |V_{tq} V_{tb}^*|^2 , \qquad (1.62)$$

where m_{B_q} is the mass of the oscillating meson, η_{2B} is a perturbative QCD correction factor calculated to the next to leading order (NLO), f_{B_q} is the decay constant of the meson and $\hat{B}_{B_q}$ is the "bag-factor". The product $f_{B_q}\sqrt{\hat{B}_{B_q}}$ is related to non-perturbative corrections, then is the most important source of uncertainty in the Δm_q prediction. On the other hand the ratio

$$\xi = \frac{f_{B_d}\sqrt{\hat{B}_{B_d}}}{f_{B_s}\sqrt{\hat{B}_{B_s}}} \qquad (1.63)$$

is calculated with a better precision in Lattice QCD (LQCD) than the individual $f_{B_q}\sqrt{\hat{B}_{B_q}}$ because statistical and systematic uncertainties cancel in part. With this ratio, $|V_{td}/V_{ts}|$ can be determined from the ratio of oscillation frequencies $\Delta m_d/\Delta m_s$

and used to constrain the side R_t. The present constraint as reported on the PDG is $|V_{td}/V_{ts}| = 0.215 \pm 0.001 \pm 0.011$ [7].

A graphical representation of the oscillation probabilities of the $B_q^0 - \overline{B}_q^0$ mesons is shown in Fig. 1.8. It can be noticed that the oscillation frequency of the $B_s - \overline{B}_s^0$ system is much higher than the $B^0 - \overline{B}^0$ one. This depends on the magnitude of the CKM matrix elements that contribute to the transition probability: in fact while $\Delta m_d \propto |V_{td}V_{tb}^*|^2 m_t^2 \sim \lambda^6 m_t^2$, $\Delta m_s \propto |V_{ts}V_{tb}^*|^2 m_t^2 \sim \lambda^4 m_t^2$.
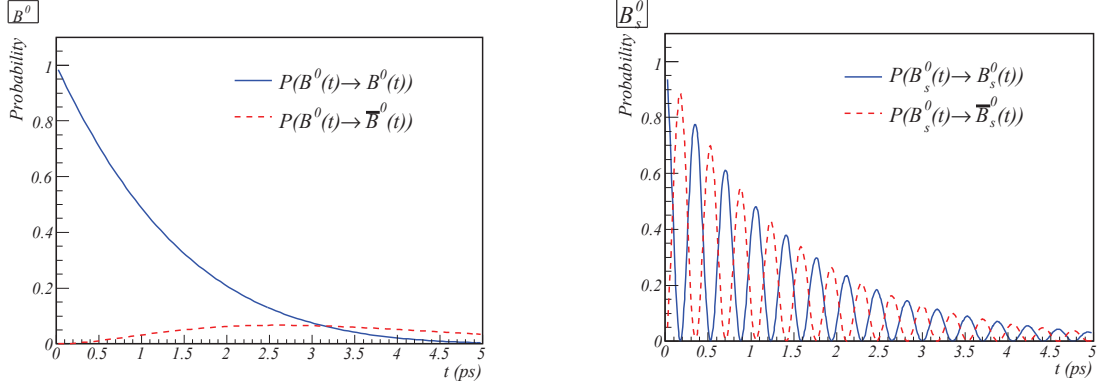
Figure 1.8: *Time evolution of the $B^0 - \overline{B}^0$ (left) and $B_s - \overline{B}_s^0$ (right) systems.*

1.6 Radiative B decays

Quark transitions $b \to s\gamma$ are only allowed in loop diagrams in the SM because of the GIM mechanism. Therefore, radiative decays of B hadrons can be a great probe to look for New Physics via the possible exchange of heavy particles in the corresponding electroweak penguin diagram (Figure 1.9). Furthermore, and since in the SM the s quark that couples to a W boson is left-handed, the emitted photon has to be left-handed, up to corrections of the order m_s/m_b. Measuring the photon polarization can then provide strong constaints on NP scenarios where the photon may acquire a significant right-handed component from a heavy fermion being exchanged in the electroweak penguin loop [24].
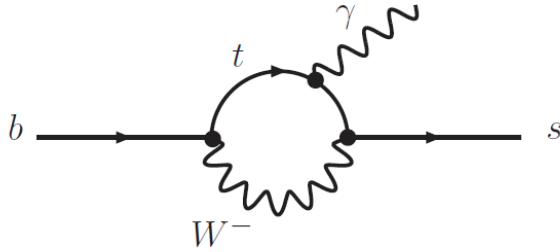
Figure 1.9: *Feynman diagram of the $b \to s\gamma$ transition.*

An effective hamiltonian relevant for decays with $b \to s\gamma$ transitions can be introduced to study the effects of NP in this sector [25]:

$$\mathcal{H}_{\text{eff}} = -\frac{G_F}{\sqrt{2}} V_{tb} V_{ts}^* \left[\sum_{i=1}^{6} C_i(\mu)\mathcal{O}_i(\mu) + \sum_{i=7}^{10} \left(C_i(\mu)\mathcal{O}_i(\mu) + C_i'(\mu)\mathcal{O}_i'(\mu) \right) \right]. \qquad (1.64)$$

Here the the operators $\mathcal{O}_{1,..,6}^{(')}$ are the SM four-quarks operators while $\mathcal{O}_7^{(')}$ is the operator for electromagnetic penguins, $\mathcal{O}_8^{(')}$ is the chromomagnetic penguin operator and $\mathcal{O}_{9,10}^{(')}$ are the semileptonic operators. Wilson coefficients $C_i^{(')}$ account for the short distance physics effects.

The $\mathcal{O}_7^{(')}$ electromagnetic penguin operators have the dominant contribution to the $b \to s\gamma$ decays :

$$\begin{aligned} \mathcal{O}_7 &\propto \bar{s}_{\alpha_L} \sigma^{\mu\nu} b_{\alpha_R} F_{\mu\nu} \\ \mathcal{O}_7' &\propto \bar{s}_{\alpha_R} \sigma^{\mu\nu} b_{\alpha_L} F_{\mu\nu} \end{aligned} \qquad . \qquad (1.65)$$

as they respectively describe the SM-favoured left-handed photon ($\mathcal{O}_7$), and the SM-suppressed right-handed photon ($\mathcal{O}_7'$). Absorbing the subleading contributions from $\mathcal{O}_{i\neq 7}^{(')}$ into effective $C_7^{(')eff}$ coefficients, the leading order amplitude for $b \to s\gamma$ transitions can be written as :

$$\langle f \,| \mathcal{H}_{\text{eff}} | \, i \rangle = -4 \frac{G_F}{\sqrt{2}} V_{tb} V_{ts} \times \left[C_7^{eff}(m_b) \langle f \,| \mathcal{O}_7(m_b) | \, i \rangle + C_7'^{eff}(m_b) \langle f \,| \mathcal{O}_7'(m_b) | \, i \rangle \right].$$
(1.66)

where f and i refer to the final and initial states.

1.6.1 The photon polarization

The decay width for a radiative B meson decay can be written as :

$$\Gamma\left(\bar{B} \to \bar{X}_s \gamma\right) \propto |c_{\text{L}}|^2 |\mathcal{M}_{\text{L}}|^2 + |c_{\text{R}}|^2 |\mathcal{M}_{\text{R}}|^2,$$
(1.67)

where c_L and c_R are the weak amplitudes involving left-handed and right-handed photons, $\mathcal{M}_L$ and $\mathcal{M}_L$ are the corresponding strong decay amplitudes. The photon polarization λ_γ can be defined as :

$$\lambda_\gamma \equiv \frac{|c_{\text{R}}|^2 - |c_{\text{L}}|^2}{|c_{\text{R}}|^2 + |c_{\text{L}}|^2},$$
(1.68)

and as in the SM we have $|c_{\text{L}}|^2 \gg |c_{\text{R}}|^2$ then $\lambda_\gamma \simeq -1$ (up to $\mathcal{O}\left(m_s^2/m_b^2\right)$ corrections).

Then, as the c_L and c_R are products of hadronic form factors and $C_7^{(')}$ Wilson coefficient it can be shown that([24]):

$$\frac{|c_{\text{R}}|}{|c_{\text{L}}|} = \frac{|C_7'|}{|C_7|},$$
(1.69)

and therefore :

$$\lambda_\gamma = \frac{|C_7'|^2 - |C_7|^2}{|C_7'|^2 + |C_7|^2}.$$
(1.70)

1.6.2 Constraints from experimental measurements

Several New Physics models introduce significant contributions with right-handed photons, therefore measuring λ_γ leads to constraining these models. A few methods are possible :

- The first method proposed by Gronau *et al.* [24] allows a direct determination of the photon polarization in the study of angular distribution of the photon in the $B \to K_{\text{res}}\gamma \to K\pi\pi\gamma$ decays. The determination of λ_γ is done via the measurement of the up-down asymmetry :

$$\mathcal{A}_{\text{ud}} \equiv \frac{\int_0^1 \text{d} \cos \tilde{\theta} \frac{\text{d}\Gamma}{\text{d} \cos \bar{\theta}} - \int_{-1}^0 \text{d} \cos \tilde{\theta} \frac{\text{d}\Gamma}{\text{d} \cos \bar{\theta}}}{\int_{-1}^1 \text{d} \cos \tilde{\theta} \frac{\text{d}\Gamma}{\cos \bar{\theta}}},$$
(1.71)

where $\tilde{\theta}$ is the angle between the photon momentum and the normal to the plane defined by the momenta of the daughter particles of the K$_{res}$ decays, in the K$_{res}$ rest frame. The LHCb collaboration measured for the first time this up-down asymmetry in $B^{\pm} \to K^{\pm}\pi^{\pm}\pi^{\mp}\gamma$ decays to be $A_{\mathrm{ud}} = -0.085 \pm 0.019(\mathrm{stat}) \pm 0.003(\mathrm{syst})$ [1]. While this is the first evidence of the polarization of the photon in $b \to s\gamma$, a simultaneous analysis of the $K^{\pm}\pi^{\pm}\pi^{\mp}$ structure is needed to gain access to λ_{γ}. This is currently under development in the collaboration.

- A way to determine the photon polarization is through the study of the time-dependent decay rate of B to CP eigenstate : $B_{(s)} \to f^{CP}\gamma$. In this case, the flavour specific decay rate is expressed as :

$$\Gamma\left(B_{(s)}\left(\bar{B}_{(s)}\right) \to f^{CP}\gamma\right)(t) \propto$$
$$e^{-\Gamma_{(s)}t}\left[\cosh\left(\frac{\Delta\Gamma_{(s)}}{2}t\right) - \mathcal{A}^{\Delta}\sinh\left(\frac{\Delta\Gamma_{(s)}}{2}t\right) \pm C\cos\left(\Delta m_{(s)}t\right) \mp S\sin\left(\Delta m_{(s)}t\right)\right],$$
$$(1.72)$$

with $\Delta\Gamma_{(s)}$ and $\Delta m_{(s)}$ the decay width and mass difference between the two $B_{(s)}$ mass eigenstates, and :

$$\mathcal{A}^{\Delta} = \frac{2\mathcal{R}e\left[(\bar{c}_L c_L^* + \bar{c}_R c_R^*)\right]}{|c_L|^2 + |\bar{c}_L|^2 + |c_R|^2 + |\bar{c}_R|^2},$$
$$C = \frac{\left(|c_L|^2 + |c_R|^2\right) - \left(|\bar{c}_R|^2 + |\bar{c}_L|^2\right)}{|c_L|^2 + |\bar{c}_L|^2 + |c_R|^2 + |\bar{c}_R|^2}, \qquad (1.73)$$
$$S = \frac{2\mathcal{I}m\left[(\bar{c}_L c_L^* + \bar{c}_R c_R^*)\right]}{|c_L|^2 + |\bar{c}_L|^2 + |c_R|^2 + |\bar{c}_R|^2}.$$

where C represents the direct CP violation, S the mixing-induced CP violation parameter and $\mathcal{A}^{\Delta}$ can be related to the polarisation of the photon with $\mathcal{A}^{\Delta} = \sin(2\psi)$ and $\tan\psi \equiv \left|A\left(\bar{B}_s^0 \to \phi\gamma_{\mathrm{R}}\right)\right| / \left|A\left(\bar{B}_s^0 \to \phi\gamma_{\mathrm{L}}\right)\right|$. The SM prediction for this observable is $\mathcal{A}_{\mathrm{SM}}^{\Delta} = 0.047 \begin{smallmatrix} +0.029 \\ -0.025 \end{smallmatrix}$ [26].

If the $B_{(s)}$ and $\bar{B}_{(s)}$ decays cannot be distinguished, the decay rates writes then

$$\Gamma(t) = \Gamma\left(B_{(s)} \to f^{CP}\gamma\right)(t) + \Gamma\left(\bar{B}_{(s)} \to f^{CP}\gamma\right)(t)$$
$$\simeq e^{-\Gamma_{(s)}t}\left[\cosh\left(\frac{\Delta\Gamma_{(s)}}{2}t\right) - \mathcal{A}^{\Delta}\sinh\left(\frac{\Delta\Gamma_{(s)}}{2}t\right)\right], \qquad (1.74)$$

and gives access to $\mathcal{A}^{\Delta}$, provided a precise knowledge of $\Delta\Gamma_{(s)}$. The sizeable width difference in the B_s system allowed the LHCb collaboration to measure it in the mode $B_s \to \phi\gamma$ [27] : $\mathcal{A}^{\Delta} = -0.98^{+0.46+0.23}_{-0.52-0.20}$.

If the flavour of the B can be tagged in the selection process, the study of the time-dependent decay rate gives also access to the CP-violating observables C and S. The BaBar and Belle experiments, so-called B factories, measured these observables in

several B^0 decays, studying the time-dependent CP asymmetry. Very recently, the LHCb collaboration published a second study of the $B_s \to \phi\gamma$ time-dependent decay rate [28], this time making use of flavour-tagging algorithms [29] to get together C, S and $\mathcal{A}^\Delta$:

$$S_{\phi\gamma} = 0.43 \pm 0.30 \pm 0.11$$
$$C_{\phi\gamma} = 0.11 \pm 0.29 \pm 0.11 \quad .$$
$$\mathcal{A}^\Delta_{\phi\gamma} = -0.67 - 0.37 \pm 0.17$$

(1.75)

To give an overview, the full list of measurements (except this very recent one) of S and C are diplayed on Figure 1.10.
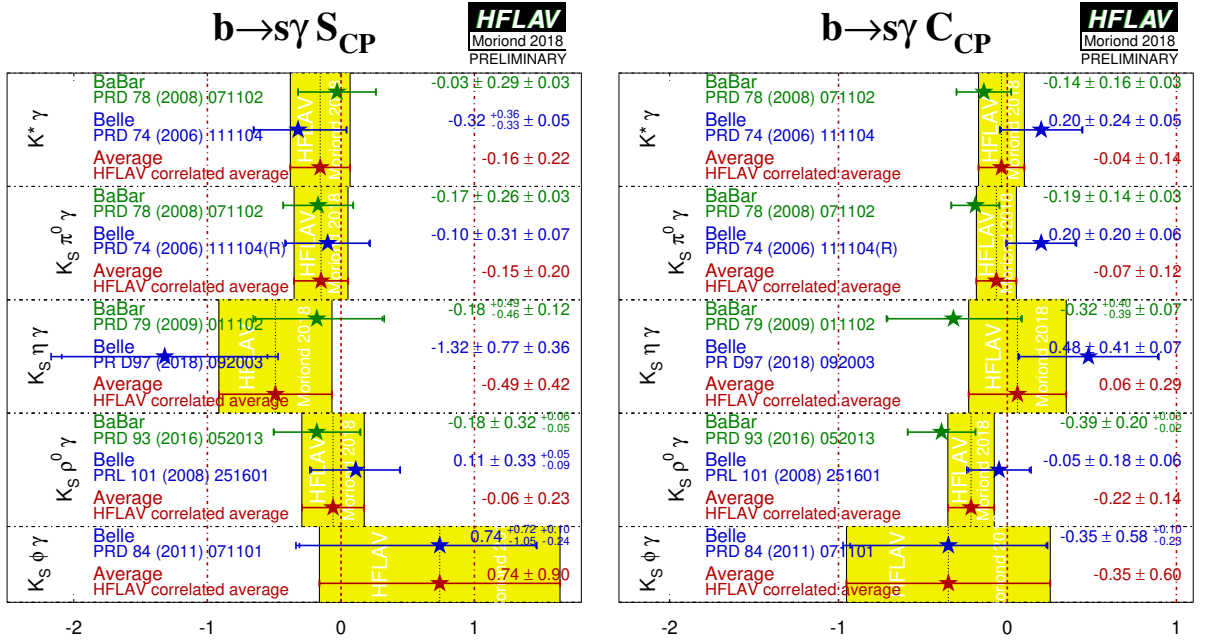
Figure 1.10: *Experimental status on the measurements of S (left) and C (right) [18].*

- Another method to look for anomalous photon polarization is through the angular analysis of $B^0 \to K^{*0}(\to K^-\pi^+)\,\ell^+\ell^-$ (or similarly $B_s^0 \to \phi\ell^+\ell^-$) decays in the low l^+l^- invariant masses [30]. In such decays one can define the angular observables $A_T^{(2)}$ and A_T^{Im} as :

$$A_T^{(2)} = \frac{|A_\perp|^2 - |A_\parallel|^2}{|A_\perp|^2 + |A_\parallel|^2}$$
$$A_T^{Im} = \frac{2\mathcal{I}\mathbb{J}\left(A_{\parallel L}A_{\perp L}^* + A_{\parallel R}A_{\perp R}^*\right)}{|A_\perp|^2 + |A_\parallel|^2} \quad ,$$

(1.76)

where $A_\parallel$ and $A_\perp$ are the amplitudes for different polarisation states of the K^{*0}, and L/R refers to the left/right chirality of the dileptons system. The LHCb and CMS experiments provided results on the studies of $B^0 \to K^{*0}e^+e^-$ [31] and $B^0 \to K^{*0}\mu^+\mu^-$ ([32], [33]).

- We have only been discussing B meson decays up to now, but the polarization of the photon can also be extracted in b-baryon decays [34, 35]. In this approach, the angular distributions of the photon and the proton in $\Lambda_b \to \Lambda(\to ph)\gamma$ decays (with $h = K/\pi$) are exploited.

Overall, the measures of branching ratios of radiative decays and of observables related to the photon polarisation add constraints to the $C_7^{(')}$ Wilson coefficients, and therefore the space still alowed for New Physics scenarios. A fairly recent status on these constraints in the global fit of $C_7^{(')}$ is given in [36], and displayed on Figure 1.11.
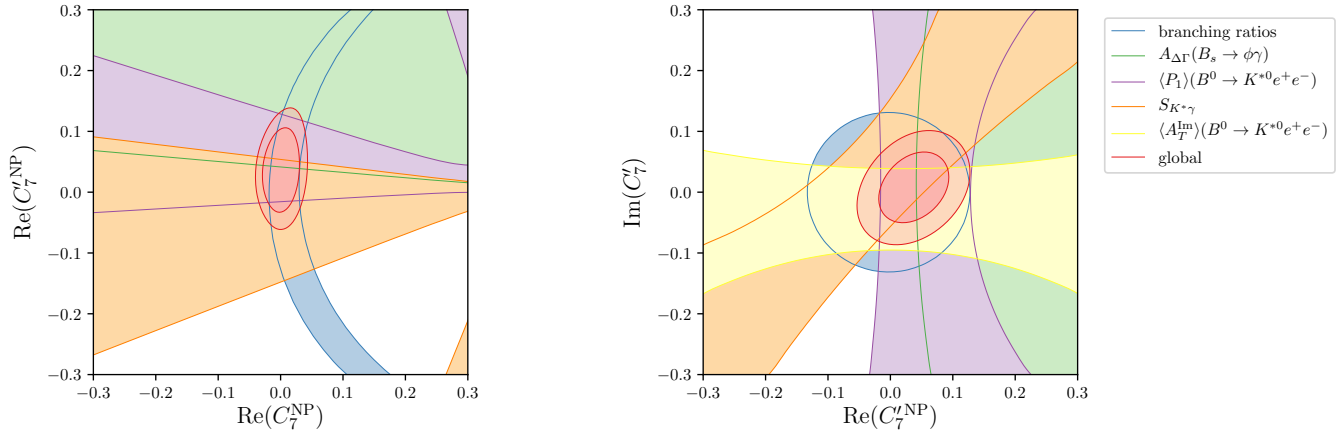
Figure 1.11: *Constraints on* NP *contributions to the Wilson coefficients* C_7 *and* C_7'. *For the global constraints (in red), 1 and 2 σ contours are shown, while the individual constraints are shown at the 1 σ level. The SM expectation is (0,0).*

Chapter 2

The LHC and the LHCb experiment

2.1 The Large Hadron Collider

The Large Hadron Collider (LHC [37]) is built at CERN, the European Laboratory for Particle Physics, under the Franco-Swiss border close to Geneva. With its circumference of 27 km and a center-of-mass energy designed to be up to 14 TeV, it is the largest and more powerful particle accelerator ever created. The LHC is inside the tunnel which originally hosted its predecessor, the LEP (Large Electron Positron Collider), at an average depth of 100 m. (Fig. 2.1). The LHC collides bunches of protons obtained from ionized hydrogen atoms. They require a pre-acceleration before the injection into the main rings. A scheme of the accelerator complex at CERN is shown in Fig. 2.2. Firstly, protons are accelerated passing through the LINAC2, from which they come out with an energy of 50 MeV. Then they pass through the PSB (Proton Synchrotron Booster) and the PS (Proton Synchtotron), reaching an energy of 1.4 GeV and 26 GeV respectively. Finally, before the injection in the LHC, the SPS (Super Proton Synchrotron) increases the energy of protons up to 450 GeV. Once in the collider, the protons are kept on their orbits by means of super-conducting magnets providing a magnetic field of 8.34 T. At the nominal operation regime, the LHC rings store 2808 proton bunches per ring, each of them composed of 1.1×10^{11} protons, colliding with a frequency of 40 MHz. This complex achieves an instantaneous luminosity for proton-proton collisions of 10^{34} cm^{-2}s^{-1}. One of the main motivations for building such a collider was the experimental search for the Brout-Englert-Higgs boson. The two detectors ATLAS and CMS are then dedicated to the direct search of physics beyond the Standard Model and to study the properties of the Higgs boson and the top quark. The LHC is also capable of accelerating heavy ions (Pb) at an energy of 2.8 TeV. ALICE is a specialized detector dedicated to the study of the quark-gluon plasma and makes use of Pb-Pb and Pb-p collisions. The LHCb detector is dedicated to the study of heavy flavour physics with charm and beauty hadrons and $\mathcal{CP}$ violation, and will be described in details in the next sections.
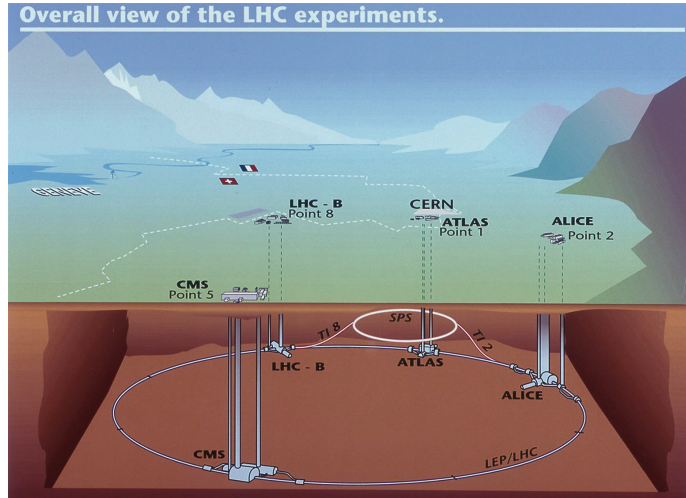
Figure 2.1: *Schematic view of the LHC collider. The figure also shows the four main experiments (ALICE, ATLAS, CMS and LHCb).*

2.2 The LHC beauty experiment

The LHCb experiment is designed to exploit the great production cross sections of $b\bar{b}$ pairs in pp collisions at the LHC energies, which has been measured to be $\sim 280\,\mu$b at $\sqrt{s} = 7\,\text{TeV}$ and $\sim 560\,\mu$b at $\sqrt{s} = 13\,\text{TeV}$ [38]. The LHCb detector [39] is a single-arm spectrometer with a forward geometry covering a region of angular acceptance between 10 mrad and 300 mrad in the horizontal plane (xz) and between 10 mrad and 250 mrad in the vertical plane (yz). The reason behind this choice of geometry is that at high energies $b\bar{b}$ pairs are mostly produced with a strong boost along the beam line. As a consequence, B hadrons are predominantly produced with a small angle. The difference between horizontal and vertical angular acceptances is due to the fact that the horizontal plane is the bending plane in which charged particles are deflected by the dipole magnetic field of LHCb. Such a geometrical acceptance corresponds to a pseudorapidity between 2 and 5, which is defined as:

$$\eta = -\ln\left[\tan\left(\frac{\theta}{2}\right)\right] \qquad (2.1)$$

, where θ is the angle between the beam direction and the particle direction. In the acceptance of the detector, the cross-section is measured to be $72.0 \pm 0.3 \pm 6.8\,\mu$b and $144 \pm 1 \pm 21\,\mu$b for 7 and 13 TeV [38].

The integrated luminosities corresponding to the various years of data taking are shown in Fig. 2.3. A full data set of about 3 fb^{-1} was collected during the Run 1 (between 2010 and 2012). The center-of-mass energy was $\sqrt{s} = 7$ TeV in 2010 and 2011 and $\sqrt{s} = 8$ TeV
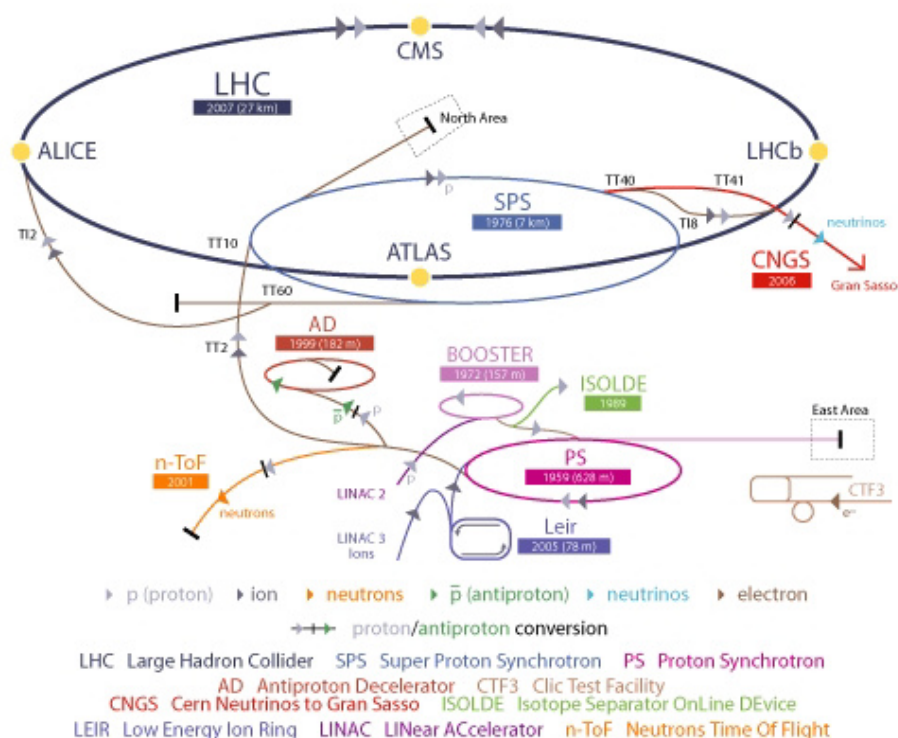
Figure 2.2: *Sketch representing the various pre-accelerating machines. The four main detectors (yellow points) are asymetrically positioned along the beam line.*

in 2012. A Long Shutdown (LS1) was then needed to increase the center-of-mass energy to $\sqrt{s} = 13$ TeV, and LHCb re-started the collection of pp collision data in 2015, until the end of the Run 2 phase in 2018 with an additional 6 fb^{-1} of data. The instantaneous luminosity at the LHCb experiment is 4×10^{32}cm^{-2}s^{-1}, one order of magnitude lower than the one achieved for the general purpose experiments. This is due to the fact that LHCb could not efficiently operate in the same pile-up conditions as ATLAS and CMS.

The ambitious physics program of LHCb requires a detector capable of a great precision in the reconstruction of pp interaction vertices and B hadrons decay vertices. This is crucial to perform studies such as the measurement of neutral B meson oscillations, for which it is necessary to have a good proper-time resolution. Also, an excellent particle identification (PID) system is needed in order to discriminate between charged pions, charged kaons and protons with momentum in a range between few GeV/c up to 100 GeV/c. Furthermore the analysis of final states containing leptons requires an optimal PID of muons and electrons. The invariant mass resolution must also be as small as possible in order to discriminate the signals from possible partially reconstructed backgrounds and in order to distinguish
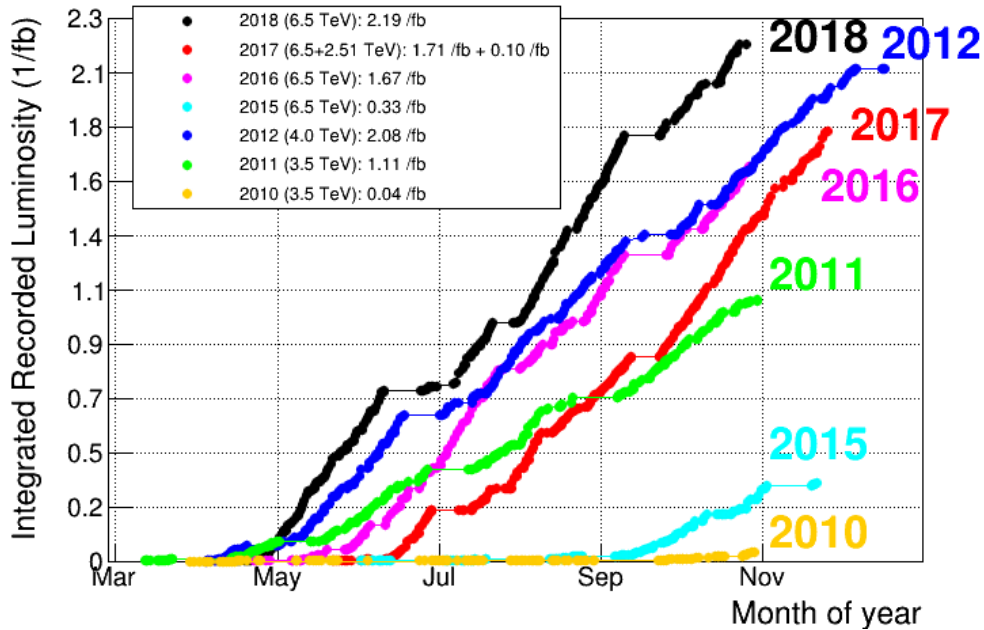
Figure 2.3: *Integrated luminosities recorded by the LHCb experiment during Run 1 (2010-2012) and Run 2 (2015-2018) data taking periods, for p-p collisions. Corresponding beam energies are also displayed.*

between B^0 and B_s mesons decays. For these reasons, the momentum of charged tracks must be measured with a relative precision of about 10^{-3}. Since the production cross sections of $b\bar{b}$ pairs is considerable, the trigger system must have a very high background rejection in order to reduce the acquired data samples to a manageable size. In order to reach this purpose, the LHCb trigger is organized in multiple levels, each processing the output of the previous one. Also, the large amount of data collected by the experiment requires efficient and reliable computing resources, both for processing and storing the data.

The Figure 2.4 shows an overview of the entire LHCb detector. The different elements of the detector are displayed :

- the VErtex LOcator (**VELO**) is placed around the interaction region and allow the reconstruction of primary and secondary vertices;

- the first Ring Imaging CHerenkov (**RICH1**) detector is placed just after the VELO and is dedicated to the identification of charged particles;

- the Tracker Turicensis (**TT**) is placed after the first RICH and is part of the tracking system;

- the dipole magnet of LHCb provides the magnetic field used to bend particles tracks in order to evaluate their charge and momentum;
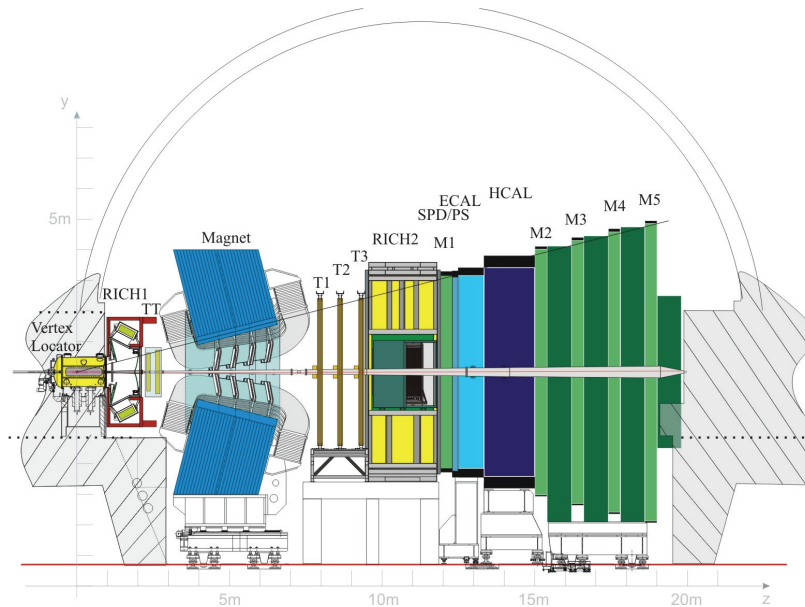
Figure 2.4: *Overview of the entire LHCb detector.*

- the three tracking stations (**T1,T2,T3**) are placed behind the magnet and are also dedicated to track reconstruction;

- the second Ring Imaging CHerenkov detector (**RICH2**) is designed to provide efficient particle identification in a different momentum range with respect to RICH1;

- the Electromagnetic CALorimeter (**ECAL**) system is placed just after the RICH2 and is necessary for an efficient trigger and for the identification of electrons and photons. It is preceded by two auxiliary sub-detectors : the Scintillating Pad Detector (**SPD**) and the PreShower (**PS**);

- the Hadronic CALorimeter (**HCAL**) is placed behind the ECAL and is exploited by the hadronic trigger;

- the Muon Stations are placed just before the SPD/PS (**M1**) and at the end of the detector (**M2** to **M5**), where only muons can arrive without being stopped by the calorimeter system. They are used both for an efficient trigger on decays with muons in the final state and for muon identification.

Overall, the VELO, the TT and the three tracking stations together with the magnetic dipole form the LHCb tracking system. The RICH1 and RICH2 detectors, the electromagnetic and hadronic calorimeters and the muon stations form the LHCb particle identification system.

2.3 LHCb vertexing and tracking systems

The purpose of the whole tracking system is to identify the particle trajectories, measure their momenta and reconstruct the interaction and decay vertices. The latter is accomplished by the VELO, which also allows the track reconstruction together with the Tracker Turicensis and the three tracking stations placed after the magnet.

2.3.1 The Vertex Locator

The VELO provides precise measurements of the track coordinates close to the interaction point. These coordinates are used to identify any displaced secondary vertex, which is a distinctive feature of B hadron decays. Since B hadrons average lifetime is of the order of 1.5×10^{-12} s they cover, at LHC energies, a mean distance of about 1 cm inside the detector and gives rise to secondary vertices distant from the primary pp interaction vertex. For this reason, in order to select signals and reject most of the combinatorial background, it is necessary for the vertex detector to have a micrometric precision.

The VELO [40] consists of a series of 21 circular silicon modules arranged perpendicularly along the beam line direction as shown in Fig. 2.5, each providing a measurement of the $R = \sqrt{x^2 + y^2}$ and ϕ coordinates. Each module is divided into two halves which can be moved horizontally away from the beam pipe. The VELO aperture can vary from an open position, required during the beam stabilization phase, to a closed position maintained during data-taking. For this reason, VELO modules are mounted on a moveable device inside a vessel maintaining the vacuum, and each half can be moved between 3 cm and 8 mm away from the beam. The module halves are composed of two planes of 300 μm thick silicon microstrip sensors that provide a measurement of radial (R sensors) and polar (ϕ sensors) coordinates of the hits generated by ionizing particles crossing the active material of the VELO. The z coordinate is given by the precisely measured module positions, knowing which modules provided a signal for a given particle hit. The R sensors of each half modules are divided into four parts of about $45°$ each. The microstrips are modeled in a semi-circular shape and their width varies from 38 μm (close to the beam) to 102 μm (far from the beam): the smaller width close to the interaction region is due to the higher number of particles expected in that zone.

The ϕ sensors are divided into two regions, inner and outer. The pitch size of the inner region increases linearly as a function of the radius, ranging from 38 μm to 78 μm. The outer region, that starts at a radius of 17.25 mm, has instead a pitch ranging from 39 μm to 97 μm. Inner and outer regions have different tilts to the radial direction in order to improve pattern recognition: they are tilted by $20°$ and $10°$ respectively. Furthermore, in order to achieve a better track reconstruction, the longitudinally adjacent ϕ sensors have opposite skew to each other.

The performances of the VELO detector have been extensively studied using the data collected in 2011 [41]. In particular a primary vertex resolution of 13 μm in the transverse plane (x, y) and 71 μm along the beam axis is achieved for vertices with 25 tracks or more. An impact parameter resolution of less than 35 μm is achieved for particles with transverse
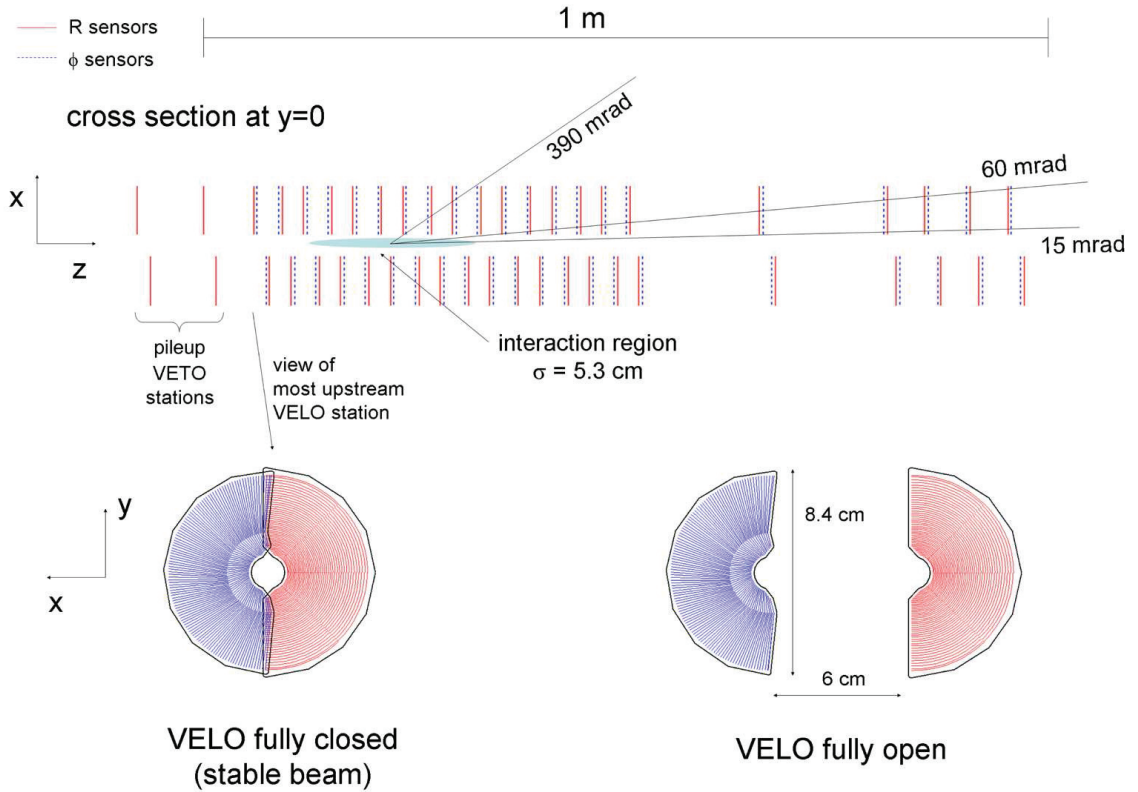
Figure 2.5: *Top view of the VELO silicon modules, with the detector in the fully closed position (top). Front view of the modules in both the closed (bottom left) and open positions (bottom right).*

momentum greater than 1 GeV/c.

2.3.2 The Tracker Turicensis

The Tracker Turicensis (TT, [42]) is placed between the first RICH detector and the dipole magnet in a region where a residual magnetic field is present (0.15 Tm). The TT purpose is to provide reference segments which are used to combine the tracks reconstructed in the tracking stations after the magnet and those reconstructed in the VELO: this allows to improve the resolution on momentum and trajectory of the reconstructed tracks. The system consists of four stations, divided into two groups called respectively TTa and TTb, spaced by approximately 30 cm and placed at a distance of about 2.4 m from the interaction region. Each of the four stations cover a rectangular region of about 130 cm in height and about 150 cm wide. The scheme of the TT sub-detector is shown in Fig. 2.6. Each TT station is made up of silicon microstrip sensors with a pitch of about 200 μm and is arranged into up to 38 cm long readout strips. In the first and fourth stations the

strips are parallel to the vertical plane, while in the second and third station they are tilted by $+5°$ (*u*-layer) and $-5°$ (*v*-layer) respectively. This arrangement allows to obtain a better precision in the reconstruction. The TT has a typical single-hit resolution of about 50 μm.
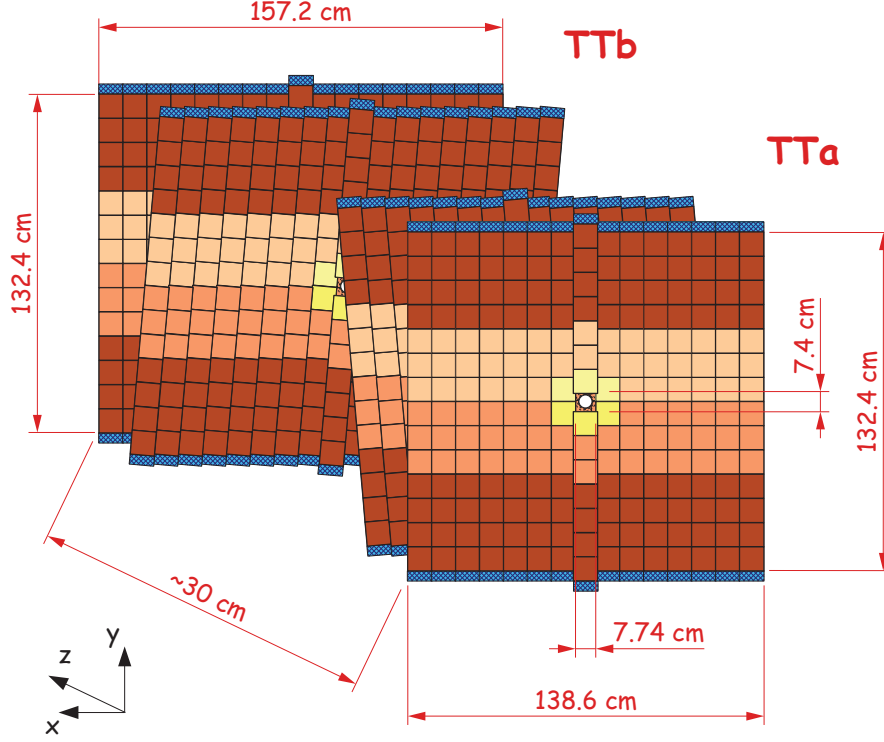
Figure 2.6: *Scheme of the four TT stations.*

2.3.3 Downstream tracking stations

The three tracking stations T1, T2 and T3 are placed just after the dipole magnet and are divided into two main parts. The inner part of the tracking stations, the Inner Tracker (IT), uses silicon microstrip sensors while the outer part, the Outer Tracker (OT), exploits drift straw tubes. As shown in Fig. 2.7 the IT part of each station is placed in front of the OT part.

The Inner Tracker [43] covers the region around the beam pipe and consists of four detection planes arranged as shown in Fig. 2.7 and 2.8. Similarly to the TT, in the first and fourth planes the silicon sensors are parallel to the vertical plane (*x*-planes), while in the second and third plane sensors are tilted respectively by $+5°$ (*u*-plane) and $-5°$ (*v*-plane). The features of microstrip sensors are analogous to those used for the Tracker Turicensis since they have a pitch of about 200 μm and they are up to 22 cm long. The
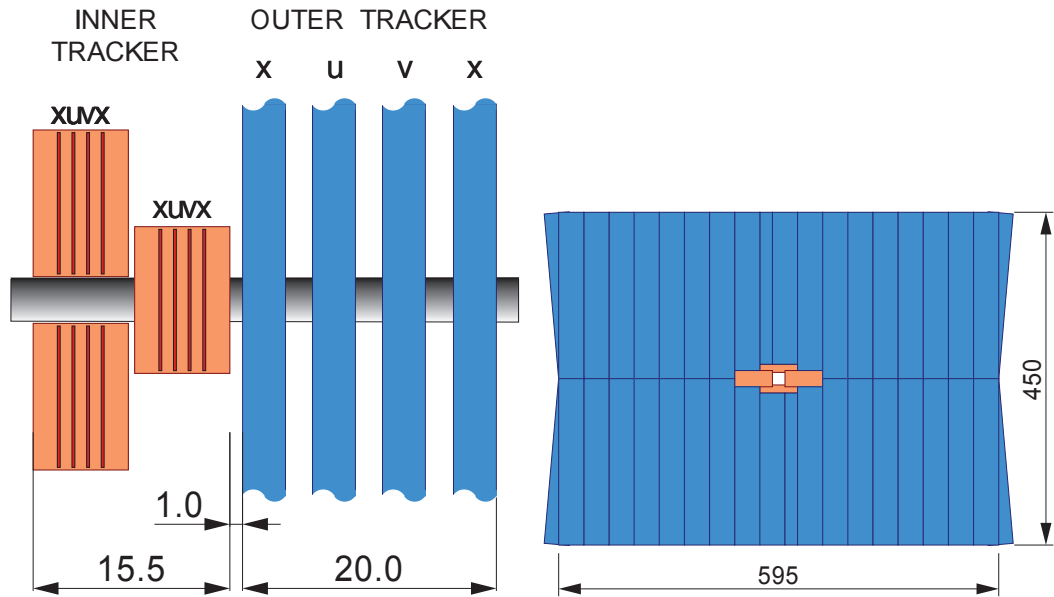
Figure 2.7: *Layout of a T station from a side view (left) and from a front view (right). The dimensions are in centimeters. In the left part it can be seen that the IT sub-detector is placed in front of the OT sub-detector and the x- u- v-planes mentioned in the text are shown. In the right part it can be seen that the IT sub-detector (in orange) is placed around the beam pipe, while the OT sub-detector covers the outer region of the station.*
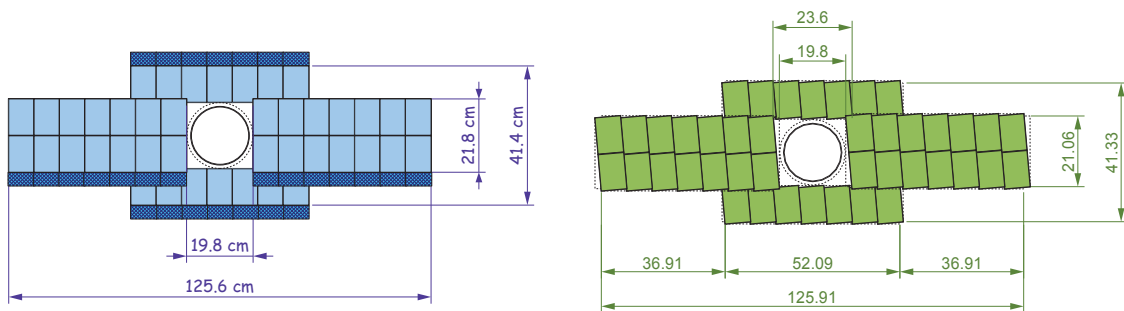
Figure 2.8: *Frontal view of the x-plane (left) and u-plane (right) of the IT sub-detector.*

total size of the IT sub-detector is about 1.2 m in the bending plane and about 40 cm in the vertical plane. The hit resolution in the IT is about the same as in the TT.

The Outer Tracker [44] is realized using gas-filled straw tubes detectors and consists of four planes of tubes arranged in the same way as the TT and IT sensors. In fact the first and fourth planes have tubes parallel to the vertical plane (x-planes), while the second and third planes have tubes tilted by $+5°$ (u-plane) and $-5°$ (v-plane). Furthermore each plane has two rows of tubes arranged in a honeycomb structure (see Fig. 2.9) in order to optimize the sensitive area. The straw tubes have a radius of 5 mm and are filled with a mixture of $Ar/CO_2/O_2$ (70/28.5/1.5 %) which guarantees a fast drift-time, below 50 ns. The OT resolution on the coordinate of the hits is typically around 200 μm [45].
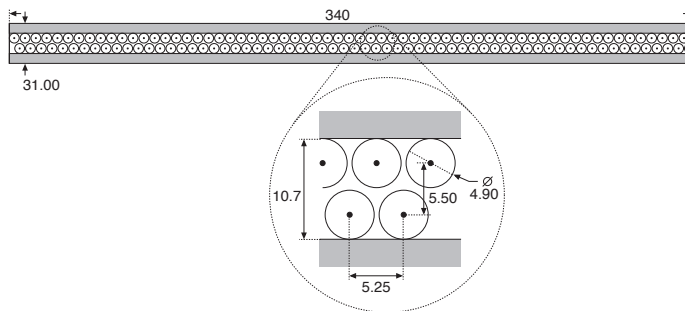
Figure 2.9: *Cross section of a straw tube plane in the OT. The zoomed part shows the honeycomb structure of the two rows of tubes.*

2.3.4 The LHCb magnet

The magnetic field of LHCb is provided by a warm dipole magnet (*i.e.* non superconducting) placed between the TT and the first tracking station T1 [46]. As already mentioned the magnetic field is needed to identify the particles charge and to measure their momentum. The magnet (see Fig. 2.10) is formed by two coils inclined by a small angle with respect to the beam direction.The magnetic field is directed along the y coordinate perpendicular to the xz bending plane. The maximum intensity of the magnetic field is about 1 T, while the magnetic field integral is approximately 4 Tm.
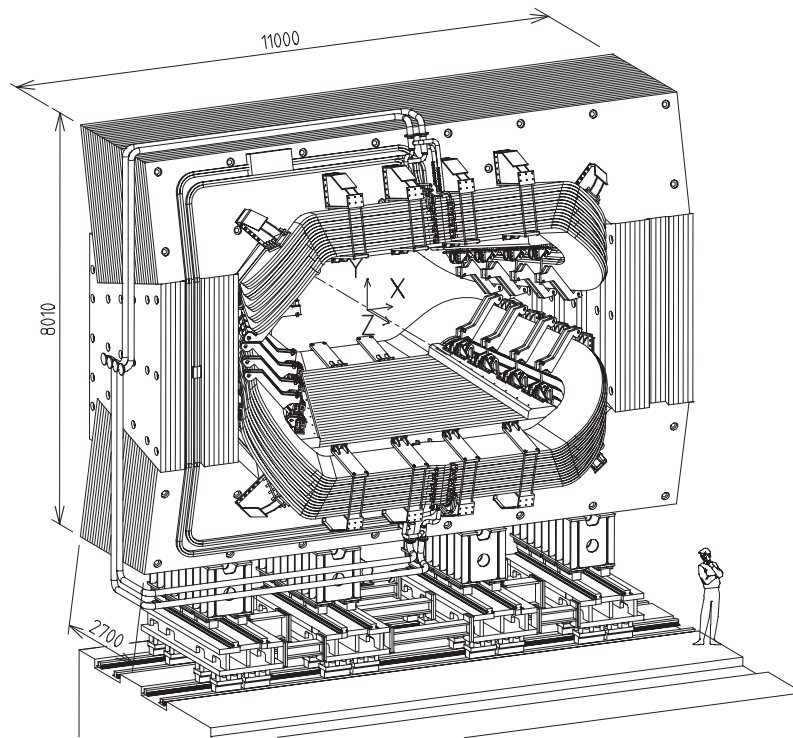
Figure 2.10: *Sketch of the dipole magnet of LHCb.*

2.3.5   Track types

The hits in the VELO, the TT, the IT and the OT detectors are combined to form particle trajectories from the VELO to the calorimeters. Depending on their trajectories different classes of tracks are defined, illustrated in Figure 2.11 :

- Long tracks,traversing the full tracking system from the VELO to the T stations. These have the most precise momentum determination and therefore are the most important set of tracks for b-hadron decay reconstruction.

- Upstream tracks, traversing only the VELO and TT stations. These are in general lower momentum tracks that are bent out of the detector acceptance by the magnetic field.

- Downstream tracks, traversing only the TT and T stations. The most relevant cases are the decay products of K_S^0 and Λ^0 that decay outside the VELO acceptance.

- VELO tracks, measured in the VELO only and are typically large angle or backward tracks, useful for the primary vertex reconstruction.

- T tracks only hits the T stations. They are typically produced in secondary interactions, but are useful for the global pattern recognition in RICH 2.
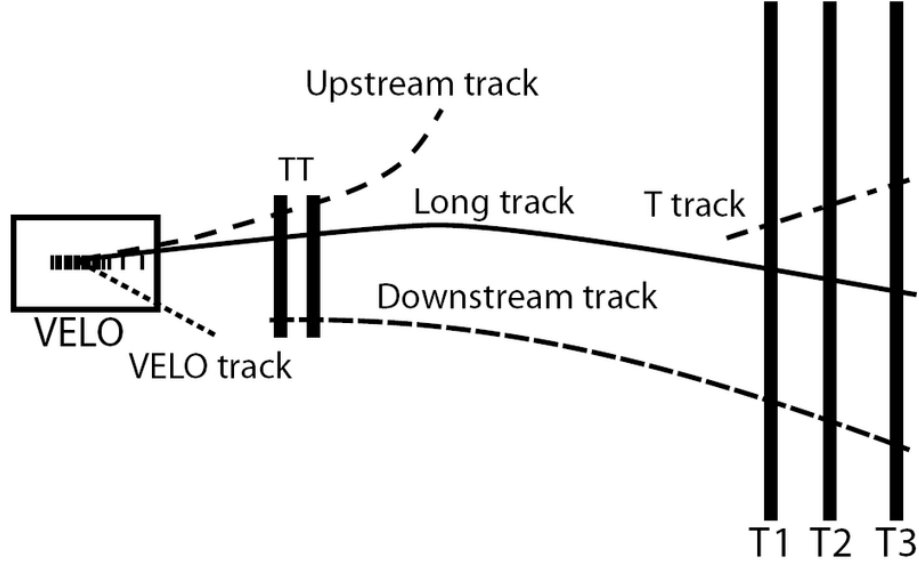
Figure 2.11: Illustration of the different track types: long, upstream, downstream, VELO and T tracks.

2.4 LHCb particle identification systems

The purpose of the particle identification system is to provide an efficient and reliable identification of charged leptons and hadrons as well as photons and neutral pions. This task is accomplished by the two Ring Imaging Cherenkov detectors (RICH1 and RICH2), the calorimeters and the muon stations.

2.4.1 RICH detectors

The Cherenkov effect is the emission of electromagnetic radiation that occurs when a charged particle passes through a dielectric medium at a speed greater than the phase velocity of light in that medium. This effect is exploited to discriminate charged pions, kaons and protons in a momentum range between few GeV/c up to about 100 GeV/c. It also contributes to the identification of electrons and muons. A schematic representation of this effect is shown on Fig. 2.12. Cherenkov light detectors exploit the following relation between the particle momentum and the emission angle of Cherenkov photons

$$\cos(\theta_C) = \frac{1}{\beta n}, \tag{2.2}$$

where θ_C is the emission angle of Cherenkov photons with respect to the particle direction of flight, $\beta = v/c$ is the particle velocity normalized with respect to the speed of light in the vacuum and n is the refraction index of the radiator medium. Measuring this angle together with the momentum, it is possible to determine the mass of the particle.
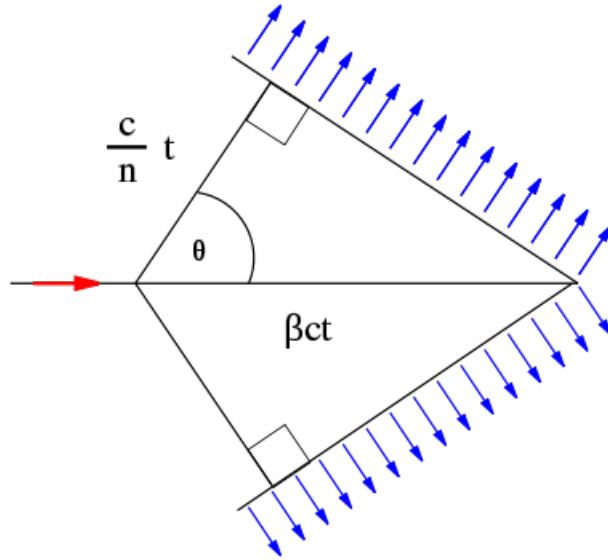
Figure 2.12: *Geometric representation of the Cherenkov emission.*

The RICH detectors exploit different radiators because for particles approaching the speed of light the Cherenkov angle saturate at the value $\theta_C = \arccos(1/n)$.

The RICH1 [42], located immediately after the VELO with a geometrical acceptance from 25 mrad to 330 mrad, is optimized to identify low momentum tracks, in a range between 1 GeV/c and about 60 GeV/c. The RICH1 exploits two different types of radiators: the first is a 5 cm thick Aerogel layer with $n = 1.03$ optimal for low momentum particles (up to 10 GeV/c), while the second, gaseous C_4F_{10} with $n = 1.0015$ that fills a gap of about 85 cm, is dedicated to particles with higher momenta (up to 60 GeV/c).

The RICH2 is instead optimized for the identification of particles with higher momenta, from 15 GeV/c up to 100 Gev/c, and hence is complementary to the RICH1. It is placed after the last tracking station and has a geometrical acceptance of about 100 mrad in the vertical plane and about 120 mrad in the horizontal plane. The radiator used for the RICH2 is gaseous CF_4 that has a refraction index $n = 1.00046$.

The schematic picture of the two RICH detectors of LHCb is reported in Fig. 2.13. Both RICH detectors exploit an optical system made of spherical and plane mirrors in order to convey the emitted Cherenkov light on a lattice of photo-detectors (Hybrid Photon Detector, HPD). The HPD planes are placed out of the detector acceptance and are carefully shielded from the residual magnetic field.

The LHCb RICH detectors have excellent particle identification performances and provide a very clear discrimination of charged pions, kaons and protons. Fig. 2.14 shows the Cherenkov angle as a function of particle momentum using information from the C_4F_{10} radiator for isolated tracks selected in data (a track is here defined as isolated when its Cherenkov ring does not overlap with any other ring from the same radiator) [47].

As can be seen from the figure, events are distributed into distinct bands according to their mass. Although the RICH detectors are primarily used for hadron identification, it
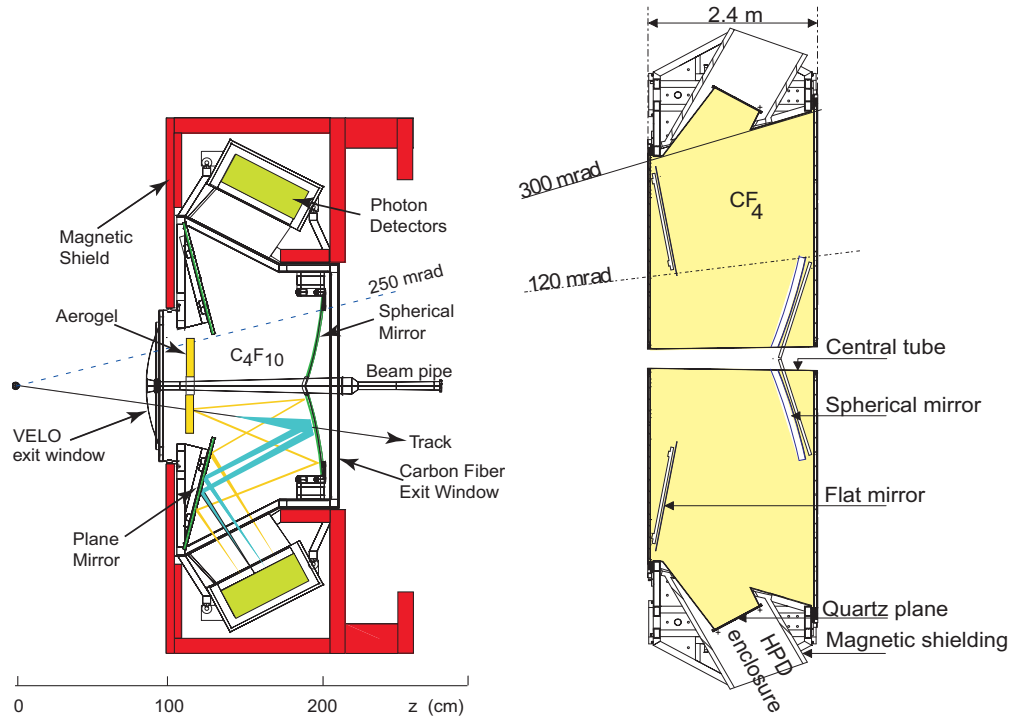
Figure 2.13: *Schematic view of the RICH1 (left) and RICH2 (right) detectors. The different radiators and the optical systems are also shown.*

is worth noting that a distinct muon band can also be observed.

2.4.2 Calorimeters

The calorimeter system [48] is used to identify electrons, photons and neutral pions and to measure their energy. Furthermore, it provides crucial information for the Level-0 trigger (L0-trigger), evaluating the transverse energy E_T of hadrons, electrons and photons. The calorimeter system is divided into four sub-detectors:

- Scintillator Pad Detector (SPD);

- PreShower (PS);

- Electromagnetic CALorimeter (ECAL);

- Hadronic CALorimeter (HCAL).

In Fig. 2.15 is schematically represented the interaction of electrons, hadrons and photons with the various sub-detectors. Each sub-detector is divided into regions where different cell sizes are used. Indeed, aiming to reach a compromise between occupancy and a
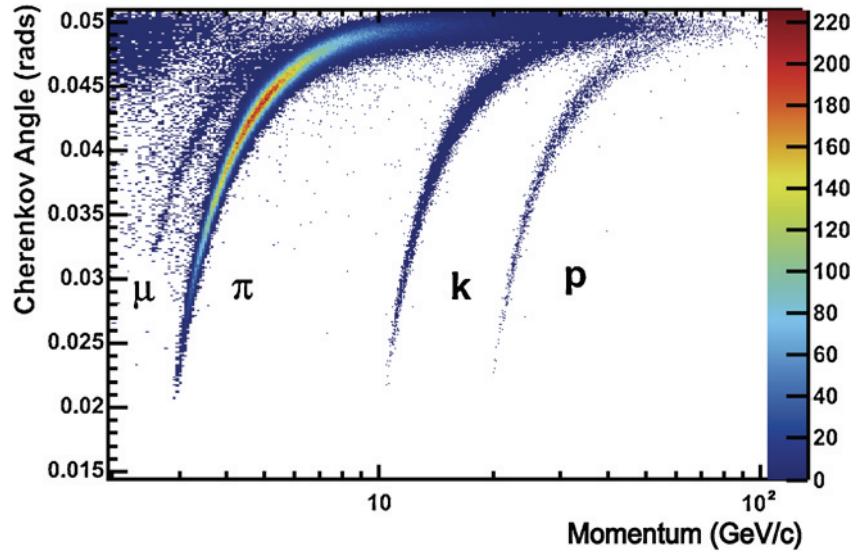
Figure 2.14: *Reconstructed Cherenkov angle as a function of track momentum in the C_4F_{10} radiator [47].*

reasonable number of read-out channels, the size of the sensor elements increases going far from the beam-pipe and the high occupancy region. SPD, PS and ECAL are divided into three regions (inner, middle and outer) while the HCAL is composed of only two regions (inner and outer). A schematic overview of these subdivisions is shown in Fig. 2.16.
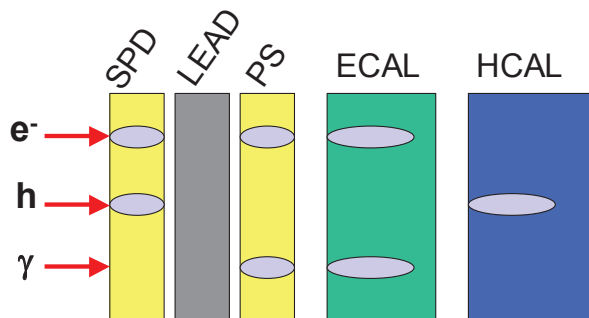
Figure 2.15: *Energy deposited in the different parts of the calorimeter by an electron (e), a hadron (h) and a photon (γ).*
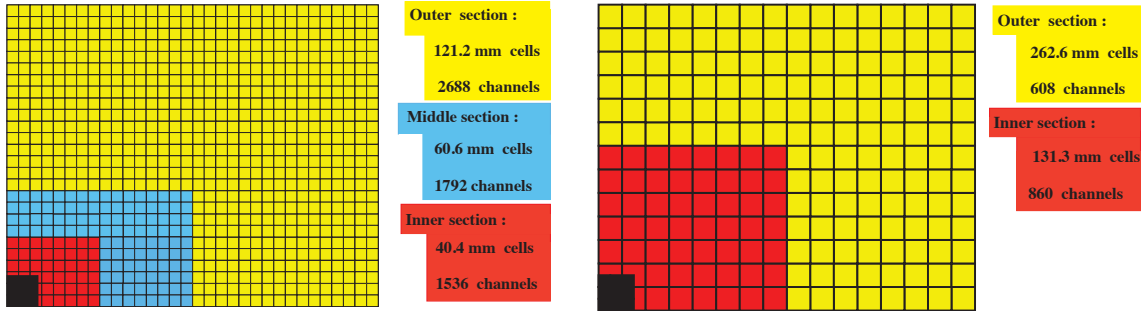
Figure 2.16: *Left: frontal view of the SPD/PS and ECAL detectors where the three regions mentioned in the text are shown. Right: frontal view of the HCAL where there are only two regions.*

The SPD and the PS are auxiliary sub-detectors of the electromagnetic calorimeter and they are placed in front of it. Both the SPD and the PS are composed by a scintillator plane about 15 mm thick. They are separated by a 2.5 radiation lengths * lead converter layer. The light emitted by the scintillator material is collected by means of wavelenght-shifting optical fibers (WLS) connected to clear fibers which convey the light to multi-anode photomultipliers placed outside the detector. The SPD determines if the particle hitting the calorimeter system is charged or neutral, since the former produces light when passing through a scintillator material while the latter does not. The PS determines the electromagnetic character of the particle, namely whether it is an electron/photon or not.

The ECAL is a sampling calorimeter using the Shashlik technology and separated into different independent modules. This particular type of calorimeters exploit WLS optical fibers which cross longitudinally the entire module and carry the scintillation light to the read-out photomultipliers. The ECAL modules are composed by 66 lead converter layers of thickness of about 2 mm separated by plastic scintillator layers which are about 4 mm thick. ECAL modules have a total size of about 25 radiation lengths and 1.1 nuclear interaction lengths [†]. Each module has a section of 12×12 cm^2. In the inner region, a module corresponds to 9 read-out channels of 4×4 cm^2. In the middle region, a module

---

*The radiation lenght is defined as follows

$$X_0 = \frac{A \cdot 716.4}{Z(Z+1)\ln(287/\sqrt{Z})} \ g/cm^2 \qquad (2.3)$$

where A is the mass number and Z is the atomic number of the material considered. This quantity corresponds to the distance over which the energy of an electron is reduced by a factor $1/e$ only due to radiation loss [49].

[†]The nuclear interaction length $\lambda_I \propto A^{1/3}$, similarly to the radiation length X_0, is the mean path length required to reduce the energy of a relativistic charged particle passing through matter by a factor $1/e$.

has 4 read-out channels of 6×6 cm^2. In the outer region, a module corresponds to a single read-out channel. A schematic view of an ECAL module is shown in Fig. 2.17.

The HCAL provides the measurement of the energies of hadronic showers, which is the fundamental information for the Level-0 hadronic trigger. The HCAL modules consist of 4 and 6 mm thick iron plates interspaced with scintillating tiles arranged parallel to the beam pipe. HCAL modules have a total size of approximately 5.6 nuclear interaction lengths. Each module has a section of 13×13 cm^2 in the inner region and 26×26 cm^2 in the outer region. An HCAL module corresponds to a single read-out channel.

The performances of the calorimeter system have been evaluated with various tests performed before the start of the data taking. The energy resolutions of the calorimeter modules have been measured to be [50] :

$$\text{ECAL :} \quad \frac{\sigma(E)}{E} = \frac{(8.5 - 9.5)\%}{\sqrt{E}} \oplus 0.8\%, \tag{2.4}$$

$$\text{HCAL :} \quad \frac{\sigma(E)}{E} = \frac{(69 \pm 5)\%}{\sqrt{E}} \oplus (9 \pm 2)\%.$$

However, the effective calorimeter resolution is limited due to pile-up and conversion effects.

The ECAL calibration is performed by reconstructing resonances decaying to two photons like $\pi^0 \to \gamma\gamma$. The calibration of the HCAL is achieved by measuring the ratio E/p between the energy E, as measured in the calorimeter, for a hadron with momentum p, as measured by the tracking system.

2.4.3   The muon system

The final part of the LHCb detector is the muon system which provides the identification of muons. Muons are present as final decay products in different fundamental LHCb measurements such as $B^0 \to K^{*0}\mu^+\mu^-$ [51], $B_s^0 \to J/\psi(\mu^+\mu^-)\phi$ [52] or $B_s \to \mu^+\mu^-$ [53], [54].

The muon system [55] (see Fig. 2.18) is made of five stations (M1 to M5) covering an angular acceptance of ± 300 mrad in the horizontal plane and ± 200 mrad in the vertical plane. This corresponds to a geometrical efficiency of approximately 46% for the detection of muons arising from B hadrons. The first muon station, M1, is placed before the calorimeters in order to avoid possible multiple scattering effects that could modify the particle trajectory. The remaining stations, M2 to M5, are placed after the calorimeter system, at the end of the LHCb detector, and are separated by iron planes 80 cm thick. Each muon station is divided into four regions (R1-R4) as shown in Fig. 2.19. The R1 region is the closest to the beam-pipe and has the most dense segmentation while the R4 region is the farther. The segmentation defined per region is such that the charged particle occupancy is expected to be approximately the same in each region. All the muon chambers are composed by Multi-Wire Proportional Chambers, except for the inner region of the M1 station, which exploits three gas electron multiplier foils sandwiched between anode and cathode planes (GEM detectors). In total, the muon system consist of 1368 MWPC and 12 GEM detectors.
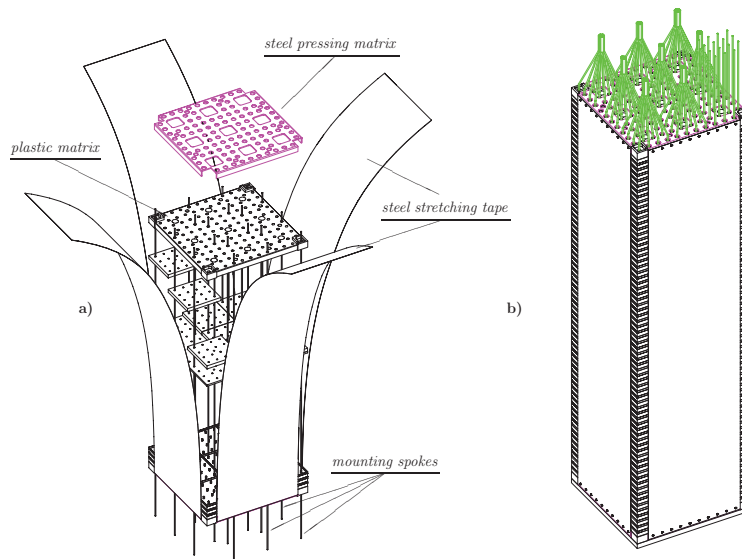
Figure 2.17: *Left: picture of an ECAL module during the assembly phase, the lead/scintillator layers are also shown. Right: representation of an assembled ECAL module of the inner region, the green lines represent the optical fibers conveying the light to photo-multipliers.*

2.4.4 Multivariate PID methods

The particle identification (PID) in LHCb is achieved by combining the information coming from the various sub-detectors. The RICH detectors, the calorimeters and the muon stations are used for the identification of charged particles (e, μ, π, K and p), while photons (γ) and neutral pions (π^0) are identified using the calorimeter system.

For each particle the available PID information is elaborated from two variables of different nature, but with the same purpose: the log-likelihood difference (DLL) and the ProbNN variable which has been introduced later in the collaboration.

The first variable, the DLL, is defined as the difference between a given PID hypothesis (x) and the pion hypothesis as

$$DLL_{x\pi} = \ln \mathcal{L}_x - \ln \mathcal{L}_\pi = \ln \left(\frac{\mathcal{L}_x}{\mathcal{L}_\pi} \right) \ , \tag{2.5}$$

where each likelihood function $\mathcal{L}_i$ ($i = x$ or π) combines the information coming from the various PID sub-detectors. The DLL_{xy} related to any particle hypotheses x and y can then be defined accordingly. The higher the variable DLL_{xy} is, the higher the probability of the candidate to be x.

The second kind of variable, the ProbNN, is built by running multivariate analysis tools (in particular Neural Networks [56]) based on the detector PID information. Differently from the likelihood functions, the multivariate analyses take into account the correlations between the information coming from the different detectors. The ProbNN variables
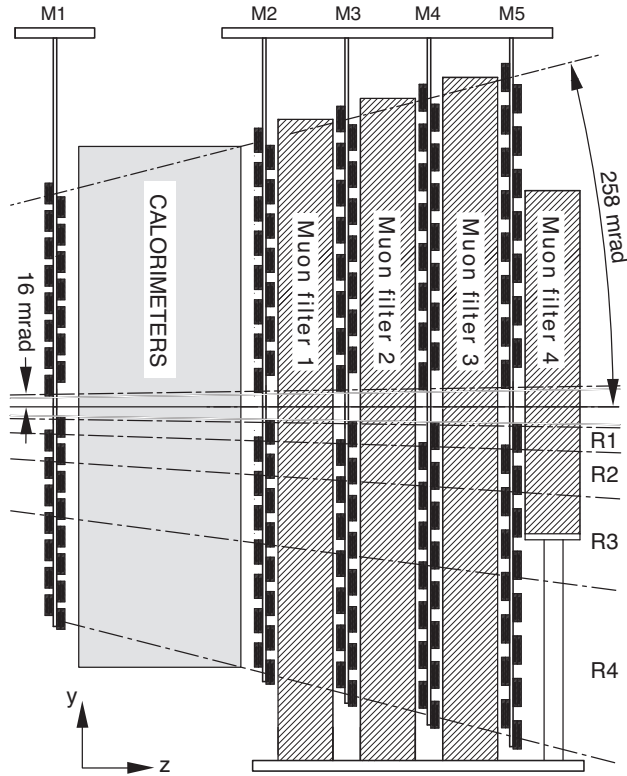
Figure 2.18: *Side view of the LHCb muon system.*

produced as output are defined between 0 and 1, as a probability would be, and can be used to separate between different tracks hypothesis: in particular they are referred to as ProbNNx according to the particle hypothesis which is tested.

In the analysis presented in this thesis, ProbNN variables are used to distinguish between charged hadrons (kaon, pion and protons). For what concerns the identification of neutral particles, which is very important in analyses involving radiative decays, this is achieved using dedicated PID variables described in detail in Sec. 2.5.

2.5 Neutral objects reconstruction

The reconstruction of neutral particles is achieved by combining the information coming from the Electromagnetic (ECAL) and Hadronic (HCAL) CALorimeters together with the information coming from the Scintillating Pad Detector (SPD) and the PreShower (PS) auxiliary sub-detectors. The identification of neutral objects and their separation is a key element when performing physics analyses with decays involving photons or neutral pions in the final state. This is something very challenging since LHCb has not been specifically designed to accomplish it. Neutral pions decay into two photons with a branching ratio of
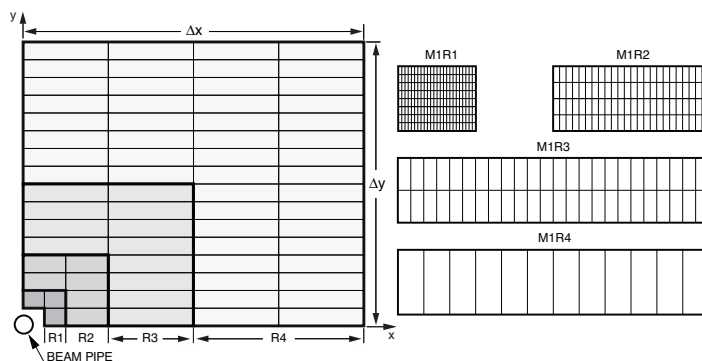
Figure 2.19: *Left: front view of a quadrant of a muon station, each rectangle represents a chamber. Right: segmentation of the four types of chambers corresponding to the four region of M1. In M2, M3 (M4, M5), the number of columns per cell is double (half) with respect to M1, while the number of rows is the same.*

$(98.823 \pm 0.034)\%$ [57] and for high p_T values, typically $p_T > 2.5$ GeV/c, the two resulting γ start to merge in a single ECAL cell faking a true radiative photon. These neutral pions are called *merged* π^0. Decays that involve merged π^0 are an important source of background for radiative channels. Conversely, when the two photons of a π^0 decay are detected in two separate ECAL cells, we have a *resolved* π^0.

2.5.1 Photon reconstruction

The energy from the interaction of photons and electrons with the detector is mainly absorbed in the ECAL. The reconstruction process of electromagnetic showers begins with the identification of the ECAL cell that has an excess in energy deposition compared to all its direct neighbors. Such cell is also called *seed*. The number of neighbor cells is 8 per 'regular' cells which are far from boundaries of ECAL detector, and it varies from 3 to 9 for cells close to the boundaries. These cells are selected only if the transverse energy is larger than 50 MeV [58]. The reference cell will originate the cluster according to the clusterisation procedure adopted in the Cellular Automaton algorithm [59]. As direct consequence of these formal definitions, the seed cells of two reconstructed clusters are always separated at least by one cell. If a calorimeter cell is shared between two overlapping clusters, the energy of the cell is shared between the clusters depending on the cluster energies and its distance to the clusters' barycenters.

In order to determine the 4-momentum of the corresponding particle, the total energy of the electromagnetic shower and the transversal barycenter are calculated according

to [60]

$$\epsilon = \sum_i \epsilon_i \quad x_b = \frac{1}{\epsilon} \sum_i x_i \epsilon_i \quad y_b = \frac{1}{\epsilon} \sum_i y_i \epsilon_i \; , \tag{2.6}$$

where ϵ_i stands for the energy deposit in each cell of the cluster, x_i and y_i are the coordinates of the cell center and the sum runs over all cells forming the cluster.

The selection of neutral clusters ("photon candidates") is performed using anti-coincidence techniques with reconstructed tracks. In order to discriminate photons from charged particles, the main criterion is the isolation of the cluster with respect to the tracks extrapolated to the ECAL reference plane. This requirement is implemented defining the bi-dimensional χ^2

$$\chi^2_{2D}(\vec{\mathbf{p}}) = (\vec{\mathbf{p}}_{tr} - \vec{\mathbf{p}})^T \, C_{tr}^{-1} \, (\vec{\mathbf{p}}_{tr} - \vec{\mathbf{p}}) + (\vec{\mathbf{p}}_{cl} - \vec{\mathbf{p}})^T \, S_{cl}^{-1} \, (\vec{\mathbf{p}}_{cl} - \vec{\mathbf{p}}) \; , \tag{2.7}$$

where $\vec{\mathbf{p}}_{tr}$ is the extrapolated track 2D-point to the calorimeter plane, C_{tr} is the covariance matrix associated to $\vec{\mathbf{p}}_{tr}$ parameters, $\vec{\mathbf{p}}_{cl}$ is the cluster barycenter position and S_{cl} is the 2×2 cluster second momenta matrix. For each track the χ^2_{2D} is minimized with respect to the 2D-point $\vec{\mathbf{p}}$ in the calorimeter plane. The smallest value over all the tracks is used to distinguish neutral particles clusters (large χ^2_{2D}) from charged particles ones (low χ^2_{2D}): in particular clusters with $\chi^2_{2D} > 4$ are selected as photon candidates. This criterion is highly efficient on clusters related to photons and allows to significantly suppress the clusters due to charged particles such as electrons.

We can distinguish two types of photons, namely converted and unconverted. Due to the material placed between the interaction point and the calorimeter system, 30% of the photons coming from the interaction region convert into an e^+e^- pair before the calorimeter front face. There are two kinds of converted photons, namely photons converted before the magnet (about 23% of the converted photons [61]) or after the magnet. In the first case the tracks associated to the electron pair can be reconstructed, then the photon information is coming from two separated electron tracks. In the second case the electrons mostly end up in a single ECAL cluster and the charged nature of the conversion can be identified using the signal left in the SPD. A cluster with no matching tracks but with a deposit in the SPD is the signature of a photon converted after the magnet. Dedicated calibrations are determined for those converted photons.

The geometry of the calorimeter system has been designed in such a way that the ECAL cells coincide with the PS and SPD cells. The photon energy is evaluated by summing the ECAL cluster energy with the energy deposit in the PS cells in front. The main energy loss arises from the fact that the cluster is reconstructed as a 3×3 matrix of ECAL cells centered around the cluster seed and the transversal energy deposited outside this matrix is not taken into account. Additionally, the dead material between the modules of the calorimeter cells introduces intrinsic losses that need to be compensated. These leakages are corrected according to

$$E_c = \alpha E_{ECAL} + \beta E_{PS} + \gamma, \tag{2.8}$$

where E_c is the corrected photon energy, E_{ECAL} stands for the energy deposit in the 3×3 ECAL cluster and E_{PS} is the measured energy in the PS cells. The α, β and γ coefficients are extracted from data and depend on the ECAL region.

$$(2.9)$$

2.5.2 π^0 reconstruction

The π^0 signature in the ECAL depends on its kinematics, the higher is the momentum of the π^0 the closer the two photons are at the entry of the calorimeter. These two photons can then produce two separated clusters or share a single cluster in which their individual signals are not clearly distinguishable. The π^0 are classified as resolved π^0 in the former case and as merged π^0 in the latter one. The transverse momentum spectrum of merged π^0 starts around 2 GeV/c.

Resolved π^0 Resolved π^0 are reconstructed pairing the two photons in the final state and requiring their reconstructed invariant mass $m_{\gamma\gamma}$ to be in the range [105; 165] MeV/c^2, with the π^0 mass. Only photons with transverse momentum $p_T > 200$ MeV/c and with a track matching χ^2_{2D} greater than 4 are taken into account. Using those criteria and according to the simulation, the global reconstruction and identification efficiency of resolved π^0, with respect to events where both photons are in the ECAL acceptance, both with transverse momentum greater than 200 MeV/c, is about 50% [60]. The inefficiency is mostly due to photons showering in the material upstream the calorimeter. Part of this inefficiency can be recovered by considering converted photons reconstructed as a pair of electrons. Fig. 2.20 displays the invariant mass distribution for $\pi^0 \to \gamma\gamma$ candidates obtained using Run 1 LHCb data [62]. The plot shows the $\gamma\gamma$ mass distribution before (red) and after (blue) applying the fine ECAL calibration procedure. The details of this procedure are not reported here and can be found in Ref. [63]. Looking at the blue curve in Fig. 2.20 we can notice that the final resolution on $m_{\gamma\gamma}$ is about 9 MeV/c^2.

Merged π^0 Each electromagnetic cluster is split into two subclusters defined from the two most energetic cells in the cluster. An algorithm calculates the barycenter of each sub-cluster using the expected transverse shower shape of individual photons. The positions of the two barycenters depend on the energy sharing between the two sub-clusters, which itself depends on the positions of the two barycenters. According to that, the calculation is done using an iterative procedure [60]. After the preparation of the two photon sub-clusters, the following criteria are applied to identify the cluster as arising from a π^0.

- The cluster is identified as coming from a neutral particle requiring a track matching $\chi^2_{2D} > 1$.

- The cluster energy has to be compatible with the merged π^0 hypothesis. To ensure that, a cut is applied on the minimal distance allowed by the kinematics between
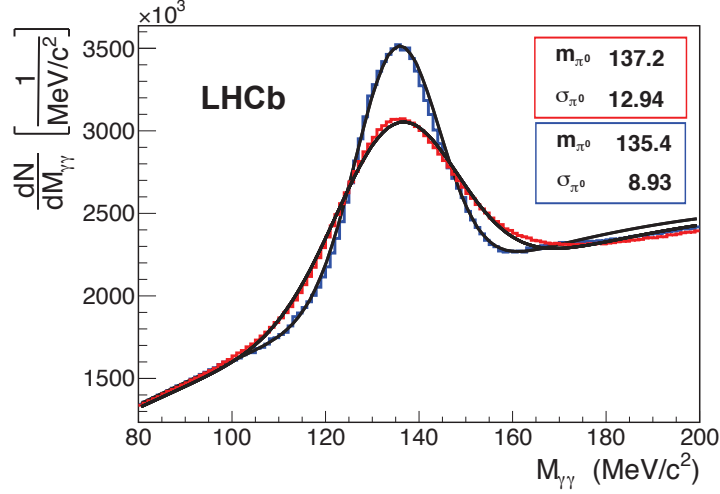
Figure 2.20: *Invariant mass distribution for $\pi^0 \to \gamma\gamma$ candidates before (red curve) and after (blue curve) applying the fine ECAL calibration procedure. Values in the red (blue) box are the mean and sigma of the signal peak distribution in* MeV/c^2 *before (after) applying the calibration.*

the impacts of the two photons on the ECAL front face

$$d_{\gamma\gamma} = 2 \times z_{ECAL} \times m_{\pi^0}/E_{\pi^0} < 1.8\Delta \ , \tag{2.10}$$

where Δ is the transverse size of the calorimeter cell, m_{π^0} is fixed to 135 MeV/c^2, E_{π^0} is the π^0 energy and z_{ECAL} is the position of the ECAL front face with respect to the nominal interaction point.

- The reconstructed merged π^0 mass is required to be in the range 75 to 195 MeV/c^2. The wider mass range compared to resolved π^0 is due to the wider $m_{\gamma\gamma}$ resolution, which is typically 12-15 MeV/c^2.

2.5.2.1 Photon identification

The default algorithm currently used in the collaboration in order to achieve the photon identification (ID) is a Neural Network (specifically, a Multi-Layer Perceptron) discriminant. Two independent estimators, IsNotH and IsNotE, are built to establish the photon hypothesis: the former is aimed to distinguish the γ from non-electromagnetic deposits associated to hadrons while the latter allows to separate between photons and electrons. These classifiers are described in Ref. [64] and represent a significant improvement compared to the previous photon identification procedure used in LHCb.

Here we discuss only the IsNotH discriminant (also called γ_{CL}). It exploits the following variables:

- The track matching χ^2_{2D}.

- The energy deposits in the PS: E_{PS}.

- The ratio of the energy of the seed cell and that of the 3×3 cluster in the ECAL: E_{seed}/E_{ECAL}.

- The ratio of the energy in the PS cell in front of the seed cell and the total energy measured in the PS: E_1/E_{PS}.

- The ratio of the energy in the HCAL, in the projective area matching the cluster, and the cluster energy in the ECAL: E_{HCAL}/E_{ECAL}.

- The 2×2 matrix of PS cells with the highest energy deposit in front of the reconstructed cluster: PSE4Max.

- The shower shape variables

$$S_{XX} = \frac{\sum_{i=1}^{N} \epsilon_i (x_i - x_c)^2}{\sum_{i=1}^{N} \epsilon_i}, \quad S_{YY} = \frac{\sum_{i=1}^{N} \epsilon_i (y_i - y_c)^2}{\sum_{i=1}^{N} \epsilon_i}, \tag{2.11}$$

$$S_{XY} = S_{YX} = \frac{\sum_{i=1}^{N} \epsilon_i (x_i - x_c)(y_i - y_c)}{\sum_{i=1}^{N} \epsilon_i}, \tag{2.12}$$

where (x_c, y_c) is the transversal barycenter of the cluster.

- The second order momenta $r2$ related to the spread of the shower and defined using the shape variables of Eq. 2.11

$$r2 = \langle r^2 \rangle = S_{XX} + S_{YY} = \frac{\sum_{i=1}^{N} \epsilon_i [(x_i - x_c)^2 + (y_i - y_c)^2]}{\sum_{i=1}^{N} \epsilon_i} \tag{2.13}$$

- The number of PS cells in front of the cluster with non-zero energy deposit: PSMulti.

- The multiplicity of hits in the 3×3 SPD cells matrix in front of the reconstructed cluster: SPDMulti.

The combination of these variables in the Neural Network classifier gives as output the IsNotH distributions displayed on the left side of Fig. 2.21 for $B^0 \rightarrow K^{*0}\gamma$ data (red dots) and MC (blue triangles). The efficiencies as a function of the IsNotH (NN in the plot) applied cut for $B^0 \rightarrow K^{*0}\gamma$ data (dashed red line) and MC (solid blue line) are shown on the right side of Fig. 2.21. In both plots the data are background subtracted using the s$\mathcal{P}lot$ method [65] and a fit to the B invariant mass with a dedicated model for the background. As can be noticed, for low values of the IsNotH cut data and MC exhibit a good agreement.
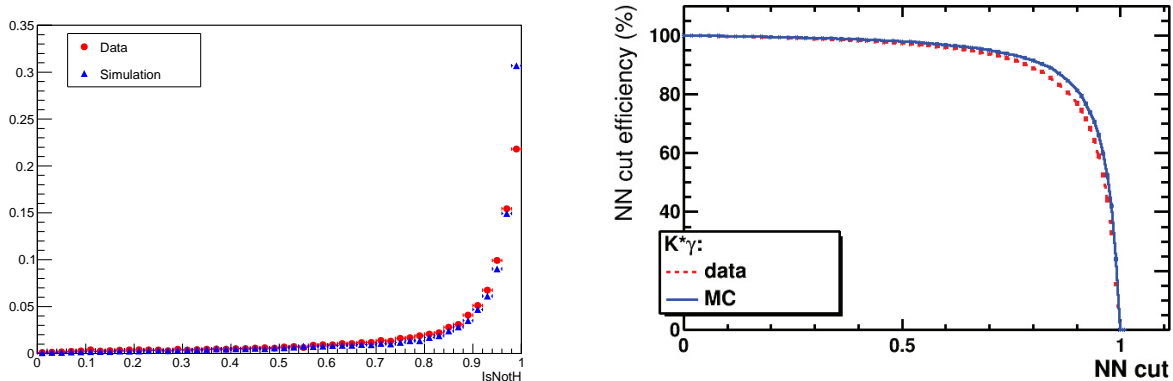
Figure 2.21: *IsNotH distributions (left) and corresponding efficiencies [64] (right) for* $B^0 \to K^{*0}\gamma$ *data (red dots/dashed line) and MC (blue triangles/solid line). Data points are background subtracted.*

2.5.3 γ/π^0 separation

The γ/π^0 separation, needed to reject backgrounds coming from high p_{T} neutral pions, is achieved using a dedicated multivariate-based tool developed in LHCb [66]. Such tool exploits a specific set of variables describing the shape of the cluster similarly for the PreShower (PS) and the ECAL. In addition multiplicity variables in the PS are also used. All the variables are combined with a Neural Network called IsPhoton, whose output allows to obtain a good discrimination between γ and π^0.

The discriminating variables used for the ECAL, some of which are defined according to the shower shape variables of Eq. 2.11 and 2.12, are:

- The second order momenta r2 of Eq. 2.13.

- The quantity

$$r2r4 = 1 - \frac{\langle r^2 \rangle^2}{\langle r^4 \rangle} \ , \tag{2.14}$$

  $\langle r^4 \rangle$ being defined similarly to $\langle r^2 \rangle$ (see Eq. 2.13), that informs about the importance of the tails.

- The κ variable related to the ratio of the eigenvalues of the matrix S, which is $(1+\kappa)/(1-\kappa)$. This way κ relates to the major and minor semiaxes of an ellipse

$$\kappa = \sqrt{1 - 4\frac{S_{XX}S_{YY} - S_{XY}^2}{(S_{XX} + S_{YY})^2}} = \sqrt{1 - 4\frac{\det S}{\mathrm{Tr}^2 S}} \ . \tag{2.15}$$

  This variable describes how squeezed is the cluster [67].

60

- The *asym* variable which provides information about the orientation of the ellipse related to the correlation between X and Y coordinates

$$asym = \frac{S_{XY}}{S_{XX}S_{YY}} \ .$$ (2.16)

- The ratio E_{seed}/E_{ECAL} between the energy of the seed cell and the energy of the cluster in the ECAL.

- The ratio $(E_{seed} + E_{2nd})/E_{ECAL}$, where E_{2nd} is the energy of the ECAL cell with the second highest energy deposit in the cluster.

Analogous variables are defined for the PS:

- $r2PS$ and $asymPS$ using the 3×3 PS cells matrix in front of the ECAL cluster.

- The energy ratios E_{max}/E_{PS} and E_{2nd}/E_{PS}, where E_{max} (E_{2nd}) is the energy measured in the PS cell with the (second) highest energy deposit and E_{PS} is the total energy deposited in the PS cluster.

In addition, a set of variables related to the multiplicity of hits in the 3×3 PS cells matrix is used. These variables, which have different requirements on the minimum energy deposited in the cells, are *multi*, *multi*15, *multi*30 and *multi*45, where the number refers to the energy threshold in MeV (the threshold for *multi* is 0).

The combination of these variables in the Neural Network classifier gives as output the IsPhoton distributions displayed on the left side of Fig. 2.22 for $B^0 \to K^{*0}\gamma$ (red dots) and $D^0 \to K^-\pi^+\pi^0$ (blue triangles) background subtracted data. We can notice that the IsPhoton distributions for high $p_{\rm T}$ photons and merged π^0 look very different, allowing to achieve a good γ/π^0 separation. On the right side of Fig. 2.22 is shown the photon identification efficiency with respect to the π^0 rejection efficiency for simulation and data. We can notice that a photon identification efficiency of 93% can be obtained while rejecting 50% of the merged π^0 reconstructed as photons. The IsPhoton distributions are obtained using $B^0 \to K^{*0}\gamma$ events and $D^0 \to K^-\pi^+\pi^0$ events. The plot on the right side of Fig. 2.22 is taken from Ref. [62].

Calibration samples

The Monte Carlo simulations do not perfectly reproduce the distribution of the IsPhoton : in Fig. 2.23 is shown the comparison of IsPhoton distributions in data and MC for $B^0 \to K^{*0}\gamma$ (left) and $D^0 \to K^-\pi^+\pi^0$ (right) modes. Therefore, a data-driven approach using dedicated calibration samples allows to extract the correct IsPhoton efficiency as a function of the IsNotH cut, the pseudorapidity η and the $p_{\rm T}$ of the photon or the π^0 candidates. The calibration samples exploit the $B^0 \to K^{*0}(K^+\pi^-)\gamma$ decays for photons and $D^{*+} \to D^0(K^-\pi^+\pi^0)\pi^+$ decays for neutral pions. These samples are background subtracted, performing a mass fit and using the $_s\mathcal{P}lot$ technique [65], to obtain quasi-pure samples for photons and π^0. Exploiting the calibration samples, for IsPhoton > 0.6, which
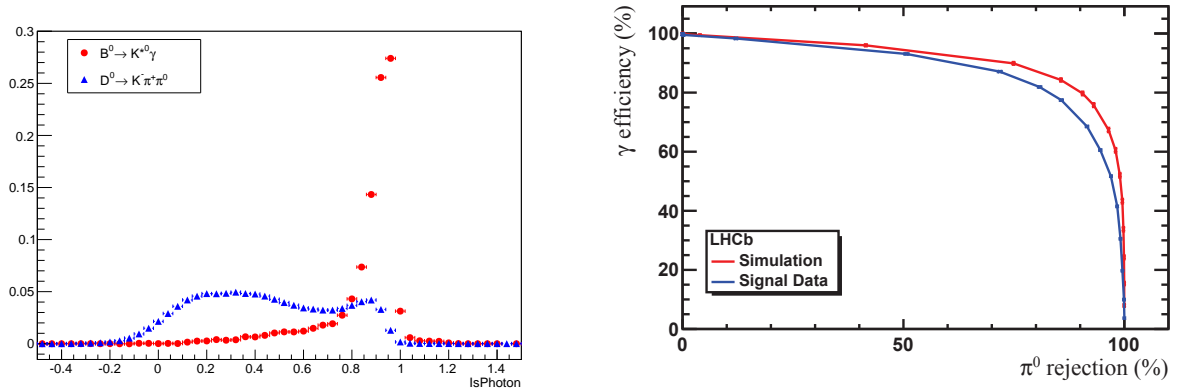
Figure 2.22: *IsPhoton distributions (left) for $B^0 \to K^{*0}\gamma$ (red dots) and $D^0 \to K^-\pi^+\pi^0$ (blue triangles) background subtracted data. Photon identification efficiency as a function of π^0 rejection efficiency [62] (right) for the γ/π^0 separation tool for simulation (red curve) and data (blue curve).*

is the standard requirement for the study of radiative decays, photons are selected with an efficiency of about 94% while π^0 are selected with a 44% efficiency. This corresponds to a 56% rejection of the merged π^0 background.
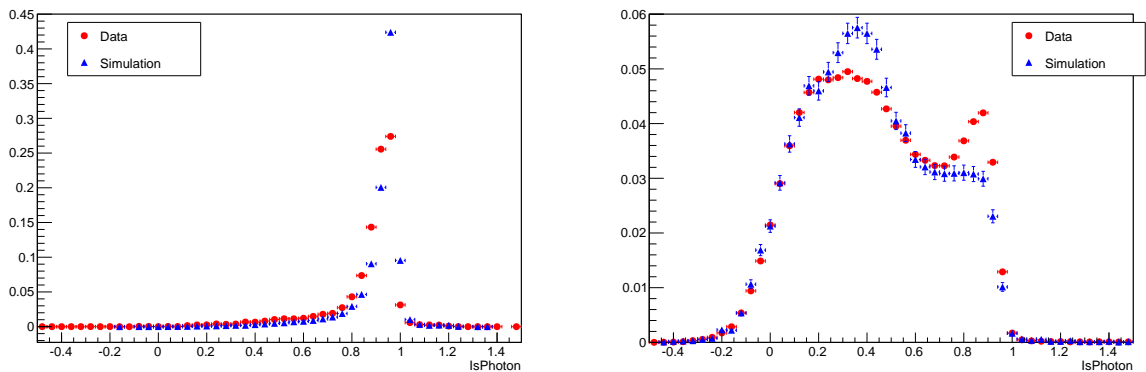
Figure 2.23: *Data/MC comparison of the IsPhoton distributions for $B^0 \to K^{*0}\gamma$ (left) and $D^0 \to K^-\pi^+\pi^0$ (right) channels, in the Run 1 data. Red dots stand for background subtracted data while blue triangles are for MC events.*

2.6 The LHCb trigger

As already said, the production cross section of $b\bar{b}$ pairs is rather large but still two orders of magnitude smaller than the inelastic pp cross section $\sigma_{\text{inel}} = (66.9 \pm 2.9 \pm 4.4)$ mb [68]. Furthermore the capabilities to store data are naturally limited by cost and technological reasons. This means that the LHCb trigger has to efficiently select the interesting events

while rejecting most of the background events. The necessary performances have been achieved by separating the trigger into different levels, each processing the output of the previous level as shown in Fig. 2.24. The LHCb trigger system is divided into three stages:

Level-0 (L0): this is the first level and consists of a hardware trigger based on custom electronics. It is designed to accomplish a first filtering of the events and to reduce significantly the input rate of 40 MHz to an output rate of only 1 MHz;

High Level Trigger 1 (HLT1): the second trigger level is software based. The HLT1 purpose it to filter heavy hadron events in an inclusive way and to reduce the rate to 50 kHz;

High Level Trigger 2 (HLT2): this is the last trigger level and it is also software based. The HLT2 trigger further reduces the output rate to 5 kHz applying exclusive and inclusive selections of beauty and charm decays. The output is sent to mass storage.

The L0 trigger operates synchronously with the 40 MHz LHC clock and has a fixed latency of 4 μs. It reduces the rate to about 1 MHz at which the entire detector may be read out. The L0 information is coming from the pile-up sensors of the VELO, the calorimeters and the muon system. It is sent to the *Level 0 Decision Unit* (L0DU) where the L0 selection algorithms are run.

The L0 calorimeter trigger system uses information from the four components of the calorimeter system, SPD, PS, ECAL and HCAL. It computes the transverse energy deposited in 2×2 clusters. Then the clusters with the largest E_T are selected and identified either as hadron, photon or electron candidates. The hadron candidate is defined from the highest E_T HCAL cluster. The photon candidate is the highest E_T ECAL cluster with at least one PS cell with energy higher than a 5 MIP (Minimum Ionizing Particle) threshold and no hit in the corresponding SPD cells. The electron candidate is defined as the photon candidate except that at least one hit is required in the SPD cells in front of the PS cells above the 5 MIP threshold. The total number of hits in the SPD is also computed. It is used to reject high multiplicity events which would proportionally take too much time to be processed by the High Level Trigger.

The L0 muon trigger system performs a stand-alone reconstruction of muon tracks with a p_T resolution of $\sim 25\%$. Tracks are searched combining the pad data from the five muon stations to form towers pointing towards the interaction region. The muon stations are divided into quadrants and there is no exchange of information between the quadrants. In each quadrant, the two muon candidates with highest p_T are selected.

The High Level Trigger (HLT) is a fully software trigger. It consists of a C++ application executed on an Event Filter Farm (EFF) composed of 29000 CPU cores running up to about 26000 copies of the application. The HLT application has access to all the data of a given event and runs the selection algorithms, called "trigger lines", optimized to cover a certain class of events of interest. In Run 1 the HLT processing time per event was of the order of 30 ms. The HLT reduces the rate from the level 0 output to ~ 5 kHz in Run 1, and ~ 12.5 kHz in Run 2. For timing reasons, the HLT is divided into two stages, HLT1 and HLT2.
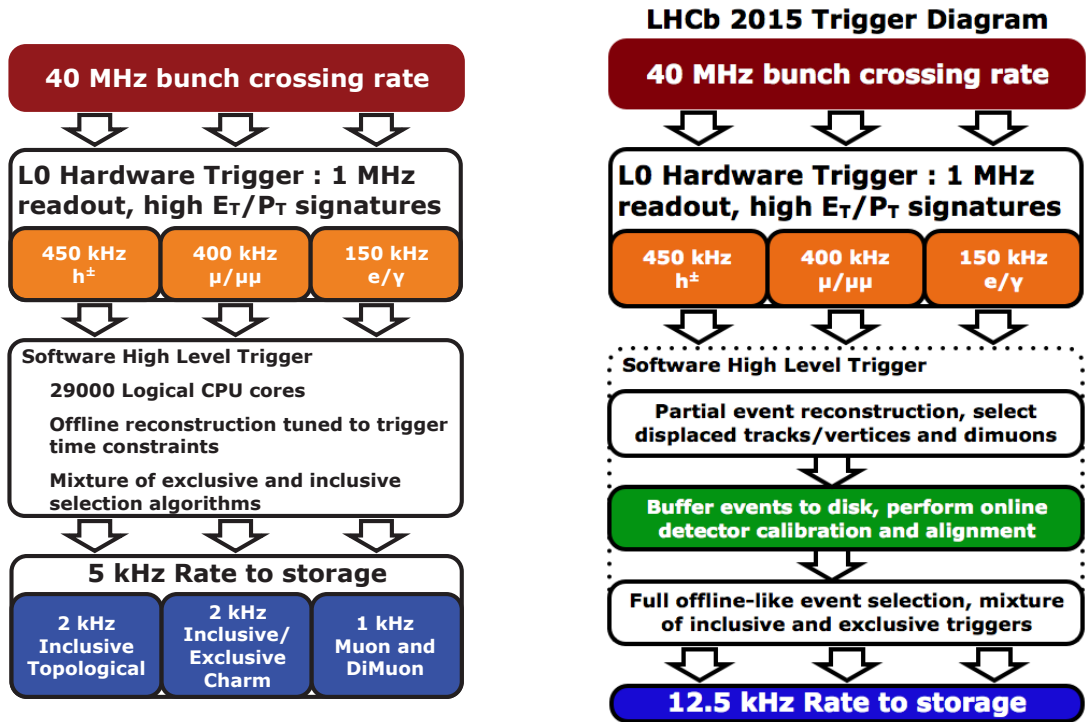
Figure 2.24: *Flow-diagram of the different trigger stages in Run 1 (left) and Run 2 (right). Software High Level Trigger indicates HLT1 and HLT2 stages.*

The HLT1 reduces the level 0 input rate by a factor of about 20. It performs a partial event reconstruction limited to high transverse momentum tracks using information from the VELO and the tracking stations. The selection requires a single high p_T track displaced from all primary vertices (PV). Along with some track quality requirements, the track should have an IP larger than 125 μm with respect to any PV, $p_T > 1.8$ GeV/c and $p > 12.5$ GeV/c. For events triggered by the L0 photon and electron lines, the p_T requirement is relaxed to 0.8 GeV/c.

At the HLT2 stage a simplified full event reconstruction is performed. HLT1 rate allows an HLT2 tracking close to the offline one. Only tracks with $p > 5$ GeV/c and $p_T > 0.5$ GeV/c are reconstructed. The HLT2 runs exclusive and inclusive selections. Special inclusive lines have been developed to trigger on partially reconstructed b hadron decays. These so-called topological lines [69] are based on displaced vertices with 2, 3 or 4 associated tracks. The topological lines were first implemented as cut based selections. To improve the performances, additional lines using a multivariate approach were then added [70].

2.6.1 The Level-0 Trigger

The L0 trigger uses information coming mostly from the tracking system and from the calorimeter system and its basic task is to measure the transverse momentum (p_T)

and energy (E_T) of electrons, photons, hadrons and muons. The system exploits three independent systems running in parallel:

Electron/photon trigger: it uses the information coming from the SPD/PS and ECAL detectors to discriminate between charged and neutral particles. Custom electronics boards are programmed to measure the energy of electromagnetic showers and identify those with highest momentum. The event is accepted if there is at least one cluster with E_T exceeding a certain threshold.

Hadronic trigger: it uses the information coming from HCAL and it works in the very same way as the electron/photon trigger.

Muon trigger: it uses the information coming from the five muon stations. Events are accepted if there is at least one muon candidate with a transverse momentum greater than a certain threshold. Furthermore the trigger contains a line to select muon pairs.

The final trigger decision is taken by an electronic module named *L0 Decision Unit* performing the logical OR of the three subsystem decisions. Therefore events are accepted when at least one of the subsystem reaches a positive decision.

2.6.2 The HLT1

The purpose of this trigger level is to reduce the input rate coming from the L0 trigger to a lower rate. This task is performed by rejecting events with an OT occupancy larger than 20% since they would take more than $\sim$ 25 ms to be successfully processed. After this first selection the remaining events are reconstructed taking into account that:

- High mass B hadrons and their production processes imply that the particles arising from a B hadron decay chain have large p and p_T compared to the other light-quark hadrons.

- The average decay length of B hadrons produced within the LHCb acceptance is about 1 cm and so their decay products will have a large Impact Parameter (IP) with respect to their primary vertex (PV).

- Each B hadron decay has in the final state at least one particle with large p, p_T and a large IP.

- The VELO reconstruction must be fast enough to allow a full and reliable 3-dimensional reconstruction of the PV.

- The full reconstruction can be performed only for a limited number of tracks due to limited available time.

The last two points lead to the choice of subdividing the reconstruction in two stages. In the first step VELO tracks and PV are reconstructed: VELO tracks are selected requiring large impact parameters with respect to the closest PV and a minimum number of hits in the VELO. If the difference between the expected number of hits and the observed number of hits in the Vertex Locator is greater than a certain threshold, the track is rejected.

2.6.3 The HLT2

The lower input rate of the High Level Trigger 2 allows to require the conditions $p > 5$ GeV/c and $p_T > 0.5$ GeV/c on all tracks. HLT2 filtering is mainly based on three inclusive selections, the so-called topological lines. Furthermore several dedicated lines for the LHCb core analysis are used.

The main strategy of topological lines is to build multibody candidates in the following way:

- Two particles are combined to form a two-body object.

- A further input particle is added to the two-body object to form a three-body object, or objects of higher multiplicity.

- The pion mass hypothesis is adopted for all tracks.

In this way, n-body objects are built combining the $(n-1)$-body candidate with another particle and so on (saving CPU time with respect to combining directly n particles). In addition to the topological lines, HLT2 contains lines which exploit tracks identified as muons. Dimuon candidates are formed and, depending on their mass, cuts are applied on the flight distance and p_T of the dimuon candidate.

Chapter 3

Multichannel $B \to h^+h^-\gamma$ study

In the Standard Model (SM), the $B \to h^+h^-\gamma$ decays proceed at leading order through $b \to s(d)\gamma$ one-loop electromagnetic penguin transitions, dominated by a virtual intermediate top quark coupling to a W boson, as shown in Fig. 3.1. Extensions of the SM predict additional one loop contributions that can introduce sizeable effects on the dynamics of the transition. The precise measurements of these decays' branching ratios, analysis of angular distributions and time dependent decay rate (which give access to photon polarization) can therefore be a powerful probe in the indirect search of New Physics.
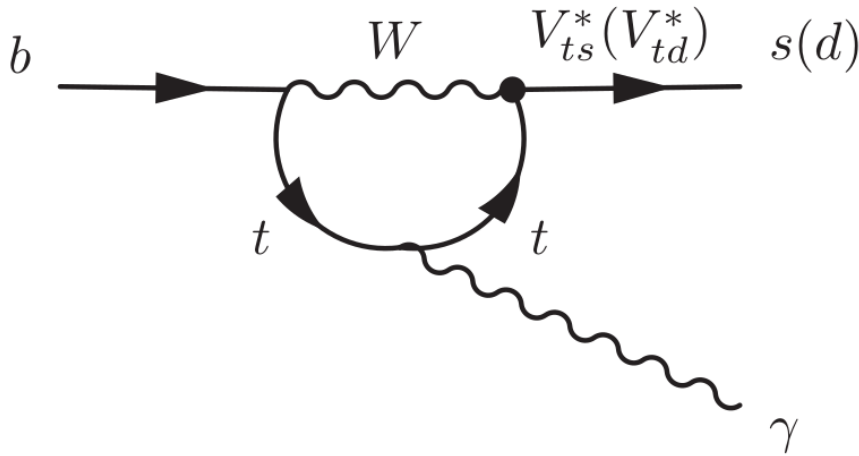
Figure 3.1: *Feynman diagram for $b \to s(d)\gamma$ transitions.*

While the modes $B^0 \to K^{*0}\gamma$ and $B_s \to \phi\gamma$ have been studied with the data collected during Run 1 of the LHC ([71], [72]), the total amount of data collected after the Run 2 may permit the measurement of rarer modes at higher $(h^+h^-)_{res}$ mass such as $B^0 \to K^*(1410)\gamma$, $B^0 \to K_2^*(1430)\gamma$ or $B_s \to f_2'(1525)\gamma$, where the B goes to an orbitally excited meson and a photon. The study of $h^+h^-\gamma$ final states depicted here aims at improving the mass models for $B^0 \to K^{*0}\gamma$ and $B_s \to \phi\gamma$ studies with a better

understanding of the non-resonant states and high mass contamination, as well as measuring branching ratios and ΔA_{CP} of exclusive radiative modes where the B goes to an orbitally excited mesonic state.

A multichannel selection of $B \to h^+h^-\gamma$ decays (where $B = \{B^0/B_s/\Lambda_b\}$ and $h = \{p/K/\pi\}$) is developed for this study. This chapter describes this multichannel selection and sWeighting of the data that is used for the analysis of the hadronic structure in $B^0 \to K^\pm\pi^\mp\gamma$ and $B_s \to K^+K^-\gamma$, that will be discussed in Chapter 4. While not presented here, we note that this procedure could be extended in the future to study $B^0 \to \pi^\pm\pi^\mp\gamma$ suppressed decays, as well as baryonic decays $\Lambda_b \to p^\pm K^\mp\gamma$.

3.1   Analysis strategy

The study is performed amongst the data recorded at LHCb during the Run 1 and Run 2 of the LHC. Simulated samples of signal and background species are used to optimize the selection in terms of sensitivity to the signal. This selection exploits LHCb stripping lines and triggers, as explained in Sec.3.3.1, in order to gather all the events reconstructed as $B \to h^+h^-\gamma$. After a set of cuts inherited from previous radiative decay studies ([71], [72]), the data is split into different samples according to the nature of the final state hadrons :

- $B^0 \to K^+\pi^-\gamma$ and $\overline{B}^0 \to K^-\pi^+\gamma$

- $B_s \to K^+K^-\gamma$

- $\Lambda_b \to pK^-\gamma$ and $\overline{\Lambda}_b^0 \to \overline{p}K^+\gamma$

This filtering of the data is performed by applying a mutually exclusive criteria based on particle identification (PID) variables of the tracks, and is discussed in section 3.6. Processing the data in such a way allows to control simultaneously the signal efficiency and the mis-identification rate in each channel, allowing to estimate the contamination of cross-feed backgrounds (e.g. $B^0 \to K^\pm\pi^\mp\gamma$ reconstructed as $B_s \to K^+K^-\gamma$ when the π is misidentified) without the use of previous measurements of these modes, thus reducing systematics from the background estimation.

Once the cut based selection is applied to both real and simulated data, a first fit to the $h^+h^-\gamma$ invariant mass is performed, using a generic model for radiative decays, for each year of data taking and each sample. This mainly aims at getting a correct estimation of the cross-feed contaminations when optimizing the PID selection (Section 3.6). The fit is then done a second time, to correct the signal MC samples in terms of kinematics and isolation variables. As a final selection step, a Boosted Decision Tree (BDT) is trained to discriminate the MC signal against the Right Handed Side Band (RHSB) of the data B invariant mass. After cutting on the output of the BDT, the background reduction is good enough to fit the B mass and extract sWeights from the data model one last time, with a detailed description of all the remaining backgrounds in

the fit model.

3.2 Data and Monte Carlo samples

This analysis is performed using the data collected by the LHCb experiment during the Run 1 and Run 2 p-p collision campaigns, with the exception of the year 2010 and the first months of 2011 as the stripping line (see Sec. 3.3.2) used to gather $B \to h^+h^-\gamma$ events was not yet implemented. The corresponding integrated luminosity is about 8.7 fb^{-1}. The running conditions, *e.g.* trigger, background level, and calorimeters resolution and calibration are varying by a sizeable amount between 2011, 2012, 2015 and the rest of the Run 2, therefore the corresponding datasets have been processed independently. The events are reconstructed using dedicated versions of the reconstruction software for each year of data taking.

MC simulated samples

Monte Carlo (MC) generated samples are produced using the physics generator `Pythia 8` [73] with different simulation versions and configurations. They are used to study the behaviour of the signal and background species in terms of selection efficiency and line shape, needed to define the mass models. The number of MC events produced for each decay mode and year is summarized in Table 3.1. All the MC samples used in the analysis have been reconstructed using the same stripping versions as for the data and under the three $h^+h^-\gamma$ hypotheses (namely $K^\pm\pi^\mp\gamma$, $K^+K^-\gamma$ and $p^\pm K^\mp\gamma$).

Decay mode	Event type	Stat. 2011	Stat. 2012	Stat. 2015	Stat. 2016	Stat. 2017	Stat. 2018
$B^0 \to K^{*0}\gamma$	11102202	$9.5.\times10^6$	$9.5.\times10^6$	3.7×10^6	$4.\times10^6$	4.2×10^6	$4.\times10^6$
$B^0 \to K_2^*(1430)\gamma$	11102242	$2.\times10^6$	$2.\times10^6$	2.2×10^6	1.9×10^6	$2.\times10^6$	1.9×10^6
$B^0 \to K^*(1410)\gamma$	11102252	1.9×10^6	$2.\times10^6$	$2.\times10^6$	$2.\times10^6$	$2.\times10^6$	1.9×10^6
$B_s \to \phi\gamma$	13102202	8.2×10^6	$9.5.\times10^6$	$4.\times10^6$	$4.\times10^6$	$4.\times10^6$	$4.\times10^6$
$B_s \to f_2'(1525)\gamma$	13102222	$2.\times10^6$	$2.\times10^6$	$2.\times10^6$	1.8×10^6	$2.\times10^6$	1.9×10^6
$\Lambda_b \to \Lambda^*(1520)\gamma$	15102203	2.5×10^6	$4. \times10^6$	0.3×10^6	$1.\times10^6$	$1.\times10^6$	$1.\times10^6$
$\Lambda_b \to \Lambda^*(1670)\gamma$	15102228	2.5×10^6	5.5×10^6	0.2×10^6	0.4×10^6	0.5×10^6	0.5×10^6
$\Lambda_b \to \Lambda^*(1820)\gamma$	15102230	2.26×10^6	2.7×10^6	0.16×10^6	0.45×10^6	0.5×10^6	0.5×10^6
$\Lambda_b \to \Lambda^*(1830)\gamma$	15102240	2.26×10^6	3.2×10^6	0.16×10^6	0.48×10^6	0.5×10^6	0.5×10^6
$B^0 \to K\pi\pi^0$	11202401	-	1.7×10^6	-	$3.\times10^6$	-	-
$B_s \to K\pi\pi^0$	13202401	-	0.9×10^6	-	1.9×10^6	-	-
$B^+ \to K_1(1270)\gamma$	12203224	-	1.9×10^6	-	$2.\times10^6$	-	-
$B^0 \to K_1(1270)\gamma$	11202602	-	1.8×10^6	-	1.9×10^6	-	-
$B^0 \to K^{*0}\eta$	11102441	-	0.9×10^6	-	$2.\times10^6$	-	-
$B^+ \to K_1(1270)\eta$	12203410	-	0.9×10^6	-	$1.\times10^6$	-	-
$B_s \to KK\pi^0$	13102411	-	0.9×10^6	-	$1.\times10^6$	-	-

Table 3.1: *Processed signal and background MC samples.*

3.3 Event reconstruction and online selection

3.3.1 Trigger strategy

For radiative decays, the trigger relies in part on the photon which is required to have large E_T in order to reduce the large combinatorics coming from pp collisions. At the L0 trigger level, this is achieved by requiring a high E_T electromagnetic cluster, with thresholds set at 2.5 GeV during the Run 1 and 2.96 GeV for the Run 2, and a SPD multiplicity below 600 [74]. As around $\sim 40\%$ of the photons reconstructed as a single cluster in the LHCb calorimeter are converted into electrons before the SPD detector, both the `L0Photon` and `L0Electron` lines are included in the trigger selection. The `Hlt1TrackAllL0` line (see Tab. 3.2) imposes standard track requirements. In radiative decays, the efficiency is improved by an additional $\sim 20\%$ by also using the `Hlt1TrackPhoton` line which imposes looser track requirements for events passing a higher photon E_T threshold in the L0 trigger. The corresponding requirements are gathered in Tab. 3.2. For the Run 2, the HLT1 trigger lines take advantage of a neural network allowing a better fake track reduction [75].

The HLT2 selection exploits the inclusive radiative topological lines `Hlt2RadiativeTopoTrack` and `Hlt2RadiativeTopoPhoton` [76] for Run 1, and `Hlt2RadiativeIncHHGamma` for Run 2. These lines are designed to efficiently trigger on any B decay with at least 2 tracks and one high p_T photon. The B candidates are selected using the criteria of Tab. 3.3. In this table the first and third sections give the cuts on the input tracks and photons respectively. The second corresponds to the combination of the two tracks. At least one of the two tracks is required to have a track fit χ^2 per degree of freedom lower than 3. The two tracks should have a Distance Of Closest Approach (DOCA [77]) lower than 0.15 mm and form a good quality vertex. The track four-momenta, under the pion hypothesis, are added and the combination is required to

		Hlt1TrackAllL0	Hlt1TrackPhoton
VELO track hits		> 9	
VELO missed hits		< 3	< 4
VELO track IP	μm	$--\ (> 100)$	
Track p	GeV/c	$> 10\,(3)$	$> 6\,(3)$
Track p_T	GeV/c	$> 1.7\,(1.6)$	> 1.2
Track χ^2/ndf		< 2	
Track χ^2_IP		> 16	

Table 3.2: *Selection requirements applied on the HLT1 lines relevant to radiative decays (more detailed values can be found in Ref. [74]). Missed VELO track hits refer to the difference between the number of hits assigned to the VELO track and the number of hits expected given the track direction and the first measured point on the track.*

have an invariant mass below 2 GeV/c^2 and a transverse momentum above 1500 MeV/c. The cuts on the B candidate are reported in the fourth section of Tab. 3.3. The B decay vertex should be separated from the associated PV requiring a minimal flight distance χ^2 per degree of freedom of 64. The last section of the table is a Global Event Cut (GEC). Since these inclusive lines were introduced later during the 2011 data taking, the actual integrated luminosity available for this year is 0.7 fb^{-1}. The full trigger sequence used in the analysis is displayed in Tab. 3.4. All the lines are required to be "Triggered On Signal" (TOS): the two tracks and the photon from the reconstructed B decay are sufficient to fulfill the trigger line requirement.

Variable		Cut
Track p_T	MeV/c	> 700
Track p	GeV/c	$> 5.$
Track χ^2_{IP}		> 10
Track χ^2/ndf		< 5
Min track χ^2/ndf		< 3
2-track DOCA	mm	< 0.15
2-track $\chi^2_{\mathrm{vtx}}/\mathrm{ndf}$		< 10
2-track m	GeV/c^2	< 2
2-track p_T	GeV/c	> 1.5
$E_T(\gamma)$	GeV	> 2.5
$p_T(B)$	GeV/c	$> 1.$
$m(B)$	MeV/c^2	$[4000; 7000]$
$\chi^2_{FD}(B)$		> 64
Daughters $\sum p_T(B)$	MeV/c	> 5000
# of forward tracks with $p_T > 500$ MeV/c		< 120

Table 3.3: *Selection criteria for the radiative topological lines.*

Trigger level		Trigger Requirement
L0		L0Photon $\parallel$ L0Electron
HLT1	(Run 1)	Hlt1TrackAllL0 $\parallel$ Hlt1TrackPhoton
	(Run 2)	Hlt1TrackMVA $\parallel$ Hlt1TwoTrackMVA
HLT2	(Run 1)	Hlt2RadiativeTopoTrack $\parallel$ Hlt2RadiativeTopoPhoton
	(Run 2)	Hlt2RadiativeIncHHGamma

Table 3.4: *Summary of the trigger conditions used throughout the analysis.*

3.3.2 Stripping

After being collected and stored, raw data are centrally reconstructed by the collaboration and a loose preselection is applied in order to minimize the computing time and the

required storage space. In this preselection step, called stripping, the candidates to be used in the analyses are created filtering the raw events with a combination of different inclusive and exclusive lines that contain a set of dedicated cuts fixed according to the physics targets. As already mentioned, the stripping line used in this analysis is the `StrippingB2XGamma2pi_Line` semi-inclusive line. It allows to select a generic $B \to (h^+ h'^-)\gamma$ candidate with an intermediate resonance, decaying into two charged hadrons, and a high transverse momentum photon in the final state. Events can be processed in order to build up the decay of interest. The B candidate is selected in a large invariant mass range [3280; 9000] MeV/c^2. It is also required to have a secondary (hh) vertex χ^2 per degree of freedom lower than 9, a reconstructed B impact parameter (IP) χ^2 lower than 9 and a positive DIRection Angle (θ_{DIRA}). The sum of the transverse momenta of the daughter particles (h^+, h'^- and γ) is required to be greater than 5000 MeV/c. The two charged tracks must have both $p_T > 300$ MeV/c and $p > 1000$ MeV/c. The sum of their transverse momenta has to be greater than 1500 MeV/c. The minimum of the IP χ^2 with respect to any primary vertex (PV) shall be greater than 16 and the χ^2 per degree of freedom of the track fit shall be below 3. Tracks must also have a ghost probability (probability for this track to be reconstructed from hits in the tracking system that does not belong to a single track) lower than 0.4. The photon is required to have a transverse momentum greater than 2000 MeV/c and a γ_{CL} (see Sec. 3.6.2) greater than 0. The stripping cuts are reported in Tab. 3.5.

Variable		Cut
$m(B)$	MeV/c^2	[3280; 9000]
Daughters $\sum p_T(B)$	MeV/c	> 5000
$\theta_{DIRA}(B)$		> 0
$\chi^2_{\text{vtx}}/\text{ndf}(B)$		< 9
$\chi^2_{\text{IP}}(B)$		< 9
Track p_T	MeV/c	> 300
Track p	MeV/c	> 1000
Tracks $\sum p_T$	MeV/c	> 1500
Track χ^2/ndf		< 3
Track χ^2_{IP}		> 16
Tracks GhostProb		< 0.4
$p_T(\gamma)$	MeV/c	> 2000
γ_{CL}		> 0

Table 3.5: *Selection requirements applied in the* ***StrippingB2XGamma2pi_Line*** *stripping line to select* $B \to hh\gamma$ *events.*

3.4 Offline preselection

First, a loose preselection is applied to the stripped candidates. The set of cuts is listed in Table 3.6. The applied criteria are close to the ones used to perform the LHCb measurements of the ratio of branching ratios $\mathcal{B}(B^0 \to K^{*0}\gamma)/\mathcal{B}(B_s \to \phi\gamma)$ [71] and of the photon polarization in $B_s \to \phi\gamma$ decay [72].

For this pre-selection, the two tracks used to build the hh resonance are required to have $p_T > 500$ MeV/c for the least energetic one, and $p_T > 1200$ MeV/c for the most energetic one, with p in the range $[500; 100000]$ MeV/c and pseudo-rapidity within $[1.5; 5]$. They must also point away from any reconstructed pp interaction vertices by requiring the minimal IP χ^2 to be greater than 16. The identification of the kaon and pion tracks is made by applying cuts on the particle identification (PID) information provided by the RICH system, the structure of these cuts and the ProbNN variables are defined in Sec 3.6.1. The ranges used for the tracks momenta and pseudo-rapidities match the phase space covered by the PID calibration samples on Table 3.7. Also the $(h^+h^-)_{res}$ mass is limited to just below the charm threshold $(m((h^+h^-)_{res}) < 1.8\,\text{GeV}/c^2)$, and no explicit cut to the helicity angle of the $(h^+h^-)_{res}$ system is applied. This selection, with respect to previous radiative studies in LHCb, should show a large increase of background contamination from charmless $B \to X^0\pi^0$ and $B \to X^{\pm}\pi^{\mp}$ with π^0 mis-identification, and partially reconstructed charm decays from D^0/D_s^+ (as well as from B radiative decays or decays with a $\eta(\to \gamma\gamma)$ in the final state). Therefore we apply an additional cut to the $(h^{\pm}\gamma_{\to\pi^0})$ mass, applying the mass of the π^0 to the reconstructed photon, asking it to be greater than 2 GeV/c^2. This also vetoes the charmless $B^0 \to (K\pi^0)\pi^{\pm}$ and $B^0 \to (\pi\pi^0)\pi^{\pm}$. The $h^+h^-\gamma$ candidate is selected in the mass range $[4000; 7000]$ MeV/c^2 and required to have a transverse momentum greater than 2000 MeV/c, an IP χ^2 (impact parameter significance) lower than 9. In addition a requirement on the isolation of the reconstructed B vertex is applied by imposing smallest $\Delta\chi^2_{\text{vtx}}(B) > 3$, which corresponds to the χ^2 increase of the vertex of the reconstructed B candidate when adding an extra most compatible track.

Two cuts are applied on the photon identification: $\gamma_{CL} > 0.2$ and IsPhoton > 0.6. The IsPhoton variable is dedicated to the discrimination between clusters from photons and clusters from neutral pions. It is discussed in details in Sec. 3.6.2.

Variable	Cut
Track p	$[500; 100000]$ MeV/c
$\min(h^+p_T, h^-p_T)$	> 500 MeV/c
$\max(h^+p_T, h^-p_T)$	> 1200 MeV/c
Track η	$[1.5; 5]$
Track χ^2_{IP}	> 16
$h^{\pm}$PID	$\sum_i^{(i \neq j)} h_j\_\mathrm{ProbNN}_{h_j} > h_j\_\mathrm{ProbNN}_{h_i}, (h_{i,j} = K, \pi, p)$
	$h_j\_\mathrm{ProbNN}_{h_j} > 0.05$
$\chi^2_{\mathrm{vtx}}((h^+h^-)_{res})$	< 9
γ_{CL}	> 0.2
IsPhoton	> 0.6
$m(B)$	$[4000; 7000]$ MeV/c^2
$p_T(B)$	> 2000 MeV/c^2
$\chi^2_{\mathrm{IP}}(B)$	< 9
Smallest $\Delta\chi^2_{\mathrm{vtx}}(B)$	> 3

Table 3.6: *Initial cut-based selection. The trigger requirements of Table 3.4 as well as the stripping selection of Table 3.5 are applied.*

3.5 Preliminary study

A primary study of the $h^+h^-\gamma$ events is needed for two reasons :

- Anticipating on the optimization of different cuts for the final selection, one may need to make an estimation of the signal and background yields, using therefore already measured or estimated branching ratios. While branching ratios for $B^0 \to K^{*0}\gamma$ and $B_s \to \phi\gamma$ decays are known, this study is applied to the inclusive $K^\pm\pi^\mp\gamma$ and $K^+K^-\gamma$ final states. A first fit of the B^0 and B_s^0 invariant mass will allow us to estimate more precisely, for example, how many $K^\pm\pi^\mp\gamma$ falls in the $B_s \to f_2'(1525)\gamma$ region. This will be used in Section 3.6 to optimise the PID cuts.

- Monte Carlo simulations used in the analysis may not reproduce the data distributions perfectly, leading to incorrect efficiency estimations. Using background subtracted data is then of prime importance in order to validate or correct the simulation.

3.5.1 Background species

Any B decay with at least two tracks and a high-E_T neutral particle (photon or π^0) in the final state is a potential candidate to be reconstructed as signal. To correctly model the mass distribution in each final state we need to assess the potentially very large remaining background contaminations. The background species in radiative decays can be separated in three categories:

- Combinatorial background : it is associated to random combinations of reconstructed particles that pass the signal selection. These events have significantly different topology and kinematics compared to the signal and can be reduced using multivariate analysis techniques.

- Partially reconstructed backgrounds : they are decays with at least one additional particle (such as π^0, $\pi^\pm$, K or γ) in the final state with respect to the signal, this particle being missed in the reconstruction of the decay. The contributions coming from these decays, which are dominant in the left side of the reconstructed B mass spectrum, are difficult to correctly evaluate since they can come from various decays.

- Peaking backgrounds : decays for which the mass distribution peaks under the signal peak. It can come from two types of decay : either $h^+h^{'-}\gamma$ decays for which at least one track is misidentified, or $h^+h^{'-}\pi^0$ decays for which a high p_T π^0 is misidentified as a photon. They are the most dangerous backgrounds since they cannot be distinguished from signal within the reconstructed B mass resolution. It is then crucial to carefully describe their shapes in the mass fit and to precisely evaluate their actual contaminations to the invariant mass spectrum.

3.5.2 Preliminary mass fits

A first fit of the $K\pi\gamma$, $KK\gamma$ and $pK\gamma$ invariant masses is performed, using a generic model for radiative decays derived from previous studies of $B^0 \to K^{*0}\gamma$, $B_s \to \phi\gamma$ and $\Lambda_b \to \Lambda^*(1520)\gamma$. The three models are quite similar. They consist of :

- a double-tail Crystal Ball [78] Probability Density Function (PDF) to describe the signal shape.

- ARGUS [79] functions to describe the partially reconstructed backgrounds, convoluted with a Gaussian PDF to reproduce the detector's mass resolution. For these, two generic contributions are considered associated respectively to one or two missing pions in the final state.

- a decreasing exponential function for the combinatorial background.

No peaking contributions are included in this fit and the shapes of the signal and of the one-missing-pion Argus PDFs are fixed to the ones used in former radiative studies. The other parameters of the PDFs are left free to float. This is a simplified fit model, but a complete description of all the background sources is not needed at this stage.
The massfits have been performed for each year up to 2016 independently to be able to correct distributions in MC specific to each year. The Figures 3.2, 3.3 and 3.4 show the fit results for 2012 and 2016. One can clearly see a significant increase in the combinatorial background in the 2016 fits, that is due to the increase in beams energy causing a higher number of prompt particles in the detector, on each bunch crossing, which can pass the trigger and preselection requirements.
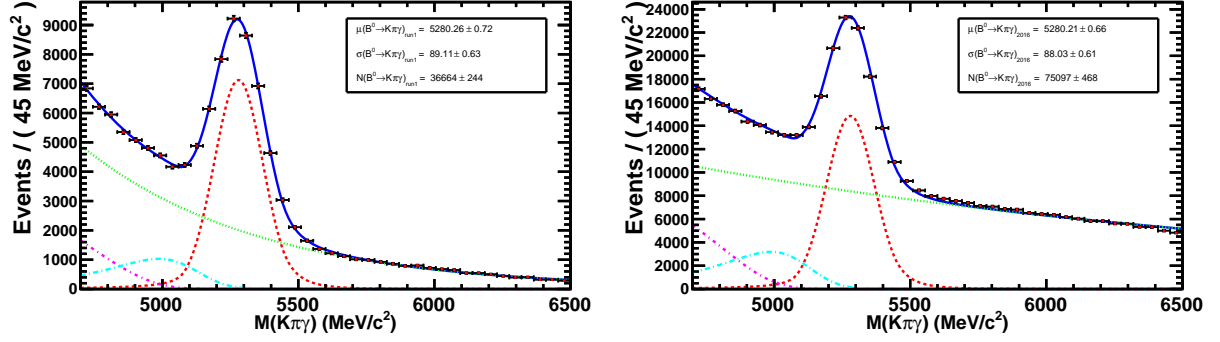
Figure 3.2: $B^0 \to K^\pm \pi^\mp \gamma$ mass fits for 2012 and 2016 data at the preselection level. The data distribution(black dots), signal (red line), combinatorial (green line), one-missing-pion part. reco. (light blue line) and inclusive part. reco. models (pink line) are displayed.
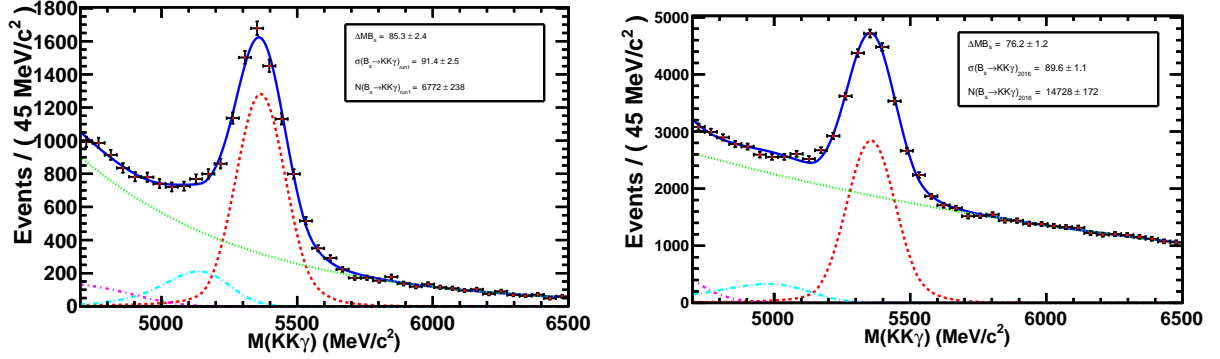
Figure 3.3: $B_s \to K^+ K^- \gamma$ mass fits for 2012 and 2016 data at the preselection level. The data distribution(black dots), signal (red line), combinatorial (green line), one-missing-pion part. reco. (light blue line) and inclusive part. reco. models (pink line) are displayed.

3.5.3   Reweighting the track multiplicity

The $_s\mathcal{P}$lot technique [65] is used during the fit of the invariant mass to compute signal weights, to be able to statistically substract the background contributions when looking at the data distributions. The sWeighted data is then compared to the signal MC distributions in order to validate the MC. The charged track multiplicity distributions is known to be significantly different in the simulations, and therefore needs correcting method. We choose to reweight the simulations : weights are calculated as the normalized ratio of the multiplicity distributions in sWeighted data and signal MC and are used to reweight all the MC samples considered in the analysis. This procedure is done separately for each year of data taking, using the $B^0 \to K^\pm \pi^\mp \gamma$ sWeighted samples. The multiplicity in data and MC before and after the reweighting are displayed in Fig. 3.5 for 2016 as an example,
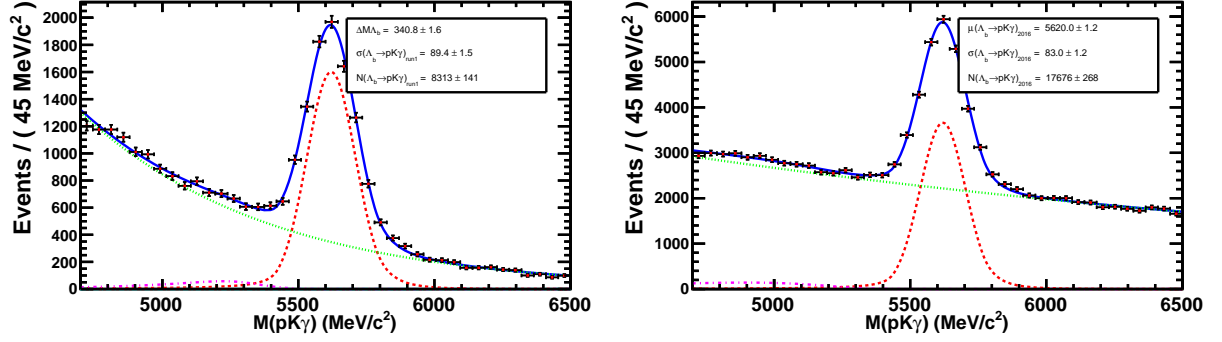
Figure 3.4: $\Lambda_b \to p^\pm K^\mp \gamma$ mass fits for 2012 and 2016 data at the preselection level. The data distribution(black dots), signal (red line), combinatorial (green line), one-missing-pion part. reco. (light blue line) and inclusive part. reco. models (pink line) are displayed.

as well as the distributions in the data in 2011, 2012 and 2016.
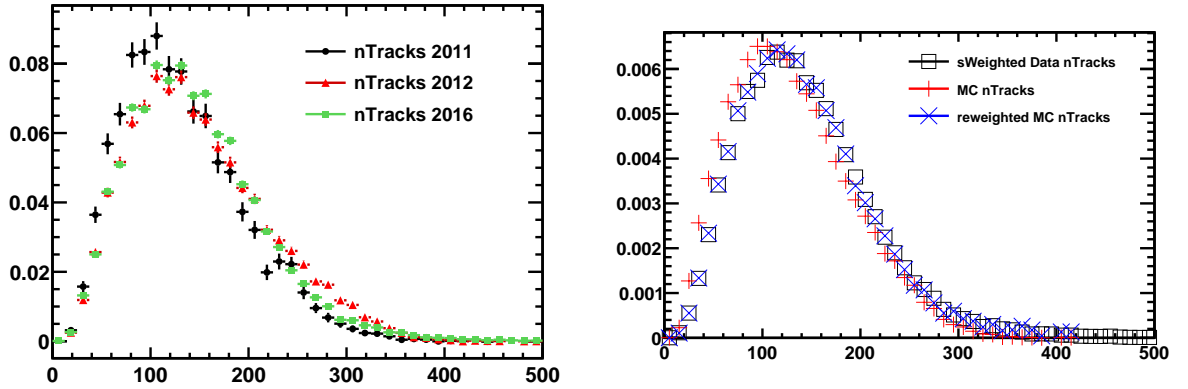
Figure 3.5: Track multiplicity distributions in 2011, 2012 and 2016 (left) and 2016 reweighting (right).

3.6 PID selection

The particle identification (PID) is of prime importance for this study : the correct identification of charged hadron tracks allows to separate different final states and to limit the cross-feed backgrounds. Concerning neutrals, the good identification of photons in the ECAL is crucial to remove the background coming from high momenta π^0. These two background contributions have to be controlled since they are peaking close to the signal mass.

3.6.1 Charged PID

As introduced in Section 3.1, so called ProbNN variables are used to select the hadrons, and therefore separate hhγ events into three samples corresponding to the final states studied K$\pi\gamma$, KKγ and pKγ. These variables are the result of the training of Neural Networks putting together the information coming from the various PID sub-detectors (essentially the RICHes for the $p/K/\pi$ separation). For a given track, values associated to the various PID hypotheses are given (ProbNNk for Kaon, ProbNNpi for pion and ProbNNp for proton). ProbNN variables can be combined in different ways according to the PID approach used in the analysis.

Aiming to reduce the cross-feeds contamination as well as separate the different final states, we apply two sets of cuts on the ProbNNs of each track :

- a mutually exclusive criteria :

$$\sum_i^{(i \neq j)} h_j\_\text{ProbNN}_{h_j} > h_j\_\text{ProbNN}_{h_i}, (h_{i,j} = K, \pi, p)$$

- an offset :

$$h_j\_\text{ProbNN}_{h_j} > x_j$$

While the orthogonal cuts are mandatory to get mutually exclusive samples, the offset x_j has to be tuned to optimise the signal purity by reducing the crossfeed background. To do so, the efficiency of the overall PID cuts for each specie has to be estimated. However, the simulation does not reproduce PID variables with sufficient accuracy, therefore we cannot rely on MC to extract the efficiency for a given cut. We then use a data-driven approach employing dedicated high statistics calibration samples that can be accessed thanks to the `PIDCalib` tool [80] developed by a dedicated performance working group in the LHCb collaboration. These samples, which contain millions of events of high-purity pion, kaon and proton candidates, are produced exploiting the channels displayed in Tab. 3.7. For a given set of cuts PIDCalib generates efficiency maps for the individual tracks (π, K and p). The overall event efficiency is then obtained by applying the generated efficiency maps to the MC simulated events containing the full event information and the kinematics of the individual tracks, for each of the three selected final states. At this

stage the correlations between tracks in the MC events are taken into account. These event-by-event efficiencies are averaged to obtain the probability of a certain decay mode to pass a given set of PID cuts.

Species	Soft p_T	Prompt p_T
$\pi^\pm$	$K_S^0 \to \pi^+\pi^-$	$D^{*+} \to [K^-\pi^+]_{D^0}\pi^+$
$K^\pm$	$D_s^+ \to [K^+K^-]_\phi\pi^+$	$D^{*+} \to [K^-\pi^+]_{D^0}\pi^+$
$p/\overline{p}$	$\Lambda^0 \to p^+\pi^-$	$\Lambda^0 \to p^+\pi^-,\ \Lambda_c^+ \to p^+K^-\pi^+,\ \Lambda_b^0 \to [p^+K^-\pi^+]_{\Lambda_c^+}\mu^-\overline{\nu}_\mu$

Table 3.7: *Summary of the modes collected in the pion, kaon and proton PIDCalib calibration samples.*

PIDCalib produces the efficiency maps with a custom three-dimensional binning scheme in momentum of the track, pseudorapidity of the track and in track multiplicity of the event. This scheme is built using a dedicated "Binning Optimizer" algorithm developed in the collaboration to accurately capture changes in the PID efficiency in the calibration samples. As the track multiplicity distribution is not properly reproduced in the simulation, we apply the weights presented in Section 3.5.3, when getting the mean efficiency, to get it similar to the preselected data. The optimization of the cuts is carried out by maximizing a figure of merit (FoM), the significance of the signal, considering only backgrounds from mis-identification of the tracks :

$$\text{FoM (PID)} = \frac{S}{\sqrt{S + \sum_i B_i^{Cross-Feed}}} \tag{3.1}$$

where the $S(B)$ term stands for the $B \to h^+h^-\gamma$ signal(cross-feeds) expected yields, written as follows

$$S(B) = \mathcal{L} \times 2 \times \sigma(b\bar{b}) \times f_{d/s/\Lambda_b} \times \mathcal{B}(B \to h^+h^-\gamma) \times \epsilon^{MC} \times \epsilon^{Sel} \times \epsilon^{PID}. \tag{3.2}$$

$\mathcal{L}$ is the integrated luminosity for the corresponding year of data taking, $\sigma(b\bar{b})$ is the production cross-section of $b\bar{b}$ pairs at LHCb, $f_{d/s/\Lambda_b}$ is the $b \to B^0(B_s/\Lambda_b)$ hadronization fraction, $\mathcal{B}(B \to h^+h^-\gamma)$ is the branching fraction of the corresponding signal mode, ϵ^{MC} is the overall generation efficiency of the related MC sample, ϵ^{Sel} is the MC selection efficiency (reconstruction, trigger and preselection requirements) and ϵ^{PID} is the PID efficiency for the corresponding PID cuts.

This is the generic equation to estimate the yields, note that in this ratio the production terms cancel. Each of the terms and branching ratio used in the calculations are described in details in Section 3.9. The figure of merit is then computed for each PID cut, i.e. for each track of the event the orthogonal cut and the offset, for which the tested values goes from 0.0 to 0.95 by steps of 0.05. The result of this 2-dimensional scan is drawn for each sample/year/magnet polarity. Examples are shown in Figure 3.6, 3.7 and 3.8.

81
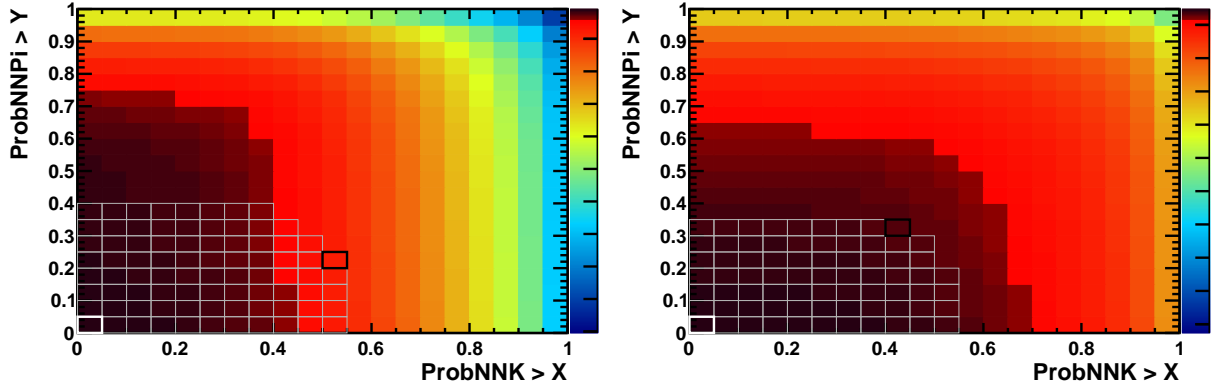
Figure 3.6: $B^0 \to K^{\pm}\pi^{\mp}\gamma$ FoM for 2012 (left) and 2016 (right).
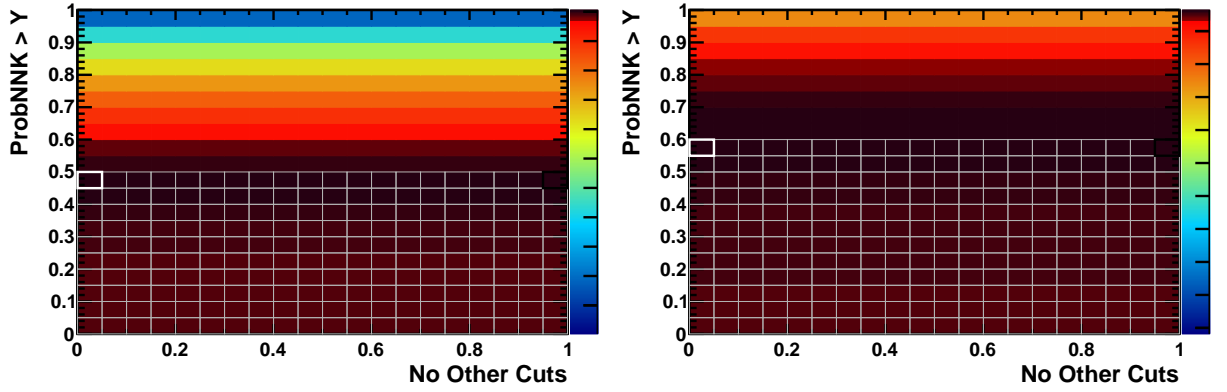
Figure 3.7: $B_s \to K^+K^-\gamma$ FoM for 2012 (left) and 2016 (right).
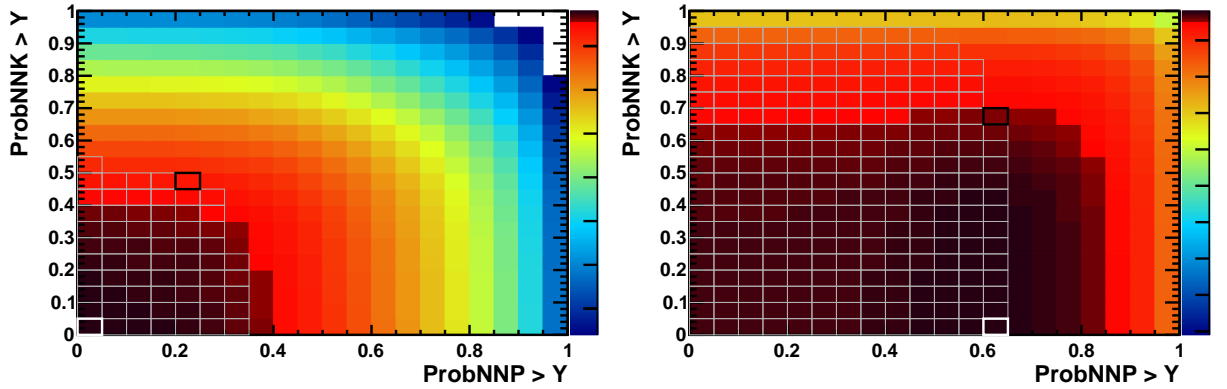
Figure 3.8: $\Lambda_b \to p^{\pm}K^{\mp}\gamma$ FoM for 2012 (left) and 2016 (right).

This scan exhibits a wide plateau on the low cut values both for $B^0 \to K^{\pm}\pi^{\mp}\gamma$ and $\Lambda_b \to p^{\pm}K^{\mp}\gamma$ FoM. It has therefore been decided to go for a tighter criteria : the signal

and peaking background yields are evaluated in the sWeighted data extracted in 3.5.3, in the mass region of the $B^0 \to K_2^*(1430)\gamma$ and $B_s \to f_2'(1525)\gamma$. Examples for this new scan are shown in Figure 3.6, 3.7, and 3.8. The scan has not been performed specifically with 2017 and 2018 MC and data, instead the 2016 cuts are applied, as no significant change in the data is expected. The final cuts are chosen as the highest background reduction in one standard deviation range around the best Figure of Merit value (dark red region in the plots). Cuts and corresponding PID efficiencies are gathered in Table 3.8. The per-track efficiency computed by PIDCalib and corresponding to the final PID working point and will be used in the following steps of the analysis, correcting the MC to match the PID selected data. The mean efficiencies for each possible cross-feed contribution are gathered in Tables 3.9, 3.10 and 3.11.

eff		Final Cuts							
Period		2011		2012		2015		2016/2017/2018	
$B \to h_1 h_2 \gamma$		h_1	h_2	h_1	h_2	h_1	h_2	h_1	h_2
$B^0 \to K^\pm \pi^\mp \gamma$		0.35	0.45	0.5	0.2	0.65	0.1	0.4	0.3
$B_s \to K^+ K^- \gamma$		0.45	0.45	0.45	0.45	0.55	0.55	0.55	0.55
$\Lambda_b \to p^\pm K^\mp \gamma$		0.1	0.5	0.2	0.45	0.35	0.65	0.65	0.65

Table 3.8: *Final PID cuts.*

eff	2011	2012	2015	2016	2017	2018
$\epsilon_{K\pi\to K\pi}$	$78.44 \pm 0.26\%$	$78.48 \pm 0.21\%$	$88.43 \pm 0.09\%$	$89.02 \pm 0.09\%$	$88.63 \pm 0.10\%$	$88.00 \pm 0.10\%$
$\epsilon_{KK\to K\pi}$	$6.66 \pm 0.19\%$	$6.54 \pm 0.15\%$	$3.29 \pm 0.07\%$	$3.07 \pm 0.07\%$	$3.83 \pm 0.08\%$	$3.77 \pm 0.07\%$
$\epsilon_{K\pi\to\pi K}$	$0.12 \pm 0.05\%$	$0.14 \pm 0.05\%$	$0.12 \pm 0.05\%$	$0.11 \pm 0.05\%$	$0.10 \pm 0.05\%$	$0.10 \pm 0.05\%$
$\epsilon_{pK\to K\pi}$	$0.82 \pm 0.07\%$	$0.59 \pm 0.06\%$	$0.34 \pm 0.06\%$	$0.28 \pm 0.06\%$	$0.38 \pm 0.06\%$	$0.37 \pm 0.06\%$
$\epsilon_{pK\to\pi K}$	$8.09 \pm 0.11\%$	$6.61 \pm 0.10\%$	$1.98 \pm 0.08\%$	$1.92 \pm 0.07\%$	$2.87 \pm 0.07\%$	$2.83 \pm 0.07\%$

Table 3.9: *PID efficiencies for each possible mis-identification contributing to* $B^0 \to K^\pm \pi^\mp \gamma$

eff	2011	2012	2015	2016	2017	2018
$\epsilon_{KK\to KK}$	$69.78 \pm 0.39\%$	$69.67 \pm 0.31\%$	$86.19 \pm 0.11\%$	$86.61 \pm 0.11\%$	$85.57 \pm 0.12\%$	$85.17 \pm 0.12\%$
$\epsilon_{K\pi\to KK}$	$0.53 \pm 0.06\%$	$0.55 \pm 0.06\%$	$1.18 \pm 0.07\%$	$1.08 \pm 0.06\%$	$0.73 \pm 0.06\%$	$0.83 \pm 0.06\%$
$\epsilon_{pK\to KK}$	$8.30 \pm 0.28\%$	$6.47 \pm 0.18\%$	$8.00 \pm 0.35\%$	$8.18 \pm 0.22\%$	$8.85 \pm 0.22\%$	$8.58 \pm 0.21\%$

Table 3.10: *PID efficiencies for each possible mis-identification contributing to* $B_s \to K^+ K^- \gamma$

Sample	2011	2012	2015	2016	2017	2018
$\epsilon_{pK\to pK}$	$60.05 \pm 0.33\%$	$61.58 \pm 0.24\%$	$80.93 \pm 0.29\%$	$81.50 \pm 0.18\%$	$79.27 \pm 0.19\%$	$79.27 \pm 0.19\%$
$\epsilon_{KK\to pK}$	$1.77 \pm 0.07\%$	$2.01 \pm 0.07\%$	$1.79 \pm 0.06\%$	$1.92 \pm 0.06\%$	$1.85 \pm 0.06\%$	$2.07 \pm 0.06\%$
$\epsilon_{K\pi\to Kp}$	$0.57 \pm 0.05\%$	$0.57 \pm 0.05\%$	$0.57 \pm 0.05\%$	$0.54 \pm 0.05\%$	$0.45 \pm 0.05\%$	$0.55 \pm 0.05\%$
$\epsilon_{K\pi\to pK}$	$0.01 \pm 0.05\%$	$0.01 \pm 0.05\%$	$0.03 \pm 0.05\%$	$0.03 \pm 0.05\%$	$0.02 \pm 0.05\%$	$0.02 \pm 0.05\%$
$\epsilon_{pK\to Kp}$	$0.23 \pm 0.06\%$	$0.26 \pm 0.05\%$	$0.30 \pm 0.06\%$	$0.27 \pm 0.06\%$	$0.31 \pm 0.06\%$	$0.32 \pm 0.06\%$

Table 3.11: *PID efficiencies for each possible mis-identification contributing to* $\Lambda_b \to p^\pm K^\mp \gamma$

3.6.2 Neutral PID

Another dangerous peaking background for the study of radiative decays is occurring through the mis-identification of a high energy π^0, such as in $B^0 \to K\pi\pi^0$ or $B^0_{(s)} \to KK\pi^0$.

In order to reject backgrounds coming from high p_T neutral pions, we use the dedicated Neural Network output variable called IsPhoton [66] described in Sec.2.5.3. This IsPhoton variable gives a good discrimination between γ and π^0. However, it is not correctly reproduced by the MC simulation. Then, to extract the real efficiency for a given cut, calibration samples have to be used as for the charged PID. To do so we use a dedicated tool (`GammaPi0SeparationCalib`).The calibration samples that can be accessed with the tool exploit the channels $B^0 \to K^{*0}(K^+\pi^-)\gamma$ for photons and $D^{*+} \to D^0(K^-\pi^+\pi^0)\pi^+$ for neutral pions. We note here that at the moment no calibration samples have been produced for the Run 2, we therefore apply the efficiencies from the Run 1 samples, assuming the possible discrepancies are suppressed in the procedure as the reweighting is done event-by-event and keeping correlation between cut efficiency and kinematic variables. The binning used to compute the IsPhoton cut efficiency is bi-dimensional in the variables $\{p_T, \eta\}$ for a total number of bins of $\{12 \times 4\}$. The binning scheme used to extract the γ/π^0 separation cut efficiency for each year is summarized in Table 3.12.

p_T boundaries (MeV/c)	η boundaries
{3000; 3500; 3780; 4100; 4450; 4800; 5200; 5650; 6200; 6900; 8000; 9800; 25000}	{1.5; 2.5; 2.95; 3.4; 5.0}

Table 3.12: *Binning scheme used to extract the γ/π^0 (mis)identification efficiency.*

The cuts to the neutral PID variables selecting photons are fixed according to previous radiative analysis conducted at LHCb, namely $\gamma_{CL} > 0.2$ and $\gamma\_$IsPhoton> 0.6. The efficiency corresponding to this requirement is about 94% for modes with a photon and 44% for the modes with a π^0.

3.7 Simulation corrections

Despite the fair description of the decay kinematics in the simulations, some relatively large discrepancies can be found between the real data and the MC data, just as it is for the PID variables. This section describes a multivariate method that can be used to correct the simulated samples in terms of kinematic and isolation variables.

Data/MC discrepancies

In order to extract the correct signal distributions from the data, as for the track multiplicity reweighting, we fit the B invariant mass distributions with the generic model described in Section 3.5.3, in the samples after applying the PID cuts tuned in Section 3.6.1. The sPlotted distributions of B_P, B_η and track multiplicity, known to be poorly reproduced in the MC simulations, as well as the variables we want to use later in the selection, are then compared to the simulated ones. Some of them exhibit significant discrepancies, therefore we decided to correct the MC using the data in the K^* and ϕ regions.

GB-Reweight method

Rather than using a binned approach that uses ratios of histograms to extract correction weights for each of the variables we wish to reweight, we choose to use a multivariate approach called GB-reweighting. As described in Ref. [81], this procedure makes use of a boosted decision tree to split the space of the relevant variables being reweighted into a few large regions in accordance with the problem. To define the regions that are suitable for reweighting, the symmetrized χ^2 is maximized:

$$\chi^2 = \sum_{leaf} \frac{(w_{leaf,MC} - w_{leaf,data})^2}{w_{leaf,MC} + w_{leaf,data}} \tag{3.3}$$

where $w_{leaf,MC/data}$ are the weights associated to MC and real data. The higher the symmetrized χ^2 is, the more important the region for reweighting will be. This procedure will be iterated as many times as the number of trees specified for the boosting. After the choice of the regions, the reweighting follows the same steps as in the binned technique, the distinctions being that the bins are selected differently.

   The MC is then reweighted in all the variables employed in the MVA described in Sec. 3.8. Since the binning choice is multi-dimensional, this should help in preserving correlations among the variables that the MVA is sensitive to, thereby yielding a better agreement between Data and MC in the MVA itself. However, when plotting Data-MC comparisons together with the GB-weighted MC (Figure 3.10), one can see that the reweighting gives bad results on some variables. This might be due to the fact that the GB-reweighter optimizes the data-MC accordance in a multivariate space, and not directly the data-MC accordance in one variable. In [81] it is proposed to test the capacity of a separate MVA to disentangle between the real data and the GB-weighted MC. However,

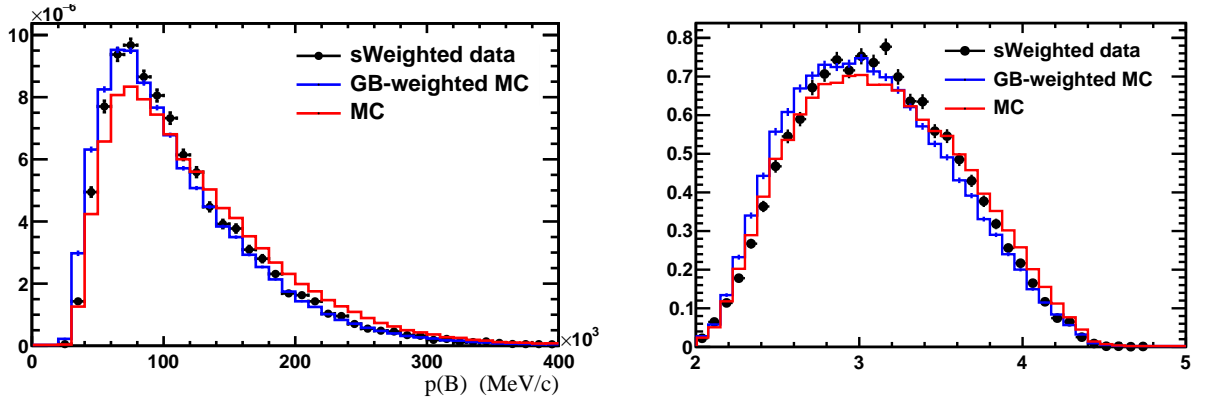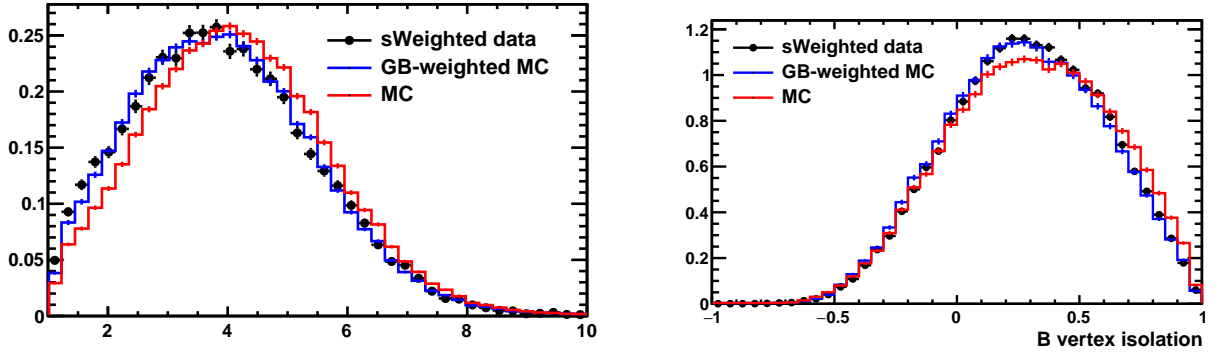Figure 3.9: *Results of the GB-weighting procedure on $B^0 \to K^{*0}\gamma$ MC ($p(B)$ left, $\eta(B)$ right).*

Figure 3.10: *Results of the GB-weighting procedure on $B^0 \to K^{*0}\gamma$ MC ($\log(Smallest\Delta\chi^2_{vtx}(B))$ on the left, B vertex isolation on the right).*

this crosscheck has not yet been performed. The impact of the reweighting will be taken into account in the systematics studies.

3.8 MVA based selection

After passing the whole stripping, trigger, offline and tuned PID selection requirements, the $h^+h^-\gamma$ samples are still highly contaminated with combinatorial background. Thus, a dedicated multivariate discriminator making use of Boosted Decision Trees (BDT, [82] [83]) has been developed to reduce it as much as possible. The `TMVA` package [84] (*Toolkit for Multivariate Data Analysis*) is used to implement this classifier.

3.8.1 Training the BDT

A BDT classifier aims at distinguishing signal from background events by exploiting differences between signal and background distributions of a set of appropriately chosen variables. During the training stage the BDT builds a discriminating variable, interpretable as a measurement of signal-likeness. For our case, there are several degrees of freedom and choices to make when it comes to training the BDTs :

- Training samples: For the background distributions, the best solution is to select the events in the Right-Handed Side Band of the B mass distribution in the real data (which goes from the nominal $B^0/B_s/\Lambda_b + 300$ MeV/c^2 to 7000 MeV/c^2), as it is expected. For the signal distributions it is decided to use reweighted (Sections 3.6, 3.7) MC samples. However, there are several possibilities, as several intermediate $(h^+h^-)_{res}$ resonances are simulated for our study. In the end, in order to optimise the selection for the high mass $(h^+h^-)_{res}$, we decided to train the BDT on the simulated $B^0 \to K_2^*(1430)\gamma$ and $B^0 \to K^*(1410)\gamma$ for the $K^\pm\pi^\mp\gamma$ selection, on the $B_s \to f_2'(1525)\gamma$ for the $K^+K^-\gamma$ selection and on the mixture of the four Λ^* simulated resonances for the $p^\pm K^\mp\gamma$ selection (see Table 3.1).

- Training variables: In order to use the most efficient set of variables, and since BDTs performances are known to be stable with respect to the number of variables used and the correlations between them, we start with a BDT using most of the kinematical and topological variables available. Then we iteratively remove the less used variables from the training until the estimated background rejection of the BDT (portrayed by the area under the ROC-*Receiver-Operating-Characteristic* curve) is significantly worsen. The final set of 12(13) variables for the Run 1 (Run 2) selection is displayed on Table 3.13. Their distributions for the $K\pi\gamma$ 2016 signal MC and data side band are displayed on Figure 3.11.

- Decision trees: `TMVA` offers a list of degrees of freedom when it comes to growing decision trees, namely the number of trees in the forest, the depth of the trees and the size of the leaves, as well as the boosting procedure. These are optimised to offer the best ROC integral, and the training uses the AdaBoost [85] algorithm.

- n-folds method: In order to avoid overtraining, which occurs when a BDT learns the particular fluctuations of the data used for training instead of the global patterns, a

Variable	Description
$p(B)$	The momentum of the reconstructed B candidate.
$\eta(B)$	The pseudo-rapidity of the reconstructed B candidate.
$\chi^2_{\mathrm{IP}}(B)$	χ^2 increase of the primary vertex when adding the tracks of the reconstructed B candidate.
$\mathrm{FD}(B)$	Flight distance of the reconstructed B candidate.
Smallest $\Delta\chi^2_{\mathrm{vtx}}(B)$	χ^2 increase of the vertex of the reconstructed B candidate when adding an extra most compatible track.
$IP(h^{\pm})$	The impact parameter of the charged track
$p_{\mathrm{T}}\,(h^{\pm})$	χ^2 increase of the primary vertex when adding one of the two charged. tracks of the reconstructed B candidate.
$\mathrm{IP}(h^+h^-)_{res}$	The impact parameter of the reconstructed hh resonance.
$p(\mathrm{h}^+h^-)_{res}$	The momentum of the reconstructed hh resonance.
$p_{\mathrm{T}}(h^+h^-)_{res}$	The transverse momentum of the reconstructed hh resonance.
Cone p_{T} asym	The transverse momentum asymmetry in a cone (1.7 mrad) around the B momentum.

Table 3.13: *List of variables used as inputs in the training of the BDT. The last one (cone variable) is only available in the Run 2 samples.*

two-fold technique is chosen : the background and signal samples are split in two halves, making use of a random criteria, then each of them is used to train a separate BDT, which is applied to the other half.

3.8.2 Testing and performances

When a BDT is trained, its performance in terms of signal efficiencies, background reduction and overtraining is tested on a part of the available training sample. Making use of the 2-folds method, each half is used to test the BDT trained with the other one. The output distribution of the BDT in the training and the test samples are compared (Figure 3.12, 3.13) and show no sign of overtraining, validating the MVA for the selection.

3.8.3 BDT selection

In order to optimize the cut on the MVA output we take, as in the PID selection optimization, the figure of merit of the selection as:

$$\text{FoM (MVA)} = \frac{S}{\sqrt{S + c \times B_{Comb}}} \quad \text{with} \quad c = \frac{N^{3\sigma}_{bkg}}{N^{RHSB}_{bkg}}. \tag{3.4}$$

All the yield terms S and $c \times B_{Comb}$ are calculated in the $\pm3\sigma$ signal mass region. The computation of the yields is the same as the one for the PID optimisation, adding the BDT cut efficiency to the product.

B_{Comb} is the number of combinatorial background events in the RHSB passing the MVA cut and c is a scaling factor used to estimate the number of expected background

events $c \times B^{Comb}$ under the signal peak. The factor c, which is calculated without applying any MVA cut, is given by the ratio $N_{bkg}^{3\sigma}/N_{bkg}^{RHSB}$ where N_{bkg}^{RHSB} is the total number of events in the RHSB and $N_{bkg}^{3\sigma}$ is the number of events extrapolated under the signal region, after a linear fit of the RHSB. The optimal final cuts are gathered in Table 3.14. The corresponding signal efficiency is around 97% while the remaining background is of the order of 5%.

Final MVA Cuts						
Mode × Period	2011	2012	2015	2016	2017	2018
$B^0 \to K^\pm \pi^\mp \gamma$	0.01	-0.04	-0.01	-0.01	-0.01	-0.02
$B_s \to K^+ K^- \gamma$	0.01	-0.02	0.	-0.02	-0.01	-0.01
$\Lambda_b \to p^\pm K^\mp \gamma$	-0.18	-0.06	-0.03	-0.02	-0.01	0.

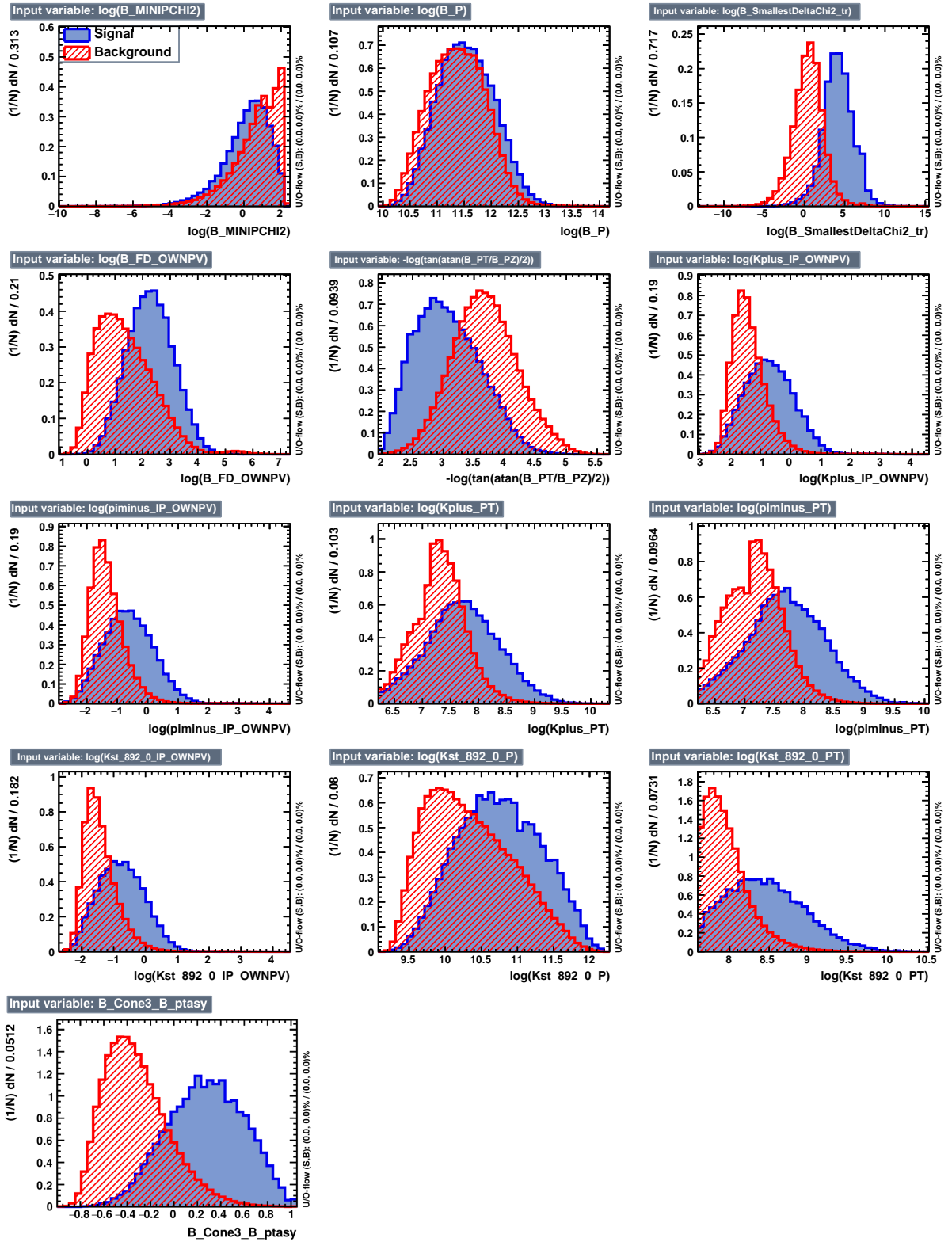Table 3.14: *Optimized MVA selection. The selected data is required to have a BDT output greater than this value.*

Figure 3.11: *Training variables distributions for the $B^0 \to K^{\pm}\pi^{\mp}\gamma$ 2016 MVA selection, with signal MC in blue and data side band in red.*

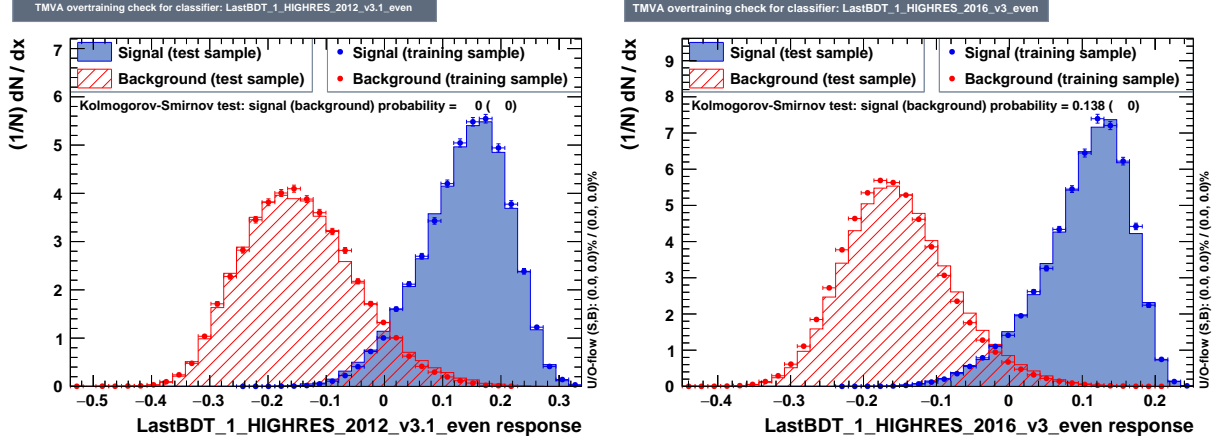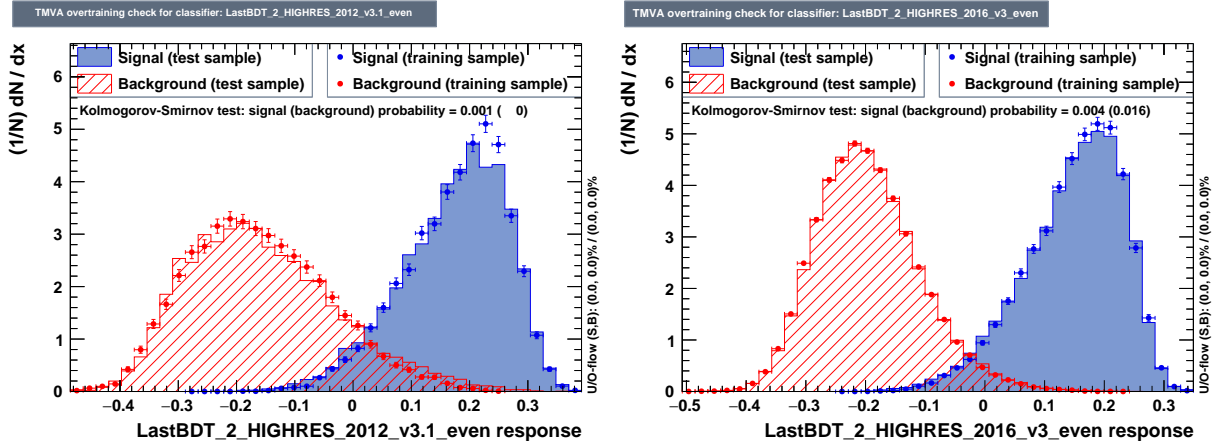Figure 3.12: $B^0 \to K^\pm \pi^\mp \gamma$ BDT outputs for 2012 and 2016 selection.

Figure 3.13: $B_s \to K^+ K^- \gamma$ BDT outputs for 2012 and 2016 selections.

3.9 Background studies

This section displays the estimation of the various contaminations for the peaking backgrounds, while the description of the mass shapes for each specie is depicted in Section 3.10.

3.9.1 Relative background contamination

The final selection being set, background contaminations from specific decays can be evaluated. To do so, the selection efficiencies have to be evaluated for each of them by applying the selection to the corresponding MC simulated samples, if available (listed in Section 3.2). Furthermore, the individual production rate for each specie must be computed. The contamination of the $H_b \to X$ decay is computed as a fraction of the signal yields and defined as

$$
\mathcal{C}^{signal}_{H_b \to X} = \frac{N^{\mathrm{sel}}(H_b \to X)}{N^{\mathrm{sel}}(signal)} = \frac{\mathcal{E}^{signal}_{H_b \to X}}{\mathcal{E}^{signal}} \times \frac{f_{H_b}}{f_d} \times \frac{\mathcal{B}(H_b \to X)}{\mathcal{B}(signal)} \times \frac{\mathcal{B}^{Eff}_{H_b \to X}}{\mathcal{B}^{Eff}_{signal}}, \tag{3.5}
$$

where $signal$ corresponds to either the $B^0 \to K^\pm \pi^\mp \gamma$, $B_s \to K^+ K^- \gamma$ or $\Lambda_b \to p^\pm K^\mp \gamma$ mode. f_{H_b}/f_d is the ratio of hadronization fractions, and $\mathcal{E}^{signal}$ and $\mathcal{E}^{signal}_{H_b \to X}$ are the global efficiencies for the signal and background of interest. $\mathcal{B}^{Eff}_{H_b \to X}$ is $\mathcal{B}(K^{*0} \to K^+ \pi^-) = (66.507 \pm 0.014) \times 10^{-2}$ for $B^0 \to K^{*0}\gamma$, $\mathcal{B}(\phi \to K^+ K^-) = (48.9 \pm 0.5) \times 10^{-2}$ for $B_s \to \phi\gamma$ and 1 for the other modes. The global efficiency $\mathcal{E}$ can be written as :

$$
\mathcal{E} = \epsilon^{MC} \times \epsilon^{Sel} \times \epsilon^{PID} \times \epsilon^{IsPhoton} \times \epsilon^{BDT} , \tag{3.6}
$$

following the notation introduced in Eq. 3.2: here ϵ^{BDT} refers to the MVA cut and ϵ^{PID} stands for the overall PID efficiency.

3.9.2 Decays with a merged π^0

When the transverse momentum of a π^0 is above 2 GeV/c^2, the electromagnetic shower of the photon pair it decays to may not be resolved in the ECAL granularity. Charmless $B^0 \to hh\pi^0$ decays with $\mathcal{B} = \mathcal{O}(10^{-5})$ can thus be a dangerous background for $B_{d/s} \to (h^+ h^-)\gamma$ studies.

The measured branching ratio $\mathcal{B}(B^0 \to K\pi\pi^0) = (3.78 \pm 0.32) \times 10^{-5}$ [18] is used to evaluate its contamination to the $K^\pm \pi^\mp \gamma$ final state. A sample of $B^0 \to K\pi\pi^0$ simulated decays, inherited from previous studies ([72]), is used to evaluate the shapes and selection efficiencies of this decay. However, its generator level composition, displayed in Table 3.15 is limited to decays that are not vetoed by the selection of $B^0 \to K^{*0}\gamma$. In our analysis, other poorly known decays with scalar/tensor mesons may also significantly contribute to this background ($B^0 \to K_0^*(1430)\pi^0$, $B^0 \to K_2^*(1430)\pi^0$). Also, the requirement on the $h^\pm \gamma_{\to \pi^0}$ mass applied in Section 3.5 vetoes the $K^{*+}\pi^-$ and $\rho^+ \pi^-$ intermediate states. For this contribution to the $B^0 \to K^\pm \pi^\mp \gamma$ final state, we make

Decay mode	Relative contribution(%)
$B^0 \to K^*(892)^+\pi^-$	23.04%
$B^0 \to \rho^- K^+$	58.48%
$B^0 \to K^*(892)^0\pi^0$	6.67%
$B^0 \to K^+\pi^+\pi^0_{non-resonant}$	11.81%

Table 3.15: *Composition at generator level of the $B^0 \to K\pi\pi^0$ simulated samples, based on known branching fractions of the different modes.*

the assumption that the selection efficiencies are consistent between the different channels leading to the $B^0 \to K\pi\pi^0$, which leads to an order of magnitude for the contamination at the 1% level.

In a similar way, the possibly contributing, but not yet observed, $B_s \to K^+K^-\pi^0$ and $B_s \to K^+\pi^-\pi^0$ are neglected, following the discussion on [71]. However, there is an evidence for the $B^0 \to K^+K^-\pi^0$ decay at Belle([86]), for which the $f_0(980)\pi^0$, $\phi\pi^0$ and NR (non-resonant) parts could contaminate our $K^+K^-\gamma$ sample. Taking the corresponding measurement $\mathcal{B}(B^0 \to K^+K^-\pi^0) = (2.17 \pm 0.60) \times 10^{-6}$ and estimating selection efficiencies with MC samples (generated flat in the phase space), the relative contamination would be of 0.5%.

3.9.3 Cross-feeds from radiative decays

Firstly, an irreducible contribution arises in the $K^\pm\pi^\mp\gamma$ sample from the suppressed $b \to d\gamma$ transition of the B_s meson, that is predicted to be $\mathcal{B}(B_s \to \overline{K}^{*0}\gamma) = (1.26 \pm 0.25 \pm 0.18) \times 10^{-6}$. Assuming this branching ratio value, the corresponding contamination is directly :

$$\frac{f_s}{f_d} \times \frac{\mathcal{B}(B_s \to \overline{K}^{*0}\gamma)}{\mathcal{B}(B^0 \to K^{*0}\gamma)} = (0.8 \pm 0.2)\%$$

Then, because of the inclusive $h^+h^-\gamma$ selection performed with an open $(h^+h^-)_{res}$ mass criterion, cross-feeds between the three studied final states due to charged track mis-identification have to be carefully evaluated. To do so, the $B^0 \to K^{*0}\gamma$, $B_s \to \phi\gamma$ and $\Lambda_b \to \Lambda^*(1520)\gamma$ MC samples are all reconstructed in each of the final states hypothesis. The corresponding selection efficiencies are evaluated, corrected with the mis-identification rate of each true hadron into each track hypothesis extracted from calibration data with PIDCalib(see Section 3.6). All the efficiencies for each possible cross-feed contributions are then available, including the correct IsPhoton and BDT requirements, for each year of data taking. The contaminations, i.e. the cross-feed rate relative to the signal yields (Eq. 3.5), can then be derived (Tables 3.16, 3.17 and 3.18).

PID	Contaminations						Average
	2011	2012	2015	2016	2017	2018	
$KK \to K\pi$	$1.80 \pm 0.46\%$	$1.64 \pm 0.42\%$	$0.86 \pm 0.22\%$	$0.80 \pm 0.20\%$	$0.96 \pm 0.24\%$	$1.02 \pm 0.26\%$	1.0%
$pK \to \pi K$	$2.48 \pm 0.58\%$	$1.96 \pm 0.44\%$	$0.50 \pm 0.12\%$	$0.40 \pm 0.09\%$	$0.60 \pm 0.13\%$	$0.63 \pm 0.14\%$	0.75%

Table 3.16: *Estimated contaminations from crossfeeds to $B^0 \to K^\pm \pi^\mp \gamma$ sample, for each year and rough average taking into account the expected signal yields for each year.*

PID	Contaminations						Average
	2011	2012	2015	2016	2017	2018	
$K\pi \to KK$	$3.70 \pm 0.96\%$	$4.18 \pm 1.07\%$	$6.06 \pm 1.53\%$	$5.59 \pm 1.41\%$	$3.96 \pm 1.00\%$	$4.17 \pm 1.05\%$	4.5%
$pK \to KK$	$14.07 \pm 4.67\%$	$11.38 \pm 3.69\%$	$9.10 \pm 3.05\%$	$7.86 \pm 2.54\%$	$8.92 \pm 2.87\%$	$8.44 \pm 2.72\%$	8.8%

Table 3.17: *Estimated contaminations from crossfeeds to $B_s \to K^+ K^- \gamma$ sample, for each year and rough average taking into account the expected signal yields for each year.*

PID	Contaminations						Average
	2011	2012	2015	2016	2017	2018	
$\mathcal{C}^{\Lambda_b \to p^\pm K^\mp \gamma}_{B_s \to K^+ K^- \gamma}$	$2.57 \pm 0.85\%$	$2.83 \pm 0.91\%$	$2.15 \pm 0.71\%$	$2.82 \pm 0.91\%$	$2.64 \pm 0.85\%$	$3.01 \pm 0.97\%$	2.78%
$\mathcal{C}^{\Lambda_b \to p^\pm K^\mp \gamma}_{B^0 \to \pi^\pm K^\mp \gamma}$	$2.88 \pm 0.67\%$	$2.85 \pm 0.64\%$	$2.65 \pm 0.55\%$	$2.55 \pm 0.57\%$	$2.23 \pm 0.50\%$	$2.55 \pm 0.57\%$	2.5%
$\mathcal{C}^{\Lambda_b \to p^\pm K^\mp \gamma}_{B^0 \to K^\pm \pi^\mp \gamma}$	$0.07 \pm 0.02\%$	$0.09 \pm 0.02\%$	$0.14 \pm 0.03\%$	$0.16 \pm 0.04\%$	$0.11 \pm 0.02\%$	$0.13 \pm 0.03\%$	0.12%
$\mathcal{C}^{\Lambda_b \to p^\pm K^\mp \gamma}_{\Lambda_b \to K^\pm p^\mp \gamma}$	$0.30 \pm 0.10\%$	$0.33 \pm 0.10\%$	$0.31 \pm 0.10\%$	$0.28 \pm 0.08\%$	$0.32 \pm 0.10\%$	$0.33 \pm 0.10\%$	0.3%

Table 3.18: *Estimated contaminations from crossfeeds to $\Lambda_b \to p^\pm K^\mp \gamma$ sample, for each year and rough average taking into account the expected signal yields for each year.*

In addition, the contaminations can be expressed relatively to the contributing mis-identified final state, without the use of branching ratio measurements, simply as ratios of efficiencies :

$$\mathcal{R}^{signal}_{H_b \to X} = \frac{N^{\text{Mis-ID}}(X \to signal)}{N^{\text{sel}}(H_b \to X)} = \frac{\mathcal{E}^{signal}_{H_b \to X}}{\mathcal{E}_{H_b \to X}}, \tag{3.7}$$

where $\mathcal{E}^{signal}_{H_b \to X}$ is the efficiency for the considered mode to be reconstructed as the signal mode (mis-identification efficiency), and $\mathcal{E}_{H_b \to X}$ corresponds to its correct reconstruction efficiency. These $\mathcal{R}$ numbers, referred to simply as "cross-feed rate", can be directly used to normalise the cross-feeds backgrounds to a simultaneously fitted mode without the use of previous measurement.

3.10 Signal extraction

After applying the full selection, various background contributions remain and populate the B mass spectra. In order to perform a reliable measurement, the sPlot method can again be used to statistically extract the signal from the data. In this section we describe how the signal and background shapes are extracted for each final states and how the total PDF used to fit the data is built up.

3.10.1 Mass models

The shapes to be included in the mass fit model are extracted through a fit to the invariant mass distribution of MC events passing the full selection except for the PID cuts, since the ProbNN and IsPhoton variables are not well described in the simulation. However, the PID requirements can affect the shape of the mass distribution, thus we apply the dedicated event-by-event PID efficiency evaluated in Section 3.6 as weights to the histogram to take this effect into account.

All the signal and background shapes are extracted through an unbinned extended maximum likelihood fit to the reconstructed B mass spectrum in the channel of interest.

Signal and peaking background

The signal invariant mass distribution is extracted fitting the simulated events in the full mass range [4000; 6600] MeV/c^2 and using an asymmetric double tail Crystal-Ball PDF [78] defined as

$$\mathrm{DCB}(m; \mu, \sigma, \alpha_L, n_L, \alpha_R, n_R) = \begin{cases} A_L \left(B_L - \dfrac{m-\mu}{\sigma} \right)^{-n_L} & \text{for } \dfrac{m-\mu}{\sigma} \leq -\alpha_L \\[2mm] \exp\left\{ -\dfrac{(m-\mu)^2}{2\sigma^2} \right\} & \text{for } -\alpha_L < \dfrac{m-\mu}{\sigma} < \alpha_R \\[2mm] A_R \left(B_R + \dfrac{m-\mu}{\sigma} \right)^{-n_R} & \text{for } \dfrac{m-\mu}{\sigma} \geq \alpha_R \end{cases} \tag{3.8}$$

where $\alpha_{L(R)} > 0$ and $A_{L(R)}$ and $B_{L(R)}$ are

$$\begin{aligned} A_i &= \left(\frac{n_i}{|\alpha_i|} \right)^{n_i} \exp\left\{ -\frac{|\alpha_i|^2}{2} \right\} \\ B_i &= \frac{n_i}{|\alpha_i|} - |\alpha_i| \quad . \end{aligned} \tag{3.9}$$

The difference between left and right resolutions is considered by defining two independent sigmas, σ_L and σ_R, according to

$$\sigma = \begin{cases} \sigma_L = \sigma - \delta & \text{if } m < \mu \\ \sigma_R = \sigma + \delta & \text{else} \end{cases} \tag{3.10}$$

where δ characterizes the asymmetry of the shape. If we do not take into account such difference, the function of Eq. 3.8 reduces to a symmetric double-tail Crystal Ball with a single resolution σ. We chose an asymmetric PDF as reference to extract the signal shapes because this function allows to obtain a better fit on MC. However, the shape seems to be more symmetric in the data fit, as we will see later. The tail at high mass models the imperfections of the tracking. However, in the case of radiative decays, large pile-up deposits in the ECAL cluster forming the photon candidate are also likely to contribute. The invariant mass resolution of the B candidate depends on the ECAL resolution as it is dominated by the γ contribution. The value of the μ parameter depends on the ECAL average calibration.

Partially reconstructed background

The partially reconstructed backgrounds are fitted in the mass range [4700; 5600] MeV/c^2 and using an ARGUS function [79] convoluted with a specific PDF needed to model the detector resolution. The generalized ARGUS function has three parameters (m_t, c, p) and is given by

$$\text{ARGUS}(m; m_t, c, p) = \frac{2^{-p}c^{2(p+1)}}{\Gamma(p+1) - \Gamma(p+1, c^2/2)} \cdot \frac{m}{m_t}\left(1 - \frac{m^2}{m_t^2}\right)^p \exp\left[-\frac{1}{2}c^2\left(1 - \frac{m^2}{m_t^2}\right)\right]$$

(3.11)

where $\Gamma(n)$ and $\Gamma(n, x)$ are respectively the usual Gamma function and incomplete Gamma function. The parameter m_t describes the threshold: if $m > m_t$ the function evaluates zero. The parameter p controls the curvature of the function and the parameter c controls the falling of the slope. The total function used to fit the partially reconstructed backgrounds is then defined as

$$\text{Partial}(m; c, p, \Delta M, \sigma) = \text{ARGUS}(m; c, \mu + \Delta M, p) \otimes \text{DCB}_{signal}(\mu = 0)$$

(3.12)

where μ is fixed to the value of μ extracted in the fit to MC signal events and ΔM is the mass shift.

The PDF used to model the detector resolution is the one of the corresponding signal. The threshold of the ARGUS in Eq. 3.11 is then $m_t = \mu + \Delta M$, where ΔM can be 0, $-m_{\pi^0}$, $-m_{\pi^+}$ or $-m_K$ according to the missing particles ($\Delta M = 0$ in case of one or more unreconstructed photons). In fact, many different modes with similar shapes compete in the same mass region of the spectra. Additionally, the branching fractions of most of these decays are unknown. For this reason, the contamination of the various partially reconstructed backgrounds are not calculated. The shape that will be used in the final fit for these contributions is extracted from a simultaneous fit of the $B^0 \to K^{*0}\gamma$ MC, the $B^+ \to K^{*0}\pi^+\gamma$ one and the $B^0 \to K_1(1270)\gamma$ one, reconstructed in the $B^0 \to K^{\pm}\pi^{\mp}\gamma$ hypothesis (Figs.3.14,3.15 and 3.16). As can be seen, the χ parameter can be common to the two partially reconstructed shapes, while the p parameter is different. Therefore we
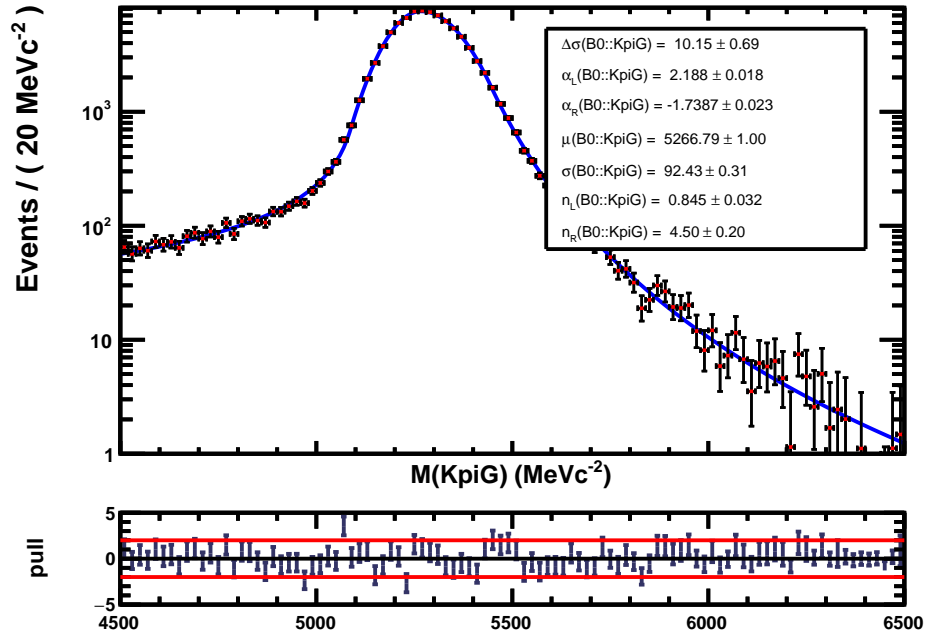
Figure 3.14: *Fit to the reconstructed B mass in $B^0 \to K^{*0}\gamma$ MC 2012 (log scale).*

decide to let it free to float in the final fit to the data, as well as the relative contamination of the one-missing-pion partially reconstructed.
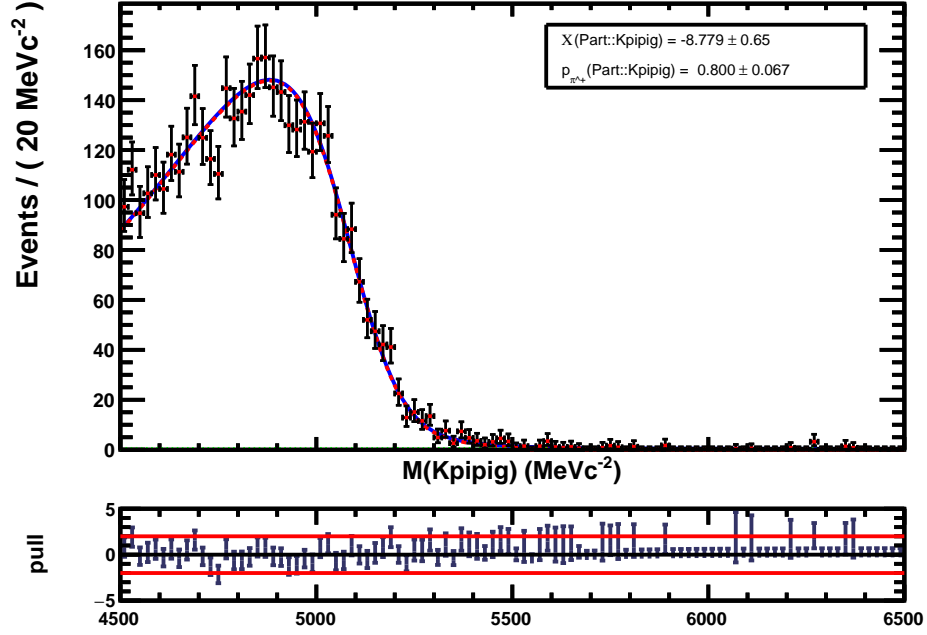
Figure 3.15: *Fit to the B mass in $B^+ \to K^{*0}\pi^+\gamma$ MC 2012, reconstructed in the $B^0 \to K^{\pm}\pi^{\mp}\gamma$ hypothesis.*

3.10.2 Final B mass fit

Once again, and following the MVA selection, the data invariant mass is fitted, this time using the MC extracted shapes for the model. The inclusive partially reconstructed and combinatorial PDF are left free as in the intermediate mass fits, and the peaking backgrounds are not described, and taken as signal in the sWeighting. They will be treated later in the amplitude fits.

The total function used to fit the data is built as an extended PDF given by

$$\mathcal{F}(m) = N_S \cdot S(m) + \sum_i N_i \cdot B_i(m) \tag{3.13}$$

where $S(m)$ is the signal PDF and $B_i(m)$ is the partially reconstructed or combinatorial background PDF where i stands for the different background contributions. N_S is the total number of signal event to be extracted in the fit and N_i is the number of events from either the combinatorial background or one of the partially reconstructed backgrounds. All the N_i are left free.

We perform an unbinned extended maximum likelihood fit according to the following prescriptions:

- The signal is modeled with an asymmetric double-tail Crystal Ball PDF (see Sec. 3.10.1) with the μ, σ_L and σ_R parameters free to float.
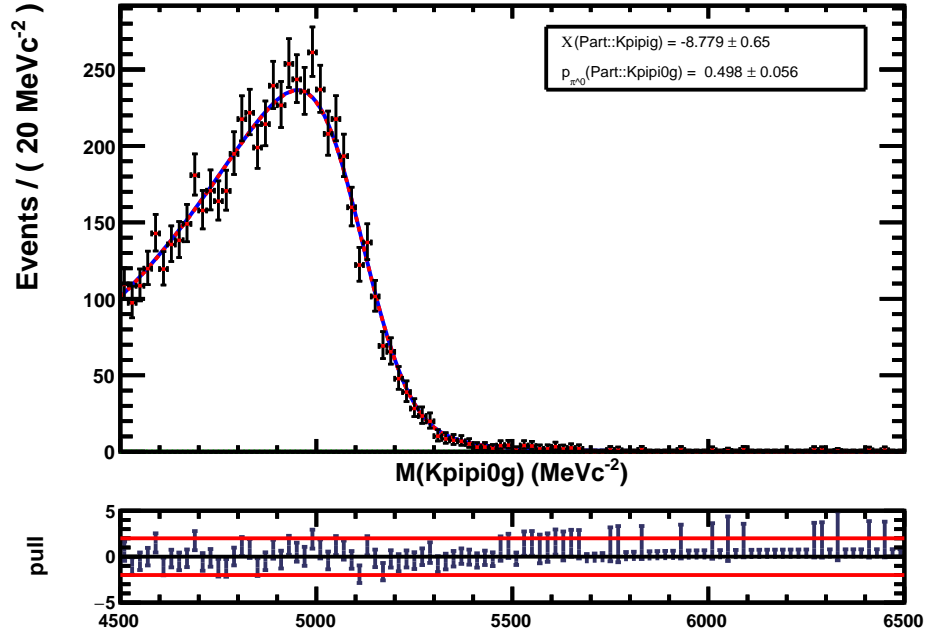
Figure 3.16: *Fit to the B mass in $B^0 \to K_1(1270)\gamma$ MC 2012, reconstructed in the $B^0 \to K^\pm \pi^\mp \gamma$ hypothesis.*

- The combinatorial background shape is modeled with a decreasing exponential

$$\mathrm{Comb}(m; c) = exp(c \cdot m). \tag{3.14}$$

- The partially reconstructed backgrounds are modeled with an ARGUS function, according to the discussion in the precedent section, convoluted with the signal PDF (with $\mu = 0$).

The final fits to the $B^0 \to K^\pm \pi^\mp \gamma$, $B_s \to K^+ K^- \gamma$ and $\Lambda_b \to p^\pm K^\mp \gamma$ invariant masses of each independent year of data taking are shown in Figures 3.17 to 3.25. The corresponding yields and the free parameters of the signal shapes (namely μ, σ and δ as described in Sec. 3.10) are gathered in Tables 3.19, 3.20 and 3.21. These results expose the quality of the LHCb calorimeter calibration along the years of data taking. In 2011 and 2015, due to the restart of the data taking and the calibration methods being developed, the calibration has been less accurate, leading to a wider resolution on the B mass.
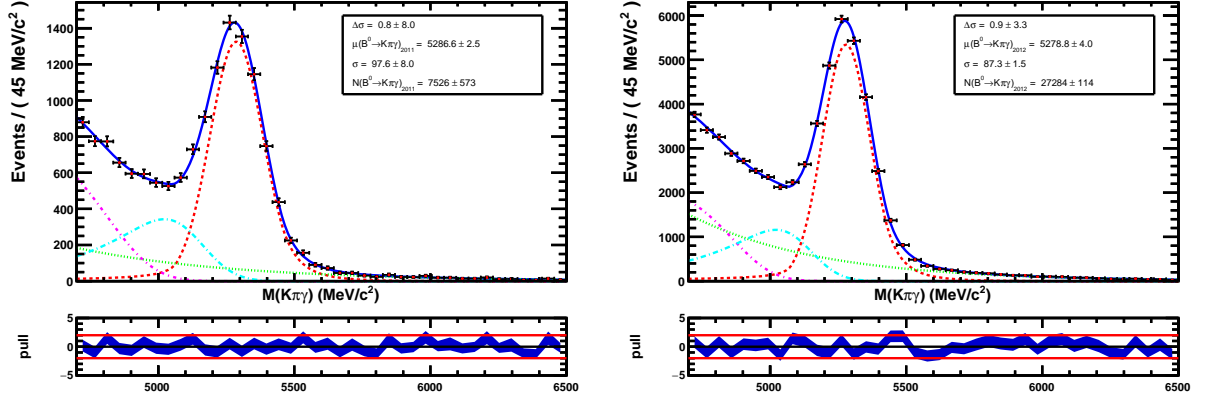
Figure 3.17: *Final $B^0 \to K^\pm \pi^\mp \gamma$ mass fits for 2011 and 2012 data.*
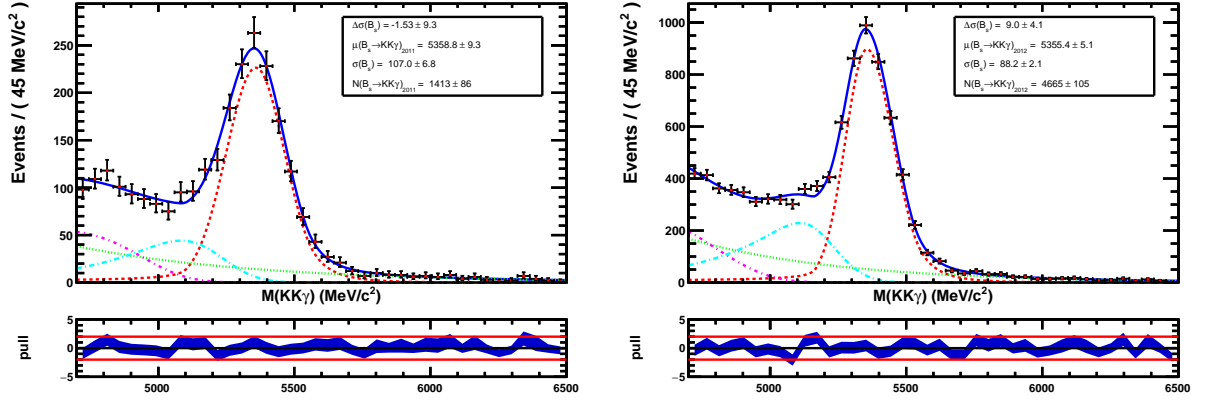
Figure 3.18: *Final $B_s \to K^+ K^- \gamma$ mass fits for 2011 and 2012 data.*
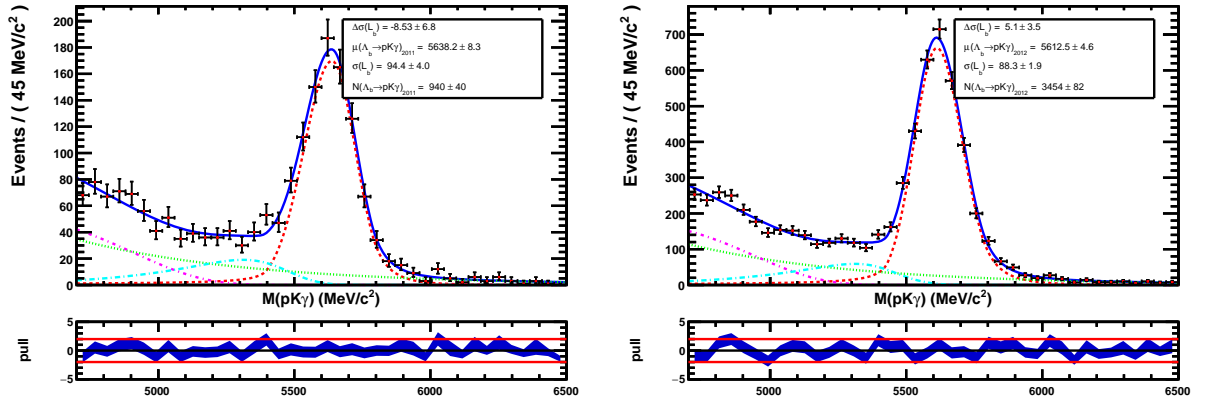
Figure 3.19: *Final $\Lambda_b \to p^\pm K^\mp \gamma$ mass fits for 2011 and 2012 data.*

102
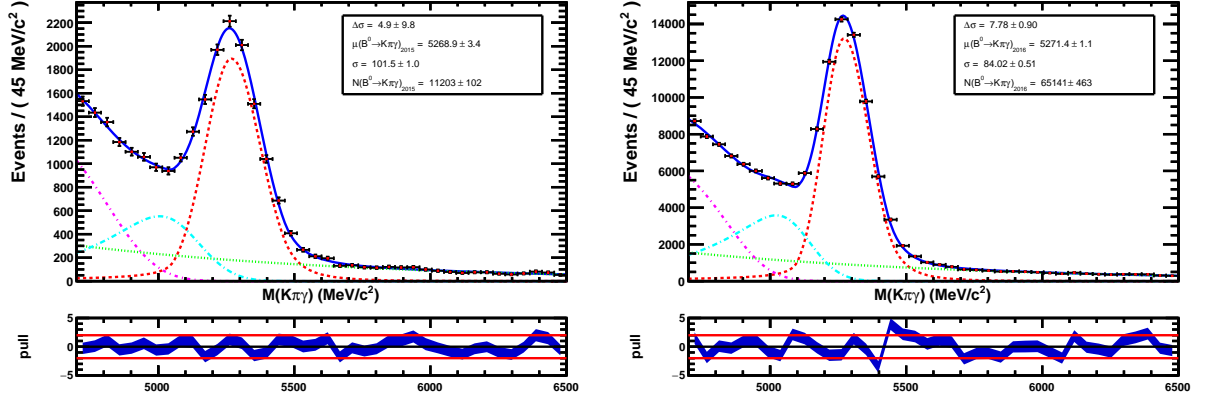
Figure 3.20: *Final $B^0 \to K^{\pm}\pi^{\mp}\gamma$ mass fits for 2015 and 2016 data.*
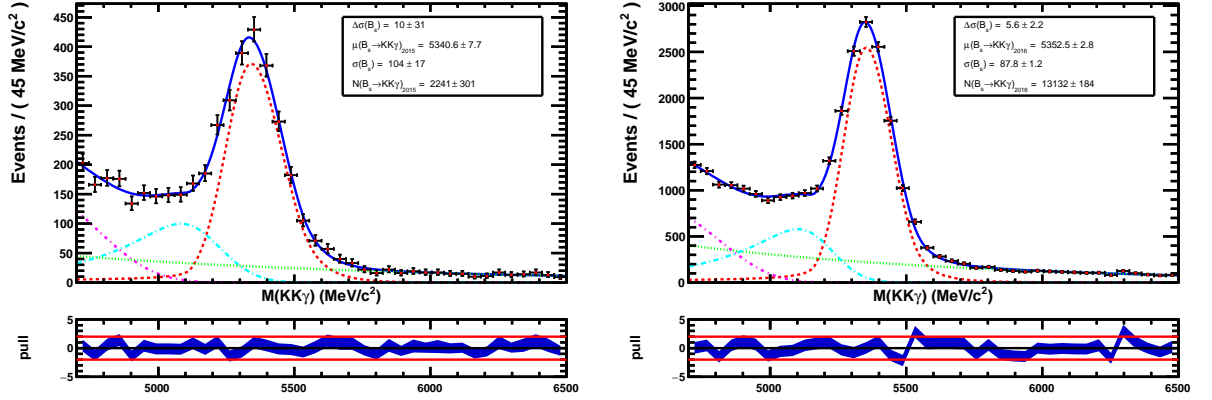
Figure 3.21: *Final $B_s \to K^+K^-\gamma$ mass fits for 2015 and 2016 data.*
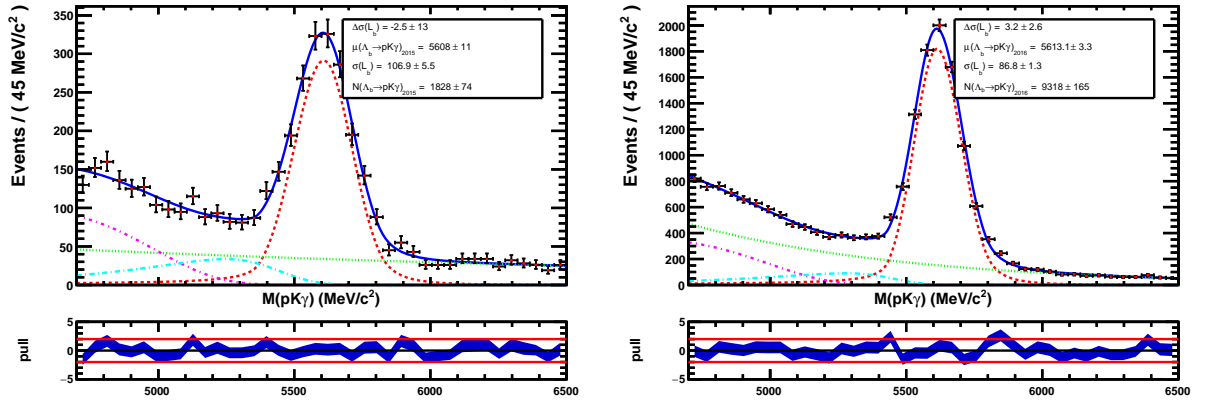
Figure 3.22: *Final $\Lambda_b \to p^{\pm}K^{\mp}\gamma$ mass fits for 2015 and 2016 data.*
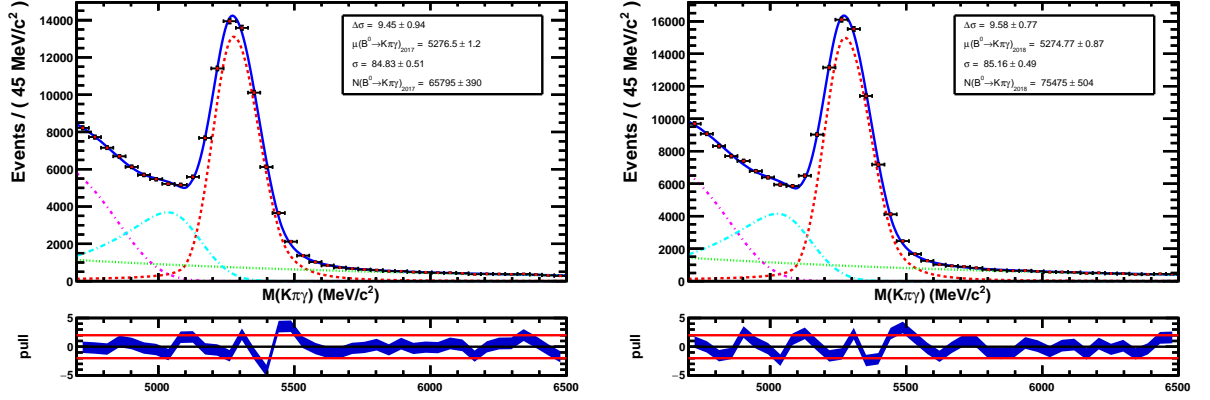
Figure 3.23: *Final $B^0 \to K^\pm \pi^\mp \gamma$ mass fits for 2017 and 2018 data.*
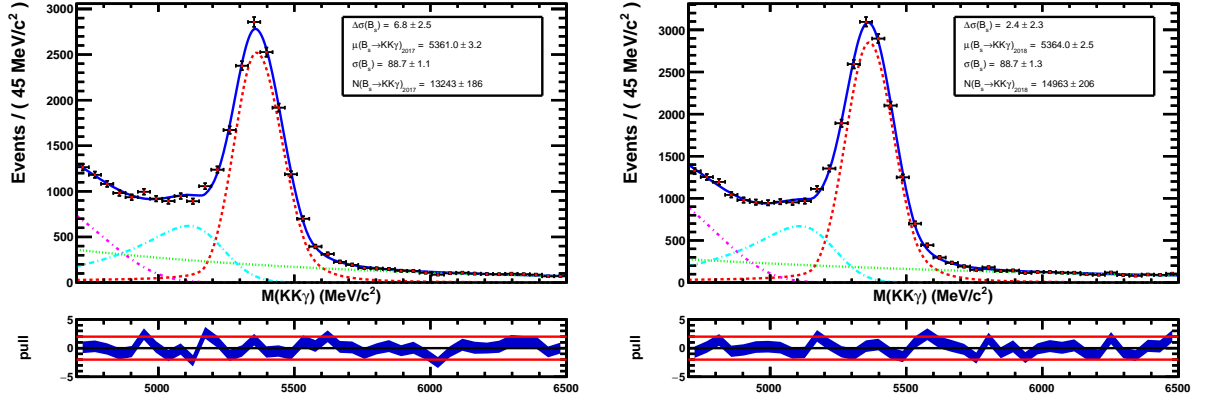
Figure 3.24: *Final $B_s \to K^+ K^- \gamma$ mass fits for 2017 and 2018 data.*
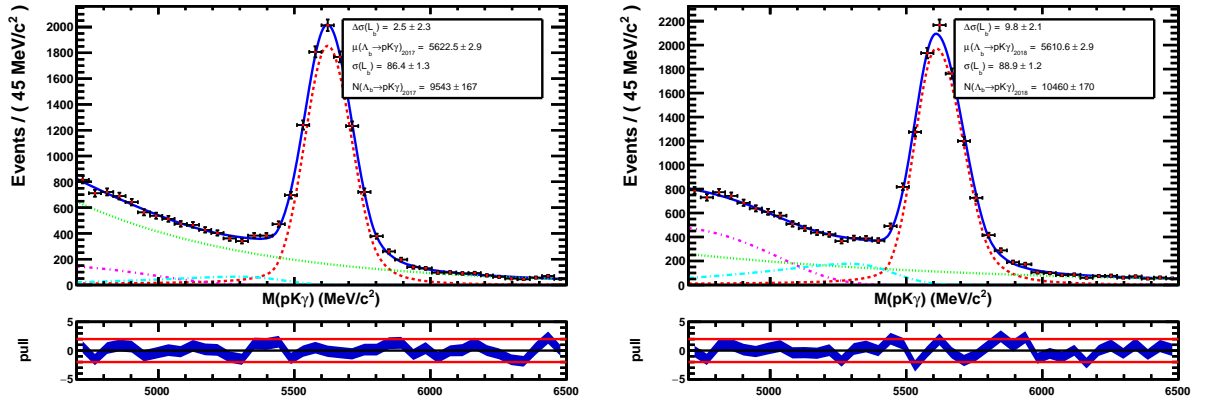
Figure 3.25: *Final $\Lambda_b \to p^\pm K^\mp \gamma$ mass fits for 2017 and 2018 data.*

| Period	N_{signal}	$\mu_B(\,\mathrm{MeV}/c^2)$	$\sigma_B(\,\mathrm{MeV}/c^2)$	$\delta_B(\,\mathrm{MeV}/c^2)$
2011	7520 ± 570	5286.6 ± 2.5	97.6 ± 8.0	0.82 ± 8.05
2012	27280 ± 110	5278.8 ± 3.9	87.3 ± 1.5	0.94 ± 3.3
2015	11200 ± 100	5268.9 ± 3.4	101.5 ± 1.1	4.9 ± 9.8
2016	65140 ± 460	5271.4 ± 1.1	84.0 ± 5.1	7.8 ± 9.1
2017	65790 ± 390	5276.5 ± 1.2	84.8 ± 5.1	9.4 ± 9.4
2018	75470 ± 500	5274.8 ± 0.8	85.2 ± 4.9	9.6 ± 0.78

Table 3.19: *Fit parameters of the signal in the invariant mass fits of $B^0 \to K^\pm \pi^\mp \gamma$.*

Period	N_{signal}	$\mu_B(\,\mathrm{MeV}/c^2)$	$\sigma_B(\,\mathrm{MeV}/c^2)$	$\delta_B(\,\mathrm{MeV}/c^2)$
2011	1410 ± 85	5358.8 ± 9.3	107.0 ± 6.8	-1.5 ± 9.3
2012	4660 ± 100	5355.4 ± 5.0	88.2 ± 2.1	9.0 ± 4.1
2015	2240 ± 300	5340.6 ± 7.7	103.6 ± 1.7	9.9 ± 31.0
2016	13130 ± 180	5352.5 ± 2.8	87.8 ± 1.3	5.6 ± 2.3
2017	13243 ± 190	5361 ± 3.2	88.7 ± 1.1	6.8 ± 2.5
2018	14960 ± 200	5364 ± 2.5	88.7 ± 1.4	2.4 ± 2.3

Table 3.20: *Fit parameters of the signal in the invariant mass fits of $B_s \to K^+ K^- \gamma$.*

Period	N_{signal}	$\mu_B(\,\mathrm{MeV}/c^2)$	$\sigma_B(\,\mathrm{MeV}/c^2)$	$\delta_B(\,\mathrm{MeV}/c^2)$
2011	939 ± 40	5638.2 ± 8.3	94.4 ± 4.0	-8.5 ± 6.8
2012	3450 ± 82	5612.5 ± 4.6	88.3 ± 1.9	5.1 ± 3.5
2015	1820 ± 73	5608.1 ± 1.0	106.9 ± 5.5	-2.5 ± 13.0
2016	9320 ± 160	5613.1 ± 3.3	86.8 ± 1.3	3.2 ± 2.6
2017	9540 ± 170	5622.5 ± 2.9	86.4 ± 1.3	2.5 ± 2.3
2018	10460 ± 170	5610.6 ± 2.9	88.9 ± 1.2	9.8 ± 2.1

Table 3.21: *Fit parameters of the signal in the invariant mass fits of $\Lambda_b \to p^\pm K^\mp \gamma$.*

3.11 Conclusion

A selection of $B^0 \to K^\pm \pi^\mp \gamma$, $B_s \to K^+ K^- \gamma$ and $\Lambda_b \to p^\pm K^\mp \gamma$ decay channels has been presented. It makes use of dedicated inclusive LHCb trigger and stripping lines to gather the most $B_{d/s} \to (h^+ h^-)\gamma$ events as possible from the Run 1 and Run 2 data taking. The events are selected in a wide hh mass range, up to 1.8 GeV, as the final goal of the analysis is to study the hadronic structure in $B^0 \to K^\pm \pi^\mp \gamma$ and $B_s \to K^+ K^- \gamma$. Studying similarly $\Lambda_b \to p^\pm K^\mp \gamma$ decays is a way to better control its contamination to the two other modes through the mis-identification of the proton. A special emphasis is placed on the control of peaking backgrounds expected from mis-identified tracks and/or π^0, which can significantly pollute the $h^+ h^- \gamma$ invariant mass in the B region, especially when selecting the whole hh spectra. After tight PID requirements tuned to suppress the cross-feeds of the different radiative modes, a large part of the selected data is combinatorics. A dedicated BDT classifier is then trained against it with MC signal, which is corrected in a multivariate manner beforehand. However, it seems that the tool allowing this multivariate reweighting does not offer a very good correction of all the input variables, when looking at them independently. More work will be needed to understand the impact and the difficulties of this reweighting. The trained BDT allows anyways a very good background reduction and a final fit is performed after an optimal cut to the BDT output. While a few different possible background contributions are discussed, the model for the final mass fit does not include any peaking backgrounds as the $_s\mathcal{P}lot$ method does not allow to substract contributions that are fixed or constrained in the fit. These contributions are therefore treated as signal and will have to be addressed in the amplitude analyses.

In the end, the procedure allows to select $\sim$250k $B^0 \to K^\pm \pi^\mp \gamma$ events, $\sim$50k $B_s \to K^+ K^- \gamma$ events, and $\sim$35k $\Lambda_b \to p^\pm K^\mp \gamma$ events.

Chapter 4

Amplitude analysis of $B_s \to K^+ K^- \gamma$

4.1 Analysis strategy

The analyses depicted in this chapter and the following one focus on the study of the resonant structure of the hadronic hh system in the $B_s \to K^+ K^- \gamma$ and $B^0 \to K^{\pm} \pi^{\mp} \gamma$ decays. It aims at improving the mass models for $B^0 \to K^{*0} \gamma$ and $B_s \to \phi \gamma$ studies with a better understanding of the non-resonant states and high mass contamination, as well as measuring branching ratios and A_{CP} of exclusive radiative modes where the B goes to an orbitally excited mesonic state. For that, a time-integrated amplitude fit of the decay distributions in a modified Dalitz plane - the $h^+ h^-$ resonance invariant mass versus its helicity - is performed. The data and the sWeights referred to in this chapter are the ones described in Section 3.10.2. As already stated, the samples are still poluted with backgrounds that will be modelled in the amplitude fit.

After a common description of the formalism of the two separate amplitude analyses (Section 4.2), the mass and helicity models used in the fits are developed (Section 4.3). These are common to the to separate analyses. Then, the fit to the sWeighted $B_s \to K^+ K^- \gamma$ data is described in detail: considered resonances in the nominal model (4.4.1), mass and angular resolutions (4.4.2), detector acceptance description (4.5), and finally the model (4.6) and the fit to the data (4.7). The Section 4.8 is then dedicated to various systematics estimations, and the results in terms of fit-fractions are discussed in Section 4.9. The fit to $B^0 \to K^{\pm} \pi^{\mp} \gamma$ data will be discussed in the next chapter.

4.2 Amplitude analysis formalism

The kinematics of a three-body transition $X \to R_{12}(\to x_1 x_2) x_3$, where R_{ij} is an intermediate resonance, can be completely described using, in a traditional Dalitz analysis [87], the squares of invariant masses of two pairs of the decay products $s_{ij} = m_{ij}^2 = m^2(x_i x_j)$. They are related by:

$$s_{12} + s_{13} + s_{23} = M_X^2 + \sum_i m_i^2 \tag{4.1}$$

and allow to represent the phase space of the decay in a single plane : the Dalitz plot. The phase space is constrained by the conservation of the momentum and by the masses of the mother and daughter particles, as well as in our case the cuts applied to the invariant masses in the selection of the data (Section 3.5). The typical boundaries on a Dalitz plot and the actual phase space we are considering in our analyses are displayed on Figure 4.1
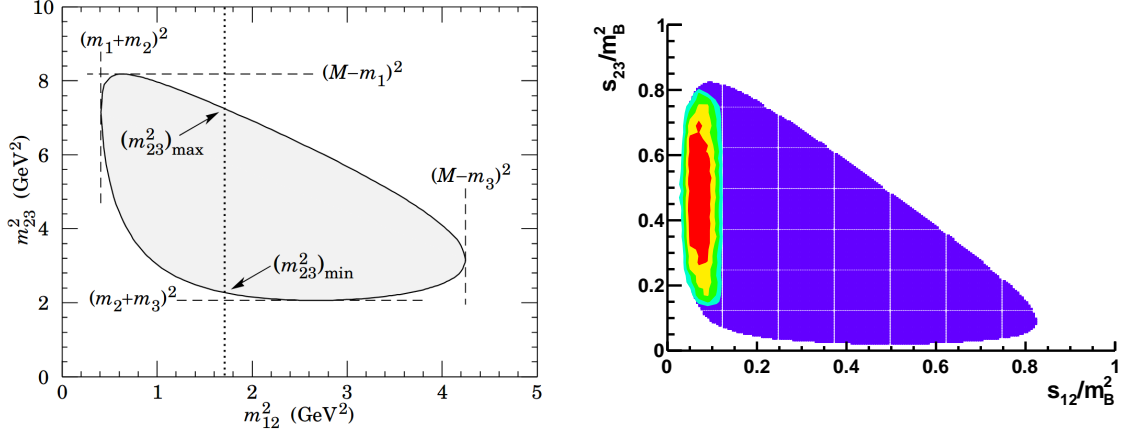
Figure 4.1: Kinematical boundaries of a typical Dalitz plot [88](left), and the actual phase space region of the selected data (right).

The Lorentz-invariant three-body decay rate is given by:

$$d\Gamma = \frac{(2\pi)^4}{2M_X}|\mathcal{M}(s_{12}, s_{23})|^2 d\phi_3 \tag{4.2}$$

where the phase-space element $d\phi_3$ is proportional to the Dalitz volume $ds_{12}ds_{13}$ and the matrix element $\mathcal{M}(s_{12}, s_{23}) = <x_1x_2x_3|H|X>$ represents the transition amplitude.

The helicity angle is defined as the angle between the x_1 direction in the R_{12} rest-frame and the R_{12} direction in the X rest-frame, and is related to the Dalitz coordinates as:

$$cos(\theta_{12}) = \frac{(s_{13} - s_{23})\sqrt{s_{12}}}{4M_X q_R q_X} \tag{4.3}$$

where q_R is the momentum of x_1 (or x_2) in the R_{12} rest-frame and q_X is the momentum of R_{12} (or x_3) in the X rest-frame. q_R and q_X can be written as:

$$q_R = \mathcal{Q}_2(m_{12}, m_1, m_2) \tag{4.4}$$
$$q_X = \mathcal{Q}_2(M_X, m_{12}, m_3) \tag{4.5}$$

where $\mathcal{Q}_2$ is the 2-body kinematical function:

$$\mathcal{Q}_2(m_{ab}, m_a, m_b) = \left[\frac{(m_{ab}^2 - (m_a + m_b)^2)(m_{ab}^2 - (m_a - m_b)^2)}{4m_{ab}^2}\right]^{\frac{1}{2}} \tag{4.6}$$

The partial decay rate in the $(m_{12}, cos(\theta_{12}))$ coordinates system can then be derived as:

$$d\Gamma = \mathcal{J}_3(m_{12})|\mathcal{M}(m_{12}, cos(\theta_{12}))|^2 dm_{12} dcos(\theta_{12}) \tag{4.7}$$

where $\mathcal{J}_3(m_{12})$ represents the 3-body phase-space Jacobian[*]:

$$\mathcal{J}_3(m_{12}) \propto \frac{1}{M_X^2} \times q_R \times q_X = \frac{1}{M_X^2} \times \mathcal{Q}_2(m_{12}, m_1, m_2) \times \mathcal{Q}_2(M_X, m_{12}, m_3) \tag{4.8}$$

4.3   Transition amplitude of the radiative B decays

We aim at determining the amplitude structure of the $B^0 \to K^+\pi^-\gamma$ and $B_s \to K^+K^-\gamma$ decays that both are, in term of helicity, the radiative decay of a scalar state to a pair of pseudo-scalar mesons, $S \to (P_1P_2)\gamma$. Due to the initial spin-0 state, the angular momentum conservation imposes the hadronic system to be in the same helicity state as the radiated photon, i.e. $\lambda = \pm 1$. In addition, as the hadronic intermediate state consists in a pair of pseudo-scalar mesons, the relative orbital momentum in the (P_1P_2) system is the same as its spin. As a consequence, the allowed spin-parity states for the hadronic $K\pi$ and KK systems are limited to J^P where $J > 0$ and $P = (-1)^L$ $(L = J)$, i.e. $J^P = 1^-, 2^+, 3^-, ...$

In the three-body $(P_1P_2)\gamma$ final-state, the azymuthal angle of the (P_1P_2) decay plane relative to the photon polarisation is undetermined. In other words, the measured angular dependency in the (P_1P_2) decay is unsensitive to the photon polarization, i.e. independent on the sign of the $\lambda = \pm 1$ helicity[†]. The transition probability, that is obtained by summing incoherently over the unobserved helicity states, thus simplifies as:

$$|\mathcal{M}|^2 = \sum_{\lambda=\pm 1} |\mathcal{M}_\lambda|^2 = |\mathcal{M}_{|\lambda|=1}|^2 \tag{4.9}$$

since $\mathcal{M}_{\lambda=+1}$ exhibits the same angular dependency (on the polar angle θ_{12} only) than $\mathcal{M}_{\lambda=-1}$. To describe this amplitude transition, we use an isobar approach consisting in a coherent sum of the individual intermediate (non)resonant state amplitudes

$$\mathcal{M}_{|\lambda|=1}(m_{12}, \theta_{12}) = \sum_R c_R^{|\lambda|=1} \mathcal{A}_R(m_{12}, \theta_{12}) \tag{4.10}$$

where $c_R^{|\lambda|=1} = |c_R|e^{i\delta_R}$ is a complex coefficient and $\mathcal{A}_R$ represents the individual amplitude for the intermediate state R.

---

[*]Unrelevant constant factors are omitted here.

[†]The dynamics is different for the half-spin baryonic decay $\Lambda_b \to pK^-\gamma$ for which the (pK) amplitude structure is sensitive to the photon polarisation. The amplitude analysis of the large sample of selected $\Lambda_b \to pK^-\gamma$ candidates discussed in Section 3.10.2 would be an interesting extension of the work presented here.

The amplitudes $\mathcal{A}_R$ are modelled as:

$$\mathcal{A}_R(m_{12}, \theta_{12}) = A_R(m_{12})\mathrm{d}_{10}^{J_R}(\theta_{12}), \qquad (4.11)$$

where $A_R(m_{12})$ is the mass line-shape of the intermediate state R with spin J_R .The angular dependency is given by the Wigner d-functions, $\mathrm{d}_{\lambda,\lambda_{P_1}-\lambda_{P_2}}^{J_R}=\mathrm{d}_{10}^{J_R}(\theta_{12})$ that encodes the matrix elements of the operator rotating the angular momentum basis from the B decay axis to the (PP) decay axis. Figure 4.2 displays the behaviour of the $\mathrm{d}_{10}^{J_R}(\theta_{12})$ functions for spin $J_R =1,2,3$ and 4 given by:

$$\mathrm{d}_{10}^1(\theta_{12}) = -\sqrt{\frac{1}{2}}sin(\theta_{12}), \qquad (4.12)$$

$$\mathrm{d}_{10}^2(\theta_{12}) = -\sqrt{\frac{3}{2}}sin(\theta_{12})cos(\theta_{12}), \qquad (4.13)$$

$$\mathrm{d}_{10}^3(\theta_{12}) = -\sqrt{\frac{3}{16}}sin(\theta_{12})(5cos^2(\theta_{12}) - 1), \qquad (4.14)$$

$$\mathrm{d}_{10}^4(\theta_{12}) = -\sqrt{\frac{5}{16}}sin(\theta_{12})(7cos^3(\theta_{12}) - 3cos(\theta_{12})). \qquad (4.15)$$

As no S-wave is allowed in the decay, a nominal model based on the relativistic Breit-
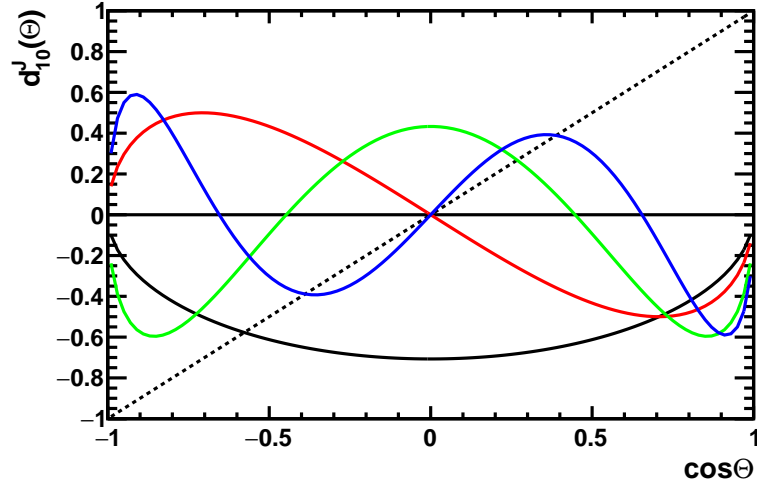
Figure 4.2: *Wigner d-functions $d_{10}^J(\theta)$ that describe the angular dependency in the $B \to R_J\gamma$ decay amplitude, as a function of $cos(\theta)$ for J=1 (black curve), J=2 (red), J=3 (green) and J=4 (blue). The diagonal dashed line represents the $d_{00}^1(\theta) = cos(\theta)$ function, that appears in the Scalar to Vector-Scalar decays, $S \to VS$, e.g. $B^0 \to K^{*0}\pi^0$.*

Wigner is adopted to describe the mass line-shape, $A_R(m_{12})$, for each resonant state:

$$A_R(m_{12}) = \mathcal{F}_R.\mathcal{F}_B.\mathcal{B}_R(m_{12}; \mu_R, \Gamma_R) \qquad (4.16)$$

where $\mathcal{F}_R$ and $\mathcal{F}_B$ are the Blatt-Weiskopf factors [89] accounting for the centrifugal barrier effect in the decays of the R resonance and the B meson, respectively.

$$\mathcal{B}_R(m_{12}; \mu_R, \Gamma_R) = \frac{1}{(\mu_R^2 - m_{12}^2) - i\mu_R \mathcal{W}(m_{12}; \Gamma_R)} \tag{4.17}$$

is the Breit-Wigner complex pole for the resonance R, with μ_R and Γ_R, the corresponding pole mass and width, respectively. The mass-dependent width is defined as:

$$\mathcal{W}(m_{12}; \Gamma_R) = \Gamma_R \frac{q_R}{\bar{q}_R} \frac{\mu_R}{m_{12}} \mathcal{F}_R^2 \tag{4.18}$$

where $q_R = \mathcal{Q}_2(m_{12}, m_1, m_2)$ is the momentum of any of the resonance decay products in the resonance rest-frame at mass m_{12}, and $\bar{q}_R = \mathcal{Q}_2(\mu_R, m_1, m_2)$ is a reference momentum evaluated at the nominal mass pole of the resonance.

The normalized Blatt-Weiskopf form-factors:

$$\mathcal{F}_R = \mathcal{F}(q_R, \bar{q}_R, L_R) \tag{4.19}$$
$$\mathcal{F}_B = \mathcal{F}(q_B, \bar{q}_B, L_B) \tag{4.20}$$

are derived from the spherical Hankel functions of first kind [89]:

$$\mathcal{F}(q, \bar{q}, L) = \left| \frac{\mathcal{H}_L(r\bar{q})}{\mathcal{H}_L(rq)} \right| = \left(\frac{q}{\bar{q}} \right)^L \frac{h_L(r\bar{q})}{h_L(rq)} \tag{4.21}$$

where the parameter r is the meson radius that accounts for the size of the centrifugal barrier effect and L is the relative angular momentum in the resonance decay. The L-dependent functions $h_L(z)$ for $L \leq 4$ are:

$$h_0(z) = 1, \tag{4.22}$$
$$h_1(z) = \sqrt{1 + z^2}, \tag{4.23}$$
$$h_2(z) = \sqrt{9 + 3z^2 + z^4}, \tag{4.24}$$
$$h_3(z) = \sqrt{225 + 45z^2 + 6z^4 + z^6}, \tag{4.25}$$
$$h_4(z) = \sqrt{11025 + 1575z^2 + 135z^4 + 10z^6 + z^8}. \tag{4.26}$$

In the following, the nominal radius value r=1.5 GeV^{-1} $\sim$0.3 fm is chosen for all resonances R and r=5 GeV^{-1} $\sim$1 fm for the $B_{(s)}$ meson. The relative angular momentum L_R of the resonance decay products, being pseudo-scalars, is then equal to the resonance spin. The relative angular momentum of the resonance in the radiative B decay can take both $J_R \pm 1$ values. We assume the lowest value $J_R - 1$ in the nominal model and the largest value will be checked for systematics study. The Breit-Wigner isobar model assumes that all resonances are well separated and that the h^+h^- partial decay dominates over other decays close to the kinematical threshold that might distort the mass line-shape. Other line-shape models (e.g. Flatte distribution [90]) for heavy tensor resonances will have to be studied for the systematics evaluation.

4.4 The KK hadronic system

4.4.1 Resonant structure

The K^+K^- hadronic system is a $\mathcal{CP}$-eigenstate. As discussed in the previous section, the allowed J^{PC} state in B_s radiative decays are $1^{--}, 2^{++}, ...$ The known $s\bar{s}$-dominated states that we can consider to put in the model are listed in Table 4.1. While other possible contributions from $d\bar{d}$-dominated states (with low coupling to K^+K^-, thus suppressed in B_s decays) are not considered for the nominal model, they will be discussed for the systematics estimations on the model. The same goes for currently non-confirmed states. We note here that the $\phi(1680)$ decays predominantly to the $K_s^0 K\pi$ final state, then a study of $B_s \to K_s^0 K\pi\gamma$ decays, as discussed in Chapter A will possibly give additional information on the contribution of this state.

known resonance	μ_R (MeVc^{-2})	Γ_R (MeVc^{-2})	J^{PC}	$\mathcal{B}(K^+K^-)$ (%)
$\phi(1020)$	1019.46 ± 0.02	4.25 ± 0.01	1^{--}	49.2 ± 0.5
$f_2(1270)$	1275.5 ± 0.8	$186.6^{+2.2}_{-2.5}$	2^{++}	$2.30^{+0.25}_{-0.20}$
$f_2'(1525)$	1525 ± 5	73.0^{+6}_{-5}	2^{++}	44.35 ± 1.10
$\phi(1680)$	1680 ± 20	150 ± 50	1^{--}	seen
$\phi_3(1850)$	1854 ± 7	87^{+28}_{-23}	3^{--}	seen
$f_2(1950)$	1944 ± 12	472 ± 18	2^{++}	seen
$f_4(2050)$	2018 ± 11	237 ± 18	2^{++}	$0.34^{+0.17}_{-0.09}$

Table 4.1: *A list of established K^+K^- resonant states that could contribute to the radiative B_s decays.*

A first look is given on Figure 4.3 to the sWeighted $B_s \to K^+K^-\gamma$ data candidates projected onto the $(m_{\text{KK}}, cos(\theta_{\text{KK}}))$ plane. Aside from the dominant vector contribution in the $\phi(1020)$ region, one can clearly spot a tensor contribution around 1500 MeVc^{-2}, identifiable as a significant contribution from the $f_2'(1525)$.

4.4.2 $B_s \to K^+K^-\gamma$ observables

Mass resolution

The mass resolution on the kaon pair has to be discussed. It is extracted from a fit to the $B_s \to \phi\gamma$ and $B_s \to f_2'(1525)\gamma$ MC samples, using an asymmetric Apollonios [?] function (Figure 4.4). While it is essentially negligible for the higher resonances with respect to their width Γ_R (fit to the $B_s \to f_2'(1525)\gamma$ MC gives $\sigma_R = 3.81 \pm 0.03$ MeVc^{-2}while $\Gamma_{f_2'} = 76 \pm 10$ MeVc^{-2}), it has to be added to the mass model for the very narrow $\phi(1020)$ ($\sigma_R = 0.887 \pm 0.004$ MeVc^{-2}, and $\Gamma_\phi = 4.25 \pm 0.01$ MeVc^{-2}).

In the fit to the data, to avoid the huge computational ressources needed when convoluting the squared amplitudes with a resolution function, the mass resolution is
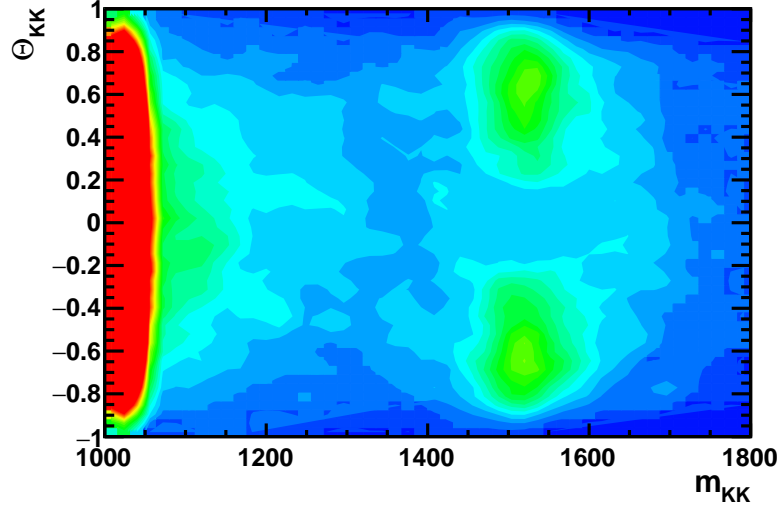
Figure 4.3: $B_s \to K^+K^-\gamma$ sWeighted candidates in the modified Dalitz plane $(m_{\mathrm{KK}}, \cos(\theta_{\mathrm{KK}}))$.
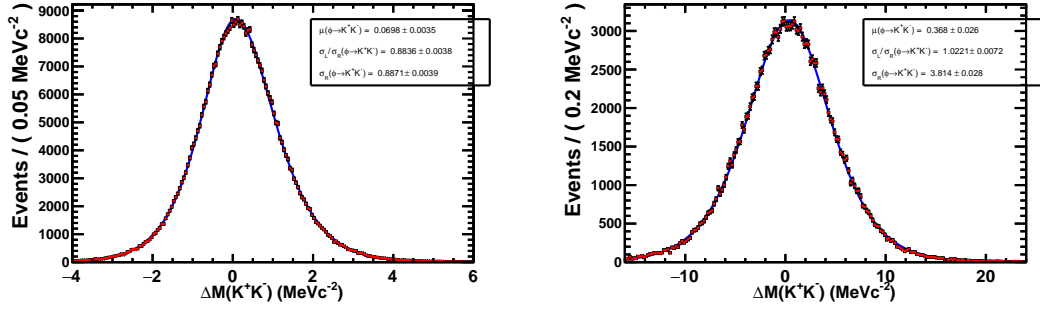
Figure 4.4: $\Delta M = m_{\mathrm{KK}}^{sim} - m_{\mathrm{KK}}^{rec}$ distribution in the ϕ (left) and $f'2$ (right) region.

included in each individual Breit-Wigner poles using an analytical approach derived from [91]. The relativistic Voigt profile is built by convoluting the Breit-Wigner profile with a Gaussian resolution function:

$$|\mathcal{V}(m; \mu, \Gamma, \sigma)|^2 = \int_{-\infty}^{\infty} |\mathcal{B}(m; \mu, \Gamma)|^2 \mathcal{G}(m - m'; 0, \sigma) dm' = \frac{1}{\sigma\sqrt{2\pi}} |\mathcal{H}(a, u_+, u_-)|^2, \quad (4.27)$$

with $u_\pm = \frac{m \pm \mu}{\sqrt{2}\sigma}$ and $a = \frac{\mu \mathcal{W}(m; \Gamma)}{2\sigma^2}$ where $\mathcal{W}$ represents the mass-dependent width of the Breit-Wigner. The result of the integration is a weighted-sum of Faddeeva functions:

$$|\mathcal{H}(a, u_+, u_-)|^2 = \frac{w(z_{++}) + w(z_{+-})}{2\Delta_+} + \frac{w(z_{-+}) + w(z_{--})}{2\Delta_-} \quad (4.28)$$

113

where $z_{\kappa\eta} = (u_+ + u_- + \kappa.\Delta_\eta)/2$, $\Delta_\eta = \sqrt{(u_+ - u_-)^2 + \eta.4ia}$ and $w(z)$ is the Faddeeva function, i.e. the scaled complementary error complex function, the real part of which defines the usual non-relativistic Voigt profile:

$$w(z) = e^{-z^2} \operatorname{erfc}(-iz), \tag{4.29}$$

The mass resolution is then included in our amplitude model by modyfing the Breit-Wigner pole definition as:

$$\mathcal{B}'_R(m_{12}; \mu_R, \Gamma_R, \sigma_R) = |\mathcal{V}(m_{12}; \mu_R, \Gamma_R, \sigma_R)|e^{iArg(\mathcal{B}(m_{12}; \mu_R, \Gamma_R))}, \tag{4.30}$$

i.e. the resolution is included in the mass line-shape but the effect of the resolution on the mass-dependent phase is neglected .

Angular resolution

As for the mass the resolution on the helicity angle, which depends inderectly on the reconstructed photon momentum, has to be checked and similarly it is extracted from fits to the simulated $B_s \to \phi\gamma$ and $B_s \to f'_2(1525)\gamma$ samples (Figure 4.5). Near the KK threshold, it is found to be $\sigma_R = 11.843 \pm 0.057$ mrad with a low dependency on the $cos(\theta)$, as shown on Figure 4.6. In the $f'_2(1525)$ region : $\sigma_R = 4.484 \pm 0.032$ mrad.
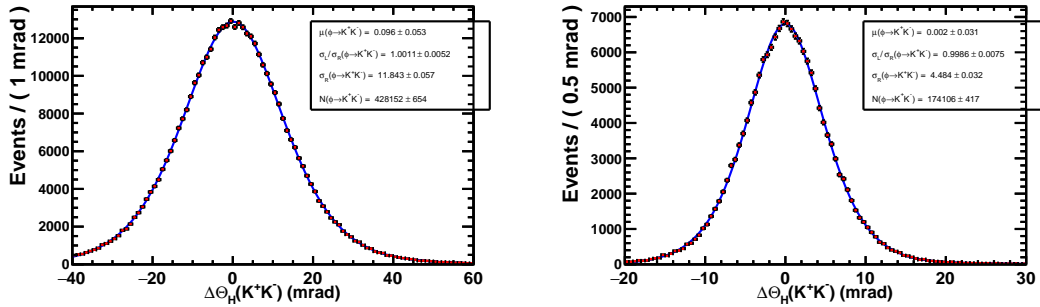
Figure 4.5: $\Delta\theta = \theta_{KK}^{sim} - \theta_{KK}^{rec}$ distribution in the $\phi(1020)$ (left) and $f'_2(1525)$ (right) region.

This resolution would only appear as lower-order σ_θ^2 corrections to the Wigner d-functions. While it is not taken into account in the nominal fit, it can still be added analytically for systematics studies. The convolution with a gaussian resolution for Vector, Tensor and V*T interferences would be as:

$$
\begin{aligned}
V\gamma &: & |d^1_{10}|^2 * \mathcal{G}(0, \sigma_\theta) &\propto sin^2(\theta) + \sigma_\theta^2 cos(2\theta) + \mathcal{O}(\sigma_\theta^3) \\
T\gamma &: & |d^2_{10}|^2 * \mathcal{G}(0, \sigma_\theta) &\propto sin^2(2\theta) + 4\sigma_\theta^2 cos(4\theta) + \mathcal{O}(\sigma_\theta^3) \\
(V*T)\gamma &: & (d^1_{10}.d^2_{10}) * \mathcal{G}(0, \sigma_\theta) &\propto sin(2\theta)sin(\theta) + \sigma_\theta^2(9cos(3\theta) - cos(\theta)) + \mathcal{O}(\sigma_\theta^3)
\end{aligned}
\tag{4.31}
$$
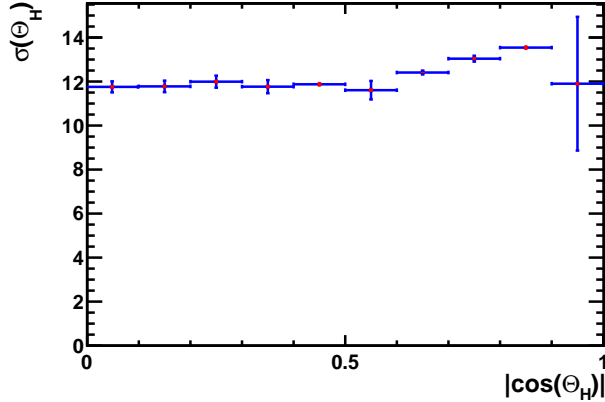
Figure 4.6: *Resolution of the $\Delta\theta = \theta^{sim}_{KK} - \theta^{rec}_{KK}$ distribution as a function of $|cos\theta_{KK}|$ in the ϕ region.*

4.5 Acceptance function

The 2-dimensional acceptance in the $(m_{KK}, cos(\theta_{KK}))$ plane is extracted from a simultaneous fit of various samples of fully simulated events: $B_s \to K^+K^-\gamma$, uniformly distributed in the phase-space ($\sim 3.10^4$ reconstructed events), $B_s \to \phi\gamma$ ($\sim 29.10^4$ events) and $B_s \to f'_2(1525)\gamma$ ($\sim 9.10^4$ events). The MC samples simulating each year of data taking, with a statistics almost proportional to the corresponding experiment integrated luminosity, are combined in a single sample to extract an average acceptance for Run 1 and Run 2 data. To alleviate the impact of imperfections in the simulation, the MC samples are reweighted using the multidimensional GB method for the BDT variables (see Section 3.7), and the data-driven PID-reweighting for the neutral and charged identification variables, IsPhoton and ProbNN(K) (see Section 3.6).

The Probability Density Function describing each MC sample, $\mathcal{P}_R$, is based on the phase-space Jacobian, the Breit-Wigner mass model for the $\phi(1020)$ and the $f'_2(1525)$ resonance and the relevant spin-dependent angular d-functions ($d^0_{00} = 1$ for the phase-space MC, d^1_{10} for the vector meson $\phi(1020)$ and d^2_{10} for the tensor meson $f'_2(1525)$) multiplied by a parametrized 2D acceptance function:

$$\mathcal{P}_R = \varepsilon(m_{KK}, \theta_{KK}; \vec{\alpha}).\mathcal{J}_3(m_{KK}).|\mathcal{A}_R(m_{KK}, \theta_{KK})|^2, \tag{4.32}$$

with $\mathcal{A}_R(m_{KK}, \theta_{KK}) = A_R(m_{KK})d^{J_R}_{\lambda,0}(\theta_{KK})$.

The set of acceptance parameters, $\vec{\alpha}$, as well as the mass pole, the width and the meson radius describing the resonances are free to vary in the fit to account for the reconstruction effects and the possible differences between the parametrization applied in the simulation and the data fit model. Due to the kaon symmetry in the $B_s \to K^+K^-\gamma$ final-state, a generic acceptance function, symmetrical in helicity, is used:

115

$$\varepsilon(m_{\text{KK}}, \theta_{\text{KK}}) = \prod_{k=0}^{3} \left[1 - \alpha_k(m_{\text{KK}}).cos^{2k}(\theta_{\text{KK}}) \right] \times \left[1 + \text{erf}\left(\frac{c_0(m_{\text{KK}}) - |cos(\theta_{\text{KK}})|}{\sigma_c} \right) \right] / 2.$$

(4.33)

where the mass-dependent coefficients $\alpha_k(m_{\text{KK}})$, vanishing at the KK threshold, are parametrized with a polynomial function of the kaons momentum in the KK rest-frame:

$$\alpha_k(m_{\text{KK}}) = \sum_{l=1}^{n_k} \alpha_{kl}.(q_R(m_{\text{KK}}))^l.$$

(4.34)

The polynomial development is extended up to order 3 for the 0-th order helicity coefficient α_0 (n_0=3) and a quadratic parametrization is applied for higher-order coefficients α_l (n_l=2 for l>0), leading to nine α_{kl} parameters.
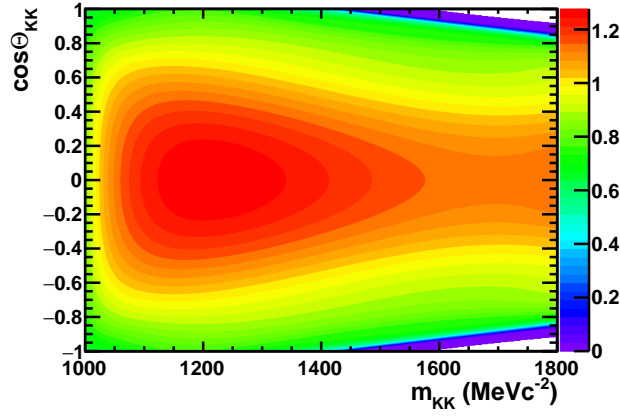
Figure 4.7: *Selection acceptance in the* $(m_{\text{KK}},cos(\theta_{\text{KK}}))$ *plane. The absolute normalisation is arbitrarily set near the* $\phi(1020)$ *pole:* $\varepsilon(1019.5, 0) = 1$.

The "anti-charm" cuts $m_{k^{\pm}\gamma \to \pi^0} > 2$ GeVc^{-2} applied at the preselection level to reduce the $(h^{\pm}\pi^0)h^{\mp}$ contamination due to $D^{\pm}_{(s)}$, $K^{*\pm}$ or $\rho^{\pm}$ intermediate resonances in the $(h^+h^-)\gamma$ sample (see Section 3.5), have a direct impact on the Dalitz acceptance and, consequently, on the helicity range in the $(m_{\text{KK}},cos(\theta_{\text{KK}}))$ plane. The corresponding cut on the substituted Dalitz observables $s_{K^{\pm}\gamma \to \pi^0} > s_{cut} = (2GeVc^{-2})^2$ can be translated into a mass-dependent helicity range:

$$|cos(\theta_{\text{KK}})| < c_0(m_{\text{KK}}) = \frac{M^2_{B_s} + 2.m^2_K + m^2_{\pi^0} - m^2_{\text{KK}} - 2.s_{cut}}{4.M_{B_s}.q_R(m_{\text{KK}}).q_B(m_{\text{KK}})}$$

(4.35)

that reaches the physical region ($|cos(\theta_{\text{KK}})| < 1$) when m_{KK} exceeds $\sim$1450 MeVc^{-2}. The error-function entering in the definition of the 2-dimensional acceptance $\varepsilon(m_{\text{KK}},cos(\theta_{\text{KK}}))$ aims at describing this helicity cut, taking into account the experimental resolution in

the actual value of the $c_0(m_{\kappa\kappa})$ upper-limit through the resolution-parameter σ_c. The 2-dimensional acceptance extracted from the fit of simulated samples is displayed on Figure 4.7. The 2-dimensional distribution of the $KK\gamma$ phase-space simulated events together with the fit model contours are shown on the left side of Figure 4.8. The right side of the same figure displays the corresponding pull distribution, showing the good agreement between the simulated data and the model.
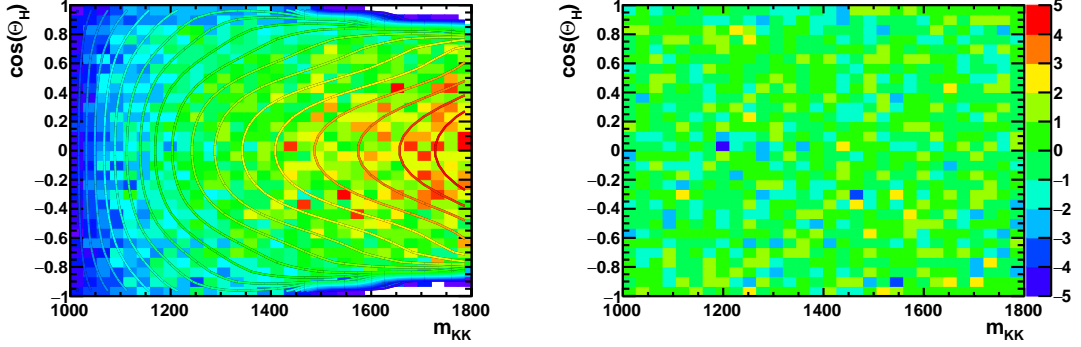
Figure 4.8: *Acceptance function on top of the phase-space MC (left) and corresponding pulls (right).*

The quality of the acceptance model can also be seen in the fit projections on both the mass and helicity observables, displayed on Figure 4.9 for the three samples of simulated data. The values of the acceptance model parameters $\vec{\alpha} = \{\alpha_{kl}, \sigma_c\}$ are reported with their statistical uncertainties in Table 4.2.

l	1	2	3
α_{0l} $(\mathrm{GeV/c})^{-l}$	-12.1±1.6	26.0±2.6	-16.7±1.3
α_{1l} $(\mathrm{GeV/c})^{-l}$	1.46±0.10	-0.87±0.18	-
α_{2l} $(\mathrm{GeV/c})^{-l}$	0.64±0.11	1.24±0.19	-
α_{3l} $(\mathrm{GeV/c})^{-l}$	2.40±0.26	-11.2±1.0	-
σ_c	$(3.54\pm0.19)\ 10^{-2}$	-	-

Table 4.2: *Acceptance parameters as fitted on the simulated samples.*

4.6 Amplitude fit model

As K^+K^- is a CP-eigenstate, the flavour of the decaying B_s is undefined in this time-integrated analysis. The measured decay angle in the symmetrical KK system, θ_H, is defined as the angle between the momentum of the positively charged kaon and the B
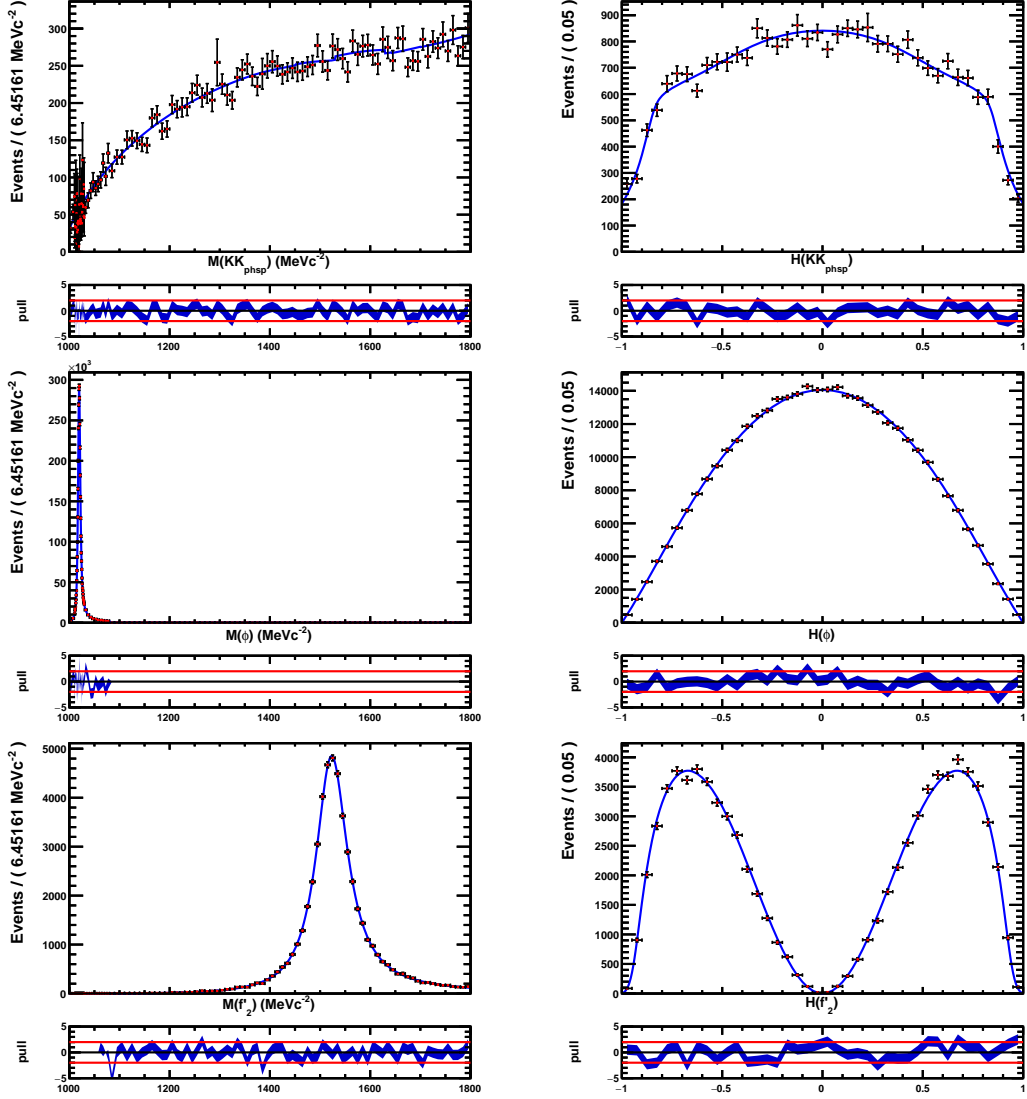
Figure 4.9: *Projection of the simultaneous fit to MC data on the m_{KK} (left) and $\cos(\theta_{\mathrm{KK}})$ (right) observables for the phase-space $KK\gamma$ (top line), $\phi(1020)\gamma$ (middle line), $f'_2(1525)\gamma$ (bottom line) samples. An adaptative binning is applied on the m_{KK} observable, with a fine granularity in the region of the narrow $\phi(1020)$.*

momentum in the KK rest-frame. This measured angle matches the helicity angle for one of the B flavour, $\theta_H = \theta_{\mathrm{KK}}$, but corresponds to the symmetrical $\theta_H = \pi - \theta_{\mathrm{KK}}$ for the opposite flavour. The Probability Density Functions (PDF) for the B_s and $\bar{B}_s$ signal are then defined as:

$$\mathcal{P}_{B_s}(m_{\text{KK}}, \theta_{\text{KK}}) = \varepsilon(m_{\text{KK}}, \theta_{\text{KK}}).\mathcal{J}_3(m_{\text{KK}}).|\sum_R c_R \times \mathcal{A}_R(m_{\text{KK}}, \theta_{\text{KK}})|^2, \qquad (4.36)$$

$$\mathcal{P}_{\bar{B}_s}(m_{\text{KK}}, \theta_{\text{KK}}) = \mathcal{P}_{B_s}(m_{\text{KK}}, \pi - \theta_{\text{KK}}). \qquad (4.37)$$

where $\mathcal{A}_R$ is the amplitude for the component R and $c_R = |c_R|e^{i\delta_R}$, the associated complex factor. The only consequence of the angular ambiguity is that the interference terms between odd- and even-spin components have a reverted sign in $\mathcal{P}_{\bar{B}_s}$ with respect to $\mathcal{P}_{B_s}$. The isobar amplitudes sum is based on the known resonant states having their mass poles in the analysis range ($m_{\text{KK}} < 1.8 \text{GeVc}^{-2}$), with an additional non-resonant, (NR), component:

$$R = \{\phi(1020), f_2(1270), f_2'(1525), \phi(1680), (\text{NR})_{\text{KK}}\}. \qquad (4.38)$$

The non-resonant amplitude is modelled as a pure P-wave, with a constant phase, uniformly distributed in mass:

$$\mathcal{A}_{\text{NR}}(m_{\text{KK}}, \theta_{\text{KK}}) = \text{d}_{10}^1(\theta_{\text{KK}}) \qquad (4.39)$$

Thanks to the fast B_s oscillation, any small flavour-asymmetry at the production level is diluted to a negligible level when integrating over time. Assuming, in addition, that there is no violation of the $\mathcal{CP}$-symmetry in the radiative B_s decay, an equal decay rate for B_s and $\bar{B}_s$ is considered. The PDF modelling the data is then defined as:

$$\mathcal{P}(m_{\text{KK}}, \theta_{\text{KK}}) = \mathcal{N}_s \times \frac{\mathcal{P}_{B_s} + \mathcal{P}_{\bar{B}_s}}{2} + \sum_{\text{BKG}} \mathcal{N}_{\text{BKG}} \times \mathcal{P}_{\text{BKG}}. \qquad (4.40)$$

where $\mathcal{N}_s$ is the overall $(B_s + \bar{B}_s) \to K^+K^-\gamma$ yield and $\mathcal{N}_{\text{BKG}}$ represents the yields of the unsubtracted backgrounds. As the signal PDF normalisation is related to the yield parameter $\mathcal{N}_s$, one reference factor in the signal amplitudes sum (and the unrelevant global phase) can be fixed. This is done by setting to unity the complex coefficient for the $\phi(1020)$ component, $c_{\phi(1020)} = 1$. Moreover, in the limit of no $B_s/\bar{B}_s$ decay asymmetry, the interferences between odd- and even-spin components cancel out in the sum, and a reference phase can also be fixed for the even-spin components. This is done by setting to 0 the phase of the $f_2'(1525)$ amplitude factor, $\delta_{f_2'(1525)} = 0$. With that convention, the $f_2(1270)$ complex phase is measured relative to $f_2'(1525)$, and the phase of the vector components are relative to $\phi(1020)$.

After subtraction of the combinatorial background and the partially reconstructed B decays, the residual contamination is dominated by the unsubtracted peaking backgrounds due to the misidentified $B^0 \to K\pi\gamma$ and $\Lambda_b \to pK\gamma$ decays, with an expected contribution at the level of few percent, each. Other identified peaking contaminations, e.g. $KK\pi^0$, are assumed to be small and therefore neglected in our nominal model. This asumption will be addressed in the systematics studies. The two-dimensional distribution of the $K\pi\gamma$ contamination in the $(m_{\text{KK}}, cos(\theta_{\text{KK}}))$ observable plane, is modelled using the reconstructed $K\pi\gamma$ data sample described in Chapter 3. The sPlot method is used to extract the

$B^0 \to K\pi\gamma$ contribution and the di-hadron mass and helicity angle are both computed under the di-kaon hypothesis, i.e. by assigning a kaon mass to the pion candidate. Similar method is applied for the baryonic $\Lambda_b \to pK\gamma$ decay, assigning the kaon mass to the proton candidate. The obtained distributions, displayed on Figure 4.10, are used to define the background PDFs, $\mathcal{P}_{\mathrm{BKG}}$.
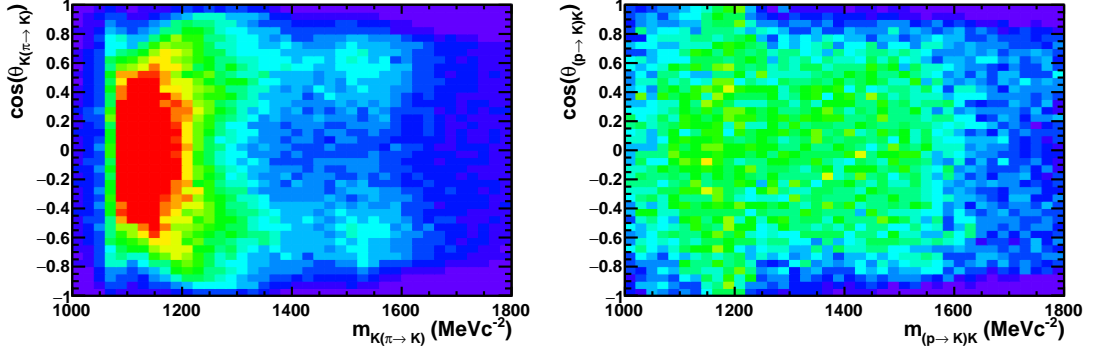
Figure 4.10: *Projection in the $(m_{\mathrm{KK}}, cos(\theta_{\mathrm{KK}}))$ plane for the reconstructed and sWeighted $B^0 \to K\pi\gamma$ candidates (left) and $\Lambda_b \to pK\gamma$ (right). The di-hadron mass and helicity are computed assigning a kaon mass to the pion (proton) candidate.*

The nominal PDF model, $\mathcal{P}$, eventually depends on 12 parameters:

- the overall normalisation yields, $\mathcal{N}_s$, $\mathcal{N}_{B^0}$ and $\mathcal{N}_{\Lambda_b}$ parametrizing the data composition.

- four relative amplitude factors $|c_R|$ ($f_2(1270)$, $f_2'(1525)$, $\phi(1680)$ and $(KK)_{\mathrm{NR}}$) with three relative phases δ_R ($f_2'(1525)$, $\phi(1680)$ and $(KK)_{\mathrm{NR}}$)), weighting the isobar amplitude model.

- the $f_2'(1525)$ Breit-Wigner mass and width parameters, $\mu_{f_2'}$ and $\Gamma_{f_2'}$, as their value reported by the Particle Data Group are presented as "educated" estimates.

Other line-shape parameters are fixed to the world average reported in Table 4.1, as well as one amplitude factor ($|c_{\phi(1020)}|=1$) and two reference phases for the odd-spin ($\delta_{\phi(1020)}=0$) and the even-spin ($\delta_{f_2'(1525)}=0$) components.
Although it is not required by the minimization process, each individual amplitude of the isobar model is normalized to unity to allow an easier interpretation of the associated amplitude factors $|c_R|$:

$$\int_{-1}^{+1} \int_{2m_{\mathrm{K}}}^{1.8\mathrm{GeV}c^{-2}} |\mathcal{A}_R(m_{\mathrm{KK}}, \theta_{\mathrm{KK}})|^2 d\phi_3(m_{\mathrm{KK}}, \theta_{\mathrm{KK}}) = 1, \qquad (4.41)$$

where $d\phi_3(m_{\mathrm{KK}}, \theta_{\mathrm{KK}}) = \mathcal{J}_3(m_{\mathrm{KK}})dm_{\mathrm{KK}}dcos(\theta_{\mathrm{KK}})$ is the phase-space volume.

4.7 Fit to data

4.7.1 Fit minimization

An unbinned extended Likelihood fit of the nominal model is applied to the data sample. The data are fitted by minimizing the negative log-Likelihood ($\mathcal{LL}$) function defined as

$$- log\mathcal{L} = - \sum_i^N \mathcal{W}_i \times log\left[\mathcal{P}_i(m_{\text{KK}}, cos(\theta_{\text{KK}}); \vec{p})\right], \tag{4.42}$$

where $\mathcal{P}_i$ is the PDF evaluated for the event i, given the set of parameters $\vec{p}$ and $\mathcal{W}_i$ is the event weight provided by the sPlot method. The PDF is implemented in the RooFit toolkit [92] and the minimization is performed using Minuit algorithm [93]. The PDFs normalization is realized with a two-dimensional analytical integration. To ensure the fit correctly converges towards the global minimum of the negative log-Likelihood, the starting value of the fit parameters are varied randomly and a large number of repeated fits to data ($\sim 10^3$) are performed.

Two quasi-degenerated minima are found in this process, with $\mathcal{LL}_{min}$ separated by less than one unit. The best-fit minimum (hereafter denoted $\mathcal{B}_0$) exhibits an unexpected large $\phi(1680)$ contribution, together with a globally destructive interference pattern. The second-best mininum (hereafter denoted $\mathcal{B}_1$), with $\Delta\mathcal{LL} = +0.78$, favours a smaller $\phi(1680)$ contribution, with overall constructive interferences. Other observed local minima of the negative log-Likelihood function are well separated ($\Delta\mathcal{LL} > 15$) from these two solutions. Except for the $\phi(1680)$ component factor, both solutions $\mathcal{B}_0$ and $\mathcal{B}_1$ converge towards almost identical parameters value.

The left side of Figure 4.11 displays the negative log-Likelihood scan of the amplitude factor $|c_{\phi(1680)}|$. An symmetrical shape is observed with two quasi-degenerated minima clearly separated. On the right side are shown the superimposed scans of the amplitude factor $|c_{f_2'(1525)}|$, performed in the vicinity of the two minima $\mathcal{B}_0$ and $\mathcal{B}_1$, respectively. The minimum is located almost at the same value of $|c_{f_2'(1525)}|$ for both scans. Similar behaviour is obtained for the other parameters of the fit.

The $\phi(1680)$ decay rate is expected to be dominated by the $\bar{K}^{*0}K$ final-state. The relative ratio:

$$\frac{\Gamma(\phi(1680) \rightarrow \bar{K}K)}{\Gamma(\phi(1680) \rightarrow \bar{K}^{*0}K)} = 0.07 \pm 0.01 \tag{4.43}$$

has been measured [94] at DM1, making unlikely a large contribution to the $K^+K^-\gamma$ final state. This presumption is also supported by the amplitude analysis of the $B_s \rightarrow J/\Psi(K^+K^-)$ decay [95] which reports the Fit-Fraction,

$$\mathcal{F}[\phi(1680)] = 3.4 \pm 0.3 \text{ (stat)} \ ^{+4.4}_{-0.3} \text{ (syst)} \ \%. \tag{4.44}$$

Additional inputs on the $B_s \rightarrow \phi(1680)\gamma$ rate could be obtained from the detailed analysis of the hadronic structure in the $B_s \rightarrow (K_S^0 K^+\pi^-)\gamma$ final-state. A preliminary selection for this decay mode at LHCb is presented in Chapter A. Extending the analysis range above
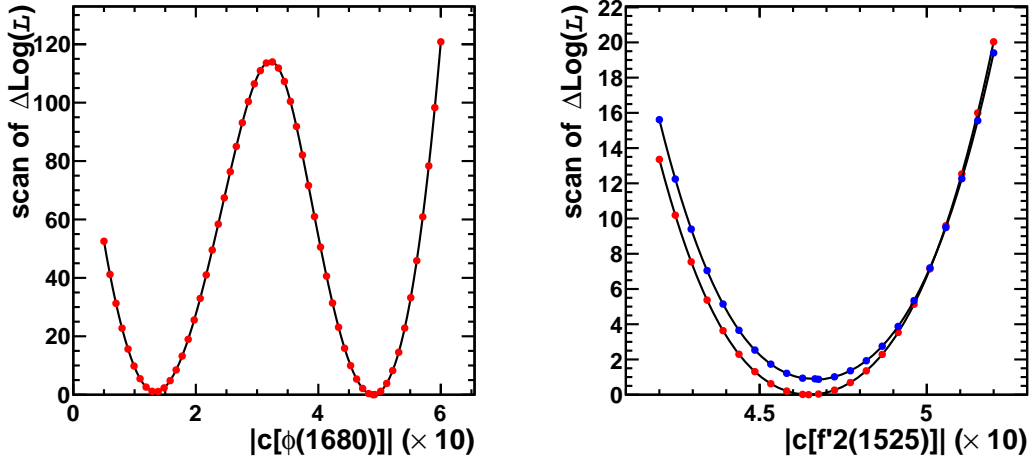
Figure 4.11: *Left: log-Likelihood scan of the $|c_{\phi(1680)}|$ parameter. The best-fit minimum, $\mathcal{B}_0$, is found near $|c_{\phi(1680)}| \times 10 \sim 5$. The second minimum, $\mathcal{B}_1$, ($\Delta\mathcal{LL} = +0.78$), is found at $|c_{\phi(1680)}| \times 10 \sim 1.2$. Right: log-Likelihood scans of the $|c_{f_2'(1525)}|$ parameters performed in the vicinity of $\mathcal{B}_1$ (red points) and $\mathcal{B}_0$ (blue points). The minimum of both scans is located around the same value $|c_{f_2'(1525)}| \times 10 \sim 4.6$. Similar behaviour is observed when projecting the log-Likelihood on the other fit parameters.*

the charm threshold could also improve the constraint on the heavy $\phi(1680)$.

In the current state, however, no clear statement on the $\phi(1680)$ contribution can be derived from our amplitude fit, given the statistical proximity of the two $\mathcal{LL}$ minima. Still, the contribution from the $f_2'(1525)$ can be studied, as the two fit solutions lead to an almost degenerated value.

The fit model projected on the two observables m_{KK} and $cos(\theta_{\text{KK}})$ is displayed on the Figure 4.12 for the solution $\mathcal{B}_1$. The global PDF is represented by the blue solid curve, the red points with error-bars are the data. The $B_s \to K^+K^-\gamma$ PDF contribution is indicated by the red solid curve, while the purple and the green solid curves represent the misidentified $\Lambda_b \to pK^-\gamma$ and $B^0 \to K^+\pi^-\gamma$ backgrounds[‡], respectively. The dashed curves represent the individual component contributions to the (KK) amplitude: $\phi(1020)$ (red), $f_2(1270)$ (green), $f_2'(1525)$ (purple), $\phi(1680)$ (light blue) and non-resonant (dark blue). The dashed grey curve is the integrated interference contribution.

Similar projections for the solution $\mathcal{B}_0$ are shown on the Figure 4.13.

[‡]The small peaking structure visible at the $\phi(1020)$ mass in the data-driven background model is due to $B_s \to \phi\gamma$ events passing the pK or $K\pi$ PID criteria, and thus contaminating at the few percent level the $\Lambda_b \to pK^-\gamma$ and the $B^0 \to K^+\pi^-\gamma$ samples that are used to build the background PDFs. This structure, that represents a negligible fraction of the actual $\phi(1020)$ signal has no impact on the fit result.
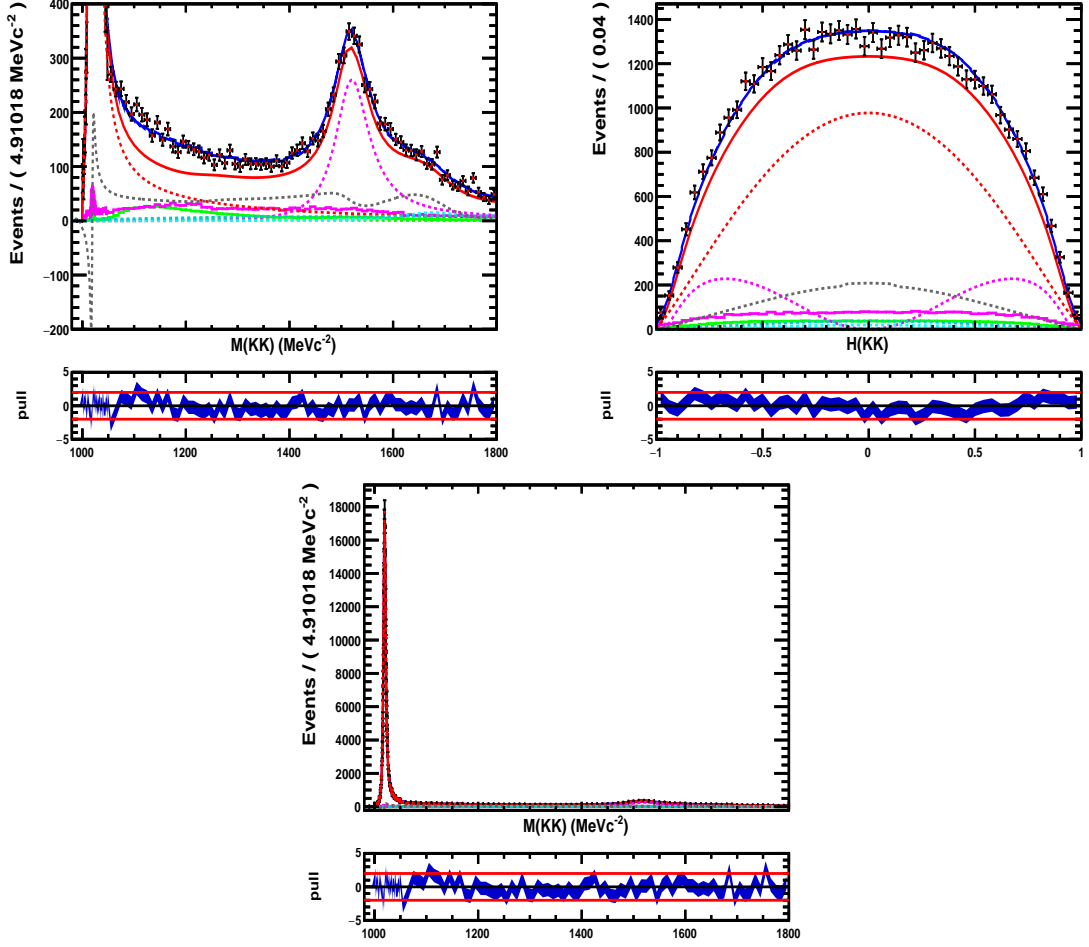
Figure 4.12: *One-dimensional projection of the nominal fit on the observables m_{KK} (top left with zoom, and bottom) and $\cos(\theta_{KK})$ (top right), for the second log-Likelihood minimum $\mathcal{B}_1$ with $\Delta\mathcal{LL}=+0.78$. Red points with error-bars are the data, the blue solid curve represents the global PDF model (see text for details on the different contributions to the model). An adaptative binning is applied on the m_{KK} observable, with a finer granularity in the region of the narrow $\phi(1020)$. The corresponding 2D Poisson likelihood χ^2 per degree of freedom is $\chi^2/_{dof}=1.22$.*

4.7.2 Data composition and Fit-Fractions

The data composition is given by the yield parameters $\mathcal{N}$, associated to the normalized PDFs. The same values are obtained for the two fit minima, they are reported in Table 4.3. The measured relative contaminations from the cross-feed backgrounds are consistent with the MC expectation discussed in Section 3.9.

The individual contribution of the component R to the $KK\gamma$ amplitude model is

123
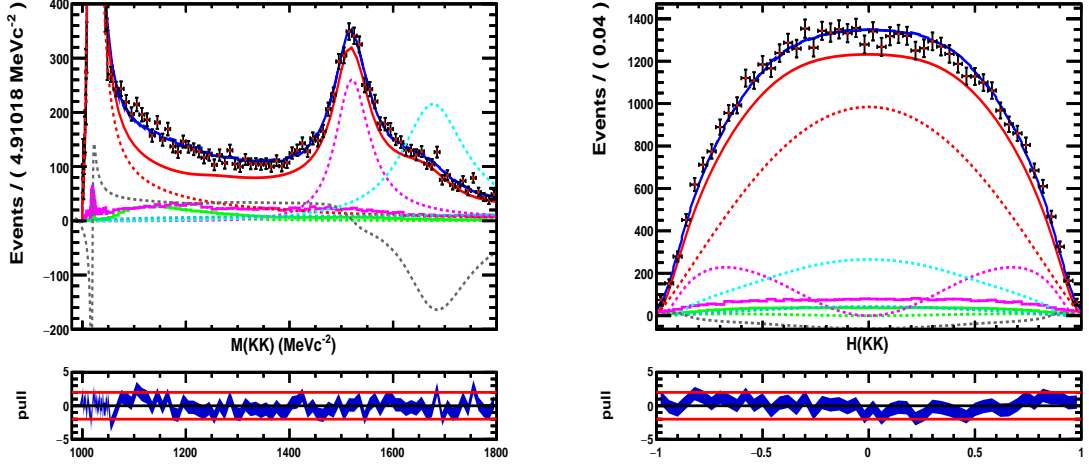
Figure 4.13: *One-dimensional projection of the nominal fit on the observables m_{KK} (left) and $\cos(\theta_{\text{KK}})$ (right), for the log-Likelihood minimum $\mathcal{B}_0$. Red points with error-bars are the data, the blue solid curve represents the global PDF model (see text for details on the different contributions to the model). An adaptive binning is applied on the m_{KK} observable, with a finer granularity in the region of the narrow $\phi(1020)$. The corresponding 2D Poisson likelihood χ^2 per degree of freedom is $\chi^2/_{\text{dof}}=1.22$.*

contribution	Yield ($\times 10^3$)	contamination $\mathcal{N}_{\text{BKG}}/\mathcal{N}_s$ (%)
$B_s \to K^+ K^- \gamma$ signal ($\mathcal{N}_s$)	44.6 ± 0.4	-
$B^0 \to K^+ \pi^- \gamma$ bkg ($\mathcal{N}_{B^0}$)	1.5 ± 0.2	3.3 ± 0.5
$\Lambda_b \to p K^- \gamma$ bkg ($\mathcal{N}_{\Lambda_b}$)	3.1 ± 0.3	7.1 ± 0.7

Table 4.3: *PDF component yields and relative background contamination from the fit.*

measured by defining the Fit-Fractions:

$$\mathcal{F}_R = \frac{\int_{-1}^{+1} \int_{2m_{\text{K}}}^{1.8\text{GeVc}^{-2}} |c_R \times \mathcal{A}_R(m_{\text{KK}}, \theta_{\text{KK}})|^2 d\phi_3(m_{\text{KK}}, \theta_{\text{KK}})}{\int_{-1}^{+1} \int_{2m_{\text{K}}}^{1.8\text{GeVc}^{-2}} |\sum_k c_k \times \mathcal{A}_k(m_{\text{KK}}, \theta_{\text{KK}})|^2 d\phi_3(m_{\text{KK}}, \theta_{\text{KK}})}, \tag{4.45}$$

where $d\phi_3(m_{\text{KK}}, \theta_{\text{KK}}) = \mathcal{J}_3(m_{\text{KK}}) dm_{\text{KK}} d\cos(\theta_{\text{KK}})$ is the phase-space volume.

The measured Fit-Fractions and relative Fit-Fractions normalized to the $\phi(1020)$ are given in Table 4.5 for the fit solution $\mathcal{B}_1$, together with the amplitude factors moduli and phases. The Fit-Fractions for the best-fit solution $\mathcal{B}_0$ are given in Table 4.4. Only the $\phi(1680)$ parameters differ significantly. The quoted errors are the statistical uncertainties returned by the fit minimizer. The reliability of their evaluation is discussed in the next section.

Eventually, the fitted mass and width parameters for the $f_2'(1525)$ Breit-Wigner are

component	Fit-Fraction (%)	relative Fit-Fraction (%)	phase (rad)	$|c_R|$
$\phi(1020)$	69.2±0.6	100	0 (fixed)	1 (fixed)
$f_2(1270)$	0.5±0.2	0.7±0.2	-2.40±0.44	0.086±0.014
$f_2'(1525)$	15.0±0.8	21.7±1.1	0 (fixed)	0.469±0.015
$\phi(1680)$	1.2±0.2	1.7±0.2	2.46±0.18	0.132±0.009
$(KK)_{\rm NR}$	2.3±0.3	3.3±0.4	-3.13±0.32	0.183±0.011
$\int$ interference	11.8			

Table 4.4: *(relative) Fit-Fractions and isobar parameters for the fit solution $\mathcal{B}_1$*

component	Fit-Fraction (%)	relative Fit-Fraction (%)	phase (rad)	$|c_R|$
$\phi(1020)$	69.7±0.6	100	0 (fixed)	1 (fixed)
$f_2(1270)$	0.5±0.2	0.8±0.2	-2.40±0.44	0.086±0.014
$f_2'(1525)$	15.0±0.8	21.5±1.1	0 (fixed)	0.467±0.016
$\phi(1680)$	16.9±0.5	24.3±0.7	-1.74±0.13	0.493±0.007
$(KK)_{\rm NR}$	2.6±0.4	3.8±0.6	-2.96±0.23	0.194±0.015
$\int$ interference	-4.8			

Table 4.5: *(relative) Fit-Fractions and isobar parameters for the fit solution $\mathcal{B}_0$*

measured identically for both fit minima as:

$$\mu_{f_2'} = (1524.3 \pm 1.1)\text{MeVc}^{-2}, \qquad (4.46)$$
$$\Gamma_{f_2'} = (81.0 \pm 2.5)\text{MeVc}^{-2}, \qquad (4.47)$$

in very good agreement with the measurement done in the $B_s \to J/\Psi(K^+K^-)$ amplitude analysis at LHCb [95] and the other subset of measurements based on the $f_2'(1525)$ tensor produced in e^+e^- annihilation and particles decays, as listed by the Particle Data Group [7].

4.7.3 Statistical resolution

The statistical resolution on the fit parameters has been studied using toys experiments. Large number (N=3.6×10^3) of toys data have been generated according to the two best-fit parametrizations with an event yield consistent with the real data sample. Each toys sample has been fitted using the corresponding amplitude model. The dispersion of the fit parameters are compared with the statistical uncertainty returned by the fit minimizer. As illustration, the Pull distributions of the amplitude factors are shown on Figure4.14 for the fit solution $\mathcal{B}_1$. Slightly non-gaussian profiles are observed for several parameters, with a an overestimated statistical error, on the conservative side.

The two-sided statistical intervals corresponding to 68.3%, 95.5% and 99% of the toys population are derived from the relative Fit-Fractions distributions displayed on Figure 4.15, and are reported in Table 4.6.

R	fit value (%)	toys 1σ interval	toys 2σ interval	toys 3σ interval
$f_2(1270)$	0.8 ± 0.2	$0.8^{+0.2}_{-0.2}$	$0.8^{+0.6}_{-0.3}$	$0.8^{+1.0}_{-0.5}$
$f'_2(1525)$	21.7 ± 1.1	$21.8^{+0.8}_{-0.8}$	$21.8^{+2.0}_{-2.0}$	$21.8^{+3.1}_{-2.9}$
$\phi(1680)$	1.7 ± 0.2	$1.8^{+0.2}_{-0.2}$	$1.8^{+0.5}_{-0.4}$	$1.8^{+0.8}_{-0.6}$
$(KK)_{\mathrm{NR}}$	3.3 ± 0.4	$3.3^{+0.7}_{-0.6}$	$3.3^{+2.0}_{-1.1}$	$3.3^{+3.4}_{-1.3}$

Table 4.6: *One σ statistical interval on the relative Fit-Fractions as returned by the fit minimizer (1st column), compared to the the one,two and three σ intervals evaluated from toys experiments.*
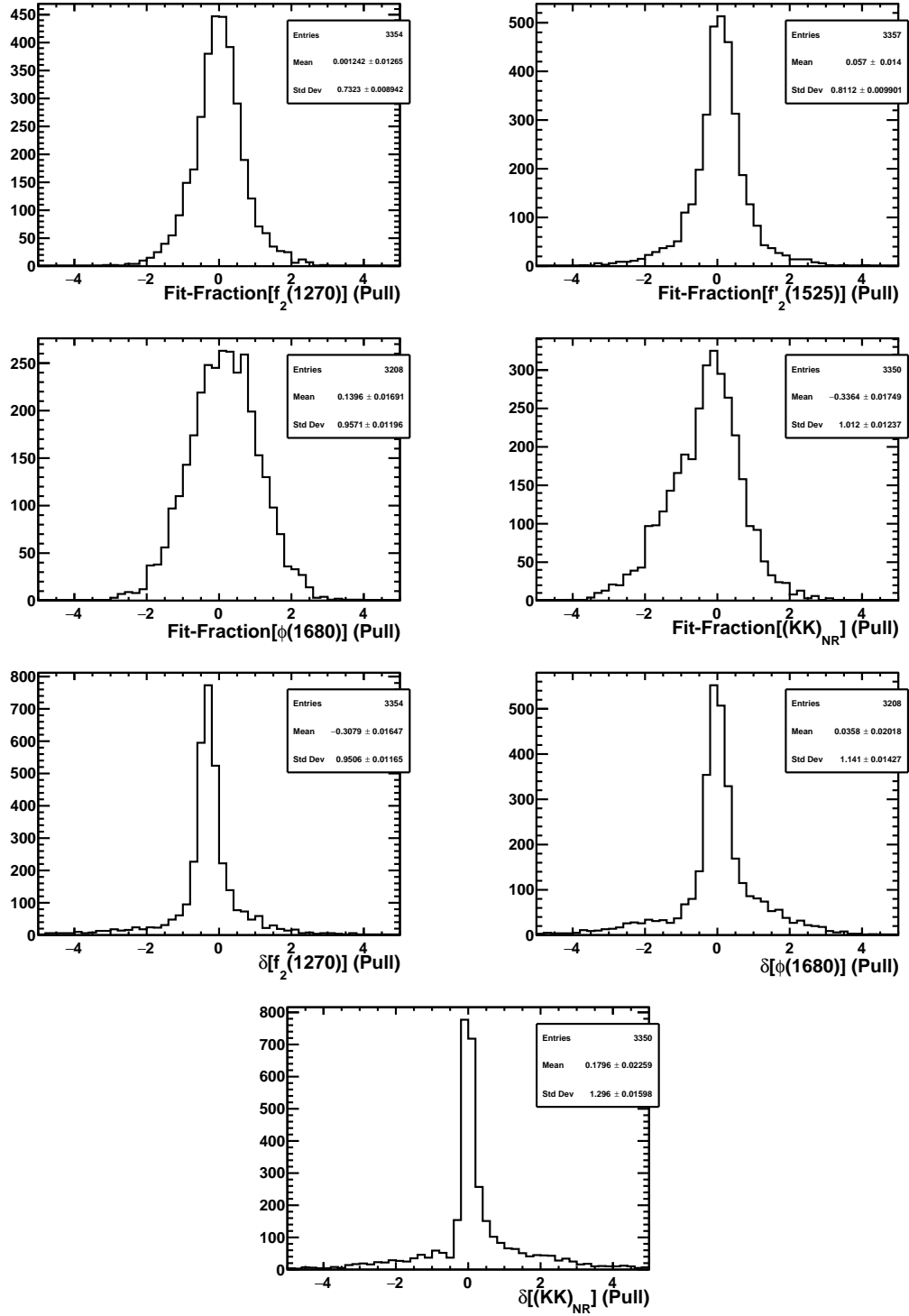
Figure 4.14: *Pull distributions of the moduli and the phases of the complex amplitude coefficients c_R for the model components from 3.6×10^3 toy experiments produced according to the $\mathcal{B}_1$ minimum.*

127
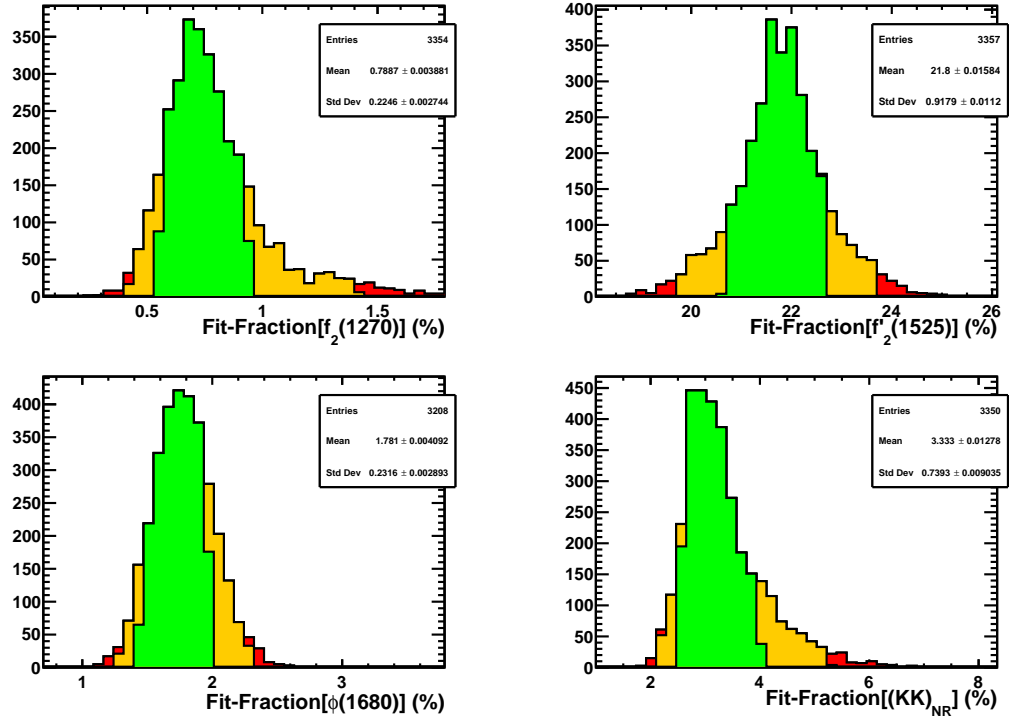
Figure 4.15: *Distributions of the relative Fit-Fraction normalized to $\phi(1020)$, for $f_2(1270)$ (top left), $f'_2(1525)$ (top right), $\phi(1680)$ (bottom left) and Non-Resonant (KK) (bottom right) from 3.6×10^3 toy experiments produced according to the $\mathcal{B}_1$ minimum. The one, two and three σ asymmetric intervals, containing 68.27%, 95.45% and 99.73% of the toy population, respectively, are indicated.*

4.8 Systematic uncertainties

Several sources of systematic uncertainties have been investigated and are discussed in this section. The various systematic effects have been studied in the vicinity of both the quasi-degenerated minima of the amplitude fit. The corresponding uncertainties are very similar for both fit solutions and, unless stated otherwise, we report here only the systematics corresponding to the second best minimum, $\mathcal{B}_1$. To avoid the large processing time in repeated fits, most of the systematic effects have been evaluated with the mass and the width of the $f_2'(1525)$ line-shape fixed to its best fit value given in Equation 4.46 and 4.47. It has been checked that the nominal fit results and the statistical errors are unaffected when those parameters are fixed.

The preliminary (and sometimes incomplete) budget of systematic errors is summarized in Table 4.7. Details are discussed in the following subsections.

σ_{syst} (%)	$\mathcal{F}_{\phi(1020)}$	$\mathcal{F}_{f_2(1270)}$	$\mathcal{F}_{f_2'(1525)}$	$\mathcal{F}_{\phi(1680)}$	$\mathcal{F}_{(KK)_{\mathrm{NR}}}$	$\mathcal{F}_{f_2'(1525)}/\mathcal{F}_{\phi(1020)}$
Acc. (MC stat.)	± 0.56	± 0.03	± 0.30	± 0.05	± 0.11	± 0.60
Acc. (MC weights)	$+0.25$	$+0.01$	$+0.33$	$+0.01$	-0.14	$+0.39$
Acc. (Run 1/Run 2)	-0.48	-0.01	$+0.13$	-0.02	$+0.17$	$+0.34$
hhπ^0 background	-0.38	$+0.01$	$+0.10$	$+0.02$	$+0.10$	$+0.27$
Heavy resonances	$+0.16$	$+0.14$	$+0.80$	$+0.04$	-0.03	$+1.12$
total	$+0.63 \atop -0.83$	± 0.14	$+0.93 \atop -0.30$	$+0.07 \atop -0.05$	$+0.22 \atop -0.18$	$+1.40 \atop -0.60$

Table 4.7: *Summary of the systematics uncertainties affecting the measured Fit-Fractions. The overal asymmetrical uncertainty is obtained by summing quadratically the negative and positive contributions, separately. The last column gives the error budget for the ratio of Fit-Fractions* $\mathcal{F}_{f_2'(1525)}/\mathcal{F}_{\phi(1020)}$

The dominant contributions to the overall systematic error are due to the acceptance definition and the possible contribution from heavy and wide (KK) resonances above the analysis threshold. Increasing the size of the MC samples and extending the analysis at higher mass could help to reduce these uncertainties.

4.8.1 Acceptance systematics

As discussed in Section 4.5, the 2D acceptance $\varepsilon(m_{\mathrm{KK}}, cos(\theta_{\mathrm{KK}}))$, is modelled with a 10-parameters function adjusted from a fit to large samples of reweighted MC data. The various sources of acceptance-related systematics are discussed below.

4.8.1.1 Systematics due to the MC statistics

The statistical resolution on the acceptance parameters, reported in Table 4.8, is limited by the size of the simulated samples. In particular, the phase-space $B_s \rightarrow KK\gamma$ MC sample, that gives a direct access to the acceptance shape when corrected from the phase-space

volume, is by nature limited by the small efficiency of the analysis selection restricted to the low-mass region. Larger-efficiency MC samples, $B_s \to \phi\gamma$ and $B_s \to f_2'\gamma$, are added to increase the overall statistics, requiring an unbiased modelisation of the simulated shape for the intermediate resonances. The impact of the limited acceptance resolution due to the MC statistics is evaluated by repeating the amplitude fit and varying the acceptance parameters within their statistical uncertainties. The 10×10 covariance matrix returned by the MC acceptance fit is used to generate 3.6×10^3 gaussianly distributed sets of correlated parameters, that are applied to refit the data. The obtained Fit-Fractions distributions are reasonably consistent with a gaussian profile, as displayed on Figure 4.16. The corresponding gaussian resolutions, reported in Table 4.8, are added to the systematics budget. This uncertainty can be reduced with an increased MC statistics for the acceptance determination.
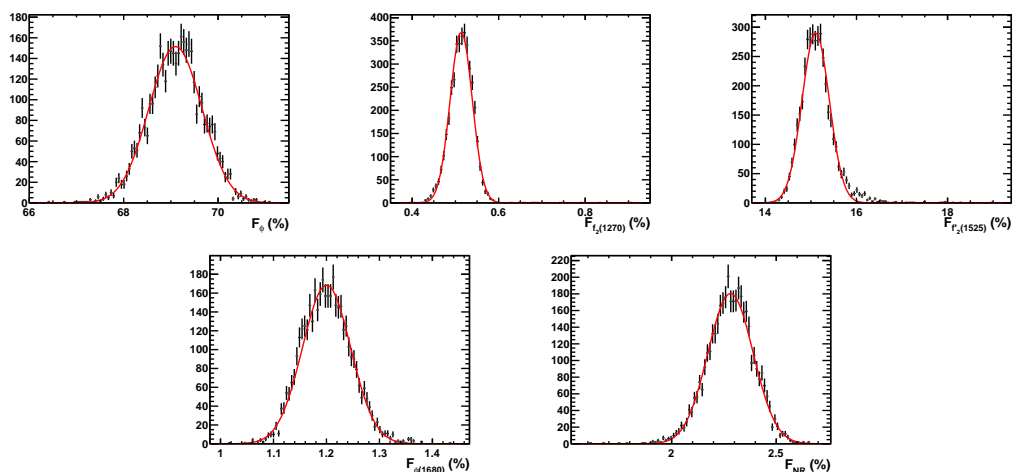
Figure 4.16: *Distribution of the amplitude Fit-Fractions when the acceptance parameters are varied wihtin their statistical uncertainty (3.6×10^3 fits).*

(KK) state	$\sigma(\mathcal{F}_R)$ (%)	$\sigma(\mathcal{F}_R/_{\mathcal{F}_\phi})$ (%)
$\phi(1020)$	± 0.56	-
$f_2(1270)$	± 0.03	± 0.04
$f_2'(1525)$	± 0.30	± 0.60
$\phi(1680)$	± 0.05	± 0.08
$(KK)_{\mathrm{NR}}$	± 0.11	± 0.18

Table 4.8: *Systematic uncertainty on the Fit-Fractions (left column) and relative Fit-Fractions (right column) due to the limited MC statistics in the evaluation of the acceptance.*

4.8.1.2 Systematics due to the MC reweighting

To account for the possible imperfection in the data simulation, the MC events used to extract the acceptance shape are reweighted. Difference in the distributions for neutral and charged PID variables, IsPhoton and ProbNN, respectively, are corrected using the dedicated calibration tools discussed in Section 3.6. The kinematical and topological variables used in the BDT selection are globally corrected according to the multidimensional GB-reweighting procedure presented in Section 3.7. An event-by-event combined weight, $\mathcal{W} = \mathcal{W}_{\gamma-ID} \times \mathcal{W}_{K-ID} \times \mathcal{W}_{GB}$, is applied to the MC data entering the acceptance fit. The individual contribution of each of those weights has been studied by extracting alternative acceptance parametrizations with a partial MC reweighting. The impact of the partial reweighting on the measured $\phi(1020)$ and $f'_2(1525)$ (relative) Fit-Fractions is reported on Table 4.9.

$\mathcal{W}_X$	$\Delta\mathcal{F}_\phi$	$\Delta\mathcal{F}_{f'_2}$	$\Delta(\mathcal{F}_{f'_2}/\mathcal{F}_\phi)$	$\Delta\mathcal{F}_\phi$	$\Delta\mathcal{F}_{f'_2}$	$\Delta(\mathcal{F}_{f'_2}/\mathcal{F}_\phi)$
	removing $\mathcal{W}_X$ (%)			applying only $\mathcal{W}_X$ (%)		
neutral PID: $\mathcal{W}_{\gamma-ID}$	+0.08	-0.15	-0.24	-0.87	+0.77	+1.40
charged PID: $\mathcal{W}_{K-ID}$	+0.06	+0.13	+0.18	-0.91	+0.52	+1.05
kinematics :$\mathcal{W}_{GB}$	-0.90	+0.57	+1.11	+0.27	-0.03	-0.13

Table 4.9: *Variation of $\phi(1020)$ and $f'_2(1525)$ Fit-Fractions using an alternative acceptance parameterizations extracted with partial MC reweighting. The left part of the table indicates the Fit-Fraction shift when the individual weight $\mathcal{W}_X$ is removed and the right columns indicate the shift when only this individual weight is applied.*

As can be seen, both the neutral and charged PID reweighting have a limited impact on the acceptance definition, each of them inducing a small (and opposite) shift on the relative $f'_2(1525)$ Fit-Fraction of about 0.2%. The systematic uncertainty on the event weight can be derived from the PID calibration tools and propagated to the measured fit-fractions. This evaluation has not been done so far, however the corresponding impact is expected to be negligible regarding the overall effect of the PID reweighting.
A larger impact on the acceptance is observed from the kinematics MC correction embedded in the global GB-weights, that account for $\sim 1\%$ in the relative $f'_2(1525)$ Fit-Fraction, i.e. as large as its statistical resolution. As discussed in Section 3.7, the GB-weights aim at globally reweighting the MC data using a BDT multivariate method and taking into account the variable correlations. The performance of this tool is not perfect in all the multivariate dimensions. Moreover, the photon kinematics that might be affected by some imperfection in the L0 trigger simulation is not accounted for in the GB weighting. Furher investigations, still to be performed, are needed to precisely estimate the impact of the imperfect MC simulation of kinematical quantities on the 2D acceptance. A prelimary and incomplete evaluation of this effect is done by replacing the multidimensional GB-weight in the acceptance determination with the one-dimensional weights based on the B transverse momentum and the long track multiplicity distributions, $\mathcal{W}_{B_PT} \times \mathcal{W}_{Ntracks}$, that both are

known to be poorly reproduced in the MC simulation. The corresponding one-dimensional weights are obtained by comparing the sWeighted data distributions in the ϕ region with the distribution from the $B_s \to \phi\gamma$ MC sample. The induced Fit-Fractions shifts, $\Delta\mathcal{F}_R$, are reported in Table 4.10.

Interpreting $\Delta\mathcal{F}_R$ as the one-sided range for uniformly distributed Fit-Fraction, the asymmetrical systematic uncertainty, $\sigma_{\mathcal{F}_R} = \Delta\mathcal{F}_R/\sqrt{3}$, corresponding to the 68% confidence interval, is added to the systematics budget.

component	$\Delta\mathcal{F}_R$ (%)	$\Delta(\mathcal{F}_R/_{\mathcal{F}_\phi})$ (%)
$\phi(1020)$	+0.44	-
$f_2(1270)$	+0.02	+0.02
$f_2'(1525)$	+0.58	+0.68
$\phi(1680)$	≤ 0.02	+0.02
$(KK)_{\mathrm{NR}}$	-0.24	-0.42

Table 4.10: *Variation of the Fit-Fractions (left) and relative Fit-Fractions (right) when changing the nominal MC acceptance reweighting based on the multidimensional GB method with the one-dimensional weights based on the B transverse momentum and the track multiplicity.*

4.8.1.3 Acceptance variation with run

The MC acceptance is extracted by combining the various simulated samples configured to reproduce each year of data taking. Difference in the acceptance due to the different energy and trigger configuration between Run 1 and Run 2 has been studied by separating the two sets of data and performing a simultaneous fit of the two samples. A different acceptance parametrization is extracted for each of the two periods, as well as a different contamination map for the cross-feed backgrounds due to the misidentified $B^0 \to K^+\pi^-\gamma$ and $\Lambda_b \to pK^-\gamma$ decays. Both data samples are modelled using the same isobar parameters, while the overal signal and backgrounds yield parameters are free to vary independantly for the two periods.

The projection of the simultaneous amplitude fit on the two samples is displayed on fig 4.17. The signal and bakground yields returned by the simultaneous fit are reported on Table 4.11. The relative background contamination is in reasonable agreement with the expectation for both periods.

period	$\mathcal{N}_s \times 10^3$	$\mathcal{N}_{\mathrm{BKG}}(K\pi_{\to K}\gamma) \times 10^3$ (rel.)	$\mathcal{N}_{\mathrm{BKG}}(p_{\to K}K\gamma) \times 10^3$ (rel.)
Run 1	5.4 ± 0.1	0.2 ± 0.1 $(4.1 \pm 1.1$ %)	0.4 ± 0.1 $(7.6 \pm 1.2$ %)
Run 2	39.1 ± 0.3	1.5 ± 0.2 $(3.7 \pm 0.6$ %)	2.6 ± 0.3 $(6.8 \pm 0.7$ %)

Table 4.11: *Signal and background yields from the simultaneous fit of Run 1 and Run 2 data.*
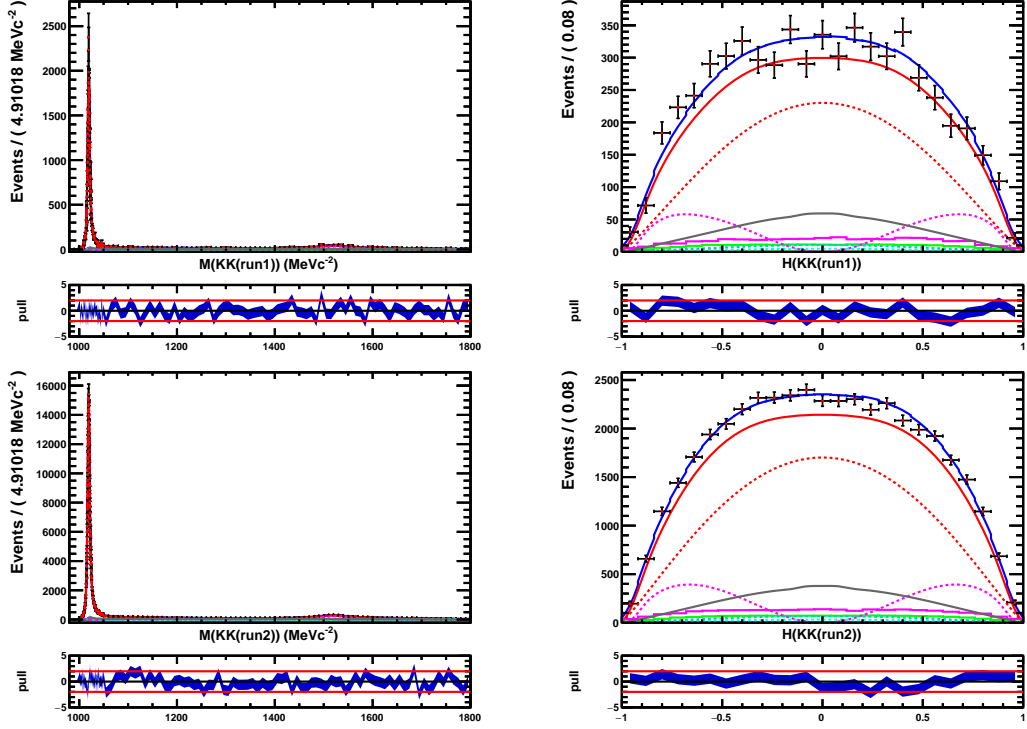
Figure 4.17: *Projection of the simultaneous fit of Run 1 (top) and Run 2 (bottom) data on the m_{KK} observable (left) and $cos(\theta_{KK})$ observable (right).*

The Fit-Fractions obtained from the simultaneous fit are consistent with those of the nominal fit, within the uncertainties due to the limited MC statistics on the acceptance determination. The Fit-Fraction difference, $\Delta\mathcal{F}_R$, between the two approaches are reported in Table 4.12. Assuming the Fit-Fractions are uniformly distributed in the one-sided $\Delta\mathcal{F}_R$ ranges, the corresponding asymmetrical systematic uncertainties, defined as $\sigma_{\mathcal{F}_R} = \Delta\mathcal{F}_R / \sqrt{3}$, are added to the systematics budget.

component	$\Delta(\mathcal{F}_R)$ (%)	$\Delta(\mathcal{F}_R/\mathcal{F}_\phi)$ (%)
$\phi(1020)$	-0.83	-
$f_2(1270)$	-0.02	-0.02
$f_2'(1525)$	+0.22	+0.59
$\phi(1680)$	-0.04	+0.04
$(KK)_{\mathrm{NR}}$	+0.29	+0.48

Table 4.12: *Fit-Fraction (left) and relative Fit-Fraction (right) difference between the Run 1/Run 2 simultaneous fit and the combined nominal fit.*

4.8.2 PDF model systematics

The amplitude analysis is performed on the selected $KK\gamma$ candidates, with a a statistical subtraction of the combinatorial and the partially reconstructed backgrounds using the sPlot method that relies on the correct modelisation of the $KK\gamma$ mass distribution. The PDF model used for the subsequent amplitude fit assumes the unsubtracted residual backgrounds are dominated by the misidentified $B^0 \to K^+\pi^-\gamma$ and $\Lambda_b \to pK^-\gamma$ decays. Other peaking backgrounds from $hh\pi^0$ decays that might contaminate the $KK\gamma$ sample are neglected. In addition, the signal PDF assumes an equal decay rate for B_s and $\bar{B}_s$ decays, leading to an exact cancellation of the interferences between odd-spin and even-spin components in the amplitude model. These asumptions are questioned below.

4.8.2.1 Effect of $B_s/\bar{B}_s$ decay asymmetry

The effect of the $B_s/\bar{B}_s$ production asymmetry expected at the 1% level at LHC, is diluted to a negligible level when integrating the decay rate over time, thanks to the fast B_s oscillation. Moreover, as the $K^+K^-\gamma$ final-state is symmetrical, any charge-dependent asymmetry in the kaon detection is expected to cancel out and could only generate an helicity-dependent effect at high (KK) mass if the detection asymmetry is significantly varying with the kaon momentum. Large physical $\mathcal{CP}$-asymmetry is also unexpected in the penguin-dominated $B_s \to K^+K^-\gamma$ transition. To test the $B_s/\bar{B}_s$ symmetry asumption, the nominal fit is repeated allowing $\mathcal{N}_{B_s}$ and $\mathcal{N}_{\bar{B}_s}$ to vary independantly. In addition, the reference phase for the even-spin states, which is fixed to 0 for the $f_2'(1525)$ in the nominal fit, is allowed to vary to account for the non-exact cancellation of the interference between odd and even spin resonances.

The projection of the fit on the $cos(\theta_{KK})$ observable is displayed on Figure 4.18 where a slight (statistically non-significant) asymmetry is nearly visible. The $B_s/\bar{B}_s$ decay asymmetry is measured to:

$$a = \frac{\mathcal{N}_{\bar{B}_s} - \mathcal{N}_{B_s}}{\mathcal{N}_{\bar{B}_s} + \mathcal{N}_{B_s}} = (3 \pm 2) \times 10^{-2}, \tag{4.48}$$

consistent with no asymmetry within 1.5 standard deviations. The impact on the Fit-Fractions that does not exceed 0.1% is neglected.

4.8.2.2 Effect of neglected $hh\pi^0$ backgrounds

The contribution of the charmless $h^+h^-\pi^0$ decays, misidentified as $K^+K^-\gamma$, is neglected in the nominal fit. The corresponding contamination, roughly estimated at the level of 0.5% (see Section 3.9), is however affected by large uncertainties, as the resonant structure of this final state is poorly known, in particular in the B_s decay. The signal most similar final state, $B_s \to \phi\pi^0$, with a predicted branching fraction of $\mathcal{B} \sim 10^{-7}$ leads to an expected negligible contamination of $\sim$0.1%. Possible contamination from the $B^0 \to K^+\pi^-\pi^0$ decay, with a measured branching fraction as large as the signal, $\mathcal{B} = (3.8 \pm 0.3)10^{-5}$, and amplified by the larger hadronization factor to B^0, is however strongly reduced due
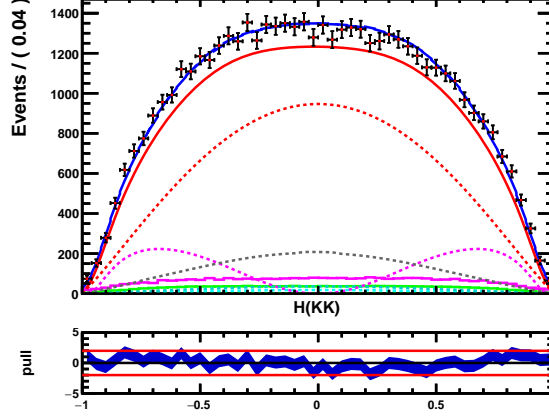
Figure 4.18: *Projection on $\cos(\theta_{KK})$ of the fit with $B_s/\bar{B}_s$ asymmetry allowed.*

to the double misidentification and to the "anti-charm" cuts $m_{h^{\pm}\pi^0} > 2~GeVc^{-2}$ that reject the dominant $K^{*+}\pi^-$ and $K^+\rho^-$ intermediate states. The residual contamination due to the color-suppressed $B^0 \to K^{*0}\pi^0$ transition, $\mathcal{B} = (3.3 \pm 0.6)10^{-6}$, is evaluated at the level of 0.2%. Eventually, Belle reported an evidence for a relatively large branching fraction for the $B^0 \to K^+K^-\pi^0$ decay: $\mathcal{B} = (3.3 \pm 0.6)10^{-6}$. As for $B^0 \to K^+\pi^-\pi^0$, the $K^{*\pm}K^{\mp}$ components are rejected by the anti-charm cuts, but the unknown S-wave $(K^+K^-)\pi^0$ contribution, through for instance $B^0 \to f^0\pi^0$, might significantly contaminate the $(K^+K^-)\gamma$ sample.

The impact of the neglected background from charmless decays with misidentified π^0 has been checked assuming different resonance models for the $KK\pi^0$ contamination,

1. a Vector-Scalar model based on $\phi\pi^0$.

2. a resonant S-wave model based on $f^0\pi^0$.

3. a non-resonant S-wave model $(KK)_{NR}\pi^0$.

The corresponding Probability Density Functions, are built applying the same acceptance as for the $KK\gamma$ final-state. Breit-Wigner shapes are used to describe the ϕ and the f^0 line-shapes. The angular dependencies are based on the relevant Wigner d-functions, d^1_{00} for the vector-scalar model and $d^0_{00} = 1$ for the S-wave models. The yield of $KK\pi^0$ background, allowed to vary freely in the fit, is reported in Table 4.13 for the three models. Adding, either $f^0\pi^0$ or $\phi\pi^0$ component in the background model improves the fit quality. The largest background contamination, $(2.8 \pm 0.2)\%$, is found for the $f^0\pi^0$ hypothesis. The corresponding Fit-Fraction shifts are reported in Table 4.14. Corresponding asymmetrical uncertainties, defined as $\sigma_{\mathcal{F}_R} = \Delta\mathcal{F}_R/\sqrt{3}$, are added to the systematics budget to account for the unknown π^0 contamination.

$KK\pi^0$ model	$\mathcal{N}_{KK\pi^0}$ ($\times 10^3$)	Contamination $\mathcal{N}_{KK\pi^0}/\mathcal{N}_s$	$\Delta\mathcal{LL}$
$\phi\pi^0$	0.39 ± 0.08	0.9 ± 0.2 %	-19.7
$f^0\pi^0$	1.26 ± 0.21	2.8 ± 0.2 %	-25.1
$(KK)_{\mathrm{NR}}\pi^0$	0.00 ± 0.03	≤ 0.2 % (95% CL)	0

Table 4.13: *Contamination from the $KK\pi^0$ background with different resonant models. The negative log-Likelihood gain is reported in the last column to indicate the fit quality improvement.*

component	$\Delta\mathcal{F}_R$ (%)	$\Delta(\mathcal{F}_R/\mathcal{F}_\phi)$ (%)
$\phi(1020)$	-0.65	-
$f_2(1270)$	+0.01	+0.03
$f_2'(1525)$	+0.17	+0.46
$\phi(1680)$	+0.03	+0.06
$(KK)_{\mathrm{NR}}$	+0.18	+0.29

Table 4.14: *Variation of the Fit-Fractions (left) and the relative Fit-Fractions (right) when a $f^0\pi^0$ contribution is included in the background model.*

4.8.2.3 B_s mass model and background subtraction

Combinatorial $KK\gamma$ and partially reconstructed $B \to KK\gamma(X)$ backgrounds are statistically subtracted using the sPlot method applied to the reconstructed invariant-mass $m(KK\gamma)$. Several parameters are fixed to their simulated values in the mass model used to extract the sWeights. In particular, the Cristal-Ball tail parameters for the B_s signal distribution might be affected by the unsubtracted peaking backgounds, accounted for in the subsequent amplitude fit. Similarly, several assumptions are made to build the mass shape of the different background contributions. A full systematical study of the $KK\gamma$ mass model, and its impact on the sWeighted amplitude fit, is still to be performed. Preliminary checks have been done by changing the B_s tail parameters, as well as the parametrisation of the partially reconstructed background $B \to KK\gamma(\pi)$, using the combined data set from Run 1 and Run 2 instead of the nominal year-dependent parametrisation. Negligible impact is observed on the amplitude fit result. Further investigations of the impact of the $m(KK\gamma)$ mass impact is in progress.

4.8.3   Amplitude model

As discussed in Section 4.3, the angular momentum in the radiative B decay to a J_R-spin state can take both $L_B = J_R \pm 1$ values. The amplitude fit is performed by applying the lowest value $J_R - 1$. Repeating the fit with $L_B = J_R + 1$ leads to negligible effect on the Fit-Fractions and no associated systematics is added to the uncertainty budget.
On another hand, the isobar $B_s \to KK\gamma$ amplitude has been limited to the known (KK) resonant states having their pole mass in the selection range, $m_{\mathrm{KK}} < 1.8$ GeVc^{-2}. Heavier

and wide resonances, that are neglected in the model, might however have an impact in the analysis region. The amplitude fit has been repeated adding coherently each of the confirmed (KK) states above the mass threshold in the isobar sum, namely: $\phi_3(1850)$, $f_2(1950)$, $f_2(2010)$ and $f_4(2050)$[§] resonance. While not formally listed in the confirmed states by the Particle Data Group, the $f_2(1810)$ resonance, observed at Belle with a 5.5σ significance [96] is also checked. The world average mass and width of those resonant states are reported in Table 4.15, together with their individual impact on the amplitude analysis result. A significant shift on the relative $f_2'(1525)$ Fit-Fraction is observed when adding any of this resonance. The largest effect is induced by the spin-2 states around $m_{\text{KK}} \sim 2000$ Mevc^{-2}. A corresponding asymmetrical systematic, defined as $\sigma_{\mathcal{F}_R} = \Delta\mathcal{F}_R/\sqrt{3}$, is provisionally added to the uncertainty budget. Extending the amplitude fit above the charm region would help to resolve the actual impact of the badly known wide (KK) resonances in the heavy region.

state R	μ_R (MeVc^{-2})	Γ_R (MeVc^{-2})	$\mathcal{F}_R$ (%)	$\Delta\mathcal{LL}$	$\Delta\mathcal{F}_\phi$ (%)	$\Delta\mathcal{F}_{f_2'}$ (%)	$\Delta(\mathcal{F}_{f_2'}/\mathcal{F}_\phi)$ (%)
$f_2(1810)$	1815 ± 12	197 ± 22	0.02 ± 0.04	-0.6	+0.15	+0.37	+0.48
$\phi_3(1850)$	1854 ± 7	150 ± 50	0.01 ± 0.04	-3.0	+0.36	+0.24	+0.24
$f_2(1950)$	1944 ± 12	472 ± 18	0.12 ± 0.32	-1.7	+0.27	+1.40	+1.94
$f_2(2010)$	2011^{+62}_{-76}	202^{+67}_{-62}	0.15 ± 0.28	-5.3	+0.76	+1.40	+1.75
$f_4(2050)$	2011 ± 11	237 ± 18	0.05 ± 0.03	-6.3	+0.20	+0.32	+0.39

Table 4.15: *Impact of heavy resonances on the amplitude fit. The world-average mass and width are reported in the first columns ([PDG]). The measured Fit-Fraction is given in the fourth column. The change in the $\phi(1020)$ and $f_2'(1525)$ (relative) Fit-Fractions with respect to the nominal fit are given by the last three columns. The negative log-Likelihood gain is also reported to indicate the fit quality improvement.*

4.8.4   Additional checks

The meson radius r that defines the centrifugal correction in the Blatt-Weisskopf form-factors, is usually not considered as a physical parameter, and is part of the definition of the amplitude model. The Fit-Fractions are then measured for a defined choice of this phenomenological quantity. However we aim at deriving the relative Branching-Fraction of the $B_s \to f_2'(1525)\gamma$ to the known $B_s \to \phi\gamma$ from the relative Fit-Fraction $\mathcal{F}_{f_2'}/\mathcal{F}_\phi$. Further studies have therefore been conducted to check the stability of this ratio against the variations of the nominal amplitude model.

Increasing the radius from its nominal value r=1.5GeV^{-1} (~ 0.3 fm) to r=5.0GeV^{-1} (~ 1 fm) modifies simultaneously, and in the same direction, the size of the relativistic tails of the Breit-Wigner for all the resonances entering the amplitude model. The Fit-Fraction

---

[§]The measured branching fraction, $\mathcal{B}(f_4(2050) \to K\bar{K}) = (0.68^{+0.34}_{-0.18})\%$, makes this spin-4 resonance unlikely to contribute in our final-state.

ratio, $\mathcal{F}_{f_2'}/\mathcal{F}_\phi$, is observed to vary within a $\pm0.6\%$ range. Assuming r is uniformly distributed in the defined range of variation, a corresponding symmetrical systematic uncertainty, $\sigma = \pm(0.6/\sqrt{3})\%$ is then accounted for the relative $\mathcal{F}_{f_2'}/\mathcal{F}_\phi$ ratio when it is used to derive the Branching fraction ratio.

In the same spirit, the amplitude fit has been repeated, allowing the pole-mass and the width describing each individual resonance to vary, the parameters of the Breit-Wigner describing the $f_2'(1525)$ being fixed to their best fit value. In addition, the complex phase of the non-resonant contribution $(KK)_{\mathrm{NR}}$, assumed to be constant in the nominal fit, has been allowed to vary linearly with the (KK) mass. Those model variations have a negligible impact on the $\mathcal{F}_{f_2'}/\mathcal{F}_\phi$ ratio, as reported in Table 4.16.

released parameter(s)	$\Delta\mathcal{F}_{f_2'}/\mathcal{F}_\phi$ (%)
$\phi(1020):\begin{pmatrix}\mu = & 1019.7\pm0.1\\ \Gamma = & 48.5\pm0.1\end{pmatrix}_{(\mathrm{MeVc}^{-2})}$	$+0.06$
$f_2(1270):\begin{pmatrix}\mu = & 1275.6\pm0.8\\ \Gamma = & 186.8\pm2.4\end{pmatrix}_{(\mathrm{MeVc}^{-2})}$	$+0.01$
$\phi(1680):\begin{pmatrix}\mu = & 1660\pm9\\ \Gamma = & 144\pm15\end{pmatrix}_{(\mathrm{MeVc}^{-2})}$	-0.02
$(KK)_{\mathrm{NR}}:\ \alpha_\delta = (3.3\pm0.3)\times10^{-3}\ (\mathrm{MeV}^{-1})$	-0.04

Table 4.16: *Variation of the Fit-Fraction ratio $\mathcal{F}_{f_2'}/\mathcal{F}_\phi$ when the mass and the width of each individual resonances is released in the fit. The last line gives the variation when the phase of the non-resonant KK contribution is allowed to vary linearly with the di-kaon mass. The value of the released parameter(s) as returned by the fit is indicated in the first column.*

Eventually, the stability of the amplitude fit has been checked by including the unconfirmed (KK) resonant states listed by the Particle Data Group in the isobar amplitude sum: $f_2(1430)$, $f_2(1565)$ and $f_2(1640)$. As reported in Table 4.17, no significant improvement of the fit quality is observed when adding any of these states and the impact on the measured Fit-Fraction ratio is negligible.

State R	μ (MeVc^{-2})	Γ (MeVc^{-2})	$\mathcal{F}_R$ (%)	$\Delta\mathcal{LL}$	$\Delta(\mathcal{F}_{f_2'}/\mathcal{F}_\phi)$ (%)
$f_2(1430)$	~1430	~20	0.01 ± 0.01	$+0.02$	$+0.03$
$f_2(1565)$	1562 ± 13	134 ± 8	0.00 ± 0.01	-0.04	-0.05
$f_2(1640)$	1639 ± 6	99^{+60}_{-40}	0.00 ± 0.00	$+0.01$	$+0.01$

Table 4.17: *Impact of unconfirmed (KK) resonant states to the measured Fit-Fraction ratio $\mathcal{F}_{f_2'}/\mathcal{F}_\phi$.*

4.9 Preliminary results and conclusion

The measured Fit-Fractions in the analysis mass range, $m_{\mathrm{KK}} \in [2m_K, 1.8\ GeV\,c^{-2}]$, for the quasi-mirror solution $\mathcal{B}_1$ are:

$$\mathcal{F}_{\phi(1020)} \times 10^2 = 69.2 \pm 0.6\ (\text{stat})\ {}^{+0.6}_{-0.8}\ (\text{syst})\ , \tag{4.49}$$

$$\mathcal{F}_{f_2(1270)} \times 10^2 = 0.5 \pm 0.2\ (\text{stat})\ \pm 0.1\ (\text{syst})\ , \tag{4.50}$$

$$\mathcal{F}_{f_2'(1525)} \times 10^2 = 15.0 \pm 0.8\ (\text{stat})\ {}^{+0.9}_{-0.3}\ (\text{syst})\ , \tag{4.51}$$

$$\mathcal{F}_{\phi(1680)} \times 10^2 = 1.2 \pm 0.2\ (\text{stat})\ \pm 0.1\ (\text{syst})\ , \tag{4.52}$$

$$\mathcal{F}_{(\mathrm{KK})_{\mathrm{NR}}} \times 10^2 = 2.3 \pm 0.3\ (\text{stat})\ \pm 0.2\ (\text{syst})\ , \tag{4.53}$$

where the first uncertainty is statistical and the second uncertainty is the systematic uncertainty corresponding to the asymmetric quadratic sum reported in Table 4.7. Systematics studies are preliminary and additional investigations are needed, in particular, to better understand the acceptance modelisation effects as well as the impact from heavy resonances above the analysis threshold.

Below the expected dominant contribution from the $\phi(1020)$ vector meson and the significant one from the $f_2'(1525)$ tensor meson, the non-resonant P-wave provides a non-negligible contribution at the level of 2%, according to our model. The sum of the Fit-Fractions does not match the unity due to the integrated interferences that contribute constructively for about +12%. The quasi-degenerated best-fit solution $\mathcal{B}_0$ exhibits almost identical Fit-Fractions value, except for the larger $\phi(1680)$ contribution and the associated destructive interference.

The Branching Fraction $\mathcal{B}(B_s \to f_2'\gamma)$ relative to $\mathcal{B}(B_s \to \phi\gamma)$ is derived from the Fit-Fractions:

$$\frac{\mathcal{B}(B_s \to f_2'\gamma)}{\mathcal{B}(B_s \to \phi\gamma)} = \frac{\mathcal{B}(\phi \to K^+K^-)}{\mathcal{B}(f_2' \to K^+K^-)} \cdot \frac{\mathcal{F}_{f_2'(1525)}}{\mathcal{F}_{\phi(1020)}}. \tag{4.54}$$

The Fit-Fraction ratio is measured to be :

$$\frac{\mathcal{F}_{f_2'(1525)}}{\mathcal{F}_{\phi(1020)}} = (21.7 \pm 0.8\ (\text{stat})\ {}^{+1.4}_{-0.7}\ (\text{syst})\ ) \times 10^{-2}. \tag{4.55}$$

where the first error is the statistical uncertainty corresponding to the 68% intervals obtained from toy experiments and the second systematical error combines the uncertainties reported in Table 4.7 with the additional one discussed in the sub-section 4.8.4. The two quasi-degenerated solutions of the amplitude fit give almost identical values. This $f_2'(1525)$ to $\phi(1020)$ Fit-Fraction ratio is remarkably close to the one observed in the B_s to charmonium decay, $B_s \to J/\Psi(K^+K^-)$, at LHCb [95], when summing the $|\lambda| = 1$ and $\lambda = 0$ helicity contributions.

Using the world average measurements [7] for the mesons decay rate: $\mathcal{B}(\phi \to K^+K^-) = 0.492 \pm 0.005$ and $\mathcal{B}(f_2' \to K^+K^-) = 0.444 \pm 0.011$, we obtain the value:

$$\frac{\mathcal{B}(B_s \to f_2'\gamma)}{\mathcal{B}(B_s \to \phi\gamma)} = (24.1 \pm 0.9 \text{ (stat)} \ ^{+1.6}_{-0.8} \text{ (syst)} \ \pm 0.6 \text{ (BR)}) \times 10^{-2}, \qquad (4.56)$$

where the last uncertainty is due to the ratio of visible branching fractions to K^+K^-.

This result establishes the first observation of the radiative B_s decay to the orbitally excited meson, $B_s \to f_2'\gamma$, and the second radiative transition ever observed in the B_s sector.

An absolute branching fraction can also be derived using the 2012 LHCb measurement[¶]:

$$\frac{\mathcal{B}\left(B^0 \to K^{*0}\gamma\right)}{\mathcal{B}\left(B_s^0 \to \phi\gamma\right)} = 1.23 \pm 0.06(\text{ stat. }) \pm 0.04(\text{ syst. }) \pm 0.10\left(f_s/f_d\right), \qquad (4.57)$$

and the recently updated world average $\mathcal{B}(B^0 \to K^{*0}\gamma) = (41.7 \pm 1.2) \times 10^{-6}$ [18]. We obtain:

$$\mathcal{B}(B_s \to f_2'\gamma) = (8.2 \ ^{+1.1}_{-0.9}) \times 10^{-6}, \qquad (4.58)$$

where the overall combined uncertainty is dominated by the external measurements.

[¶]This measurement, is based on the 2011 LHCb data only, and therefore largely uncorrelated with the data used in this analysis dominated by the Run 2 statistics. The related uncertainties include a dominant contribution from the relative hadronization factors f_s/f_d. The systematic uncertainty also embeds a contribution from the meson decay rate $\mathcal{B}(\phi \to K^+K^-)$ which is corrected for when deriving the absolute $B_s \to f_2'\gamma$ branching fraction.

Chapter 5

Amplitude analysis of $B^0 \rightarrow K^+\pi^-\gamma$

5.1 Analysis strategy

An amplitude analysis of the $B^0 \rightarrow K^+\pi^-\gamma$ decay has been performed following the same procedure as applied for $B_s \rightarrow K^+K^-\gamma$. The systematics studies are not yet finalized and only preliminary results will be presented here. The reader must refer to Chapter 4 for details on the formalism and the methodology.

The 2-dimensional distribution of the $K\pi$ candidates in the $(m_{K\pi}, cos(\theta_{K\pi}))$ observables plane is displayed on the Figure 5.1
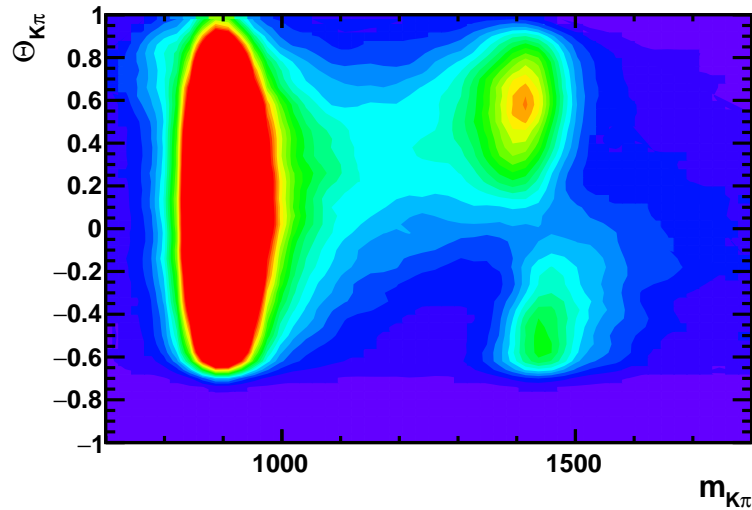

Figure 5.1: *sWeighted distribution for $K\pi$ candidates in the $(m_{K\pi}, cos(\theta_{K\pi}))$ plane.*

The main difference with $B_s \rightarrow K^+K^-\gamma$ decay is due to the fact the $K\pi$ hadronic system is asymmetrical. A direct consequence of the very unbalanced pion and kaon

momentum in the $K\pi$ rest-frame is that the selection efficiency collapses in the region of high negative value of $cos(\theta_{\kappa\pi})$, because of the transverse momentum cut applied on both hadrons. To avoid modelling the efficiency drop in that region, the amplitude analysis is conducted in the helicity range $cos(\theta_{\kappa\pi}) \in [-0.6, +1.0]$, rejecting less than 3% of the selected candidates, and in the mass range $m_{\kappa\pi} \in [m_K + m_\pi, 1.8\text{GeVc}^{-2}]$.

On the positive side, the $B^0 \to K\pi\gamma$ decay is a self-tagged final-state and there is no ambiguity in the definition of the helicity angle. Separating both charge-conjugate final-states allows to measure the $\mathcal{CP}$-asymmetry of the decay. Eventually, thanks to higher b hadronization rate into B^0 than into B_s, and the larger efficiency for $K\pi$ identification than for KK, the available statistics is almost six time larger than for the $B_s \to KK\gamma$ analysis.

5.2 The $K\pi$ hadronic system

5.2.1 Resonant structure

The allowed J^P state in the radiative B^0 decays are $1^-, 2^+, ...$ The properties of the corresponding $K\pi$ confirmed states are listed in Table5.1

known resonance	μ_R (MeVc^{-2})	Γ_R (MeVc^{-2})	J^P	$\mathcal{B}(K^+\pi^-)$ (%)
$K^{*0}(892)$	896.55 ± 0.8	47.3 ± 0.5	1^-	66.51 ± 0.01
$K^{*0}(1410)$	1421 ± 9	236 ± 18	1^-	4.4 ± 0.9
$K_2^{*0}(1430)$	1432.4 ± 2.3	109 ± 5	2^+	33.2 ± 0.8
$K^{*0}(1680)$	1718 ± 18	322 ± 110	1^-	21.8 ± 1.7
$K_3^{*0}(1780)$	1776 ± 7	159 ± 21	3^-	5.9 ± 0.7
$K_4^{*0}(2045)$	2045 ± 9	198 ± 30	4^+	$6.6 \pm +0.6$

Table 5.1: *Known strange mesonic states decaying to $K\pi$ (J > 0). The decay rates to $K^\pm\pi^\mp$ (last column) include the SU(2) factor* $\frac{2}{3}$.

Beyond the historical $B^0 \to K^{*0}(892)\gamma$ decay ($\mathcal{B} = (41.7 \pm 1.2) \times 10^{-6}$), that signed the first observation of a penguin-dominated transition [97], the $B^0 \to K_2^{*0}(1430)\gamma$ has been observed at B-factories with an averaged branching-fraction [18]:

$$\mathcal{B}(B^0 \to K_2^{*0}(1430)\gamma) = (12.4 \pm 2.4) \times 10^{-6}, \tag{5.1}$$

correponding to an experimental ratio:

$$\mathcal{R}_{K_2^{*0}/K^{*0}} = \frac{\mathcal{B}(B^0 \to K_2^{*0}(1430)\gamma)}{\mathcal{B}(B^0 \to K^{*0}(892)\gamma)} = (29.7 \pm 5.8)\%, \tag{5.2}$$

in good agreement with the theoretical expectations, for instance $\mathcal{R}_{K_2^{*0}/K^{*0}} = (29\pm9)\%$ [98], or $\mathcal{R}_{K_2^{*0}/K^{*0}} = (38 \pm 8)\%$ [99].

No evidence for the decays $B^0 \to K^{*0}(1410)\gamma$ and $B^0 \to K_3^{*0}(1780)\gamma$ has been observed to-date, and the upper limits:

$$\mathcal{B}(B^0 \to K^{*0}(1410)\gamma) \quad < \quad 130 \times 10^{-6}, \tag{5.3}$$

$$\mathcal{B}(B^0 \to K_3^{*0}(1780)\gamma) \quad < \quad 83 \times 10^{-6} \tag{5.4}$$

have been set by the Belle collaboration [100, 101]. The low coupling of those excited mesons to the two-body $K^+\pi^-$ final-state make them hardly visible in the $B^0 \to K\pi\gamma$ spectrum. Because of their dominant decay rate into three-body states, they would more likely be visible in the $B^0 \to (K_s^0\pi\pi)\gamma$ decay discussed in Appendix A.

Upper limit on the non-resonant $B^0 \to K^+\pi^-\gamma$ contribution has also been set [102], corresponding to about 6% of the $B^0 \to K^{*0}(892)\gamma$ decay rate:

$$\mathcal{B}(B^0 \to (K\pi)_{\mathrm{NR}}\gamma) < 2.6 \times 10^{-6} \tag{5.5}$$

5.2.2 $B^0 \to K^+\pi^-\gamma$ observables

As shown on Figure 5.2, the experimental resolution on the $m_{\mathrm{K}\pi}$ observable is $\sigma(m_{\mathrm{K}\pi}) \sim$ 2.7 MeVc^{-2} in the $K^{*0}(892)$ region and $\sigma(m_{\mathrm{K}\pi}) \sim 4.6$ MeVc^{-2} in the higher mass region near $K_2^{*0}(1430)$. This resolution, negligible regarding the natural width of the strange mesons, is nevertheless included in the mass line-shape model following the prescription presented in Section 4.4.2.
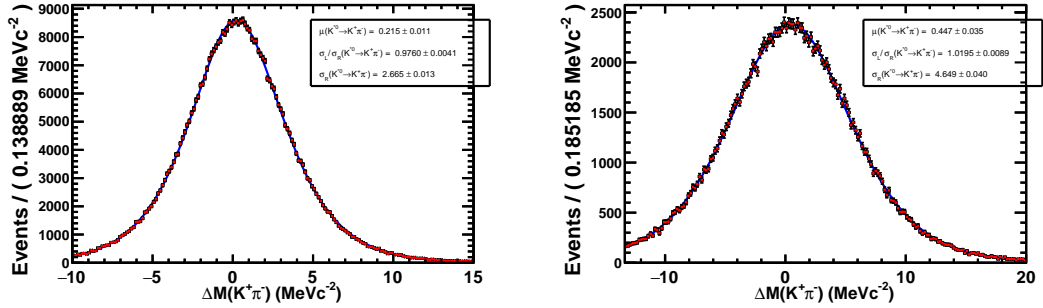
Figure 5.2: $\Delta M = m_{\mathrm{K}\pi}^{sim} - m_{\mathrm{K}\pi}^{rec}$ distribution in the K^{*0} region (left) and K_2^{*0} region (right).

The angular resolution, $\sigma(cos(\theta_{\mathrm{K}\pi})) \sim 4.8$ mrad in the $K^{*0}(892)$ region and $\sigma(m_{\mathrm{K}\pi}) \sim$ 4.1 mrad in the $K_2^{*0}(1430)$ region, also plays a negligble role in the amplitude model. The angular resolution obtained from simulated samples are displayed on Figure 5.3.

5.3 $K\pi$ acceptance

As for KK, the $K\pi$ 2-dimensional acceptance in the $(m_{\mathrm{K}\pi}, cos(\theta_{\mathrm{K}\pi}))$ plane is extracted from a simultaneous fit of various samples of fully simulated events: $B^0 \to K^+\pi^-\gamma$,

Figure 5.3: $\Delta\theta = \theta^{sim}_{K\pi} - \theta^{rec}_{K\pi}$ distribution in the K^{*0} region (left) and K^{*0}_2 region (right).

uniformly distributed in the phase-space ($\sim 3.10^4$ reconstructed events), $B^0 \to K^{*0}\gamma$ ($\sim 45.10^4$), $B^0 \to K^{*0}(1410)\gamma$ ($\sim 17.10^4$) and $B^0 \to K^{*0}_2(1430)\gamma$ ($\sim 7.10^4$). The MC samples simulating each year of data taking, with a statistics almost proportional to the experiment integrated luminosity, are combined in a single sample to extract an average acceptance for Run 1 and Run 2 data. The MC samples are reweighted using the multidimensional GB method for the BDT variables, and the data-driven PID-reweighting for the neutral and charged identification variables, IsPhoton and ProbNN(K).
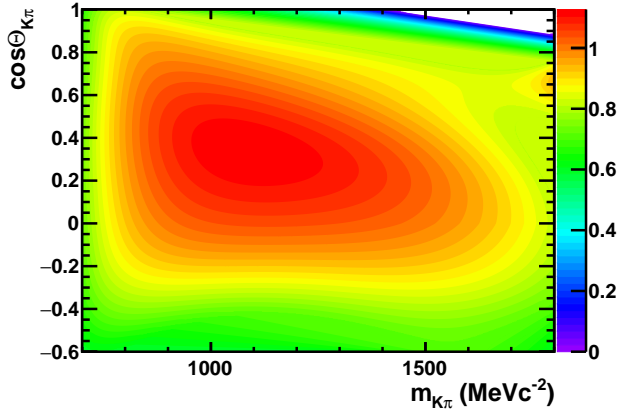
Figure 5.4: Selection acceptance in the $(m_{K\pi}, cos(\theta_{K\pi}))$ plane. The absolute normalisation is arbitrarily set near the K^{*0} pole: $\varepsilon(896.5, 0) = 1$.

The Probability Density Function describing each MC sample, $\mathcal{P}_R$, is based on the phase-space Jacobian, the Breit-Wigner mass model for the $K^{*0}_{(1,2)}$ resonnances and the relevant spin-dependent angular d-functions ($d^0_{00} = 1$ for the phase-space MC, d^1_{10} for the vector K^{*0} mesons and d^2_{10} for the tensor meson $K^{*0}_2(1430)$) multiplied by a parametrized

2D acceptance function

$$\mathcal{P}_R = \varepsilon(m_{\text{к}\pi}, \theta_{\text{к}\pi}; \vec{\alpha}).\mathcal{J}_3(m_{\text{к}\pi}).|\mathcal{A}_R(m_{\text{к}\pi}, \theta_{\text{к}\pi})|^2, \tag{5.6}$$

with $\mathcal{A}_R(m_{\text{к}\pi}, \theta_{\text{к}\pi}) = A_R(m_{\text{к}\pi})d^{J_R}_{\lambda,0}(\theta_{\text{к}\pi})$.

The set of acceptance parameters, $\vec{\alpha}$, as well as the mass pole, the width and the meson radius describing the resonances are free to vary in the fit.

Due to the unbalanced $K\pi$ final state, an asymmetrical variant of the KK acceptance function is defined:

$$\varepsilon(m_{\text{к}\pi}, \theta_{\text{к}\pi}) = \prod_{k=0}^{3} \left[1 - \alpha_k(m_{\text{к}\pi}).\left[cos(\theta_{\text{к}\pi}) - \beta_k(m_{\text{к}\pi})\right]^{2k}\right] \times \left[1 + \text{erf}\left(\frac{c_0(m_{\text{к}\pi}) - |cos(\theta_{\text{к}\pi})|}{\sigma_c}\right)\right] /2. \tag{5.7}$$

where the mass-dependent coefficients $\alpha_k(m_{\text{к}\pi})$ and $\beta_k(m_{\text{к}\pi})$, are polynomial series of the kaons momentum in the $K\pi$ rest-frame:

$$\alpha_k(m_{\text{к}\pi}) = \sum_{l=1}^{n_k} \alpha_{kl}.(q_R(m_{\text{к}\pi}))^l, \tag{5.8}$$

$$\beta_k(m_{\text{к}\pi}) = \sum_{l=1}^{n_k} \beta_{kl}.(q_R(m_{\text{к}\pi}))^l. \tag{5.9}$$

The polynomial development is extended up to order 3 for the 0-th order helicity coefficient α_0 (n_0=3) (β_0 is obviously not a relevant parameter) and a quadratic parametrization is applied for higher-order coefficients α_l and β_l (n_l=2 for l>0), leading to nine α_{kl} and six β_{kl} parameters. The error-function, parametrized with the resolution parameter σ_c, aims at describing the mass-dependent helicity threshold induced by the anti-charm kinematical selection $m_{h^\pm\gamma\to\pi^0} > \sqrt{s_{cut}} = 2$ GeVc^{-2} ($h = K, \pi$):

$$|cos(\theta_{\text{к}\pi})| < c_0(m_{\text{к}\pi}) = \frac{M_{B^0}^2 + m_\pi^2 + m_K^2 + m_{\pi^0}^2 - m_{\text{к}\pi}^2 - 2.s_{cut}}{4.M_{B^0}.q_R(m_{\text{к}\pi}).q_B(m_{\text{к}\pi})} \tag{5.10}$$

The 2-dimensional acceptance extracted from the fit of simulated samples is displayed on Figure5.4.

The 2-dimensional distribution of the $K\pi\gamma$ phase-space simulated events together with the fit model contours are shown on the left side of Figure 5.5. The right side of the same Figure displays the corresponding pull distribution, showing the good agreement between the simulated data and the model.

The quality of the acceptance model can also be seen in the fit projections on both the mass and helicity observables, displayed on Figure 5.6 for the three samples of simulated data.
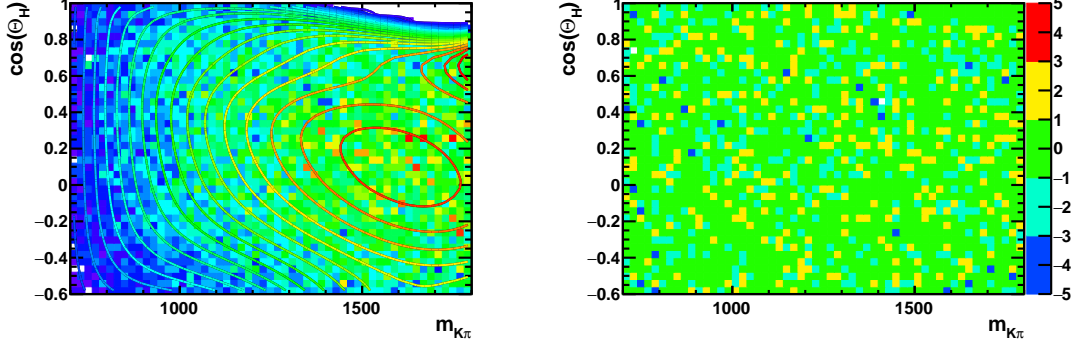
Figure 5.5: *Acceptance function on top of the phase-space MC (left) and corresponding pulls (right).*

5.4 Fit model

The decay $B^0 \to K^+\pi^-\gamma$ is a self-tagged mode. The measured decay angle between the the kaon and the B directions in the $K^\pm\pi^\mp$ rest-frame, defines unambiguously the helicity for both B^0 and $\bar{B}^0$. The Probability Density Function describing the data is defined as:

$$\mathcal{P}(m_{\kappa\pi}, \theta_{\kappa\pi}) = \mathcal{N}_s \times \mathcal{P}_s + \sum_{\mathrm{BKG}} \mathcal{N}_{\mathrm{BKG}} \times \mathcal{P}_{\mathrm{BKG}}. \tag{5.11}$$

The signal PDF:

$$\mathcal{P}_s(m_{\kappa\pi}, \theta_{\kappa\pi}) = \varepsilon(m_{\kappa\pi}, \theta_{\kappa\pi}).\mathcal{J}_3(m_{\kappa\pi}.|\sum_R c_R \times \mathcal{A}_R(m_{\kappa\pi}, \theta_{\kappa\pi})|^2), \tag{5.12}$$

is based on the confirmed resonant states having their mass pole in the analysis range ($m_{\kappa\pi} < 1.8$ GeVc^{-2}), adding a uniform non-resonant P-wave component:

$$R = \left\{ K^{*0}(892), K^{*0}(1410), K_2^{*0}(1430), K^{*0}(1680), K_3^{*0}(1780), (\mathrm{NR})_{\kappa\pi} \right\}. \tag{5.13}$$

The contamination due to misidentified $B_s \to KK\gamma$, $\Lambda_b \to pK\gamma$ and $B^0 \to K\pi\pi^0$ are included in the PDF modelling the backgrounds. The two-dimensional distributions of the B_s and the Λ_b radiative cross-feeds, are modelled using the reconstructed exclusive samples described in Chapter 3 (Figure 5.7).

The sPlot method is used to extract the $B_s \to KK\gamma$ contribution and the di-hadron mass and helicity angle are both computed under the $K\pi$ hypothesis, i.e. by assigning a pion mass to one of the kaon candidate. Similar method is applied for the $\Lambda_b \to pK\gamma$ decay, assigning the pion mass to the proton candidate. The procedure is done separately for the two charge-conjugate states, $K^+\pi^-$ and π^+K^- (ie. the $\Lambda_b \to p_{\to\pi^+}K^-\gamma$ radiative decay is contaminating the $\bar{B}^0$ signal, and the other way round). The expected contamination from doubly-misidentified $\Lambda_b \to pK^-\gamma$, where the proton is misidentified as a kaon, and the kaon as a pion, is of the order of 0.1%. Such contribution is therefore neglected in the

nominal model.

The charmless $B^0 \to K\pi\pi^0$ decay is expected to contaminate at the level of 1% and is, thus, included in the nominal model for $K\pi\gamma$. It is modelled as $K^{*0}\pi^0$ contribution, asumming the same acceptance as for radiative signal:

$$\mathcal{P}_{\pi^0}(m_{\kappa\pi}, \theta_{\kappa\pi}) = \varepsilon(m_{\kappa\pi}, \theta_{\kappa\pi}).\mathcal{J}_3(m_{\kappa\pi}).|\mathcal{B}(m_{\kappa\pi}; \mu_K^{*0}, \Gamma_K^{*0}).\mathrm{d}_{00}^1(\theta_{\kappa\pi})|^2. \qquad (5.14)$$

Alternative models for the $K\pi\pi^0$ contamination will have to be addressed for systematics study.

The nominal PDF model describing the $K^+\pi^-$ (π^+K^-) amplitude in the $(m_{\kappa\pi}, \theta_{\kappa\pi})$ observables phase-space, eventually depends on 14 parameters:

- four overall normalisation yields, $\mathcal{N}_X$ $(\overline{\mathcal{N}}_X)$ parametrizing the overall signal and background data composition.

- five complex factors c_R $(\bar{c}_R)$ weighting the signal isobar amplitudes.

The reference factor and the unrelevant global phase in the signal model, are arbitrarily assigned to the $K^{*0}(892)$ component, i.e. $c_{K^{*0}(892)} = 1$. Mass line-shape parameters are fixed to the world average values reported in Table 5.1.

Each individual amplitude of the isobar model is normalized to unity to allow an easier interpretation of the associated amplitude factors $|c_R|$:

$$\int_{-1}^{+1} \int_{m_{\kappa}+m_{\pi}}^{1.8\mathrm{GeVc}^{-2}} |\mathcal{A}_R(m_{\kappa\pi}, \theta_{\kappa\pi})|^2 d\phi_3(m_{\kappa\pi}, \theta_{\kappa\pi}) = 1, \qquad (5.15)$$

where $d\phi_3(m_{\kappa\pi}, \theta_{\kappa\pi}) = \mathcal{J}_3(m_{\kappa\pi})dm_{\kappa\pi}dcos(\theta_{\kappa\pi})$ is the phase-space volume.

5.5 Fit to data

5.5.1 Fit minimization

Unbinned extended likelihood fits to the $K^+\pi^-$ and to the π^+K^- spectra are performed separately in the two-dimensional phase-space $(m_{\kappa\pi}, \theta_{\kappa\pi})$, minimizing the weighted $\mathcal{LL}$ function derived from the model PDF. To ensure the fits converge towards a global minimun rather than local minima, the starting value of the fit parameters are varied randomly and a large number of repeated fits are processed. A well isolated minimum of the $\mathcal{LL}$ is obtained.

The fit model projected on the two observables $m_{\kappa\pi}$ and $cos(\theta_{\kappa\pi})$ is displayed on the Figure 5.8 for both charge-conjugate samples. The global PDF is represented by

the blue solid curve, the red points with error-bar are the data. The $B^0 \to K^+\pi^-\gamma$ PDF contribution is indicated by the red solid curve, while the purple, green and blue solid curves represent the misidentified $B_s \to K^+K^-\gamma$, $\Lambda_b \to pK^-\gamma$ and $B^0 \to K^{*0}\pi^0$ backgrounds, respectively. The dashed curves represent the individual components contribution to the $(K^\pm\pi^\mp)$ amplitude: $K^{*0}(892)$ (red), $K^{*0}(1410)$ (green), $K_2^{*0}(1430)$ (magenta), $K^{*0}(1680)$ (light blue), $K_3^{*0}(1780)$ (dark blue) and non-resonant (pink). The dashed grey curve is the integrated interference contribution.

5.5.2 Data composition and Fit-Fractions

The normalisation yields that describe the data composition are reported in Table 4.3. The measured relative contaminations from the cross-feed backgrounds, each contributing to about 2%, are consistent with the MC expectation discussed in Section 3.9.

contribution	$K^+\pi^-$			π^+K^-		
	Yield ($\times 10^3$)		$\mathcal{N}_{\mathrm{BKG}}/\mathcal{N}_s$ (%)	Yield ($\times 10^3$)		$\overline{\mathcal{N}}_{\mathrm{BKG}}/\overline{\mathcal{N}}_s$ (%)
$B^0 \to (K\pi)\gamma$ signal	$\mathcal{N}_s$	116.5 ± 0.4	-	$\overline{\mathcal{N}}_s$	116.9 ± 0.4	-
$B_s \to (KK)\gamma$ bkg	$\mathcal{N}_{B^0}$	2.0 ± 0.1	1.7 ± 0.1	$\overline{\mathcal{N}}_s$	2.1 ± 0.1	1.8 ± 0.1
$\Lambda_b \to (pK)\gamma$ bkg	$\mathcal{N}_{\Lambda_b}$	2.0 ± 0.3	1.7 ± 0.2	$\overline{\mathcal{N}}_s$	2.6 ± 0.3	2.2 ± 0.2
$B^0 \to (K\pi)\pi^0$ bkg	$\mathcal{N}_{\pi^0}$	2.1 ± 0.1	1.8 ± 0.1	$\overline{\mathcal{N}}_s$	2.2 ± 0.2	1.8 ± 0.1

Table 5.2: *PDF component yields and relative background contamination from the fit to $K^+\pi^-$ (left) and π^+K^- (right).*

No significant charge-asymmetry is observed in the background contamination. The overall raw-asymmetry for the $B^0 \to K\pi\gamma$ signal, defined from the measured data yields is :

$$\mathcal{A}^{\mathrm{RAW}}\left[B^0 \to K^+\pi^-\gamma\right] = \frac{\overline{\mathcal{N}}_s - \mathcal{N}_s}{\overline{\mathcal{N}}_s + \mathcal{N}_s} = (+0.19 \pm 0.25). \tag{5.16}$$

The $K\pi$ amplitude Fit-Fractions are defined by integrating the individual components over the full helicity range, and up to 1.8 GeVc^{-2} for the di-hadron mass:

$$\mathcal{F}_R = \frac{\int_{-1}^{+1} \int_{m_\kappa+m_\pi}^{1.8\mathrm{GeVc}^{-2}} |c_R \times \mathcal{A}_R(m_{\kappa\pi}, \theta_{\kappa\pi})|^2 d\phi_3(m_{\kappa\pi}, \theta_{\kappa\pi})}{\int_{-1}^{+1} \int_{m_\kappa+m_\pi}^{1.8\mathrm{GeVc}^{-2}} |\sum_k c_k \times \mathcal{A}_k(m_{\kappa\pi}, \theta_{\kappa\pi})|^2 d\phi_3(m_{\kappa\pi}, \theta_{\kappa\pi})}, \tag{5.17}$$

where $d\phi_3(m_{\kappa\pi}, \theta_{\kappa\pi}) = \mathcal{J}_3(m_{\kappa\pi}) dm_{\kappa\pi} d\cos(\theta_{\kappa\pi})$ is the phase-space volume.

The measured Fit-Fractions together with the corresponding modulus and phase of the isobar factors, are given in Table 5.3, for both charge-conjugate final-states. The quoted errors are the statistical uncertainties returned by the fit minimizer. Their reliability has

$K^+\pi^-$ component	Fit-Fraction ($\mathcal{F}_R$) (%)	$\mathcal{F}_R/\mathcal{F}_{K^{*0}(892)}$ (%)	δ_R (rad)	$|c_R|$
$K^{*0}(892)$	75.78 ± 0.66	100	0 (fixed)	1 (fixed)
$K^{*0}(1410)$	1.27 ± 0.12	1.68 ± 0.16	1.86 ± 0.08	0.130 ± 0.006
$K_2^{*0}(1430)$	13.65 ± 0.23	18.01 ± 0.35	-3.14 ± 0.08	0.424 ± 0.004
$K^{*0}(1680)$	1.02 ± 0.18	1.34 ± 0.24	-2.97 ± 0.10	0.158 ± 0.011
$K_3^{*0}(1780)$	0.34 ± 0.04	0.45 ± 0.05	0.74 ± 0.12	0.074 ± 0.004
$(K^+\pi^-)_{\mathrm{NR}}$	0.24 ± 0.22	0.31 ± 0.29	1.22 ± 0.12	0.055 ± 0.026
$\int$ interference	7.71			
$\pi^+ K^-$ component	Fit-Fraction ($\overline{\mathcal{F}}_R$) (%)	$\overline{\mathcal{F}}_R/\overline{\mathcal{F}}_{K^{*0}(892)}$ (%)	$\bar{\delta}_R$ (rad)	$|\bar{c}_R|$
$\bar{K}^{*0}(892)$	75.76 ± 0.74	100	0 (fixed)	1 (fixed)
$\bar{K}^{*0}(1410)$	1.01 ± 0.12	1.33 ± 0.15	1.76 ± 0.07	0.115 ± 0.006
$\bar{K}_2^{*0}(1430)$	13.53 ± 0.18	17.86 ± 0.32	3.09 ± 0.06	0.423 ± 0.004
$\bar{K}^{*0}(1680)$	1.69 ± 0.22	2.22 ± 0.31	-2.83 ± 0.08	0.149 ± 0.010
$\bar{K}_3^{*0}(1780)$	0.44 ± 0.04	0.59 ± 0.05	0.93 ± 0.08	0.077 ± 0.003
$(\pi^+ K^-)_{\mathrm{NR}}$	0.55 ± 0.27	0.73 ± 0.37	1.26 ± 0.06	0.086 ± 0.021
$\int$ interference	7.02			

Table 5.3: *(relative) Fit-Fractions and isobar factors for the $K^+\pi^-$ final-state (top) and the charge-conjugate π^+K^- (bottom). The quoted errors are the statistical uncertainties returned by the fit minimizer.*

been controled using a large sample of toys experiments, and the preliminary results indicate a correct coverage of the fit uncertainties.

The Fit-Fractions are all consistent with no charge-asymmetry. The expected dominant contributions from the $K^{*0}(892)$ and the $K_2^{*0}(1430)$ mesons almost saturate the $K\pi\gamma$ final state with a constructive interference pattern at the level of 7%. No significant non-resonant P-wave component is observed, contrary to $B_s \to K^+K^-\gamma$.

5.6 $B^0 \to K^+\pi^-\gamma$: summary

The amplitude analysis of the $B^0 \to K\pi\gamma$ decay indicates that the $K\pi$ spectrum is dominated at 90% with the $K^{*0}(892)$ and the $K_2^{*0}(1430)$ mesons in the mass range, $m_{\mathrm{K}\pi} \in [m_K + m_\pi, 1.8\ GeV c^{-2}]$. The integrated interference pattern accounts constructively for about 7%, and the statistical significance of other contributions is not clear without further systematics studies. The separate analysis of the charge-conjugate states, $K^+\pi^-\gamma$ and $K^-\pi^+\gamma$ allows to mesure the overall $B^0 \to K^+\pi^-\gamma$ raw asymmetry in the given mass range with a very good statistical resolution:

$$\mathcal{A}^{\mathrm{RAW}}\left[B^0 \to K^+\pi^-\gamma\right] = (+0.19 \pm 0.25)\%. \tag{5.18}$$

Looking at Fit-Fractions, no evidence for any charge asymmetry is observed within the $K^\pm\pi^\mp$ amplitude spectrum. The raw-asymmetry for the amplitude component R, defined

as:

$$\mathcal{A}^{\text{RAW}}[R] = \frac{\overline{\mathcal{F}}_R \times \overline{\mathcal{N}}_s - \mathcal{F}_R \times \mathcal{N}_s}{\overline{\mathcal{F}}_R \times \overline{\mathcal{N}}_s + \mathcal{F}_R \times \mathcal{N}_s}, \tag{5.19}$$

are measured for the dominant $K^{*0}(892)$ and $K_2^{*0}(1430)$ contributions as:

$$\mathcal{A}^{\text{RAW}}[B^0 \to K^{*0}(892)\gamma] = (+0.18 \pm 0.69)\% \tag{5.20}$$

$$\mathcal{A}^{\text{RAW}}[B^0 \to K_2^{*0}(1430)\gamma] = (-0.25 \pm 1.12)\% \tag{5.21}$$

where the uncertainties are statistical only.

The physical $\mathcal{CP}$-asymmetry is related to the measured raw asymmetry after correcting for the $K^+\pi^-$ interaction asymmetry, $\mathcal{A}_D$, and for the $B^0/\bar{B}^0$ production asymmetry, $\mathcal{A}_P$, both measured at the level of 1% at LHCb Run 1 [103]:

$$\mathcal{A}_{\mathcal{CP}} = \mathcal{A}^{\text{RAW}} - A_D(K\pi) - \kappa A_P(B^0), \tag{5.22}$$

where κ is a dilution factor due to the B^0 oscillation. The LHCb magnet polarity is regularly inverted, so that the integrated luminosity for each year of data taking is almost equivalent for both polarities and any experimental detection asymmetry is expected to mostly cancel out. The $B^0 \to K^{*0}(892)\gamma$ $\mathcal{CP}$-asymmetry has been measured at LHCb using 2011 data [71]:

$$\mathcal{A}_{\mathcal{CP}}\left[B^0 \to K^{*0}(892)\gamma\right] = +0.8 \pm 1.7 \text{ (stat)} \pm 0.9 \text{ (syst)} \%, \tag{5.23}$$

in good agreement with the SM expectation [104]: $\mathcal{A}_{\mathcal{CP}}^{\text{SM}} = (-0.61 \pm 0.43)\%$. The current analysis should improve significantly the statistical resolution on this quantity. In the absence of measurement for the B^0 production asymmetry at Run 2, and without a complete study of the systematic uncertainties affecting our measured raw asymmetries in the $B^0 \to K^+\pi^-\gamma$ decay, no attempt to derive the $\mathcal{CP}$-asymmetry from the amplitude analysis will be done here.

The branching fraction of $B^0 \to K_2^{*0}(1430)\gamma$ relative to $B^0 \to K^{*0}(892)\gamma$ could be derived from the $\mathcal{CP}$-averaged Fit-Fractions ratio:

$$\frac{\mathcal{F}_{K_2^{*0}(1430)}}{\mathcal{F}_{K^{*0}(892)}} = (17.9 \pm 0.2 \text{ (stat)})\% \tag{5.24}$$

Using the world-average decay rates $\mathcal{B}(K^{*0}(892) \to K^+\pi^-) = (66.51 \pm 0.1)\%$ and $\mathcal{B}(K_2^{*0}(1430) \to K^+\pi^-) = (32.7 \pm 1.2)\%$, the preliminary value:

$$\frac{\mathcal{B}(B^0 \to K_2^{*0}(1430)\gamma)}{\mathcal{B}(B^0 \to K^{*0}(892)\gamma)} = (36.4 \pm 0.4 \text{ (stat)} \pm 1.3 \text{ (BR)})\%, \tag{5.25}$$

is obtained, where the first uncertainty is statistical, the second is due to visible branching fraction external measurements and the systematical uncertainty is missing. This value is in good agreement with the measured $B^0 \to K_2^{*0}(1430)$ branching fraction at B-factories and with theoretical expectations.
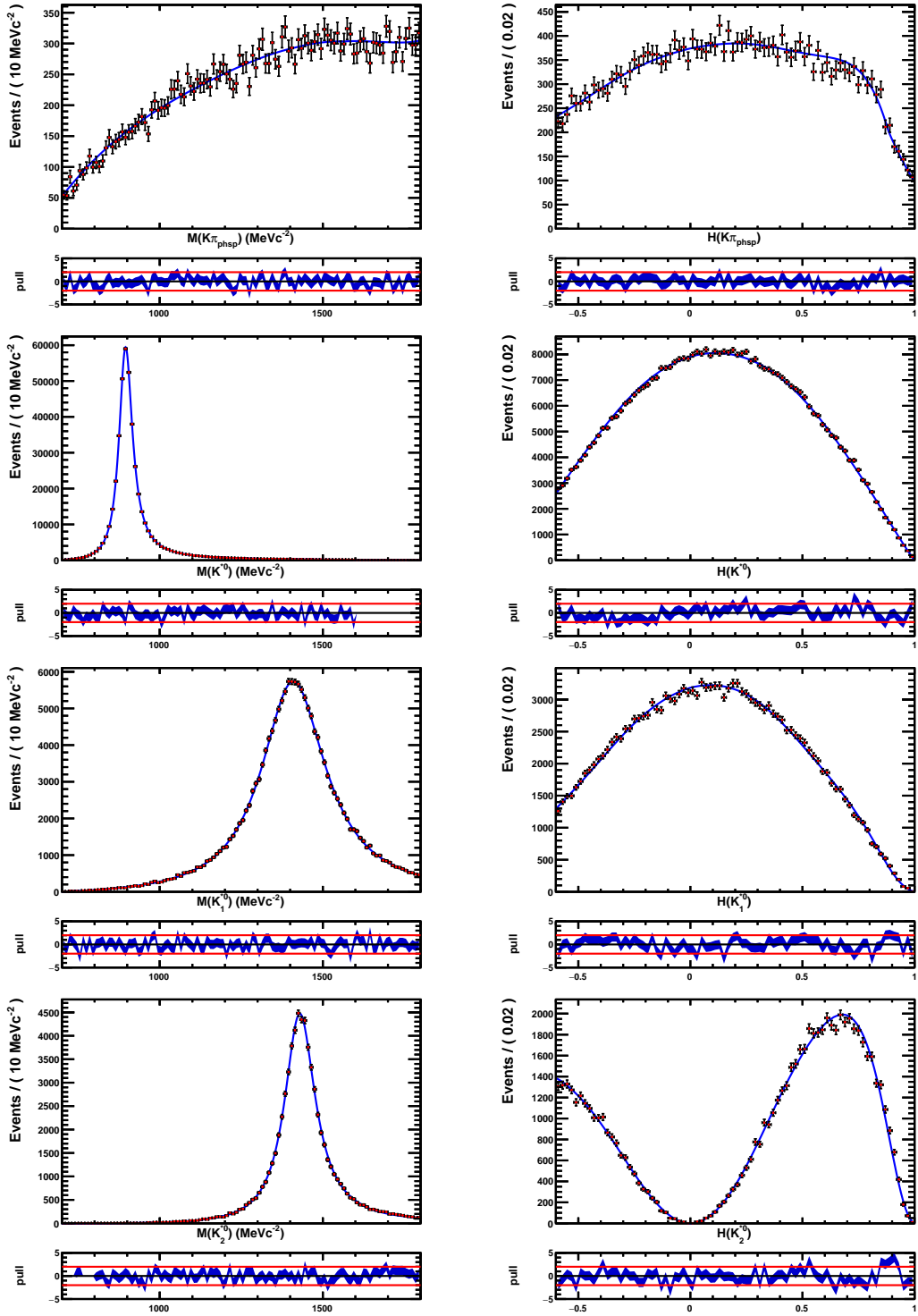
Figure 5.6: *Projection of the simultaneous fit to MC data on the $m_{K\pi}$ (left) and $cos(\theta_{K\pi})$ (right) observables for the phase-space $K\pi\gamma$ (top line), the two vector resonances $K^{*0}(892)\gamma$ (second line) and $K^{*0}(1410)\gamma$ (third line), and the tensor resonance $K^{*0}(1430)_2\gamma$ (bottom line) sample<s.*
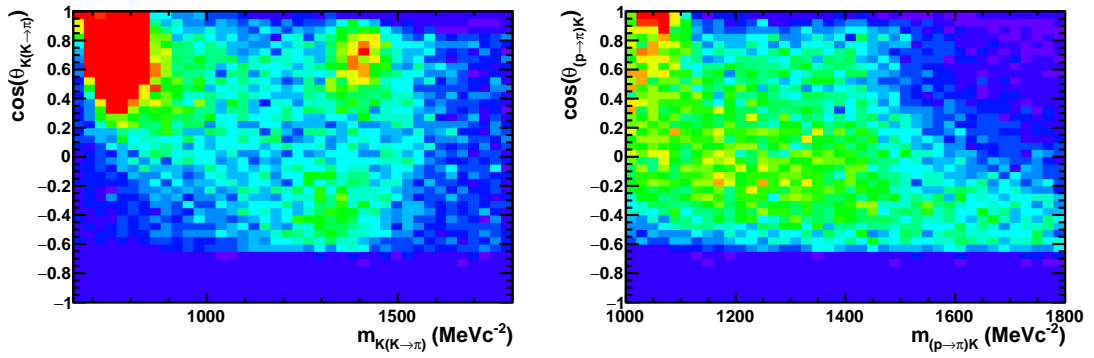
Figure 5.7: *Projection in the ($m_{\kappa\pi}$, $cos(\theta_{\kappa\pi})$) plane for the reconstructed and sWeighted $B_s \to KK\gamma$ candidates (left) and $\Lambda_b \to pK\gamma$ (right). The di-hadron mass and helicity are computed assigning a kaon (pion) mass to the pion (proton) candidate.*
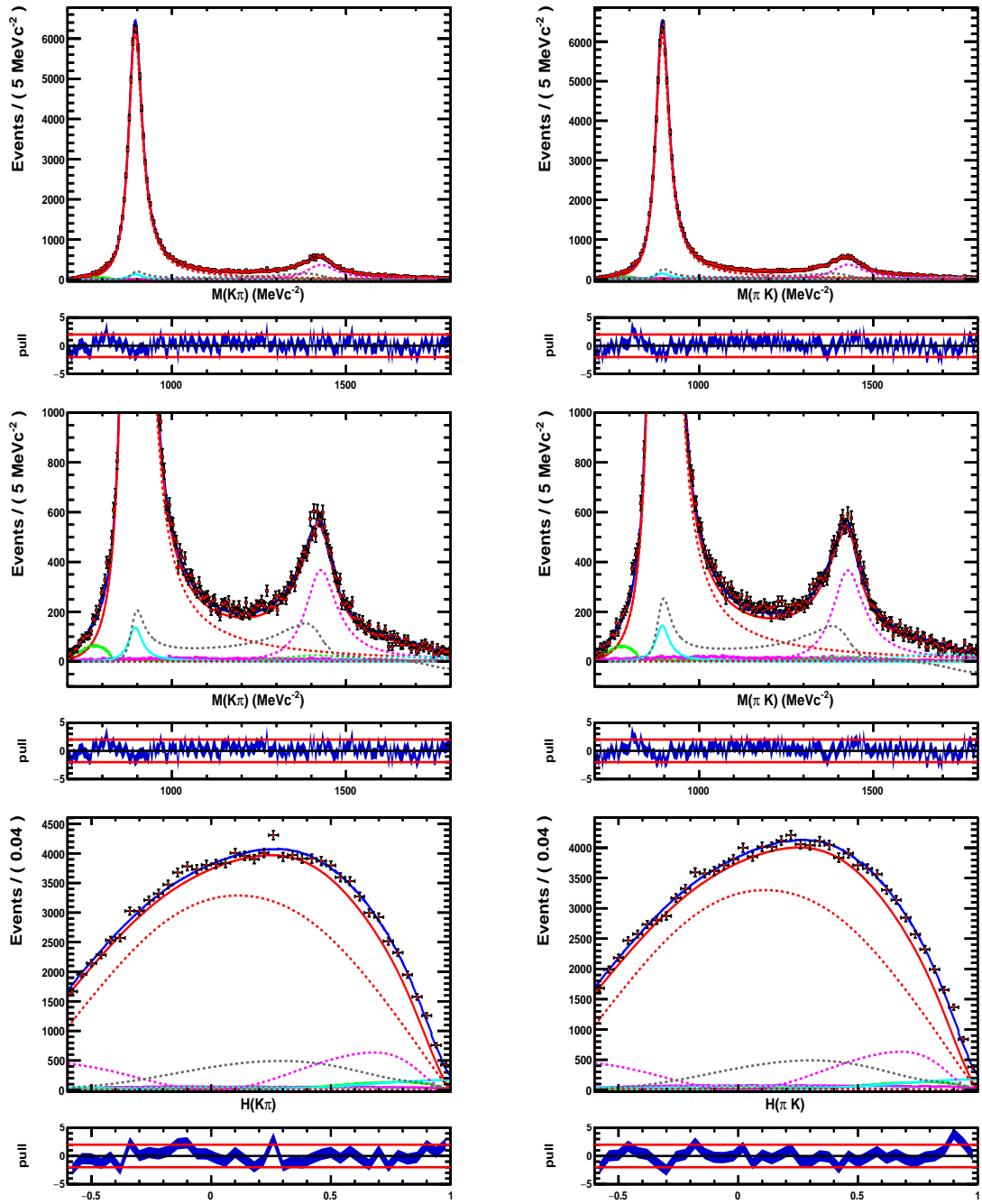
Figure 5.8: *One-dimensional projection of the nominal fit on the observables $m_{K\pi}$ (top, and middle with zoom) and $\cos(\theta_{K\pi})$ (bottom), for the $K^+\pi-$ (left) and π^+K^- (right) samples. Red points with error-bars are the data, the blue solid curve represents the global PDF model (see text for details on the different contributions to the model). The 2D Poisson likelihood χ^2 per degree of freedom corresponding to the projection binning is $\chi^2/_{\mathrm{dof}}=1.05$.*

Conclusion

This document presents a study of B radiative decays at the LHCb experiment, focusing on the description of the hadronic structures in $B_{d/s} \to (h^+ h^-)\gamma$ channels. Initially, a selection of $B^0 \to K^{\pm}\pi^{\mp}\gamma$, $B_s \to K^+ K^- \gamma$ and $\Lambda_b \to p^{\pm} K^{\mp}\gamma$ decays is presented. It makes use of the full Run 1 and Run 2 data available at LHCb, corresponding to an integrated luminosity of about 8.7 fb^{-1}. The events are selected in a wide hh mass range, up to 1.8 GeV. After tight PID requirements tuned to suppress the cross-feeds of the different radiative modes, a large part of the selected data is combinatorics. A dedicated BDT classifier is then trained against it with MC signal, which is corrected in a multivariate manner beforehand. The trained BDT allows a very good background reduction and a final fit is performed after an optimal cut to the BDT output. While a few different possible background contributions are discussed, the model for the final mass fit does not include any peaking backgrounds as the $_s\mathcal{P}lot$ method does not allow to substract contributions that are fixed or constrained in the fit. These contributions are therefore treated as signal in the sWeighting and are addressed later in the amplitude analyses. In the end, the procedure allows to select $\sim$250k $B^0 \to K^{\pm}\pi^{\mp}\gamma$ events, $\sim$50k $B_s \to K^+ K^- \gamma$ events, and $\sim$35k $\Lambda_b \to p^{\pm} K^{\mp}\gamma$ events.

A time-integrated amplitude analysis of the selected $B_s \to K^+ K^- \gamma$ decays is then developed following an isobar approach. The amplitude model takes into account a limited number of resonances allowed in radiative decays, namely the $\phi(1020)$, $f_2(1270)$, $f_2'(1525)$ and $\phi(1680)$. A non-resonant amplitude is added as a P-wave component, with a constant phase, and a uniform distribution in mass. The remaining backgrounds from other radiative decays are also considered, making use of the multichannel selection to extract a mass and helicity distribution directly from the data. Two quasi-degenerated minima are found in the unbinned extended likelihood fit, one of the solutions exhibiting an unexpectedly high contribution from the $\phi(1680)$ resonance together with a destructive interference pattern. Aside from this, both solutions converge nevertheless to almost identical parameter values. The Branching Fraction $\mathcal{B}(B_s \to f_2'\gamma)$ relative to $\mathcal{B}(B_s \to \phi\gamma)$ is derived from the Fit-Fractions:

$$\frac{\mathcal{F}_{f_2'(1525)}}{\mathcal{F}_{\phi(1020)}} = (21.7 \pm 0.8 \text{ (stat) } ^{+1.4}_{-0.7} \text{ (syst) }) \times 10^{-2},$$

where the first error is the statistical uncertainty, and the second one is the preliminary systematical uncertainties. Using the world average measurements for the meson decay

rate, we obtain the value:

$$\frac{\mathcal{B}(B_s \to f_2'\gamma)}{\mathcal{B}(B_s \to \phi\gamma)} = (24.1 \pm 0.9 \text{ (stat)} \; {}^{+1.6}_{-0.8} \text{ (syst)} \; \pm 0.6 \text{ (BR)}) \times 10^{-2},$$

where the last uncertainty is due to the ratio of visible branching fractions to K^+K^-. This result establishes the first observation of the radiative B_s decay to the orbitally excited meson, $B_s \to f_2'\gamma$, and the second radiative transition ever observed in the B_s sector.

A similar amplitude analysis has been performed on the $B^0 \to K\pi\gamma$ decays. It indicates that the $K\pi$ spectrum is dominated at 90% with the $K^{*0}(892)$ and the $K_2^{*0}(1430)$ meson in the mass range, $m_{\kappa\pi} \in [m_K + m_\pi, 1.8 \; GeVc^{-2}]$. The integrated interference pattern accounts constructively for about 7% of the spectrum, and the significance of other contributions will need further systematics studies. The separate analysis of the charge-conjugate states, $K^+\pi^-\gamma$ and $K^-\pi^+\gamma$ allows to measure the overall $B^0 \to K^+\pi^-\gamma$ raw asymmetry in the given mass range with a very good statistical resolution:

$$\mathcal{A}^{\text{RAW}} \left[B^0 \to K^+\pi^-\gamma \right] = (+0.19 \pm 0.25)\%,$$

where the uncertainty is statistical only. Looking at Fit-Fractions, no evidence for any charge asymmetry is observed within the $K^\pm\pi^\mp$ amplitude spectrum. The raw-asymmetry are measured for the dominant $K^{*0}(892)$ and $K_2^{*0}(1430)$ contributions:

$$\mathcal{A}^{\text{RAW}} \left[B^0 \to K^{*0}(892)\gamma \right] = (+0.18 \pm 0.69)\%$$
$$\mathcal{A}^{\text{RAW}} \left[B^0 \to K_2^{*0}(1430)\gamma \right] = (-0.25 \pm 1.12)\%$$

where the uncertainties are statistical only.

A preliminary branching ratio of the $B^0 \to K_2^{*0}(1430)\gamma$ mode is also derived:

$$\frac{\mathcal{B}(B^0 \to K_2^{*0}(1430)\gamma)}{\mathcal{B}(B^0 \to K^{*0}(892)\gamma)} = (36.4 \pm 0.4 \text{ (stat)} \; \pm 1.3 (\text{BR}))\%,$$

where the first uncertainty is statistical, the second is due to external measurements of visible branching fraction and the systematical uncertainty still needs to be evaluated. This value is in good agreement with the measured $B^0 \to K_2^{*0}(1430)\gamma$ branching fraction at B-factories and also with theoretical predictions.

Additionally, a very preliminary work towards the measurement of the branching ratio of $B^0 \to K_S^0\pi^+\pi^-\gamma$ is presented in the Appendix. The selection, making use of the same semi-inclusive procedure as for the $B \to h^+h^-\gamma$ analysis, allows to study a few thousand events (~ 3600). While this will not be enough for a time-dependent Dalitz analysis, a first result with the Run 1-Run 2 statistics would be the derivation of a branching ratio for this mode.

Appendix A

Preliminary study of $B_{(s)} \to K^0_S h^+ h^- \gamma$ decays

A.1 Introduction

As introduced in Section 1.6, measuring the mixing-induced CP violation parameter S in a time-dependent analysis of decays of the form $B_{(s)} \to f^{CP}\gamma$ is a way to constrain NP scenarios where the photon gets a significant right-handed component in the $b \to s\gamma$ transition. Two of the current best constraints on S in $B^0 \to K_{res}\gamma$ modes are obtained by the BaBar [105, 106] and Belle [107, 108] collaborations :

- in $B^0 \to K^0_S \pi^0 \gamma$: S =-0.15 $\pm$ 0.20

- in $B^0 \to K^0_S \rho^0 \gamma$: $S = 0.14 \pm 0.27$

While the first mode is not accessible in LHCb, the B vertex being not reconstructible, the final state $K^0_S \pi^+ \pi^- \gamma$ could be studied. Furthermore, it has been shown in [109] that a time-dependent Dalitz analysis could allow to constrain separately the real and imaginary part of $C^{7\prime}$ through interferences between the intermediate state $B^0 \to K^0_S \rho^0 (\to \pi^+ \pi^-)\gamma$ and $B^0 \to K^{*+}(\to K^0_S \pi^+)\pi^- \gamma$.

We consider in this chapter an exploratory work willing to estimate the available yields of $B_{(s)} \to K^0_S h^+ h^- \gamma$ within the data acquired during the two first runs of the LHC. This is a very first step towards branching ratio measurements of $B^0 \to K^0_S \pi^+ \pi^- \gamma$ (current average is $\mathcal{B}(B^0 \to K^0 \pi^+ \pi^- \gamma) = (1.99 \pm 0.18) \times 10^{-5}$ [7]) and $B_s \to K^0_S K^+ \pi^- \gamma$ (not measured).

A.2 Analysis strategy

The selection of the $K^0_S h^+ h^- \gamma$ modes is done similarly to what has been done for $h^+ h^- \gamma$ ones in Chapter 3, in the sense that the online selection is aiming at gathering every

events with two tracks, a high p_T photon and a K^0_S in the final state, and the available MC samples are reconstructed in each of the considered final states, namely $K^0_S\pi^+\pi^-\gamma$ $K^0_S K^+\pi^-\gamma$ and $K^0_S K^+K^-\gamma$. As K^0_S mesons flies typically for about 1m of distance at LHCb, some of them decay after the VELO and thus the two daughter pions of the decay can be reconstructed as Downstream tracks. Therefore, the strategy is to treat separately data with K^0_S reconstructed with two Long tracks (LL) and K^0_S reconstructed with two Down tracks (DD). The $B^0 \to K^{*0}\gamma$ and $B_s \to \phi\gamma$ modes are used as control channels.

A.2.1 Data and MC samples

This analysis is based on the pp collision data collected in Run 1 and Run 2 during 2011-2018 as was depicted in Figure 2.3. Again, this excludes the initial months of the 2011 data-taking, since the corresponding semi-inclusive radiative stripping lines were not yet implemented (see Section 3.3.2). The total integrated luminosity is therefore around 8.7 fb^{-1}.

A collection of simulated samples are used during the analysis to control the selection efficiencies, they are listed in Table A.1. For the control channel, the same samples as for the $h^+h^-\gamma$ multichannel selection are used. For the $K^0_S h^+h^-\gamma$ case, the signal $B^0 \to K^0_S\pi^+\pi^-\gamma$ is simulated with a cocktail of intermediate resonances $K_1(1270)^0 \to K^0_s\rho^0$ (1/3), $K_1(1270)^0 \to K^{*+}\pi^-$ (1/3) and phase space (1/3), while $B_s \to K^0_S K^+\pi^-\gamma$ and $B^0 \to K^0_S K^+K^-\gamma$ samples are generated uniformly in the allowed phase space.

Decay mode	Event type	Stat. 2011	Stat. 2012	Stat. 2015	Stat. 2016	Stat. 2017	Stat. 2018
$B^0 \to K_S^0 \pi^+ \pi^- \gamma$	11204301	$0.6{\times}10^6$	$1.8{\times}10^6$	$0.9{\times}10^6$	$1.8{\times}10^6$	$1.9{\times}10^6$	$1.8{\times}10^6$
$B^0 \to K_S^0 K^+ \pi^- \gamma$	13104323	$0.6{\times}10^6$	$1.9{\times}10^6$	$1.{\times}10^6$	$1.8{\times}10^6$	$1.8{\times}10^6$	$1.8{\times}10^6$
$B_s \to K_S^0 K^+ K^- \gamma$	11104351	$0.6{\times}10^6$	$2.{\times}10^6$	$0.9{\times}10^6$	$2.{\times}10^6$	$1.9{\times}10^6$	$1.9{\times}10^6$

Table A.1: *Processed signal MC samples.*

A.3 Online selection

Trigger lines

This study uses the same radiative LHCb trigger lines as the ones used for the $h^+h^-\gamma$ multichannel selection, described in Section 3.3.1.

Stripping

The stripping selection uses semi-inclusive lines for the Run 1 and Run 2 that look for a generic $(h^+h^{'-})K_S^0\gamma$ final state, with loose pre-selections and no PID requirement on the di-hadron system. A summary of the selections are listed in Table A.2. For the control modes, we use the similarly inclusive $(h^+h^{'-})\gamma$ lines that is used in Chapter 3 – these correspond in facts to those in the signal mode, with just the K_S^0 part removed (see Table A.3).

DIRA$_{\rm PV}$ refers to the cosine of the angle between the momentum of the b-hadron and its flight direction from the best PV to its decay vertex (ideally this should be unity). A loose requirement of $\gamma_{\rm CL} > 0$ (see Sec. 3.6.2) is also placed at the stripping level.

A.4 Offline selection

At the pre-selection level for both control and signal modes, to further trim the dataset to a manageable size, we apply several requirements summarized in Table A.4. For various charm background removal, we PID-substitute $\gamma \to \pi^0$ and require the two-body mass combinations, $m_{h^{(')}\pi^0}$, $m_{K_S^0\pi^0}$ be greater than 2 GeV/c^2. Similarly, the mass of the hadronic system has to be less than 1.85 GeV/c^2, to lie below the open charm threshold. For the $K^*\gamma(\phi\gamma)$ modes we require $m_{hh'}$ to be 100(10) MeV/c^2 around the known $K^*(\phi)$ masses. For the photon, we tighten the stripping cuts to $p_{\rm T}(\gamma) > 3\,{\rm GeV}/c$, $\gamma_{\rm CL} > 0.2$ and require the γ-π^0 separation variable $\gamma_{\rm IsPhoton} > 0.6$ (for the Data only, at this stage, since MC will need the same procedure as in Section 3.6.2). The PV's are refitted and the IP-χ^2 is required to be > 16 for the charged tracks.

A.5 Preliminar MVA selection and yields

After this relatively loose selection, the background reduction is not enough to fit the data and extract signal yields for any of the $K_S^0 h^+h^-\gamma$ modes. A preliminar BDT has been trained on MC and RHSB data corresponding to the $B^0 \to K_S^0\pi^+\pi^-\gamma$ decay, to test the possibly achievable background reduction. It largely inherits from optimisation studies performed in Section 3.8. The training is done separately for Run 1 and Run 2 (the selected statistics was too low to go for a per year training), and for each K_s^0 type (DD or LL). The output of these BDT are displayed on Figure A.1 and Figure A.2.

Variable Definition	Selection Requirement
	Photon selection
Transverse momentum	$p_T > 2000\,\mathrm{MeV}/c$
Neutral PID	$\gamma_{\mathrm{CL}} > 0$
	Di-hadron system
Track quality	$\chi^2/\mathrm{ndof} < 3$, $\mathrm{Prob}_{\mathrm{ghost}} < 0.4$
Min. track P/p_T	$P > 1000\,\mathrm{MeV}/c$, $p_T > 300\,\mathrm{MeV}/c$
Track IP from best PV	$\mathrm{IP}_{\chi^2} > 20$
Total p_T	$p_T > 1500(1000)\,\mathrm{MeV}/c$
Invariant mass	$[0, 7900]\,\mathrm{MeV}/c$
Vertexing quality	$\chi^2/\mathrm{dof} < 10(9)$
	$K_{\mathrm{S}}^0 \to \pi^+\pi^-$ selection
DD pions	$P > 2000\,\mathrm{MeV}/c$, $\mathrm{IP}_{\chi^2} > 4$
	$\|m_{\pi\pi} - m_{K_{\mathrm{S}}^0}\| < 64\,\mathrm{MeV}$, vertex $\chi^2 < 25$
LL pions	$P > 2000\,\mathrm{MeV}/c$, $p_T > 250\,\mathrm{MeV}/c$, $\mathrm{IP}_{\chi^2} > 9$
	$\|m_{\pi\pi} - m_{K_{\mathrm{S}}^0}\| < 35\,\mathrm{MeV}$, vertex $\chi^2 < 25$
Merged K_{S}^0 cuts	$p_T > 1000\,\mathrm{MeV}/c$, $\chi^2/\mathrm{ndof} < 9$, $m_{\pi\pi} \in [480, 515]\,\mathrm{MeV}/c^2$
	Requirements on the $(h^+ h^{'-})K_{\mathrm{S}}^0$ system
Combination	vertex $\chi^2/\mathrm{ndof} < 10(9)$,
	$p_T > 1500(1000)\,\mathrm{MeV}/c$, $m_{hh'K_{\mathrm{S}}^0} < 7900\,\mathrm{MeV}/c^2$
Related PV	χ^2-dist > 0, min. IP-$\chi^2 > 0$
	Requirements on the full mother b-hadron candidates
At least one track has	$P > 5000\,\mathrm{MeV}/c$, $p_T > 1000\,\mathrm{MeV}/c$,
	$\chi^2/\mathrm{ndof} < 2.5$, min. IP-dist. $> 0.1\,\mathrm{mm}$, $\mathrm{IP}_{\chi^2} > 16$
Vertexing quality	$\chi^2/\mathrm{dof} < 9$, $\mathrm{DIRA}_{\mathrm{PV}} > 0$
IP from best PV	$\mathrm{IP}_{\chi^2} < 9$
Min. p_T	$p_T > 3000\,\mathrm{MeV}/c$
Invariant mass	$[2400, 6500]\,\mathrm{MeV}/c^2$
TISTOS requirements	`Hlt2RadiativeTopo*_(TIS,TOS)` (Run 1)
	`Hlt1TwoTrackMVA_TOS` (Run 2)

Table A.2: *Stripping definitions for the signal modes:* `B2XGamma2pi_Ks0`*(Run 1) and* `Beauty2XGamma2pi_Ks0`*(Run 2). Some of the selections are slightly different between the two lines – in which case, the bracketed numbers denote the slightly looser ones for Run 2.*

The BDT output is then evaluated on the data samples, and a quite tight cut is arbitrarily applied (BDT > 0.1). Then, the generic radiative mass model described in Section 3.5 is used in an unbinned extended maximum likelihood fit to the B invariant mass, first separately for DD and LL K_s^0, and also to the full data. They are gathered in Figure A.4 and Figure A.5. For this fit, the signal shape (tails parameters of the double tail CB) is extracted from a fit to the full MC samples mass distribution (Figure A.3).

Variable Definition	Selection requirement
Requirements on the full mother b-hadron	
$m(B)$	$[3280, 9000]$ MeV/c^2
Daughters $\sum p_T(B)$	> 5000 MeV/c
$\theta_{DIRA}(B)$	> 0
$\chi^2_{\text{vtx}}/\text{ndf}(B)$	< 9
$\chi^2_{\text{IP}}(B)$	< 9
Di-hadron system using `StdAllNoPID`	
Track p_T	> 300 MeV/c
Track p	> 1000 MeV/c
Tracks $\sum p_T$	> 1500 MeV/c
Track χ^2/ndf	< 3
Track χ^2_{IP}	> 16
Tracks GhostProb	< 0.4
Photon selection using `StdLooseAllPhotons`	
$p_T(\gamma)$	> 2000 MeV/c
γ_{CL}	> 0

Table A.3: *Selection requirements applied in the* `B2XGamma2pi_Line` *stripping line to select* $B \to hh\gamma$ *events, for the control modes.*

Variable	Cut
Track p	$[500; 100000]$ MeV/c
$\min(h^+p_T, h^-p_T)$	> 500 MeV/c
$\max(h^+p_T, h^-p_T)$	> 1200 MeV/c
Track η	$[1.5; 5]$
Track χ^2_{IP}	> 16
$h^\pm$PID	$\sum_i^{(i \neq j)} h_j\_\text{ProbNN}_{h_j} > h_j\_\text{ProbNN}_{h_i}, (h_{i,j} = K, \pi, p)$ $h_j\_\text{ProbNN}_{h_j} > 0.1$
$\chi^2_{\text{vtx}}((h^+h^-)_{res})$	< 9
γ_{CL}	> 0.2
IsPhoton	> 0.6
$m(B)$	$[4000; 7000]$ MeV/c^2
$p_T(B)$	> 2000 MeV/c^2
$\chi^2_{\text{IP}}(B)$	< 9
Smallest $\Delta\chi^2_{\text{vtx}}(B)$	> 3

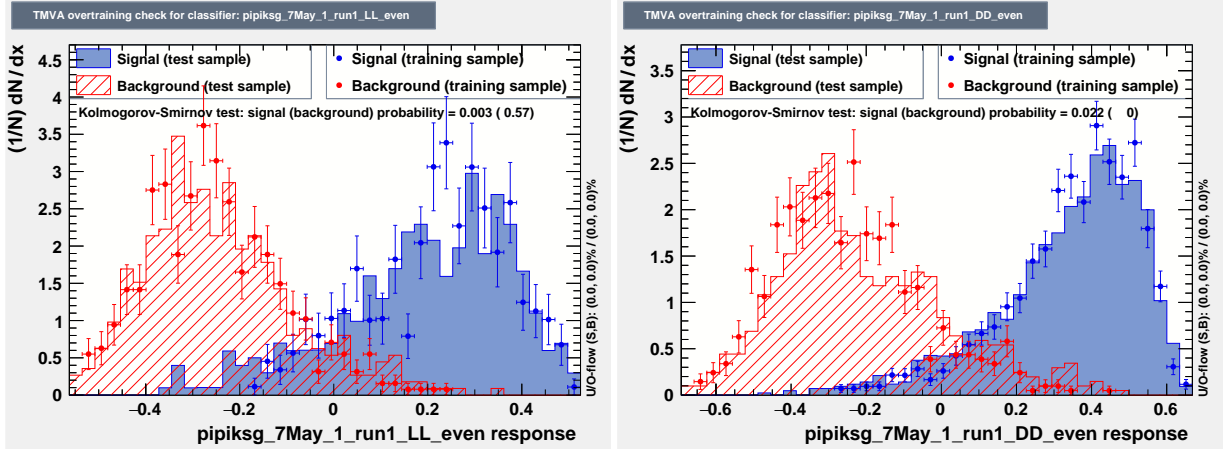Table A.4: *Initial cut-based selection. The trigger requirements as well as the stripping selection of Tab. A.3 are applied.*

Figure A.1: *Output of the preliminar BDT trained on Run 1 $B^0 \to K_S^0 \pi^+ \pi^- \gamma$, with with DD K_s^0 (left) and LL K_s^0 (right).*
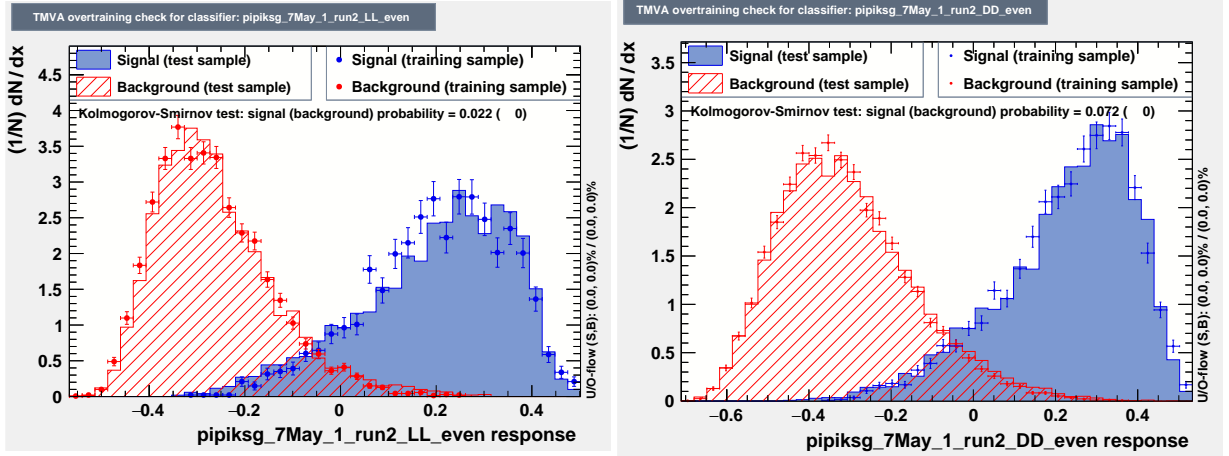

Figure A.2: *Output of the preliminar BDT trained on Run 2 $B^0 \to K_S^0 \pi^+ \pi^- \gamma$, with with DD K_s^0 (left) and LL K_s^0 (right)..*

A.6   Conclusion

In the end, this very preliminary selection of $B^0 \to K_S^0 \pi^+ \pi^- \gamma$ events in Run 1 and Run 2 LHCb data allows to gather a sample of ~ 3600 data events. As can be seen in Figure A.5, the tight cut to the BDT output allows a strict reduction of the combinatorial background. However, the contamination from partially reconstructed decays is quite high, and a further optimized selection might be needed with respect to this point. For the moment, no BDT has been trained for the two other $B \to K_S^0 h^+ h^- \gamma$ selected modes, as the lower MC statistics after selection requires a different optimisation of the training process for these modes.
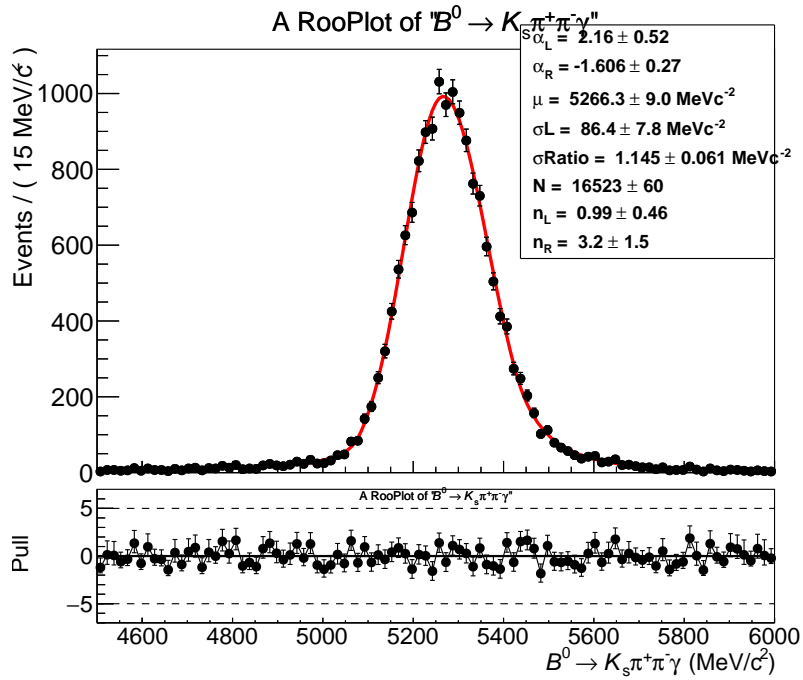
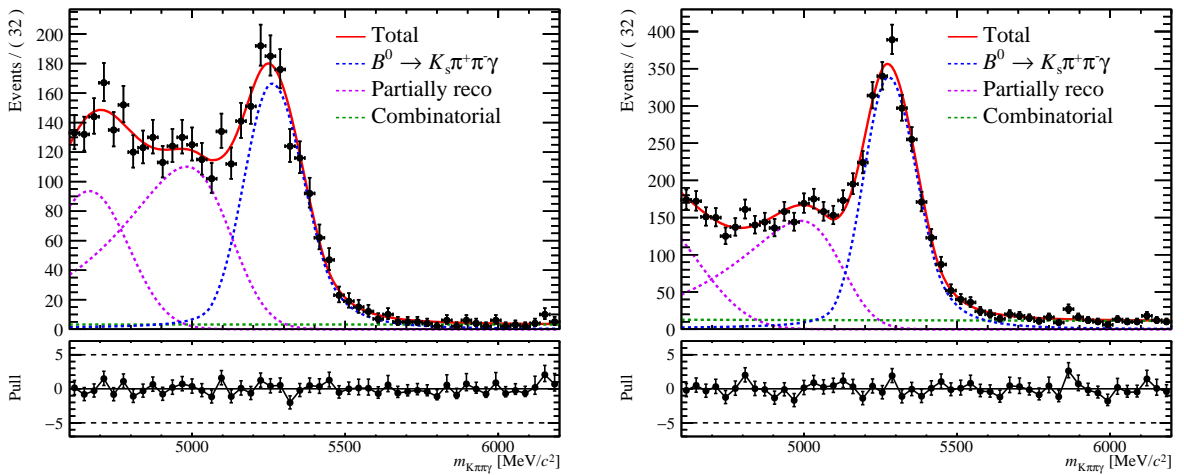Figure A.3: *Fit to the B mass distribution in the full* $B^0 \to K_S^0 \pi^+ \pi^- \gamma$ *MC available.*

Figure A.4: *Preliminary fit to the full (Run 1/Run2), data for* $B^0 \to K_S^0 \pi^+ \pi^- \gamma$, *with DD* K_s^0 *(left) and LL* K_s^0 *(right).*
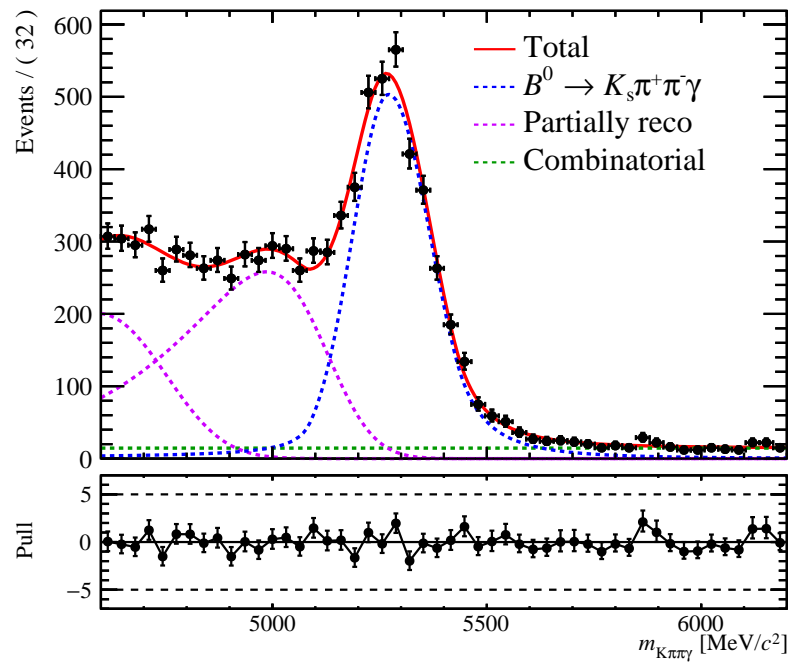
Figure A.5: *Preliminary fit to the full (Run 1/Run 2, DD/LL) data for $B^0 \to K^0_S \pi^+ \pi^- \gamma$.*

Bibliography

[1] R. Aaij *et al.*, *Observation of photon polarization in the b to s gamma transition*, Physical Review Letters **112** (2014) .

[2] Y. Nir, *CP violation in meson decays*, in *High-energy physics. Proceedings, 3rd Latin American CERN-CLAF School, Malargue, Argentina, February 27-March 12, 2005*, pp. 79–145, 2006. `arXiv:hep-ph/0510413`.

[3] ATLAS, G. Aad *et al.*, *Observation of a new particle in the search for the Standard Model Higgs boson with the ATLAS detector at the LHC*, Phys. Lett. **B716** (2012) 1, `arXiv:1207.7214`.

[4] CMS, S. Chatrchyan *et al.*, *Observation of a new boson at a mass of 125 GeV with the CMS experiment at the LHC*, Phys. Lett. **B716** (2012) 30, `arXiv:1207.7235`.

[5] ATLAS, G. Aad *et al.*, *Evidence for the spin-0 nature of the Higgs boson using ATLAS data*, Phys. Lett. **B726** (2013) 120, `arXiv:1307.1432`.

[6] CMS, S. Chatrchyan *et al.*, *Study of the Mass and Spin-Parity of the Higgs Boson Candidate Via Its Decays to Z Boson Pairs*, Phys. Rev. Lett. **110** (2013), no. 8 081803, `arXiv:1212.6639`.

[7] Particle Data Group, M. Tanabashi *et al.*, *Review of particle physics*, Phys. Rev. D **98** (2018) 030001.

[8] N. Cabibbo, *Unitary Symmetry and Leptonic Decays*, Phys. Rev. Lett. **10** (1963) 531, [,648(1963)].

[9] M. Kobayashi and T. Maskawa, *CP Violation in the Renormalizable Theory of Weak Interaction*, Prog. Theor. Phys. **49** (1973) 652.

[10] T. D. Lee and C. N. Yang, *Question of parity conservation in weak interactions*, Phys. Rev. **104** (1956) 254.

[11] C. S. Wu *et al.*, *Experimental test of parity conservation in beta decay*, Phys. Rev. **105** (1957) 1413.

[12] R. L. Garwin, L. M. Lederman, and M. Weinrich, *Observations of the failure of conservation of parity and charge conjugation in meson decays: the magnetic moment of the free muon*, Phys. Rev. **105** (1957) 1415.

[13] J. I. Friedman and V. L. Telegdi, *Nuclear emulsion evidence for parity nonconservation in the decay chain $\pi^+ \to \mu^+ \to e^+$*, Phys. Rev. **106** (1957) 1290.

[14] C. Jarlskog, *Commutator of the quark mass matrices in the standard electroweak model and a measure of maximal* CP *nonconservation*, Phys. Rev. Lett. **55** (1985) 1039.

[15] The CKMfitter Group, http://ckmfitter.in2p3.fr.

[16] L. Wolfenstein, *Parametrization of the kobayashi-maskawa matrix*, Phys. Rev. Lett. **51** (1983) 1945.

[17] A. J. Buras, M. E. Lautenbacher, and G. Ostermaier, *Waiting for the top quark mass, $K^+ \to \pi^+ \nu \bar{\nu}$, $B^0_s - \overline{B}^0_s$ mixing and CP asymmetries in B decays*, Phys. Rev. **D50** (1994) 3433, `arXiv:hep-ph/9403384`.

[18] Heavy Flavor Averaging Group, Y. Amhis *et al.*, *Averages of b-hadron, c-hadron, and τ-lepton properties as of summer 2018*, `arXiv:1909.12524`.

[19] S. L. Glashow, J. Iliopoulos, and L. Maiani, *Weak Interactions with Lepton-Hadron Symmetry*, Phys. Rev. **D2** (1970) 1285.

[20] V. Weisskopf and E. P. Wigner, *Calculation of the natural brightness of spectral lines on the basis of Dirac's theory (In German)*, Z. Phys., **63**, 54 (1930).

[21] V. Weisskopf and E. P. Wigner, *Over the natural line width in the radiation of the harmonius oscillator (In German)*, Z. Phys., **65**, 18 (1930).

[22] I. I. Bigi and A. I. Sanda, *CP violation*, Cambridge University Press, (2000).

[23] S. Aoki *et al.*, *Review of lattice results concerning low-energy particle physics*, Eur. Phys. J. **C74** (2014) 2890, `arXiv:1310.8555`.

[24] D. Atwood, M. Gronau, and A. Soni, *Mixing-inducedcpasymmetries in radiativebdecays in and beyond the standard model*, Physical Review Letters **79** (1997) 185–188.

[25] D. Bečirević, E. Kou, A. Le Yaouanc, and A. Tayduganov, *Future prospects for the determination of the wilson coefficient $c'_{7\gamma}$*, Journal of High Energy Physics **2012** (2012) .

[26] F. Muheim, Y. Xie, and R. Zwicky, *Exploiting the width difference in $b_s \to \phi\gamma$*, 2008.

[27] R. Aaij *et al.*, *First experimental study of photon polarization in radiative bs0 decays*, Physical Review Letters **118** (2017) .

[28] R. Aaij *et al.*, *Measurement of cp-violating and mixing-induced observables in* $b_s^0 \to \phi\gamma$ *decays*, Physical Review Letters **123** (2019) .

[29] The LHCb Collaboration *et al.*, *Opposite-side flavour tagging of b mesons at the lhcb experiment*, The European Physical Journal C **72** (2012) 2022.

[30] F. Krüger and J. Matias, *Probing new physics via the transverse amplitudes ofb0k*0(k+)l+lat large recoil*, Physical Review D **71** (2005) .

[31] R. Aaij *et al.*, *Angular analysis of the b0 k*0e+e decay in the low-q2 region*, Journal of High Energy Physics **2015** (2015) .

[32] R. Aaij *et al.*, *Angular analysis of the b 0 k *0 + decay using 3 fb1 of integrated luminosity*, Journal of High Energy Physics **2016** (2016) .

[33] C. Collaboration, *Angular analysis and branching fraction measurement of the decay b0 to k*0 mu+ mu-*, 2013.

[34] G. Hiller, M. Knecht, F. Legger, and T. Schietinger, *Photon polarization from helicity suppression in radiative decays of polarized to spin-3/2 baryons*, Physics Letters B **649** (2007) 152–158.

[35] T. Mannel and S. Recksiegel, *Flavour-changing neutral current decays of heavy baryons. the case*, Journal of Physics G: Nuclear and Particle Physics **24** (1998) 979–990.

[36] A. Paul and D. M. Straub, *Constraints on new physics from radiative b decays*, Journal of High Energy Physics **2017** (2017) .

[37] L. Evans and P. Bryant, *LHC Machine*, vol. 3, 2008. doi: 10.1088/1748-0221/3/08/S08001.

[38] LHCb, R. Aaij *et al.*, *Measurement of the b-quark production cross-section in 7 and 13 TeV pp collisions*, Phys. Rev. Lett. **118** (2017), no. 5 052002, `arXiv:1612.05140`, [Erratum: Phys. Rev. Lett.119,no.16,169901(2017)].

[39] LHCb, A. A. Alves, Jr. *et al.*, *The LHCb Detector at the LHC*, JINST **3** (2008) S08005.

[40] LHCb Collaboration, *LHCb VELO (VErtex LOcator): Technical Design Report*, CERN-LHCC-2001-011, CERN, Geneva, 2001.

[41] R. Aaij *et al.*, *Performance of the LHCb Vertex Locator*, JINST **9** (2014) 09007, `arXiv:1405.7808`.

[42] LHCb, *LHCb technical design report: Reoptimized detector design and performance*, CERN-LHCC-2003-030, 2003.

[43] LHCb, *LHCb: Inner tracker technical design report*, CERN-LHCC-2002-029, 2002.

[44] LHCb, *LHCb: Outer tracker technical design report*, CERN-LHCC-2001-024, 2001.

[45] LHCb Outer Tracker Group, R. Arink *et al.*, *Performance of the LHCb Outer Tracker*, JINST **9** (2014), no. 01 P01002, `arXiv:1311.3893`.

[46] LHCb, *LHCb magnet: Technical design report*, CERN-LHCC-2000-007, 2000.

[47] LHCb RICH Group, M. Adinolfi *et al.*, *Performance of the LHCb RICH detector at the LHC*, Eur. Phys. J. **C73** (2013) 2431, `arXiv:1211.6759`.

[48] LHCb, *LHCb calorimeters: Technical design report*, CERN-LHCC-2000-036, 2000.

[49] William R. Leo, *Techniques for Nuclear and Particle Physics Experiments - 2nd Revised Edition*, Springer (1994).

[50] LHCb, P. Perret, *First Years of Running for the LHCb Calorimeter System*, PoS **TIPP2014** (2014) 030, `arXiv:1407.4289`.

[51] LHCb, R. Aaij *et al.*, *Angular analysis of the $B^0 \to K^{*0}\mu^+\mu^-$ decay using 3 fb^{-1} of integrated luminosity*, JHEP **02** (2016) 104, `arXiv:1512.04442`.

[52] LHCb, R. Aaij *et al.*, *Measurement of the CP-violating phase ϕ_s in the decay $B_s^0 \to J/\psi\phi$*, Phys. Rev. Lett. **108** (2012) 101803, `arXiv:1112.3183`.

[53] LHCb, R. Aaij *et al.*, *First Evidence for the Decay $B_s^0 \to \mu^+\mu^-$*, Phys. Rev. Lett. **110** (2013), no. 2 021801, `arXiv:1211.2674`.

[54] LHCb, R. Aaij *et al.*, *Measurement of the $B_s^0 \to \mu^+\mu^-$ branching fraction and search for $B^0 \to \mu^+\mu^-$ decays at the LHCb experiment*, Phys. Rev. Lett. **111** (2013) 101805, `arXiv:1307.5024`.

[55] LHCb, *LHCb: Addendum to the muon system technical design report*, CERN-LHCC-2003-002, 2003.

[56] J. J. Hopfield, *Neural networks and physical systems with emergent collective computational abilities*, Proceedings of the National Academy of Sciences **79** (1982), no. 8 2554, `arXiv:https://www.pnas.org/content/79/8/2554.full.pdf`.

[57] Particle Data Group, C. Patrignani *et al.*, *Review of Particle Physics*, Chin. Phys. **C40** (2016), no. 10 100001.

[58] O. Callot, *Calorimeter data format and 2-D zero suppression scheme*, Tech. Rep. LHCb-99-037, CERN, Geneva, Oct, 1999.

[59] V. Breton, N. Brun, and P. Perret, *A clustering algorithm for the LHCb electromagnetic calorimeter using a cellular automaton*, Tech. Rep. LHCb-2001-123, CERN, Geneva, Sep, 2001.

[60] O. Deschamps *et al.*, *Photon and neutral pion reconstruction*, Tech. Rep. LHCb-2003-091, CERN, Geneva, Sep, 2003.

[61] L. Beaucourt and E. Tournefier, *Study of $B^0 \to K^{*0}\gamma$, $B_s^0 \to \phi\gamma$ and $B_s^0 \to K^{*0}\gamma$ decays using converted photons with the LHCb detector.*, Oct, 2016. Presented 08 Dec 2016.

[62] LHCb, R. Aaij *et al.*, *LHCb Detector Performance*, Int. J. Mod. Phys. **A30** (2015), no. 07 1530022, `arXiv:1412.6352`.

[63] I. Belyaev *et al.*, *Kali: The framework for fine calibration of the lhcb electromagnetic calorimeter*, Journal of Physics: Conference Series **331** (2011), no. 3 032050.

[64] M. Hoballah, P. Perret, and O. Deschamps, *Measurement of the photon polarization using $B_s^0 \to \phi\gamma$ at LHCb.*, Apr, 2015. Presented 03 Mar 2015.

[65] M. Pivk and F. R. Le Diberder, *SPlot: A Statistical tool to unfold data distributions*, Nucl. Instrum. Meth. **A555** (2005) 356, `arXiv:physics/0402083`.

[66] M. Calvo Gomez *et al.*, *A tool for γ/π^0 separation at high energies*, Tech. Rep. LHCb-PUB-2015-016. CERN-LHCb-PUB-2015-016, CERN, Geneva, Aug, 2015.

[67] K. G. Sobczak and S. Monteil, *Study of charmless three-body decays of neutral B mesons with the LHCb spectrometer*, 2011. Presented 15 Dec 2011.

[68] LHCb, R. Aaij *et al.*, *Measurement of the inelastic pp cross-section at a centre-of-mass energy of $\sqrt{s} = 7$ TeV*, JHEP **02** (2015) 129, `arXiv:1412.2500`.

[69] M. Williams *et al.*, *The HLT2 Topological Lines*, LHCb-PUB-2011-002, CERN-LHCb-PUB-2011-002.

[70] H.-J. Yang, B. P. Roe, and J. Zhu, *Studies of boosted decision trees for MiniBooNE particle identification*, Nucl. Instrum. Meth. **A555** (2005) 370, `arXiv:physics/0508045`.

[71] LHCb, R. Aaij *et al.*, *Measurement of the ratio of branching fractions $B(B^0 \to K^{*0}\gamma)/B(B_s^0 \to \phi\gamma)$ and the direct CP asymmetry in $B^0 \to K^{*0}\gamma$*, Nucl. Phys. **B867** (2013) 1, `arXiv:1209.0313`.

[72] LHCb, R. Aaij *et al.*, *First experimental study of photon polarization in radiative B_s^0 decays*, Phys. Rev. Lett. **118** (2017), no. 2 021801, `arXiv:1609.2032`.

[73] T. Sjöstrand *et al.*, *An introduction to pythia 8.2*, Computer Physics Communications **191** (2015) 159–177.

[74] A. Puig, *The LHCb trigger in 2011 and 2012*, LHCb-PUB-2014-046. CERN-LHCb-PUB-2014-046.

[75] LHCb Collaboration, R. Aaij *et al.*, *Design and performance of the LHCb trigger and full real-time reconstruction in Run 2 of the LHC. Performance of the LHCb trigger and full real-time reconstruction in Run 2 of the LHC*, JINST **14** (2018) P04013. 43 p.

[76] A. Puig, *The HLT2 Radiative Topological Lines*, Tech. Rep. LHCb-PUB-2012-002. CERN-LHCb-PUB-2012-002, CERN, Geneva, Feb, 2012.

[77] W. Blum, W. Riegler, and L. Rolandi, *Particle detection with drift chambers; 2nd ed.*, Springer, Berlin, 2008. doi: 10.1007/978-3-540-76684-1.

[78] J. E. Gaiser, *Charmonium Spectroscopy From Radiative Decays of the J/ψ and ψ'*, PhD thesis, SLAC, 1982.

[79] ARGUS, H. Albrecht *et al.*, *Search for Hadronic $b \to u$ Decays*, Phys. Lett. **B241** (1990) 278.

[80] L. Anderlini *et al.*, *The PIDCalib package*, Tech. Rep. LHCb-PUB-2016-021. CERN-LHCb-PUB-2016-021, CERN, Geneva, Jul, 2016.

[81] A. Rogozhnikov, *Reweighting with boosted decision trees*, Journal of Physics: Conference Series **762** (2016) 012036.

[82] L. Breiman, J. H. Friedman, R. A. Olshen, and C. J. Stone, *Classification and Regression Trees*, Statistics/Probability Series, Wadsworth Publishing Company, Belmont, California, U.S.A., 1984.

[83] B. P. Roe *et al.*, *Boosted decision trees as an alternative to artificial neural networks for particle identification*, 2004.

[84] A. Hoecker *et al.*, *TMVA - Toolkit for Multivariate Data Analysis*, `arXiv:physics/0703039`.

[85] Y. Freund and R. E. Schapire, *A decision-theoretic generalization of on-line learning and an application to boosting*, Journal of Computer and System Sciences **55** (1997), no. 1 119 .

[86] Belle, V. Gaur *et al.*, *Evidence for the decay $B^0 \to K^+K^-\pi^0$*, Phys. Rev. **D87** (2013), no. 9 091101, `arXiv:1304.5312`.

[87] R. H. Dalitz, *On the analysis of tau-meson data and the nature of the tau-meson*, Phil. Mag. Ser. 7 **44** (1953) 1068.

[88] Particle Data Group, K. A. Olive *et al.*, *Review of Particle Physics*, Chin. Phys. **C38** (2014) 090001.

[89] J. M. Blatt and V. F. Weisskopf, *Theoretial nulear physis*, John Wiley Sons, New York, 1952. doi: https://doi.org/10.1007/978-1-4612-9959-2.

[90] S. Flatté, *Coupled-channel analysis of the and kk systems near kk threshold*, Physics Letters B **63** (1976), no. 2 224 .

[91] R. A. Kycia and S. Jadach, *Relativistic Voigt profile for unstable particles in high energy physics*, J. Math. Anal. Appl. **463** (2018), no. 2 1040, `arXiv:1711.09304`.

[92] W. Verkerke and D. Kirkby, *The RooFit toolkit for data modeling*, Tech. Rep. physics/0306116, SLAC, Stanford, CA, Jun, 2003.

[93] F. James and M. Roos, *MINUIT: a system for function minimization and analysis of the parameter errors and corrections*, Comput. Phys. Commun. **10** (1975) 343.

[94] D. Bisello *et al.*, *Observation of an isoscalar vector meson at approximately = 1650-MeV/c**2 in the e+ e- —> K anti-K pi reaction*, Z. Phys. **C52** (1991) 227.

[95] LHCb Collaboration, R. Aaij *et al.*, *Resonances and CP violation in B_s^0 and $\overline{B}_s^0 \rightarrow J/\psi K^+ K^-$ decays in the mass region above the $\phi(1020)$*, JHEP **08** (2017) 037. 28 p.

[96] *Measurement of k + k - production in two-photon collisions in the resonant-mass region*, The European Physical Journal C **32** (2003) 323–336.

[97] CLEO, R. Ammar *et al.*, *Evidence for penguins: First observation of B —> K* (892) gamma*, Phys. Rev. Lett. **71** (1993) 674.

[98] D. Ebert, R. N. Faustov, V. O. Galkin, and H. Toki, *Rare radiativebdecays to orbitally excitedkmesons*, Physical Review D **64** (2001) .

[99] H. Hatanaka and K.-C. Yang, *Radiative and semileptonic b decays involving higher k-resonances in the final states*, The European Physical Journal C **67** (2010) 149–162.

[100] Belle Collaboration, S. Nishida *et al.*, *Radiative b meson decays into kπγ and kππγ final states*, Phys. Rev. Lett. **89** (2002) 231801.

[101] Belle, S. Nishida *et al.*, *Observation of B+ —> K+ eta gamma*, Phys. Lett. **B610** (2005) 23, `arXiv:hep-ex/0411065`.

[102] Belle, S. Nishida *et al.*, *Radiative B meson decays into K pi gamma and K pi pi gamma final states*, Phys. Rev. Lett. **89** (2002) 231801, `arXiv:hep-ex/0205025`.

[103] R. Aaij *et al.*, *Measurement of cp asymmetry in $d^0 \rightarrow k^- k^+ and d^0 \rightarrow \pi^+\pi^-$ decays*, Journal of High Energy Physics **2014** (2014) .

[104] M. Matsumori, A. I. Sanda, and Y.-Y. Keum, *Cp asymmetry, branching ratios, and isospin breaking effects of $b \rightarrow k^*\gamma$ with the perturbative qcd approach*, Physical Review D **72** (2005) .

[105] BaBar, B. Aubert *et al.*, *Measurement of The Time-Dependent CP Asymmetry in $B^0 \to K^{*0}\gamma$ Decays,* in *Lepton and photon interactions at high energies. Proceedings, 23rd International Symposium, LP2007, Daegu, South Korea, August 13-18, 2007,* 2007. `arXiv:0708.1614`.

[106] BaBar, P. del Amo Sanchez *et al.*, *Time-dependent analysis of $B^0 \to K_S^0 \pi^- \pi^+ \gamma$ decays and studies of the $K^+ \pi^- \pi^+$ system in $B^+ \to K^+ \pi^- \pi^+ \gamma$ decays*, Phys. Rev. **D93** (2016), no. 5 052013, `arXiv:1512.03579`.

[107] Belle, J. Li *et al.*, *Time-dependent CP Asymmetries in $B^0 \to K_S^0 rho^0 \gamma$ Decays*, Phys. Rev. Lett. **101** (2008) 251601, `arXiv:0806.1980`.

[108] Belle, Y. Ushiroda *et al.*, *Time-Dependent CP Asymmetries in $B^0 \to K_S^0 \pi^0 \gamma$ transitions*, Phys. Rev. **D74** (2006) 111104, `arXiv:hep-ex/0608017`.

[109] S. Akar *et al.*, *The time-dependent cp asymmetry in $b^0 \to k_{res}\gamma \to \pi^+\pi^- k_s^0 \gamma$ decays*, Journal of High Energy Physics **2019** (2019) , `arXiv:1802.09433`.